IMPERIAL

Nonlinear Aeroelastic Modelling for Flexible Aircraft with Multibody Wings

Kelvin Chi-Wing Cheng

Supervised by Prof. Rafael Palacios and Dr. Andrea Castrichini

Submitted in partial fulfilment of the requirements for the degree of Doctor of Philosophy in Aeronautics and the Diploma of Imperial College London, December 2025

Department of Aeronautics

Imperial College London

SW7 2AZ

Declaration

I hereby declare that the contents of this thesis are original contributions and my own work. All work done by others that is included as part of this thesis is appropriately referenced and, where needed, credit to the author is given. Permission to include copyrighted material has been sought and stated where applicable.

The copyright of this thesis rests with the author. Unless otherwise indicated, its contents are licensed under a Creative Commons Attribution-NonCommercial 4.0 International Licence (CC BY-NC).

Under this licence, you may copy and redistribute the material in any medium or format. You may also create and distribute modified versions of the work. This is on the condition that: you credit the author and do not use it, or any derivative works, for a commercial purpose.

When reusing or sharing this work, ensure you make the licence terms clear to others by naming the licence and linking to the licence text. Where a work has been adapted, you should indicate that the work has been changed and describe those changes. Please seek permission from the copyright holder for uses of this work that are not included in this licence or permitted under UK Copyright Law.

Kelvin Chi-Wing Cheng

To my grandpa Ding-Yau.

Acknowledgements

Above all I owe my supervisors Rafael Palacios and Andrea Castrichini apologies for deadlines missed and expectations unmet, second only to the immense gratitude I feel for their extraordinary patience and kindness that kept me going through the days, and the nights. I hope I have done our time together justice. Thank you!

Thank you to the examiners of this thesis, Urban Fasel and Franco Mastroddi, for taking the time to review the work and giving me valuable feedback.

I would also like to thank my ~~painful~~ multibody buddy Álvaro, for the ideas and conversations and pints that are always right when I needed it; you've always been there for me. *¡Salud por los locos!* Thank you to Thomas Wilson, whose passion in aeroelasticity education, within and outside the walls of Airbus, is contagious. I'm grateful also to Sammi Samad and Julie Chamberlain for hosting me in Airbus Filton for my six-month placement; I must thank (blame) Adrianos, Andrea, Fabrizio, and Paolo for the lovely habits of afternoon coffees and Thursday pints. Was great to have you in London, Michael; now you'll carry the SHARPy torch in Airbus!

A substantial part of this work is based on numerical models from the aeroelastics community; I am particularly grateful to Fintan Healy, Jonathan Hilger, and Keisuke Otsuka, for giving me the opportunity to apply my work on your models, and together with Natsuki Tsushima, Markus Ritter, and Xavier Carrillo, for the conversations on the sidelines of conferences, and around the world.

I am very glad to have learnt (and hopefully will retain) so much about proper coding from everyone in the Load Control and Aeroelastics Lab; in approximate order of meeting you I thank Hui Ling, Pedro, Norberto, Álvaro, Stef, Mario, Ben, Mario, Eisuke, Isabella, and Simon. Let's keep the Christmas dinners coming!

I am truly grateful for the friends I've made along the way on my PhD journey. Shoutout to Bernardo, Chi Hin, Christian, my neighbour Elise, Guglielmo, Henrik, Kazuki, Sid, Stef, Priyam, Yasine, and y'all from undergrad, Alex, Dave, Enson, Jason, and Jeffery! Imperial Aero is a special place to me, and this is all thanks to Aaron; Maria and Siti; Jackie, Jie, and Shirin; and Clodagh of course; these 8 years have flown by with you all.

On that note I'd like to thank the people I met at the Bei Shan Tang Foundation for cheering me on and awarding me the Lee Hysan Memorial Scholarship, Lloyd who is always the trailblazer, and my form teacher Elaine Li, for she saw a spark and kindled the fire within me. This work is funded through an Industrial CASE Award; the support from UKRI EPSRC and Airbus UK is very much appreciated.

In silence my parents' support roars; from nothing they gave me everything to find anything that I enjoy; for that I'm eternally grateful. That gratitude extends to my brother; for as annoying as he can be, I know you have my back. My other brother-flatmate Godfrey (and the 4E gang!) for lifting me up, Sawney for your cuddles and snuggles and messes made. And, finally, many thanks are due to Penney. For amongst the doodles and quibbles and nibbles and giggles I count myself lucky to have you on my side. Thank you for the years past and the many more to come!

I am no equal to the masters who hew the axles of a cart.
With but a span of timber, shaped in less than a morning,
they engineer axles that bear thirty-stone loads;
across vast distances without yielding or fatigue,
steadfast and enduring through the years.

Yet the kite I devised — three long years in the making —
soared for a single day... then took off into the wind.

Mo-tzu

We are all adventurers here, I suppose,
and wild doings in wild countries
appeal to us as nothing else could do.

It is good to know that there remain
wild corners of this dreadfully civilised world.

Robert Falcon Scott

Abstract

The aviation industry's growth outlook is increasingly anchored in the transition to net-zero emissions by 2050, with more efficient aircraft an important lever in the decarbonisation pathway. High aspect-ratio wing designs promise structural weight savings, unlocked by the understanding of the dynamics of flared hinged wingtips, as a passive load alleviation mechanism. Modelling the coupled flight dynamics and aeroelastics requires careful treatment of the full system of rigid-body, aeroelastic, and constraint equations, since the wing and wingtips can independently undergo large translations, deformations and rotations. This is enabled by simulations using the nonlinear aeroelastic toolbox SHARPy capturing those nonlinearities in play.

Implementation and validation of a flexible multibody aeroelastic formulation was carried out in the SHARPy nonlinear multibody aeroelastic solver, with results benchmarked against computational and experimental references to assess the geometric and aerodynamic nonlinearities modelled. To characterise the load alleviation mechanisms and to assess the nonlinearities in full aircraft dynamic response, the formulation is put to the test on both a high-altitude long-endurance (HALE) aircraft model and a representative next-generation flexible aircraft configuration, each tested with and without freely-flying wingtips.

Parametric sweeps in the definition of the aircraft and gust for the HALE vs its hinged sibling, the H^{2}ALE, give results demonstrating that flared hinged wingtips achieve static and dynamic wing root bending moment alleviation compared to fixed configurations, with load relief mechanisms driven by hinge flare angle, wing flexibility, and wingtip mass distribution. Analysis on the flexible representative aircraft SuperFLEXOP / Hinged-SuperFLEXOP uncovers nonlinear phenomena including bifurcation at higher gust intensities where the coupled rigid-elastic-multibody system exhibits transitions between equilibrium branches. The framework demonstrates potential for design maturation of next-generation sustainable aircraft architectures, enabling virtual testing for advancing understanding of coupled multibody aeroelasticity and flight dynamics beyond the limitations of linear methods.

Contents

List of Figures **16**

List of Tables **21**

1 Introduction **23**

1.1 Achieving net-zero in aviation - exploring the roadmaps and enablers 23

1.2 The enduring significance of aeroelasticity in next-generation aircraft 27

1.3 State-of-the-art modelling approaches for flexible aircraft with multibody wings 39

1.3.1 Structural modelling 39

1.3.2 Aerodynamic modelling 42

1.3.3 Modelling of flared hinged wing tips 43

1.4 Work undertaken 44

1.4.1 Research objectives 44

1.4.2 Thesis outline 46

1.4.3 Publications 48

2 Flexible multibody dynamics **51**

2.1 Theory and implementation of the geometrically-exact beam theory 51

2.1.1 Definition of reference frames and kinematics 52

2.1.2 Flexible beam equations of motion 53

2.2 Finite element equations of motion 56

2.3 Validation: Rigid and flexible crossbeam 57

2.4 Flexible multibody formulation with Lagrange multipliers 59

2.4.1 Multibody constraints for the hinged wing tip 62

Linear velocity constraint 62

Angular velocity constraint 63

2.5 Validation: Rigid double pendulum 64

2.5.1 Reference slanted-hinge double pendulum results 67

2.6 Validation: Flexible double pendulum 67

Case $\beta = 0$ . . . 69
Case $\beta = 90°$ . . . 69
Case $\beta = 45°$ . . . 70
2.7 Validation: Multibody dynamics across beam formulations and implementations 73
2.8 Summary . . . 76

3 Modelling aeroelastic multibody systems 77
3.1 Unsteady potential flow aerodynamics . . . 77
3.1.1 Panelling at the hinge line . . . 81
3.1.2 Sectional polar correction . . . 82
3.2 Coupling of the aeroelastic solution . . . 84
3.2.1 Structure to aerodynamic coupling . . . 84
3.2.2 Aerodynamic to structure coupling . . . 85
3.3 Validation: A multibody aeroelastic wing assembly . . . 86
3.4 Validation: Code-to-code-to-experiment comparison . . . 87
3.5 Trim strategies for free-flying configurations . . . 91

4 Nonlinear aeroelasticity of a HALE aircraft with flared hinged wingtips 95
4.1 Definition of the hinged (H^2ALE) and rigidly-connected (HALE) configurations 96
4.2 Aeroelastic trim and equilibrium state . . . 98
4.3 Vertical gust response . . . 99
4.3.1 Results for different gust lengths . . . 100
$\bar{L}_g = 0.75$ s . . . 101
$\bar{L}_g = 1.5$ s . . . 102
4.3.2 Effect of flare . . . 106
4.3.3 Effect of negative flare . . . 107
4.3.4 Effect of vehicle properties . . . 108
Effect of mass distribution . . . 108
Effect of stiffness . . . 109
4.4 Lateral gust response . . . 111
4.5 Discussion . . . 115

5 Nonlinear aeroelasticity of a representative flexible aircraft with flared hinged wingtips 119
5.1 SuperFLEXOP and the Hinged-SuperFLEXOP . . . 119
5.2 Aeroelastic trim and equilibrium state . . . 120
5.3 Vertical gust response . . . 123
5.3.1 Results for different gust length . . . 124

$\bar{L}_g = 0.225$ s . . . 125
$\bar{L}_g = 0.3125$ s . . . 126
5.3.2 Effect of even higher gust intensities . . . 129
5.3.3 Effect of sectional polar corrections . . . 133
5.3.4 Effect of new trim inputs . . . 137
5.4 Concluding remarks . . . 141

6 Conclusion **145**
6.1 Summary . . . 145
6.2 Key contributions . . . 147
6.3 Future work . . . 152
6.4 Data statement . . . 155

Bibliography **157**

A Symbolic expressions for the rigid constant density double pendulum **179**
A.1 Full equations of motion . . . 179

List of Figures

1.1 Air passenger per capita and inflation adjusted cost per passenger in the past two decades, compiled with data from [6, 7, 8, 9, 10, 11, 12, 13, 14] 24
1.2 Well-to-wake emissions over the life cycle of aviation fuel, based on [20]; icons from Font Awesome [21], licensed under SIL OFL 1.1 24
1.3 Emissions reduction potential by transition measures in 2050 in each roadmap, as reproduced from [31] with permission from IATA 26
1.4 Evolution of aspect ratio in successfully-flown commercial aircraft and gliders extracted from [39], [40] 28
1.5 Artist's impression of Airbus ZEROe blended-wing-body hydrogen-powered aircraft concept [48] 29
1.6 Artist's impression of NASA–Boeing X-66A truss-braced wing sustainable flight demonstrator aircraft in flight; image from NASA [60] 30
1.7 The de Marcay-Moonen monoplane with wings folded, towed near the Arc de Triomphe in Paris; image from Histolines [72], license under Apache-2.0 31
1.8 Short Folder seaplane (S.64), serial number 81, being hoisted out from HMS Hermes with wings folded [74]; image: IWM (Q 90115) 32
1.9 Artist's impression of a Cathay Pacific Boeing 777X in flight [80], © Boeing . . 33
1.10 An air-to-air rear view of an XB-70 Valkyrie aircraft with outboard wingtips pivoted downwards [86]; image: NARA (6362754) 34
1.11 Black sealing-strips mark lines of articulation on the wings of the Rey [94]; © Reed Business Information Limited 35
1.12 AlbatrossONE Phase 1 flight test, wingtips unlocked [99] 36
1.13 A re-winged Cessna Citation VII with flared hinged wingtips assembled in the foreground, as the Airbus UpNext eXtra Performance Wing demonstrator [108] 37

2.1 Labelled quantities and frames of the flexible multibody wing assembly 53
2.2 Generic crossbeam FE model used for validation, reproduced from [193] 58
2.3 Crossbeam vertical kinematic quantities at root and tip for rigid case in time . . 60
2.4 Crossbeam vertical kinematic quantities at root and tip for flexible case in time 60

2.5 Setup of the rigid-body model 65
2.6 Tip position for the rigid double pendulum with 45° flare angle. Left: Time histories. Right: Trajectory in 3D. 68
2.7 $\boldsymbol{r}_{2_{tip}}$ time histories for $\beta = 0$, $\sigma = 1$ 70
2.8 $\boldsymbol{r}_{2_{tip}}$ time histories for $\beta = 90$, $\sigma = 1$ 70
2.9 $\boldsymbol{r}_{2_{tip}}$ time histories for $\beta = 45$, $\sigma = 1$ 71
2.10 $\boldsymbol{r}_{2_{tip}}$ time histories for $\beta = 45$, $\sigma = 0.1$ 71
2.11 $\boldsymbol{r}_{2_{tip}}$ time histories for $\beta = 45$, $\sigma = 0.1$, 10 × more elements 72
2.12 $\boldsymbol{r}_{2_{tip}}$ time histories for $\beta = 45$, $\sigma = 0.01$ 72
2.13 Time histories of free-end coordinates of double pendulum, reproduced from [198] 75
2.14 Time history comparison of the horizontal tip position for the flexible double pendulum, reproduced from [199] 76

3.1 UVLM grid boundaries with beam nodes near the hinge 82
3.2 Time histories of released wing transient response 87
3.3 Wing assembly with flared hinged wing tips 88
3.4 SHARPy equilibrium and mean LCO fold angle θ for various velocity and angle of attack combinations, overlaid on numerical and experimental data from [113] 89
3.5 SHARPy LCO fold angle θ for $u_\infty = 26.8\,\mathrm{m\,s^{-1}}$ and $\alpha = 2.5°$, against numerical and experimental data from [116] 90
3.6 Closed-loop feedback control architecture for each time step in longitudinal dynamic trim 93

4.1 Geometric definition of the T-tail HALE model with all units in meters as in [211] 97
4.2 H^{2}ALE aircraft, with flared hinged wing tips coloured in increasing flare, at trim. Note where flare angle increases, trim fold angle decreases. 97
4.3 Snapshot of H^{2}ALE-f10 with force-free UVLM wake grid coloured by circulation intensity, response to 1-cos gust with $\bar{L}_g = 1.5$ s and $\bar{U}_g = 1.6$, 2 seconds post gust encounter 98
4.4 Trim histories of control input versus corresponding states 99
4.5 Time histories of wing root bending moment, normalised by the product of aircraft weight and one-eighth span length, at various gust lengths, $\bar{U}_g = 0.5$ 100
4.6 Time histories of normalised and incremental WRBM over a range of gust intensities, $\bar{L}_g = 0.75$ s. Moment increment plots include inset with values near the first peak. 103
4.7 Instantaneous values of normalised wing root bending and torsional moment over a range of gust intensities, $\bar{L}_g = 0.75$ s 103

4.8 Time histories of hinge fold angle for the H^{2}ALE-f10, $\bar{L}_g = 0.75$ s 103
4.9 Time histories of wing dihedral/hinge vertical position relative to root over a range of gust intensities, $\bar{L}_g = 0.75$ s 104
4.10 Time histories of normalised and incremental WRBM over a range of gust intensities, $\bar{L}_g = 1.5$ s. Moment increment plots include inset with values near the first peak. 104
4.11 Instantaneous values of normalised wing root bending and torsional moment over a range of gust intensities, $\bar{L}_g = 1.5$ s 105
4.12 Time histories of hinge fold angle for the H^{2}ALE-f10, $\bar{L}_g = 1.5$ s 105
4.13 Time histories of wing dihedral/hinge vertical position relative to root over a range of gust intensities, $\bar{L}_g = 1.5$ s 105
4.14 Range of trim-peak WRBM for H^{2}ALE with varying flare angle, $\bar{L}_g = 1.5$ s, $\bar{U}_g = 1.0$ 106
4.15 Time histories of key quantities for H^{2}ALE with varying flare angle, $\bar{L}_g = 1.5$ s, $\bar{U}_g = 1.0$ 107
4.16 Time histories of key quantities for H^{2}ALE with $\beta = 0, -35°$, $\bar{L}_g = 1.5$ s, $\bar{U}_g = 1.0$ 108
4.17 Time histories of key quantities for H^{2}ALE with varying flare angle (redistributed mass), $\bar{L}_g = 1.5$ s, $\bar{U}_g = 1.0$ 108
4.18 Time histories of normalised and incremental WRBM over a range of gust intensities, $\bar{L}_g = 1.5$ s, stiffened wing assembly 110
4.19 Instantaneous values of normalised wing root bending and torsional moment over a range of gust intensities, $\bar{L}_g = 1.5$ s, stiffened wing assembly 110
4.20 Time histories of hinge fold angle for the H^{2}ALE-f10, $\bar{L}_g = 1.5$ s, stiffened wing assembly 110
4.21 Time histories of wing dihedral/hinge vertical position relative to root over a range of gust intensities, $\bar{L}_g = 1.5$ s, stiffened wing assembly 111
4.22 Time histories of key quantities for H^{2}ALE with varying flare angle (stiffened), $\bar{L}_g = 1.5$ s, $\bar{U}_g = 1.0$ 111
4.23 Time histories of hinge fold angle port and starboard at various lateral gust lengths, $\bar{U}_g = 0.5$ 112
4.24 Time histories of Euler angles in degrees and their derivatives (deg / s) at the wing root, over a range of gust intensities for lateral $\bar{L}_g = 0.5$ s 114
4.25 Time histories of wing dihedral/hinge vertical positions port and starboard, relative to root, over a range of gust intensities, lateral $\bar{L}_g = 0.5$ s 114
4.26 Time histories of hinge fold angle for H^{2}ALE-f10 port and starboard, relative to root, over a range of gust intensities, lateral $\bar{L}_g = 0.5$ s 115
4.27 Time histories of hinge fold angle port and starboard, for various flare angle, lateral $\bar{L}_g = 0.5$ s, lateral $\bar{U}_g = 0.5$ 115

5.1 Reference geometry of the Hinged-SuperFLEXOP 121
5.2 Snapshot of Hinged-SuperFLEXOP with force-free UVLM wake grid coloured by circulation intensity, response to 1-cos gust of $\bar{L}_g = 0.225$ s and a very large gust of $\bar{U}_g = 1$, 0.17 seconds post encounter 122
5.3 Trim spanwise quantities for the SuperFLEXOP and Hinged-SuperFLEXOP . . 123
5.4 Time histories of normalised wing root bending moment at various gust lengths, $\bar{U}_g = 0.1$ 124
5.5 Time histories of normalised and incremental WRBM over a range of gust intensities, $\bar{L}_g = 0.225$ s. Moment increment plots include inset with values near the first peak. 127
5.6 Instantaneous values of normalised wing root bending and torsional moment over a range of gust intensities, $\bar{L}_g = 0.225$ s. 127
5.7 Time histories of vertical displacement at the 70% span station relative to the root over a range of gust intensities, $\bar{L}_g = 0.225$ s 128
5.8 Time histories of aircraft pitch angle over a range of gust intensities, $\bar{L}_g = 0.225$ s 128
5.9 Time histories of hinge fold angle for the Hinged-SuperFLEXOP over a range of gust intensities, $\bar{L}_g = 0.225$ s 128
5.10 Time histories of normalised and incremental WRBM over a range of gust intensities, $\bar{L}_g = 0.3125$ s. Moment increment plots include inset with values near the first peak. 130
5.11 Instantaneous values of normalised wing root bending and torsional moment over a range of gust intensities, $\bar{L}_g = 0.3125$ s 130
5.12 Time histories of vertical displacement at the 70% span station relative to the root over a range of gust intensities, $\bar{L}_g = 0.3125$ s 131
5.13 Time histories of aircraft pitch angle over a range of gust intensities, $\bar{L}_g = 0.3125$ s131
5.14 Time histories of hinge fold angle for the Hinged-SuperFLEXOP over a range of gust intensities, $\bar{L}_g = 0.3125$ s 131
5.21 Lift and moment coefficient curves of the wing and tail airfoil for $\mathrm{Re} = 1.3 \times 10^6$ 133
5.15 Time histories of normalised and incremental WRBM over a range of high gust intensities, $\bar{L}_g = 0.225$ s. Moment increment plots include inset with values near the first peak. 134
5.16 Instantaneous values of normalised wing root bending and torsional moment over a range of high gust intensities, $\bar{L}_g = 0.225$ s 134
5.17 Time histories of vertical displacement at the 70% span station relative to the root over a range of high gust intensities, $\bar{L}_g = 0.225$ s 135
5.18 Time histories of aircraft pitch angle over a range of high gust intensities, $\bar{L}_g = 0.225$ s 135

5.19 Time histories of hinge fold angle for the Hinged-SuperFLEXOP over a range of high gust intensities, $\bar{L}_g = 0.225$ s 135
5.20 Single-sided amplitude spectrum of normalised WRBM for the Hinged-SuperFLEXOP over the full range of gust intensities, $\bar{L}_g = 0.225$ s. The jump at low frequencies occurs between $\bar{U}_g = 0.8$ and $\bar{U}_g = 0.92$ 136
5.22 Spanwise quantities with polar corrections at gust onset for the SuperFLEXOP and Hinged-SuperFLEXOP 137
5.23 Time histories of normalised and incremental WRBM over a range of gust intensities with polar corrections, $\bar{L}_g = 0.225$ s. Moment increment plots include inset with values near the first peak. 138
5.24 Instantaneous values of normalised wing root bending and torsional moment over a range of gust intensities with polar corrections, $\bar{L}_g = 0.225$ s 138
5.25 Time histories of vertical displacement at the 70% span station relative to the root over a range of gust intensities with polar corrections, $\bar{L}_g = 0.225$ s 139
5.26 Time histories of aircraft pitch angle over a range of gust intensities with polar corrections, $\bar{L}_g = 0.225$ s 139
5.27 Time histories of hinge fold angle for the Hinged-SuperFLEXOP over a range of gust intensities with polar corrections, $\bar{L}_g = 0.225$ s 139
5.28 Spanwise quantities with polar corrections and new trim inputs at gust onset for the SuperFLEXOP and Hinged-SuperFLEXOP 140
5.29 Time histories of normalised and incremental WRBM over a range of gust intensities with polar corrections at new trim inputs, $\bar{L}_g = 0.225$ s. Moment increment plots include inset with values near the first peak. 142
5.30 Instantaneous values of normalised wing root bending and torsional moment over a range of gust intensities with polar corrections at new trim inputs, $\bar{L}_g = 0.225$ s 142
5.31 Time histories of vertical displacement at the 70% span station relative to the root over a range of gust intensities with polar corrections at new trim inputs, $\bar{L}_g = 0.225$ s 143
5.32 Time histories of aircraft pitch angle over a range of gust intensities with polar corrections at new trim inputs $\bar{L}_g = 0.225$ s 143
5.33 Time histories of hinge fold angle for the Hinged-SuperFLEXOP over a range of gust intensities with polar corrections at new trim inputs, $\bar{L}_g = 0.225$ s 143

List of Tables

2.1 Crossbeam parameters for rigid and flexible cases 59
2.2 Simulation parameters for crossbeam in Hilger [193] and SHARPy 59
2.3 Reference pendulum parameters 67
2.4 Common model parameters for rigidity ratio $\sigma = 1$ 69
2.5 Model parameters for flexible planar pendulum in [199] 73

3.1 Parameters of flared hinge wing 86
3.2 Common simulation parameters 87
3.3 Key Parameters for flexible slender prismatic wing with wing tip 88

4.1 Comparison of trimmed values for HALE and H^2ALE 99

5.1 Simulation parameters for SuperFLEXOP and Hinged-SuperFLEXOP 120
5.2 Comparison of trimmed values for SuperFLEXOP and Hinged-SuperFLEXOP . 121
5.3 Comparison of new trim inputs for SuperFLEXOP and Hinged-SuperFLEXOP with polar corrections 140

6.1 Repositories containing research contributions in the context of this thesis . . . 155

Chapter 1

Introduction

1.1 Achieving net-zero in aviation - exploring the roadmaps and enablers

For more than three hundred thousand years homo sapiens like you and me have lived [1], loved [2], gotten ill [3], but it is only at the turn of the last century [4] have we as a species conquered the skies. Aviation, a recent entry in the long list of human technological accomplishments, has fundamentally transformed civilisation. [5] For over a century, commercial aviation has bridged geographic boundaries, enabling unprecedented levels of global mobility, economic interconnectedness, and cultural exchange. Today, air travel is more popular and affordable than ever, as 20 years of data will tell. Figure 1.1 shows, on the left axis, the ratio of global air passengers [6, 7, 8, 9, 10] to population [11, 12], and on the right axis, the ratio of global total of airline expenses, adjusted for inflation [13, 14] to air passengers [6, 7, 8, 9, 10]. Data spanning two decades tells the story of an industry that has landed in furthest corners of our planet Earth, democratising the joys of travel, endured the Pandemic [15], and climbed back to new heights.

Yet this same transformative power carries an environmental cost. Aviation's climate impact extends beyond carbon dioxide alone; airplanes emit nitrogen oxides, water vapour, soot and aerosols that drive non-CO_2 effects such as ozone formation, contrails and contrail cirrus, which together add substantially to aviation's net positive radiative forcing and warming impact. [16] The imperative for drastic intervention predates even aviation itself; Jevons paradox [17], coined in 1865, explains why; decades of improvements in aircraft and engine efficiency have reduced fuel burned per passenger-kilometre and lowered real ticket prices, but these very gains have helped make flying more accessible and attractive, shoring up demand and pushing total emissions higher. [18] It is under this backdrop that the global

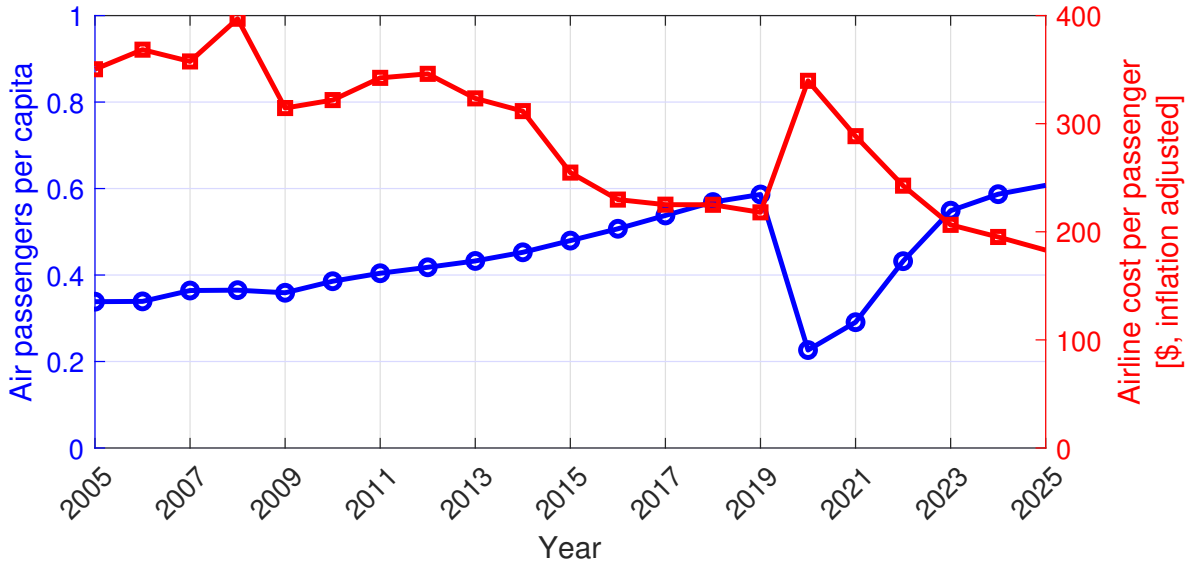


Figure 1.1: Air passenger per capita and inflation adjusted cost per passenger in the past two decades, compiled with data from [6, 7, 8, 9, 10, 11, 12, 13, 14]

aviation sector has formally pledged to achieve net-zero carbon emissions by 2050, aligning its long-term climate goals with the Paris Agreement's target. [19]

Here carbon emissions, a subset of aviation's impact on global warming, can be attributed to various sources organised from production to delivery to consumption as depicted in Figure 1.2.

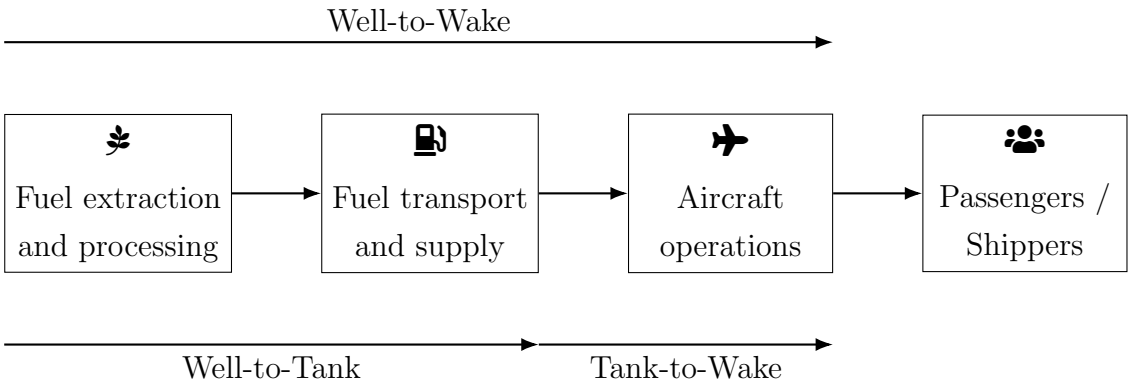


Figure 1.2: Well-to-wake emissions over the life cycle of aviation fuel, based on [20]; icons from Font Awesome [21], licensed under SIL OFL 1.1

In 2010, the International Air Transport Association (IATA) member airlines committed to an average improvement in fuel efficiency of 1.5% per year between 2010 and 2020, a cap on net aviation CO_2 emissions from 2020, and a reduction in net aviation CO_2 emissions of

50% by 2050 relative to 2005 levels. [22] The first two of these targets are declared to have been met, primarily through fleet renewal and growth in the deployment of the latest, more efficient aircraft on the market. Building on this earlier commitment, at the 77th IATA Annual General Meeting on 4 October 2021, IATA, collectively representing over 300 carriers, adopted a resolution further committing member airlines to reach net-zero Tank-to-Wake CO_2 emissions by 2050. [23]

This same Tank-to-Wake commitment was then echoed by the wider Air Transport Action Group, a multi-stakeholder partnership across the civil aviation value chain to coordinate climate action. [24] The net-zero vision is set to be achieved through the four pillars of

- Scaling up SAF production, shifting from fossil fuels to low-carbon electricity and green hydrogen
- Developing and deploying next-generation airframe and engine technologies, including electric and hydrogen-powered aircraft
- Improving air traffic management, airport operations, and systemwide efficiency
- Utilising high-quality carbon offsets (via ICAO CORSIA [25]), and investing in carbon removal technologies to address residual emissions

Soon after, at the 41st Assembly on 7 October 2022, the International Civil Aviation Organization (ICAO), as a United Nations agency enacting global aviation governance, adopted a Long-Term Global Aspirational Goal (LTAG) endorsing modified Tank-to-Wake net-zero CO_2 emissions for international aviation by 2050. [26] Though non-binding, this agreement represents the first time the UN's aviation body unified all 193 member states behind a collective net-zero objective. Countries are encouraged to work together with the ICAO, considering each of their own special circumstances and respective capabilities, to contribute to the LTAG with a State Action Plan on individual timelines.

As products of an international consensus-driven process naturally there are questions raised as to the limitations of the various ICAO initiatives. Jing et al. [27] pointed out the need for the industry and policy-makers to understand the full life-cycle (well-to-wake) greenhouse gas emissions of traditional petroleum jet fuel to put the benefits of SAF in context. Larsson et al. [28] cited the lack of measures addressing non-CO_2 emissions, and other feasible national and international levers such as taxation and quota regulation for bio-fuels. Mayer et al. [29] warned against weak leadership from ICAO as a red herring to forestall regulators from more aggressive national-level actions. Gossling et al. [30] questioned the

accurate monitoring of progress towards ICAO goals, in particular scope 3 emissions (all indirect emissions within the value chain) from airlines that are often missing or underreported.

Nonetheless the international community has forged on to chart out the roadmaps to net zero on a more granular level. Figure 1.3 presents a side-by-side view of selected aviation sector decarbonisation roadmaps, quantifying the projected shares of emissions mitigation strategies adding up to 100% abatement. The proportional contributions of respectively, technological improvements, operational enhancements, sustainable aviation fuels (both bio-based and power-to-liquid), low-carbon alternatives, direct hydrogen or electric propulsion, demand reduction, as well as carbon removal or market-based measures, are presented for each of the roadmaps.

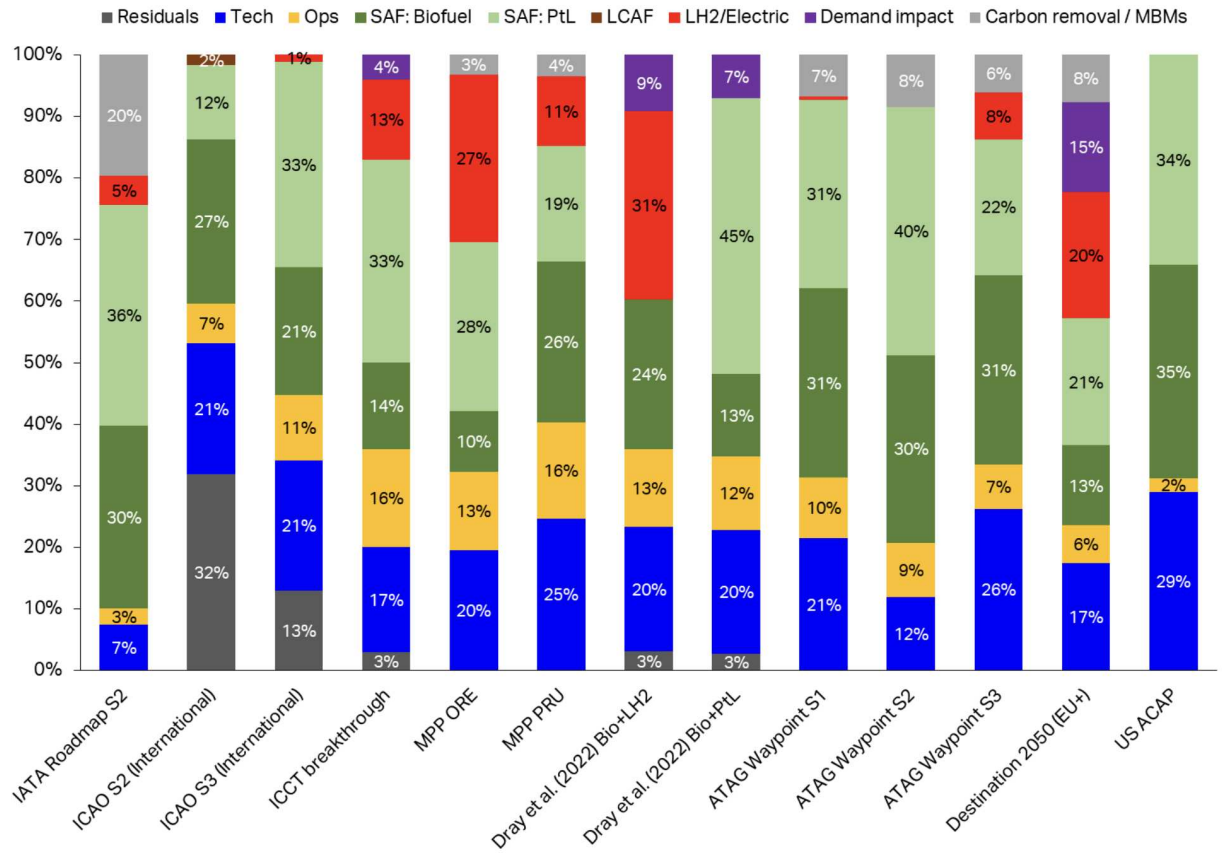


Figure 1.3: Emissions reduction potential by transition measures in 2050 in each roadmap, as reproduced from [31] with permission from IATA

Where across all roadmaps it is almost unanimous that alternative fuel and propulsion system would account for more than half of the intended projected abatement, technology efficiency improvements for conventional aircraft across most roadmaps, apart from the IATA Roadmap S2, gives around a share of 20% in 2050. For the IATA Roadmap S2 it is assumed,

perhaps optimistically, that all technological improvements in the pipeline, a result of the relatively slow technological innovation in aircraft in the decades past [32], is already realised (that A320neos will replace all A320s). [31] The other roadmaps assume aircraft technology to be frozen, i.e. all subsequent increment in technology including fleet replacement with currently-available aircraft is captured as abatement.

The 20%-by-2050 reduction in emissions from technology spans advanced airframe designs, improved engine architectures, integration of lightweight composite materials, all converging towards higher aerodynamic and thermal efficiency in next-generation aircraft. (Chapter 5, [33])

Core to many of the envisioned concepts is the exploitation of larger spans and lighter structures to reduce induced drag while managing the increasing flexibility, which fundamentally alters the interaction between aerodynamic loads and structural response across the flight envelope. This motivates a focus on coupled aeroelasticity and multibody dynamics, a central tenet of this thesis and are explored in detail in the next section.

1.2 The enduring significance of aeroelasticity in next-generation aircraft

Throughout the brief 100 years history of manned powered flight, the importance of large span for aircraft design was uncovered early and emphasised upon, as a fundamental driver to reduce aircraft induced drag, versus weight and manoeuvrability. [34] The relationship of span with induced drag at fixed span or structural weight is explored by Prandtl's work [35, 36] on the lifting line theory. Downwash from shed vorticity changes the effective angle of incidence on the span, rotating the lift vector, with the contribution to drag later coined as the induced drag, as

$$C_{D_i} = \frac{C_L^2}{\pi\, e\, AR}, \tag{1.1}$$

where the effect of higher span b, hence aspect ratio $AR = b^2/S$, on reducing induced drag is clearly laid out. Prandtl first concluded that the optimal span load for minimised induced drag at low speeds for a given span is elliptical, giving e the span efficiency factor[1]. He then revised his conclusion, conceding that if he had fixed the structural weight instead, there exists a wing solution of, specifically 22%, longer span that gives 11% less induced drag.

[1] not to be confused with the Oswald efficiency factor [37], by William Oswald, PhD advisee of Theodore von Kármán, himself advisee of Prandtl!

Those findings underpin further research in the trade-off [38], and the motivation for more slender wings in aeroelastic design across different aircraft classes, as can be seen in Figure 1.4.

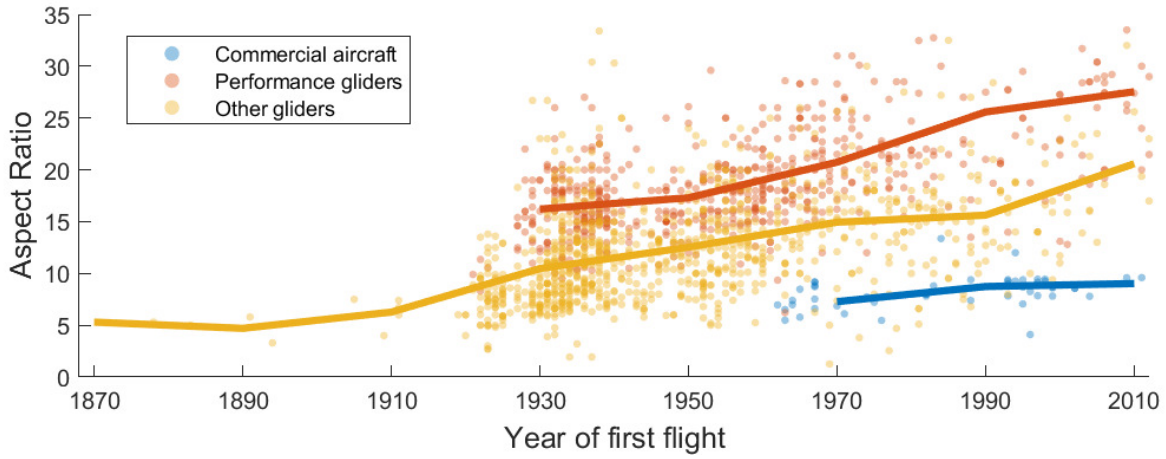


Figure 1.4: Evolution of aspect ratio in successfully-flown commercial aircraft and gliders extracted from [39], [40]

The historical evolution of aspect ratio in commercial aircraft versus gliders, despite their different performance goals and philosophy, has continuously increased with time. This should be understood as a product of compromise in aircraft design, as structural considerations, evolved and suitably relaxed with the availability of cutting-edge materials science and manufacturing technologies, put an upper limit to the aerodynamic efficiency gains from the ability of long and slender wings to reduce the adverse impact of three-dimensional flow effects, with the biggest example in recent civil aviation history being the Dreamliner [41], enabled by the commercial scaling up of the carbon-fiber reinforced polymer manufacturing. [42] It is through recognising the interplay of competing subdiscipline requirements and dynamics, here specifically between aerodynamic, elastic, and inertial forcing, that gave rise to the field of aeroelasticity, with the developments since summarised in several textbooks. [43, 44, 45, 46]

The aerospace industry has been working to develop novel aircraft configurations to meet the net zero target and the various design constraints imposed, since with the current architecture and paradigm of wing design, it is widely accepted that by fine-tuning the global aero-structural design of current wings only single digit weight savings can be achieved. [47]

One of such concepts, dating back to the last century, is the blended wing body (BWB) design. [49] Rather than the traditional tube-and-wing configuration that has dominated



Figure 1.5: Artist's impression of Airbus ZEROe blended-wing-body hydrogen-powered aircraft concept [48]

aviation for nearly a century, BWB designs integrate the fuselage and wings into a single, blended lifting surface that generates lift across the entire aircraft structure, promising much reduced parasitic drag by a drastic reduction of aircraft wetted surface. [50, 51] Recent directions in this space include the Boeing-NASA Langley effort - the X-48 [52], succeeded by the JetZero full-scale demonstrator, with conventional off-the-shelf propulsion, backed by the US DoD [53], slated for flight in 2027. The MAVERIC by Airbus UpNext is the European attempt to explore flight control for a tailless design. [54] Subsequently, it is incorporated into one of the concepts of the Airbus ZEROe hydrogen-powered aircraft program (Figure 1.5) [55], with the ambition to accelerate the entire liquid hydrogen (LH_2) ecosystem by the 2050 deadline, with that being an active area of research. [56, 57, 58, 59]

Other emerging configurations for net-zero mostly conform to the tube-and-wing configuration, and achieve the predicted efficiency gains through increased wing span and re-



Figure 1.6: Artist's impression of NASA–Boeing X-66A truss-braced wing sustainable flight demonstrator aircraft in flight; image from NASA [60]

duced chord, translating to a higher aspect ratio. One of such is the strut-braced, or truss-braced wing (SBW or TBW). [61] To disambiguate between the two, the former is a specific configuration within the latter, and both share, as a baseline, external struts supporting high-aspect-ratio wings to reduce the resultant, higher, bending loads by absorbing and providing alternate loading paths. Extra jury struts are used in the TBW architecture to increase buckling margins for both the main strut and the wing and to redistribute loads. Boeing with NASA Langley worked on the Subsonic Ultra-Green Aircraft Research (SUGAR) project, which established the viability of the TBW concept well into the transonic regime of Mach 0.80. [62] The research evolved into the X-66 Sustainable Flight Demonstrator (Figure 1.6), a MD-90 retrofitted with transonic truss-braced wings (TTBW) planned to fly in 2028 as part of America's answer to net-zero carbon emissions by 2050 [63], until it was paused in 2025. [64] Key publications include Bhatia et al. [65] describing the sensitivities to design variables of structural and aeroelastic performance, Chakraborty et al. [66] on a comparative multidisciplinary design optimisation studies establishing superior performance of the one-jury TBW system, and Wells et al. [67] on future research needs on the TTBW concept to realisation, particularly in the low-speed, deep stall, and icing regimes. It is also worth noting that in many of the demonstrators a structurally pin-jointed (with smooth aerodynamic fairing) wing-strut junction is theorised and tested [62, 68, 69], meaning a flexible multibody formulation can be appropriate to model the dynamics of the system.



Figure 1.7: The de Marcay-Moonen monoplane with wings folded, towed near the Arc de Triomphe in Paris; image from Histolines [72], license under Apache-2.0

Another possible avenue to support an elongated slender wing, i.e. a high aspect ratio wing (HARW), without additional structural elements extended from the fuselage (and also, of course, so that it would satisfy airport gate width constraints), would be the use of flared hinged wings [70, 71], in nature a flexible multibody wing capable of folding at the hinge connection outboard. We are interested in particularly ones that allow for free-flapping motion inflight akin to that of birds, to exploit the potential gust load alleviation and manoeuvring advantages, whereas when locked: extended at 0° about the hinge line relative to the wing for cruising at maximum aerodynamic efficiency, and upwards at 90° for taxiing to comply with gate restrictions.

Arguably the most important design feature of the hinge is the flare angle for the free-

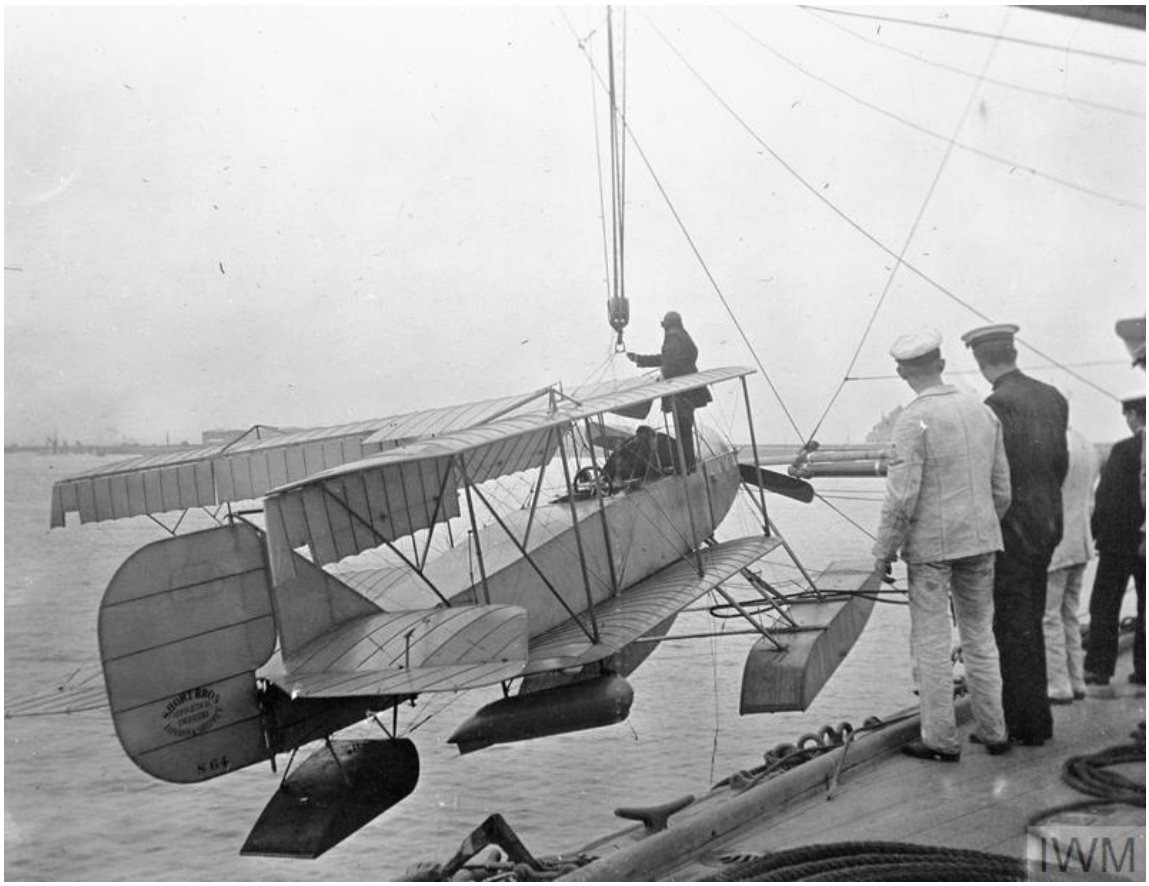


Figure 1.8: Short Folder seaplane (S.64), serial number 81, being hoisted out from HMS Hermes with wings folded [74]; image: IWM (Q 90115)

flying version of the concept - this describes how the hinge axis is oriented with respect to the freestream direction. A hinge axis pointing towards the centreline downstream (positive flare angle) produces a restoring moment by the change of angle of incidence due to rotation of the wing tips when perturbed in either direction from trim, ensuring that the mechanism is statically stable. This mechanism is analogous to the use of articulated blades in rotorcraft design, most notably in the Cierva C.4, which allows the advancing blade to flap upwards passively and thereby reduce the effective angle of attack, overcoming the dissymmetry of lift problem that had prevented earlier autogyro designs from achieving controlled, stable flight. [73]

Now looking back in history the idea of putting multibody mechanisms on the wing is certainly not new; in fact it is almost as old as powered flight itself. In 1909, the Short brothers [75, 76], having been unsuccessful in flying their first aircraft the Short No.1 biplane, obtained a license to build copies of the Wright design in Britain. While the de Marçay-Moonen monoplane (Figure 1.7) [77, 78, 79] had pioneered the folding-wing mechanism for



Figure 1.9: Artist's impression of a Cathay Pacific Boeing 777X in flight [80], © Boeing

seaplanes in 1911, the Short brothers subsequently developed the technology further, creating naval aircraft with wings that could be folded back to lie alongside the fuselage, enabling efficient stowage on warships. The family of early Short aircraft that feature the folding mechanism is fittingly called the Short Folder (Figure 1.8), within which the experimental S.41, the first of its kind, already has wings that can be unfolded from the cockpit, albeit sensibly only when on ground.

The first commercial civil aircraft to feature folding wing tips for meeting ground width restrictions was going to be the 777-200 series; Boeing had obtained a patent for the feature as early as 1995 [81], and had listed folding wing-tip related conditions under optional equipment in the type certificate. [82] It was reported that there were interest that didn't materialise on the order book, due to the additional complexities of the original 22-ft wing-tip concept (which must have included the outboard ailerons) as pitched to airlines, for a variant of the 777-200 to fit into 767 or DC-10-enabled gates. [83] That concept is brought back to life in the latest 777-X series (Figure 1.9); despite the delays to the overall program [84], the FAA has issued guidance to airports for the proper handling and accommodations for the Boeing 777 with folding wingtips [85], essentially to treat the aircraft as the smaller ADG-V type (eg. existing B777 Series/B787/A330 Family) for taxi and apron movement with tips folded; and of course when the tips are extended, as the largest ADG-VI type (eg. B747/A380). It is worth noting that the memorandum also included a call for airports to include contingency provisions in terms of apron operations and separation for the unlikely event that the fold-

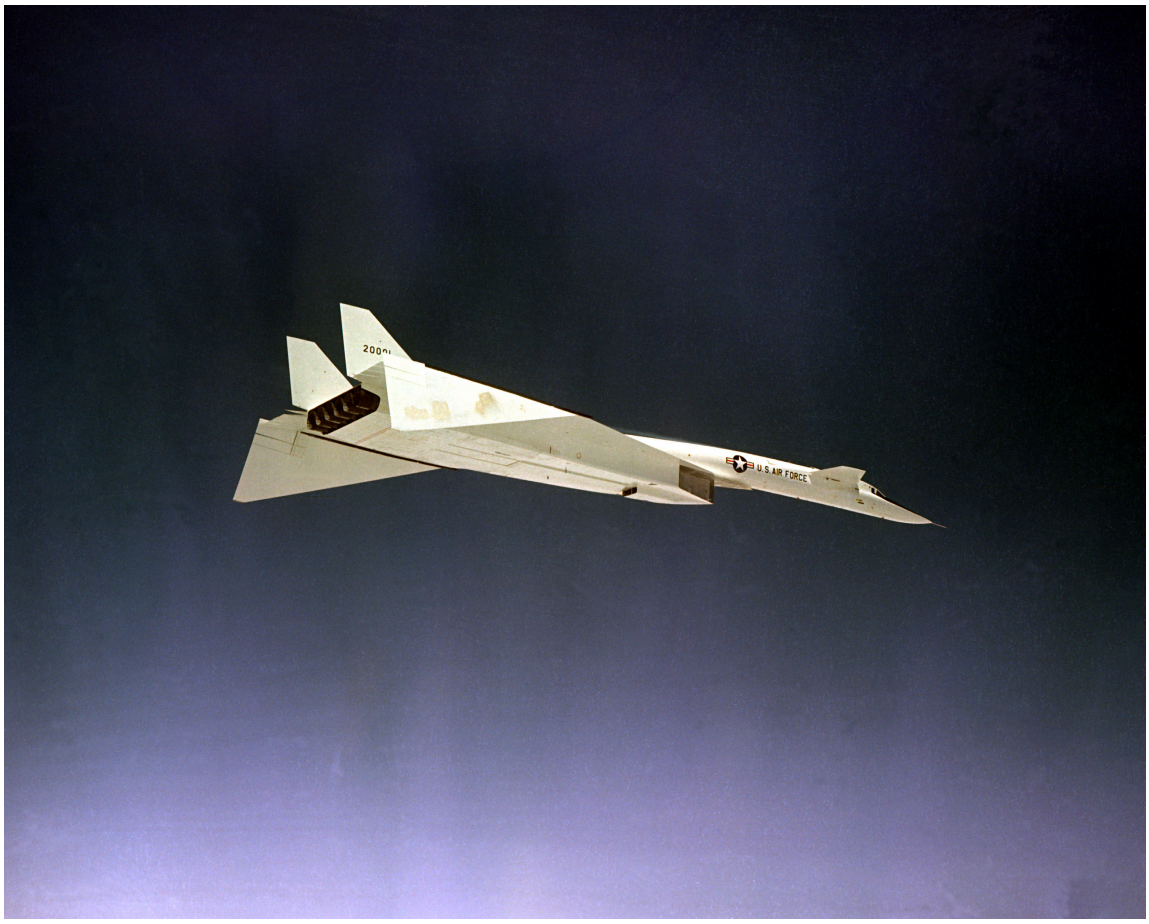


Figure 1.10: An air-to-air rear view of an XB-70 Valkyrie aircraft with outboard wingtips pivoted downwards [86]; image: NARA (6362754)

ing mechanism is inoperative and the aircraft must taxi with them extended, highlighting how the potential failure cases of novel concepts, as duly expected, drive operational planning.

Whereas the above folding concepts are all not (at least as intended by the designer) operated inflight, the efficiency gains can be summarised as the ability to operate at a different span on ground versus in flight. It is then worth exploring another class of the folding concept, where the wing tips are actuated, actively or passively, to achieve efficiency gains in atmospheric flight.

For that we first turn to the XB-70 "Valkyrie" (Figure 1.10) [87, 88, 89]; its outer wing tips, or more accurately panels (as they are ∼40% span), were designed to be lowered to about 25° for transonic/supersonic transition through to around Mach 1.4, and to around 65° for sustained supersonic cruise up to Mach 3+. The wing tips constitutes the largest movable lifting devices flown on an aircraft of this class, to the point some argue it should

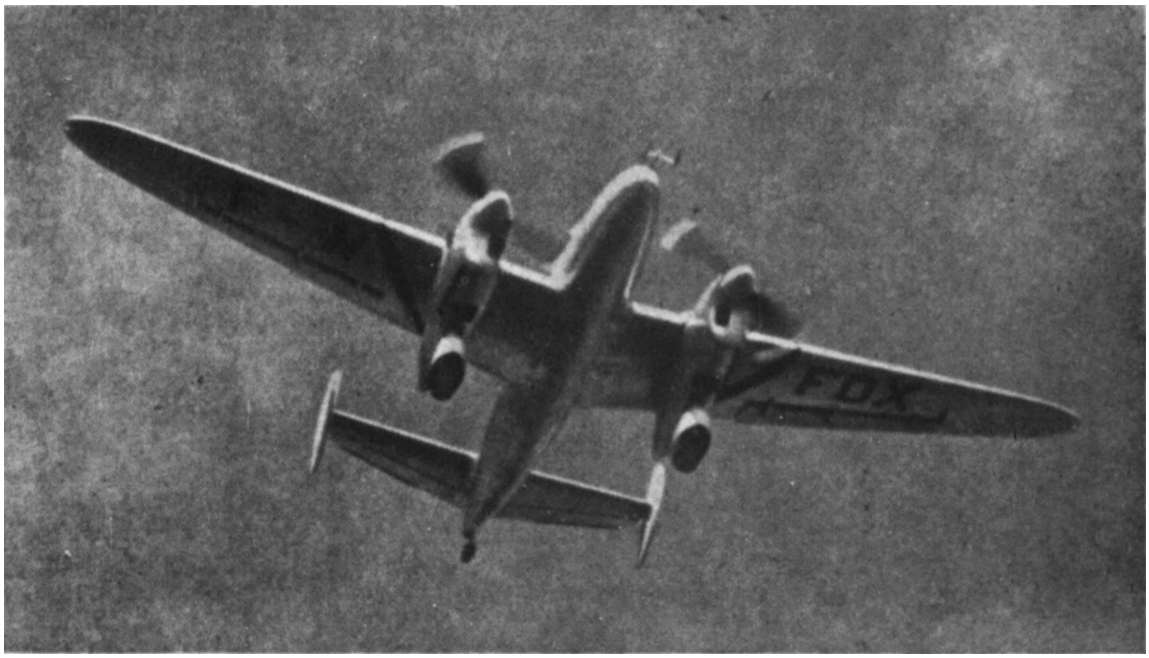


Figure 1.11: Black sealing-strips mark lines of articulation on the wings of the Rey [94]; © Reed Business Information Limited

be considered a morphing aircraft [90, 91] by virtue of the large effective change in span with wingtip actuation. [92] On the delta wings of the Valkyrie, deflecting the wing tips downwards as speed increases is done mainly to increase compression lift by capturing the shockwaves from the front body and wing better, maintaining a higher pressure region under the wing, countering the rearward shift of the centre of lift as the aircraft goes supersonic to reduce trim drag, and has the added benefit of providing extra directional stability. [93] Dussart et al. in the cited paper also drew inspiration from the Valkyrie to assess scalability of the folding mechanism to a conventional civil aircraft in terms of the dimensions and actuation loads, and established the feasibility of controlled in-flight folding.

The opposite of which would be to leverage the passive load alleviation properties of a free-flying wing tip [95], first patented in 1938 by Rouanet and Rey. Illustrations accompanying the patent application clearly shows a flared hinge axis, as described in the text, that

> *These and other objects of the invention are attained in an aircraft in which each supporting wing is pivoted to the central body about an axis which is oblique to the longitudinal plane of symmetry of the machine and whose direction is such as to obtain, during the pivoting movement of the wing under the action of the aerodynamic overloads to which it is subjected, a variation of the incidence in the proper direction for automatically limiting said overloads, the maintenance*



Figure 1.12: AlbatrossONE Phase 1 flight test, wingtips unlocked [99]

> *of the wing in the position of equilibrium being ensured by elastic and eventually damping connections whose deformation under the action of said overloads will permit a pivoting of the wing on said axis.*

The concept was then proven experimentally, rather remarkably by the first half of the 20th century by the duo, on the Rey R.1. (Figure 1.11) [96] It was reported that flight testing campaign was conducted both with the wings rigidly locked and free to rotate. A "considerable" [97], otherwise quoted at 60% [98] reduction was achieved in the gust wing stresses, and increased safety was ensured even under turbulent conditions, presumably because the flare angle all but guaranteed static stability of the free-flying wing tips. It is also worth noting that the Rey R.1., unlike the illustrations in the patent, chose to place the hinge outboard of the propellers, presumably to avoid any potential thrust induced instabilities and the additional complexities that are not warranted in this prototype aircraft.

The flared hinged wing concept never quite took off again until the very recent AlbatrossONE demonstrator (Figure 1.12), an Airbus-led sub-scale UAV based on a A321-like planform aimed to test the biomimetic flared hinged wing tips known as the *Semi Aeroelastic Hinge*, as a proof-of-concept for potential adoption in the next generation aircraft design program. [100, 101, 102] Phase 1 demonstrated qualitatively the static and dynamic stability of the wing tips in action with gust encounters, as well as the load alleviation of free flying wing tips when compared to the locked case. [103] Phase 2 returned with even longer wing tips in gate-to-gate testing, as well as in flight release of wing tips and post-gust recovery, and the safe landing of the aircraft with unlocked wing tips without wingtip strike. [104] Airbus is

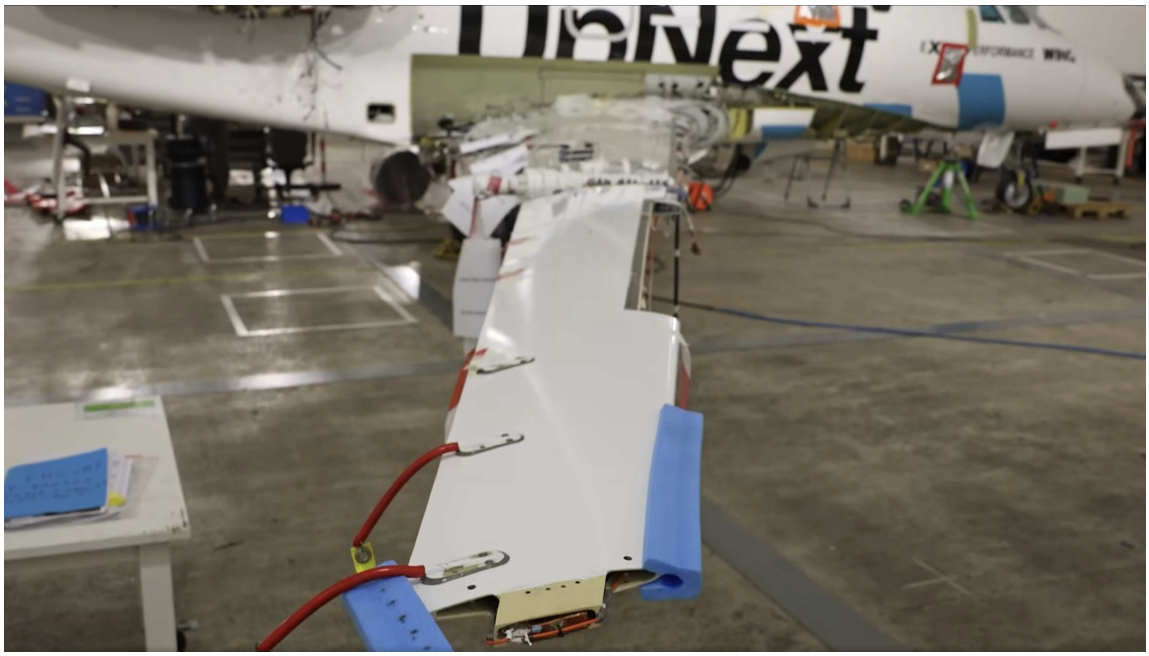


Figure 1.13: A re-winged Cessna Citation VII with flared hinged wingtips assembled in the foreground, as the Airbus UpNext eXtra Performance Wing demonstrator [108]

refining and testing the technology in the upcoming eXtra Performance Wing demonstrator (Figure 1.13), with accompanying investment in the simulation environment, notably the HINGE model developed by Mastracci et al. [105], to better capture the relevant physics. [106, 107]

Previous studies have demonstrated that flared hinged wings can provide both static and dynamic load alleviation; where the static load alleviation is mostly a function of the (positive) flare angle, and the dynamic load alleviation in a vertical 1-cos gust response is improved with the presence of flare, reduced wingtip mass, and lower hinge stiffness [70]. Subsequent static analyses in rectilinear flight have shown that, at higher angles of attack, the wingtip equilibrium angle is driven by the geometric nonlinearities, as well as the fact that sideslip angle changes the effective flare angle of the hinges. [109] Dynamic studies have also shown that load alleviation with hinged configuration appears both under vertical and lateral gusts, and that the effects of nonlinearities seen in the wingtip response do not readily translate to the main airframe. [110] Separately the observation that a lighter wing tip would react faster to the incoming vertical gust, and provide more significant load alleviation of the first positive peak load (whilst worsening the first negative peak load, and introducing extra oscillations with the wingtip flapping) is verified experimentally and numerically in [111]. A prior independent experimental campaign confirms the relative alleviation / worsening of the

first positive and negative peaks and subsequent transient oscillations of wing tip and associated loads, and also provides the sensitivity with regards to the gust length. [112] Major mechanisms of the geometric nonlinearities are identified and discussed, in the context of an experimental-numerical comparison in [113], and have also established that sideslip has little impact on the nonlinear load alleviation properties of the wing tip without rigid-body modes. [114]

Much work has been done in both the modelling and experimentation aspects of the problem and computational results have largely established the quasi-steady aeroelastic performance of flared hinged wings. Recent advances have been made in multiple directions, assessing the viability of such a wingtip device, all converging to the eventual goal of realising the concept in a commercial transport aircraft - these include a better understanding of the impact of wing stiffness and release timing [115] on the load-alleviating properties of the mechanism, the stability boundary as a function of an additional trim device on the wing tip, model parameters, and types of nonlinearities involved [116], the folding wing tips featuring in a scaled wind tunnel model aircraft with high aspect ratio wings [69], the extrapolation of wind tunnel results to a full-size model via scaling methods [117], the improvements on roll performance by reducing the roll damping and increasing the peak acceleration achieved seen on a scaled model in wind tunnel tests and associated numerical modelling [118], and the assessment of varying degrees of roll manoeuvrability by control surface location and dynamic pressure in the transonic regime. [119]

All of these directions for future aircraft design innovation point to the importance of modelling and testing; where ground and flight testing are often still the golden standard to certification, the growing confidence in aviation digital twins [120] and virtual testing means the gap is, and will be closing, pending the maturity of simulation techniques and gradual acceptance in regulatory frameworks. [121, 122] Before full Certification by Analysis (CbA) becomes reality, much work is needed to develop the numerical methods applicable for the technologies simulated - here we take the flared hinged wing tips as an example. The use of a flexible multibody formulation allows the hinge DOFs, large rotations, and geometric nonlinearities to be captured alongside wing bending–torsion, enabling prediction of e.g. tip fold angles, handling qualities, and load alleviation mechanisms that are inaccessible to rigid or single-body elastic models. Time-domain aeroelastic couplings are useful for example in reproducing the dynamic behaviour and stability observed in freely flapping tips, quantifying changes in wing-root bending, and informing robust control design that considers the in flight locking and release of wing tips. The work in building simulation capabilities, especially in aeroelastics coupled with multibody and rigid-body dynamics, generalises to other emerging

concepts - TTBW/SBW with pin-jointed junctions, BWB vs susceptibility to body-freedom flutter, morphing surfaces and hence time-varying aeroelastics; where advancements hinge on adequately resolving the coupled aerodynamic, structural, and rigid-body dynamics that govern performance.

1.3 State-of-the-art modelling approaches for flexible aircraft with multibody wings

We can now discuss the existing methods to model flexible aircraft with multibody wings, bearing in mind the compromise between simulation effort and captured physical processes. A review of the range of computational methods available for the aeroelastic analysis of flexible aircraft can be found in [123, 124, 125], whereas the reader can refer to [126, 127] for period-defining perspectives of the frontiers-then in computational aeroelasticity.

1.3.1 Structural modelling

Across a hierarchy of structural models, one typically moves from 1D beams, to 2D shells/plates, to 3D solids, trading geometric idealisations for degrees of freedom, and computational cost per element. Higher dimensional elements do not automatically mean higher accuracy; the most accurate model is the simplest one of which kinematics, constitutive assumptions, and discretisation resolve the governing physics of interest. In practice, beams are effective for slender lifting surfaces and aeroservoelastic studies when sectional properties capture bending–torsion–shear couplings; shells/plates excel for thin-walled airframes where through-thickness behaviour is well represented by plate/shell kinematics; and 3D solids are preferred for thick regions, joints, local stress hot spots, or complex materials and contact.

The reason why full 3D CSM is uncommon (though demonstrated in Yuan et al. [128]) in high aspect ratio wing aeroelasticity is that it offers little gain in accuracy of the physics involved, for the high workflow-setup and computational costs. Reduced structural models deliver adequate accuracy, and have been the powerhouse of simulating structural dynamics in the aeroelastics community.

Classical beam structural mechanics uses *a priori* assumptions about the kinematics to reduce the 3D continuum to 1D; quantities that only vary in the beam axis, assuming small deflections. The Euler-Bernoulli beam [129, 130] assumes cross-sections remain planar and

orthogonal to the neutral axis; the more general Timoshenko–Ehrenfest formulation [131] relaxes orthogonality to allow for shear deformations. They are considered linear, since geometrically, strains are linear with respect to displacements and/or rotations, and materially, the beam follows a linear constitutive relation. The linearity allows the structural dynamics be expressed readily in modal coordinates, where the relevant low frequency modes to the dynamics can be selected for the linear beam modal model, to be further coupled with linearised unsteady aerodynamics for fast and efficient analysis, prevalently in the industry, and supported by commercial off-the-shelf packages such as MSC NASTRAN.

For high aspect ratio wings, the fact that the span can be seen as the dominant length scale means the wings behave as slender structures, where deflections and stresses are primarily governed by bending and twisting along the span direction, perfect for 1D beam modelling. The dominant aeroelastic phenomena (flutter, divergence, gust response) operates in the typically low natural frequencies of the bending and torsional modes, readily predicted by 1D beam models with minimal computational effort. However, classical 1D beam models are not well-equipped to handle large displacements and rotations because of the inherent assumptions of beam kinematics and small amplitudes; that is where geometrically nonlinear composite beam models shine. To obtain a the nonlinear 1D beam model as a condensation of the 3D continuum, there are many avenues to proceed [132, 133, 134, 135, 136] to determine the appropriate mass and stiffness properties along the beam.

The process to then derive the nonlinear equations is described in detail in [46]. The choice of kinematic description is important, as it directly influences the capability to capture geometric nonlinearities due to large deformations. Four main formulation families for nonlinear 1D beams are described here: displacement-based geometrically-exact formulations employ nodal displacements and finite rotations as independent state variables; strain-based formulations adopt curvatures and axial strains as primary variables; the fully intrinsic formulation uses velocities and internal force/moment resultants as system states, in both of which spatial configuration is reconstructed through integration; whereas in the case of Absolute Nodal Coordinate Formulation (ANCF), deformations are parametrised using absolute nodal positions and rotations through position vector gradients evaluated globally. Following selection of the appropriate formulation, the system Lagrangian is constructed in terms of the chosen state variables, the weak form is derived from Hamilton's principle, and the resulting expression is discretised via finite elements to generate the governing equations, as in Section 2.1.

Geometrically-exact formulations were pioneered by Reissner [137] for two-dimensional

beam theory and subsequently extended to general three-dimensional dynamics by Simo. [138] The displacement/rotation-based model was further developed in [139, 140, 141] as the nonlinear composite beam theory, that takes into account composite materials with arbitrary anisotropy, transverse shearing deformations, and torsional warping effects. The choice of rotation parameters is open; Euler angles [142], while intuitive as the rotation about intrinsic or extrinsic axes, suffers from gimbal lock, in which a degree of freedom is lost, leading to singularities in the representation. Another option, commonly used in these formulations, is the Cartesian Rotation Vector (CRV); despite the fact that the use of quaternions [143] in finite rotation of beams [144] would avoid the issue of singularity completely, CRVs provides a minimal three-parameter representation of rotation that enables analytical derivation of tangent operators and consistent linearisation for Newton–Raphson iterations, and for small-to-moderate rotations, as typically encountered in aeroelastic simulations (as opposed to e.g. in robotics where the $\pm 90^\circ$ singularity is often crossed), it remains well-behaved with the singularity rarely encountered in practice. Géradin and Cardona [145, 146] developed a complete coupled rigid-flexible multibody framework employing Cartesian rotation vector parametrisation, enabling the formulation to account for rigid body motion through explicit reference node tracking and hence a unified simultaneous solution of coupled rigid and flexible dynamics equations. Ibrahimbegovic [147, 148] conducted a comparative analysis on the common rotation parametrisations and further demonstrated that the incremental Cartesian rotation vectors, with multiplicative rather than additive updates to the rotation, provide the optimal balance between minimal degrees of freedom (three parameters), elimination of singularities through local incremental formulation, and computational simplicity in linearisation procedures. Subsequently, Jelenić and Crisfield [149, 150] identified that the naive additive interpolation of rotation parameters violates objectivity in finite element implementations of geometrically-exact beams, i.e. the strain field is not invariant under rigid-body rotations due to the non-commutative nature of rotations in 3D space. In the absence of strategies to remove the reliance on additive rotation interpolation, such as with the use of director vectors [151, 152, 153], the use of higher order beam elements together with finer discretisation was shown to reduce associated errors and improve convergence. [154, 155]

Hodges [156] first introduced a mixed variational formulation based on exact intrinsic equations for dynamics of moving beams, treating both kinematic variables (displacement/rotation) and intrinsic variables (local velocities and generalised strains) as independent unknowns. This was later extended to a fully intrinsic geometrically exact theory, which formulates the complete governing equations solely in terms of the intrinsic variables, for initially curved and twisted anisotropic beams. [157] The mixed formulation avoids locking by treating stress resultants and strains as independent variables, thereby preventing the artifi-

cial stiffness seen in purely displacement-based beam models. The exact intrinsic equations contains only quadratic nonlinearities and is first order in both time and space, improving convergence. The dependencies on the parametrisation of displacements and rotations are removed, removing also the risk of singularities in rotations, and on the flipside, post-processing is required to recover the beam orientation. This made imposing displacement-level constraint on intrinsic beams cumbersome if not impossible, until it was only recently achieved in [158].

The strain-based formulation [159, 160, 161, 162, 163] employs generalised strains as primary variables, rather than nodal displacements or rotations. As before, the choice of adopting strains as independent variables also circumvent the singularity issues associated with naive rotation parametrisation. Likewise, the spatial configuration of the beam is subsequently reconstructed. A defining advantage of the strain-based approach is that the stiffness matrix is constant. Nonetheless, the strain-based description demands careful attention to boundary conditions and initial geometry specification. Refs [159, 164, 119] demonstrate successive approaches to multibody coupling.

The Absolute Nodal Coordinate Formulation (ANCF) [165, 166, 167], and later reviewed by [168, 169], distinguishes itself by parametrising beam deformations through absolute nodal positions and global gradient vectors, rather than through local strain or rotational measures. Complementary to the strain-based approach where the stiffness matrix is constant, in ANCF the mass matrix remains constant throughout the analysis. That comes at the cost of introducing highly nonlinear internal forces. ANCF elements also frequently require higher-order interpolation [170] or gradient-deficient elements [171] to mitigate locking, which can otherwise degrade convergence and performance. [172] Due to the parametrisation chosen, some multibody conditions such as the spherical and pin joints, while highly nonlinear in geometrically-exact formulations, appear in ANCF as linear equations. As a results there is extensive literature in ANCF multibody systems. [173, 172, 174, 175, 176, 177]

1.3.2 Aerodynamic modelling

The chosen nonlinear beam formulation coupled with multibody dynamics, mostly by utilising Lagrange multipliers [178], is integrated with a choice of aerodynamic frameworks, spanning a spectrum from low to high fidelity as before. The selection is determined by computational cost, physical assumptions, and ease of coupling considerations. Low-fidelity approaches employ classical analytical theories such as Theodorsen's theory [179] and Wagner's indicial functions [180], which provide computationally efficient formulations for small-perturbation unsteady aerodynamics. Mid-fidelity methods include the Doublet-Lattice Method (DLM)

[181] and the Unsteady Vortex Lattice Method (UVLM) [182, 183], which represents an optimal compromise between computational efficiency and modelling fidelity. High-fidelity approaches leverage computational fluid dynamics (CFD) solvers based on unsteady Euler and RANS equations, capturing nonlinear phenomena that are essential for transonic regimes, complemented more recently by machine-learning-based surrogate models trained on CFD data. [184]

For the implemented nonlinear 1D beam formulation, the Unsteady Vortex Lattice Method (UVLM) emerges as the preferred choice. [185] Recent enhancements to the UVLM framework on which this work builds are detailed in [186] and so will be omitted here.

1.3.3 Modelling of flared hinged wing tips

In terms of the numerical modelling techniques employed, some developments have been necessary in structure and aerodynamic methods. A number of structural studies have used modal-superposition based methods [70, 112, 115, 111], to enable simulations using MSC NASTRAN. The flared hinged wing tips often introduce geometric nonlinearities, and formulations have been derived based on the equations of motion for a rigid flared hinged wing tip attached to the (linear) inner wing. [109, 110, 114, 118, 116] Another class of methods obtain linearised models about the nonlinear equilibrium by iterations of corrected follower-force aeroelastic simulation. [113] To fully capture the geometric nonlinearities, a nonlinear strain-based geometrically exact beam formulation was used in [119] for coupled flexible inner wing and wing tips. As for the aerodynamic modelling, most previous studies utilised doublet lattice methods (DLM), both in the canonical form [70, 111, 115], and in the augmented form where corrections are applied to approximate follower aerodynamic forces, by applying a cosine relationship between inner wing and wing tips in the generalised aerodynamic coefficients matrix [109] for quasi-steady results, later extended to unsteady cases. [110] Follower-force aerodynamic models are also obtained through an iterative FSI process as described in [113]. Other studies have leveraged different aerodynamic models in strategy and fidelity: 1D calculation of lift from a defined polar allows for easy corrections for geometric nonlinearities [112], which readily extends to modified strip theory in 2D [118], on top of which aerodynamic nonlinearities can be considered. [116] The vortex lattice method (VLM) was implemented in [114] which lends itself to a native description of the deflected panel geometry. Finally, method of segments leveraging steady CFD solutions of the full model has been developed in [119]. They build cross-sectional surrogate models from the CFD results to capture quasi-steady transonic aerodynamic nonlinearities.

To profile the transient response of the wing assembly with the hinge mechanism it is essential that the nonlinear effects of large displacements and rotations are incorporated, both in the main, usually flexible wing, as well as the wing tips, which can assume a wide range of configurations depending on dynamical conditions. It is often computationally prohibitive to perform trade studies on the aeroelastic wing assembly with high fidelity tools. Therefore, a multibody solver has been developed in SHARPy [187], an open-source, nonlinear aeroelastic simulation toolbox that couples aerodynamics obtained with the unsteady vortex lattice method (UVLM) with a structural description given by a nonlinear displacement-based geometrically-exact composite beam model (GEBM). This work presents a general multibody solution compatible to both the UVLM and the GEBM. Such an approach often require special numerical schemes, since the rigid-body motions and elastic deformations can exhibit very different time scales. [188, 189] Among the methods for solving flexible multibody dynamics, as reviewed in [190], two formulations stand out for applications with large displacements: geometrically exact approaches and the Absolute Nodal Coordinate (ANC) formulation. The former is implemented in this work using displacements and rotations as primary variables and more details are given below. The latter has been developed by approximating the displacement spatial field as polynomials [166], and directly applying the equations of solid mechanics to the resulting ad-hoc displacement field. The two formulations have been compared in [173], with the outcome that geometrically-exact formulations are more involved in terms of implementation and mathematical modelling, but offer an edge in computational speeds and accuracy.

1.4 Work undertaken

1.4.1 Research objectives

This thesis investigates flared hinged wingtips as a potential passive load alleviation mechanism and, in doing so, develops the computational capabilities necessary to understand their behaviour. The identification of gaps in the state-of-the-art, particularly the absence of a fully nonlinear multibody aeroelastic framework and results at or above the corresponding fidelities suitable for design and performance analysis, establishes the case for the work presented herein.

Objective 1: Implementation and validation of a flexible multibody aeroelastic formulation

The first objective addresses a gap in existing openly-available simulation tools. While geometrically-exact nonlinear beam theories, multibody coupling methods, and medium-fidelity aerodynamics solvers are well established in isolation, their integration within a time-domain aeroelastic solver remains an active endeavour. This work seeks to develop and validate a coupled formulation that combines geometrically-exact composite beam theory capable of capturing arbitrarily large rotations and displacements, flexible multibody dynamics formulated via Lagrange multipliers to enforce multibody constraints, and unsteady Vortex Lattice Method (UVLM) aerodynamics with a force-free wake to capture transient lifting surface interactions.

Objective 2: Characterisation of load alleviation mechanisms

The second objective is to quantify and verify the nonlinear physical mechanisms through which flared hinged wingtips achieve structural load relief. Earlier work demonstrated that such mechanisms can reduce wing root bending moments, yet the interaction between wing flexibility, multibody kinematics, and unsteady aerodynamics remains elusive. This research addresses that gap by conducting systematic parametric studies on a highly flexible yet geometrically simple HALE planform, allowing the effects of geometry, mass and stiffness properties, and gust characteristics (including length and intensity) to be isolated more clearly. Through sweeps of these parameters, we aim to understand the static and dynamic load alleviation behaviour brought by the wingtips. Understanding these mechanisms in detail enables informed design decisions about which parameters warrant further optimisation in the next design iteration.

Objective 3: Assessment of nonlinearities in full aircraft dynamic response

The third objective extends analysis to representative aircraft platforms. Using the verified framework, this work examines the gust response of representative next-generation flexible aircraft configurations, specifically, a derivative of the SuperFLEXOP research vehicle, to bridge the insights on the coupled dynamics gained from the HALE studies to an industrially relevant configuration for future work. The analysis seeks to reveal whether load alleviation persist amidst geometric and aerodynamic nonlinearities, particularly when they are expected to become significant at higher gust intensities, and the trends of aircraft-level performance

to input parameters.

A placement at Airbus UK was also undertaken to verify and apply the methods developed for flexible multibody aircraft as part of the EPSRC Industrial CASE studentship.

1.4.2 Thesis outline

Below, a brief introduction to each of the Chapters in this thesis is given.

Chapter 2: Flexible multibody dynamics

Chapter 2 develops the theoretical and computational foundation for flexible multibody systems, beginning from first principles and progressing to formulations suitable for aircraft with multibody mechanisms. The chapter opens the description of flexible multibody systems by introducing the geometrically-exact composite beam theory, which models arbitrarily large displacements and rotations. Reference frames and kinematic quantities are defined carefully to ensure clarity in later applications. The equations of motion are derived using Lagrangian mechanics to understand constrained multibody systems. The finite element discretisation of the flexible beam equations is presented. Multibody constraints are enforced using Lagrange multipliers introducing cross-coupling in the beam states. This is then compared with the rigid double pendulum, where we verified against numerical solutions and serves as a sanity check for the numerical implementation. Validation of the flexible multibody formulation proceeds through a series of test cases: comparison of rigid and flexible crossbeam results, validation of the flexible double pendulum at various flare angles, and cross-validation against finite element solutions obtained from commercial software. These verification and validation exercises establish confidence in the structural module before it is coupled with aerodynamics.

Chapter 3: Modelling aeroelastic multibody systems

Chapter 3 integrates the structural multibody formulation developed in Chapter 2 with unsteady aerodynamics. The aerodynamic model employed is the Unsteady Vortex Lattice Method (UVLM), which discretises the lifting surfaces as a collection of vortex filaments and marches their positions and strengths forward in time to capture unsteady effects. The chapter begins by reviewing the theoretical basis of potential flow aerodynamics and the panel method implementation used to generate aerodynamic influence coefficients. The treatment of the aerodynamic discretisation at the hinge line is given special attention. The chapter also addresses the treatment of the wake convection scheme, sectional polar corrections, and the bidirectional coupling between structure and aerodynamics. The coupled aeroelastic sys-

tem is verified through multiple test cases, beginning with a standalone multibody aeroelastic wing assembly, and progressing to code-to-code and code-to-experiment comparisons. Experimental data from a published wind tunnel study of a flexible flared hinged wing assembly are used to validate both steady and dynamic aeroelastic predictions. Additionally, trim strategies for free-flying aircraft configurations are developed, establishing how the aircraft is held in equilibrium for subsequent simulations.

Chapter 4: Nonlinear aeroelasticity of a HALE aircraft with flared hinged wingtips

Chapter 4 applies the verified multibody aeroelastic framework to a representative high-altitude long-endurance aircraft configuration. The HALE model is chosen for its geometric simplicity, strong nonlinear characteristics, and prior publication in the literature, which enables reproducibility and future validation and collaboration exercises. The chapter defines both a hinged and a rigid-connection reference configuration to enable direct comparison of load alleviation effects. Aeroelastic trim conditions are computed to establish the equilibrium state of the aircraft at cruise. The analysis consists of gust response studies across gust lengths, gust intensities, hinge flare angles, and wingtip mass and stiffness parametrisations. For each configuration, transient time-domain simulations capture the aircraft's response to prescribed vertical and lateral gust profiles. The analysis quantifies structural loads through normalised wing root bending moments and torsional moments.

Chapter 5: Nonlinear aeroelasticity of a representative flexible aircraft with flared hinged wingtips

Chapter 5 extends the analysis from the HALE platform to a representative aircraft configuration: the SuperFLEXOP research platform, a numerically-tuned model of a next-generation flexible transport aircraft. A hinged variant of the SuperFLEXOP, the Hinged-SuperFLEXOP is created by adding flared hinged wingtips. The chapter largely follows the analysis methodology of Chapter 4; aeroelastic trimming, parametric gust response studies, and quantification of load alleviation. The chapter also investigates the effect of sectional aerodynamic corrections to account for nonlinear lift and pitching moment characteristics at higher angles of attack. To complete the analysis, the sensitivity of results to trim input variations is examined. This chapter serves to validate the applicability of insights drawn from the HALE analysis and to demonstrate that the multibody aeroelastic framework remains computationally tractable and robust when applied to realistic, complex aircraft configurations.

Chapter 6: Conclusion

Chapter 6 concludes the thesis, summarises the key contributions to literature, and presents opportunities for further work.

1.4.3 Publications

Journal articles

- Kelvin Chi-Wing Cheng et al. "Nonlinear Multibody Modeling of Flexible Aircraft with Flared Hinged Wingtips". In: Journal of Aircraft 62.4 (July 2025), pp. 929–948. issn: 0021-8669. doi: 10.2514/1.C038094.

In conference proceedings

- Chi Wing Cheng, Alvaro Cea and Rafael Palacios. "Static Nonlinear Trim Solutions for Flexible Multibody Aircraft featuring Flared Hinged Wing Tips". In: AIAA SCITECH 2025 Forum. Reston, Virginia: American Institute of Aeronautics and Astronautics, Jan. 2025. isbn: 978-1-62410-723-8. doi: 10.2514/6.2025-0714.

- Keisuke Otsuka, Chi Wing Cheng, and Rafael Palacios. "Absolute Nodal Coordinate Formulation for Nonlinear Multibody Modeling of Flared Hinged Wings". In: 34th Congress of the International Council of the Aeronautical Sciences, ICAS 2024 (2024).

- Chi Wing Cheng et al. "Numerical Investigation of Passive and Active Alleviation of Dynamic Loads on High-Aspect-Ratio-Wing Vehicles". In: 34th Congress of the International Council of the Aeronautical Sciences, ICAS 2024. 2024.

- Chi Wing Cheng et al. "Nonlinear Gust Effects On Flexible Aircraft With Flared Hinged Wings". In: International Forum on Aeroelasticity and Structural Dynamics IFASD 2024. 2024

- Markus Ritter et al. "Collaborative Pazy Wing Analyses for the Third Aeroelastic Prediction Workshop". In: AIAA SCITECH 2024 Forum. Reston, Virginia: American Institute of Aeronautics and Astronautics, Jan. 2024. isbn: 978-1-62410-711-5. doi: 10.2514/6.2024-0419.

- Chi Wing Cheng et al. "Nonlinear Multibody Modelling of Flexible Aircraft with Flared Hinged Wings". In: AIAA SCITECH 2024 Forum. Reston, Virginia: American Institute of Aeronautics and Astronautics, Jan. 2024. isbn: 978-1-62410-711-5. doi: 10.2514/6.2024-1441.

- Chi Wing Cheng et al. “An Integrated Nonlinear Coupled Multibody Aeroelastic Dynamic Simulation Framework for Next-Generation Flexible Aircraft Wing Design”. In: AIAA SCITECH 2023 Forum. Reston, Virginia: American Institute of Aeronautics and Astronautics, Jan. 2023. isbn: 978-1-62410-699-6. doi: 10.2514/6.2023-2073.

Poster presentations

- Ben Preston, Kelvin Chi-Wing Cheng, Rafael Palacios. ”Aeroelastic Simulation of Flexible Multibody Aircraft”. [Poster] In: Composite Centre Showcase, Imperial College London, 2025.
- Ben Preston, Kelvin Chi-Wing Cheng, Rafael Palacios. ”Aeroelastic Simulation of Flexible Multibody Aircraft”. [Poster] In: Aeronautics Research Showcase, Imperial College London, 2024.
- Keisuke Otsuka et al. ”Geometrically Nonlinear Beam Model for Slender Multibody Wings”. [Poster] In: The 22nd International Symposium on Advanced Fluid Information (AFI-2022), Sendai, Japan, 2022. [Best Poster Presentation Award]
- Kelvin Chi-Wing Cheng. ”Next Generation Aircraft: Hinge on the Wings”. [Poster] In: Aeronautics Research Showcase, Imperial College London, 2022.

Chapter 2

Flexible multibody dynamics

To capture the complex dynamics in play in the flight envelope of a next-generation high aspect ratio aircraft with hinged wing tips, it is essential to understand the various sources and attribute the relative importance of each to the overall dynamics of the coupled system. From the ground up, the overall model can be conceptualised as a multibody aeroelastic system, since the folding mechanism on a very flexible wing should lead to dynamics that is akin to a double pendulum, with a slanted hinge, with added flexibility for large deflections, under forcing that is determined by potential flow theory, with polar corrections from higher importance to lower, more accurate near stall onset lift behaviour, separation caused pitching moment changes, and viscous drag. The core challenge here, as described in the previous chapter, lies in the accurate capturing of the coupled nonlinear interactions in time domain.

In this chapter, the building pieces of a coupled flexible multibody framework for hinged wings are introduced. We will begin to give an overview of the geometrically-exact beam theory, and how it can be supplemented with multibody information to describe a flexible double pendulum. The formulation is first verified against the dynamics of a double pendulum derived from first principles. Through a series of verification and validation examples of increasing complexity and disciplines coupled, the robustness and accuracy of the implementation is demonstrated.

2.1 Theory and implementation of the geometrically-exact beam theory

This section outlines the theory and implementation of the simulation environment for flexible aircraft structural dynamics, in particular, the extension of geometrically-exact beam theory

of Ref. [46] to flexible multibody dynamics problems.

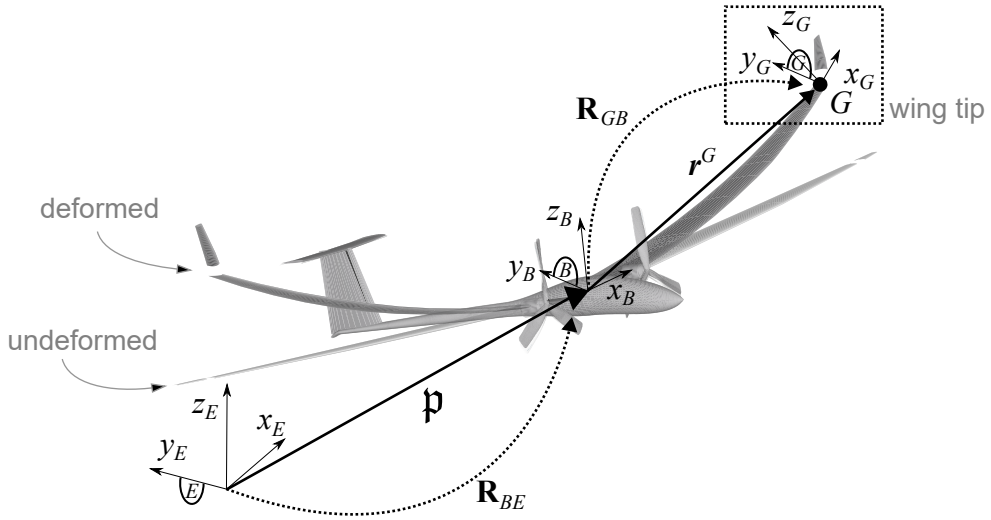
2.1.1 Definition of reference frames and kinematics

Figure 2.1 defines the notation, used to describe the kinematics of the flexible wing with hinged wing tips. We begin from the Earth frame E in Figure 2.1a, from which we define $\mathfrak{p}(t)$ as the time-varying vector to the body-attached frame B used to track the vehicle and define its absolute orientation. In this work the right-handed B frame is at the root of the wing, with positive x direction towards the left wing, and positive z direction upwards. The rotation matrix from E to B frame $\mathbf{R}_{BE}$ is defined with a choice of parametrisation, in this case the quaternion χ^B, for the generality of the description. In the B frame we define $\boldsymbol{r}_B^G$ as the vector to the material frame at the tip of the main wing, frame G. The rotation matrix from B to G frame $\mathbf{R}_{GB}$ is defined, again with a choice of parametrisation, in this case the Cartesian Rotation Vector (CRV) $\boldsymbol{\psi}_B^G$, for CRVs only uses three degrees of freedom (DoFs) which corresponds to the usual linear rotations for infinitesimal rotations.

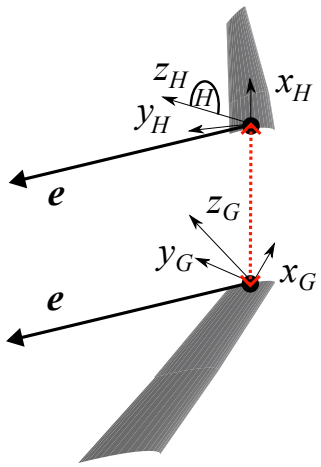
On the wing tip itself in Figure 2.1b, separated by the hinge, we define the body-attached frame H at its root where the rotation matrix from the global frame $\mathbf{R}_{HE}$ is a function of the quaternion χ^H, without loss of generality, and for ease of expressing common quantities in the Earth frame in the later sections. Inertial velocities of body-fixed frames, i.e., B and H, are given in their own frames of reference (FoRs) respectively by $\boldsymbol{v}_B^B$, $\boldsymbol{\omega}_B^B$ and $\boldsymbol{v}_H^H$, $\boldsymbol{\omega}_H^H$, where those at local frames, i.e. G, require a more involved formulation described in Section 2.4.1.

As the aeroelastic wing with the hinged wing tips undergoes displacements and rotations, the hinge line vector $\boldsymbol{e}$ in any arbitrary direction (but usually lying on the chordwise-spanwise plane of the wing in the material frame, for continuity across the hinge) as visualised, is a function of rigid body translational and rotational movements, and flexible deformations, and almost always a function of time. Defining instead the projections of the hinge line vector in the two local frames of reference gives $\boldsymbol{e}_H = \mathbf{R}_{HG}\boldsymbol{e}_G$, such that these vectors are now constant in time, from Euler's rotation theorem (Chapter 4.3.2 of Ref. [46]).

We define also the continuum quantity η as the coordinate along the undeformed beam axis - this will help us disambiguate quantities on the beam cross section.



(a) Frames and notations for aircraft with flared hinged wings



(b) Inset showing frames and notations of the wing tip

Figure 2.1: Labelled quantities and frames of the flexible multibody wing assembly

2.1.2 Flexible beam equations of motion

To arrive at the beam equations of motion we leverage the Lagrangian approach. [178] Here, to separate internal and external contributions, $\mathcal{T}$ maps the kinetic energy, $\mathcal{U}$ maps to the internal strain energy, where gravity, rather than being modelled as a potential, is treated as an external contribution to the system action as work $\mathcal{W}$, and hence we have

$$\mathcal{L} = \mathcal{T} - \mathcal{U}, \tag{2.1}$$

and the action as

$$\mathcal{S} = \int_{t_1}^{t_2} (\mathcal{L} + \mathcal{W})\, dt. \tag{2.2}$$

As described in Chapter 8 of Ref [46], the expressions for the total kinetic and strain energy as the integral of the local velocities and strains along the beam reference line are as given here.

$$\begin{aligned} \mathcal{T}(t) &= \frac{1}{2}\int_\eta \left\{ \begin{array}{cc} \overline{\mathbf{v}}_S^\top & \overline{\boldsymbol{\omega}}_S^\top \end{array} \right\} \mathcal{M} \left\{ \begin{array}{c} \overline{\mathbf{v}}_S \\ \overline{\boldsymbol{\omega}}_S \end{array} \right\} \mathrm{d}\eta, \\ \mathcal{U}(t) &= \frac{1}{2}\int_\eta \left\{ \begin{array}{cc} \boldsymbol{\gamma}^\top & \boldsymbol{\kappa}^\top \end{array} \right\} \mathcal{K} \left\{ \begin{array}{c} \boldsymbol{\gamma} \\ \boldsymbol{\kappa} \end{array} \right\} \mathrm{d}\eta, \end{aligned} \tag{2.3}$$

where S refers to the frame of reference of a point on the reference line, with the sectional mass and stiffness matrices

$$\mathcal{M}(\eta) = \left[\begin{array}{cc} m(\eta)\mathcal{I} & -m(\eta)\tilde{\mathfrak{y}}_{\mathrm{cg}}(\eta) \\ m(\eta)\tilde{\mathfrak{y}}_{\mathrm{cg}}(\eta) & \mathbf{I}_S(\eta), \end{array} \right] \tag{2.4}$$

$$\mathcal{K}(\eta) = \mathrm{diag}\left(EA, GA_y, GA_z, GJ, EI_{yy}, EI_{zz}\right), \tag{2.5}$$

where $m(\eta)$ is the mass per unit beam length, $\mathbf{I}_S(\eta)$ is the sectional inertia tensor, the cross terms as a function of the coordinates, in the local S frame, of the centre of gravity of the cross section $\tilde{\mathfrak{y}}_{\mathrm{cg}}(\eta) = (0, y_{\mathrm{cg}}(\eta), z_{\mathrm{cg}}(\eta))$ accounts for the c.g. not lying on the reference line, and similarly the cross terms in $\mathcal{K}(\eta)$ are added as the stiffness couplings arise.

Revisiting the geometrically-nonlinear cross-sectional linear and angular velocities and force and moment strains we so hastily defined earlier,

$$\begin{aligned} \overline{\mathbf{v}}_S(\eta, t) &= \mathbf{R}_{SB}(\eta, t)\dot{\mathbf{r}}_B(\eta, t) + \mathbf{R}_{SB}(\eta, t)\left(\tilde{\boldsymbol{\omega}}_B(t)\mathbf{r}_B(\eta, t) + \mathbf{v}_B(t)\right) \\ \tilde{\overline{\boldsymbol{\omega}}}_S(\eta, t) &= \mathbf{R}_{SB}(\eta, t)\dot{\mathbf{R}}_{BS}(\eta, t) + \mathbf{R}_{SB}(\eta, t)\tilde{\boldsymbol{\omega}}_B(t)\mathbf{R}_{BS}(\eta, t). \end{aligned} \tag{2.6}$$

In these *velocity-displacement kinematic relations*, the first term in the equations refers to the 'flexible contribution' to velocities as time-derivative of positions and rotations relative to the body B frame, projected onto the local material frame S. The second terms refer to the 'rigid-body contribution' as projected linear and angular velocities of the body frame at point η. The *strain–displacement kinematic relations* follow a slightly different description.

$$\begin{aligned} \boldsymbol{\gamma}(\eta, t) &= \mathbf{R}_{SB}(\eta, t)\mathbf{r}'_B(\eta, t) - \mathbf{R}_{SB}(\eta, 0)\mathbf{r}'_B(\eta, 0) \\ \tilde{\boldsymbol{\kappa}}(\eta, t) &= \mathbf{R}_{SB}(\eta, t)\mathbf{R}'_{BS}(\eta, t) - \mathbf{R}_{SB}(\eta, 0)\mathbf{R}'_{BS}(\eta, 0) \end{aligned} \tag{2.7}$$

They are instead defined as differences in time from 0 to t, of the tangent and curvature vector of the undeformed versus the instantaneous curve.

We now have all the ingredients to express the action of the system from time 0 to t_f, for it to satisfy Hamilton's principle and hence give us the equations of motion for the flexible composite beam.

$$\int_0^{t_f} \int_\eta \left(\frac{\partial \mathcal{T}}{\partial \overline{\mathbf{v}}_S} \delta \overline{\mathbf{v}}_S + \frac{\partial \mathcal{T}}{\partial \bar{\boldsymbol{\omega}}_S} \delta \bar{\boldsymbol{\omega}}_S - \frac{\partial \mathcal{U}}{\partial \boldsymbol{\gamma}} \delta \boldsymbol{\gamma} - \frac{\partial \mathcal{U}}{\partial \boldsymbol{\kappa}} \delta \boldsymbol{\kappa} + \delta \mathcal{W}_{\text{cs}} \right) \mathrm{d}\eta \, \mathrm{d}t = 0 \tag{2.8}$$

where without loss of generality the external work done can be assumed to be the result of externally applied sectional forces and moments $\overline{\mathbf{f}}_S$ and $\overline{\mathbf{m}}_S$ integrated along the reference line. When transformed to the body frame those appear, rather intuitively, as virtual displacements and rotations of the frame $\delta \mathfrak{p}_B$ and $\delta \varphi_B$, multiplied by the forces and moments expressed also in the same body frame, the latter with principle of moments applied for frame S.

$$\begin{aligned} &\int_0^{t_f} \int_\eta \left(\delta \overline{\mathbf{v}}_S^\top \mathbf{p}_S + \delta \overline{\boldsymbol{\omega}}_S^\top \mathbf{h}_S - \delta \boldsymbol{\gamma}^\top \mathfrak{f}_S - \delta \boldsymbol{\kappa}^\top \mathfrak{m}_S + \delta \mathbf{r}_S^\top \overline{\mathbf{f}}_S + \delta \boldsymbol{\phi}_s^\top \overline{\mathbf{m}}_S \right) \mathrm{d}\eta \, \mathrm{d}t \\ &+ \int_0^{t_f} \left[\delta \mathfrak{p}_B^\top \int_\eta \overline{\mathbf{f}}_B \, \mathrm{d}\eta + \delta \varphi_B^\top \int_\eta \left(\overline{\mathbf{m}}_B + \tilde{\mathbf{r}}_B \overline{\mathbf{f}}_B \right) \mathrm{d}\eta \right] \mathrm{d}t = 0 \end{aligned} \tag{2.9}$$

where $\mathbf{p}_S^\top = \frac{\partial \mathcal{T}}{\partial \overline{\mathbf{v}}_S}$ and $\mathbf{h}_S^\top = \frac{\partial \mathcal{T}}{\partial \bar{\boldsymbol{\omega}}_S}$ are the linear and angular momenta, $\mathfrak{f}_S^\top = \frac{\partial \mathcal{U}}{\partial \boldsymbol{\gamma}}$ and $\mathfrak{m}_S^\top = \frac{\partial \mathcal{U}}{\partial \boldsymbol{\kappa}}$ are the internal forces and moments. The constitutive relations, as below, are substituted into Eq. 2.3.

$$\begin{aligned} \begin{Bmatrix} \mathbf{p}_S(\eta, t) \\ \mathbf{h}_S(\eta, t) \end{Bmatrix} &= \mathcal{M}(\eta) \begin{Bmatrix} \overline{\mathbf{v}}_S(\eta, t) \\ \overline{\boldsymbol{\omega}}_S(\eta, t) \end{Bmatrix}, \\ \begin{Bmatrix} \boldsymbol{\gamma}(\eta, t) \\ \boldsymbol{\kappa}(\eta, t) \end{Bmatrix} &= \mathcal{K}^{-1}(\eta) \begin{Bmatrix} \mathfrak{f}_S(\eta, t) \\ \mathfrak{m}_S(\eta, t) \end{Bmatrix}. \end{aligned} \tag{2.10}$$

With integration by parts in space and time performed as laid out in full detail in Chapter 8.3 of [46] we arrive at the weak form of the beam equations of motion as

$$
\begin{aligned}
&\int_0^{t_f}\int_\eta \delta\mathbf{r}_B^T\left[\mathbf{R}_{BS}\left(\dot{\mathbf{p}}_S+\tilde{\bar{\boldsymbol{\omega}}}_S\mathbf{p}_S-\bar{\mathbf{f}}_S\right)+\delta\mathbf{r}_B'^{\top}\mathbf{R}_{BS}\mathfrak{f}s\right]\mathrm{d}\eta\,\mathrm{d}t\\
&+\int_0^{t_f}\int_\eta \delta\boldsymbol{\phi}_S^T\left[\left(\dot{\mathbf{h}}_S+\tilde{\bar{\boldsymbol{\omega}}}_S\mathbf{h}_S+\tilde{\bar{\mathbf{v}}}_S\mathbf{p}_S-\tilde{\mathbf{k}}_S\mathfrak{m}_S-\mathbf{R}_{SB}\tilde{\mathbf{r}}_B'\mathbf{R}_{BS}\mathfrak{f}_S-\overline{\mathbf{m}}_S\right)+\delta\boldsymbol{\phi}_S'^{\top}\mathfrak{m}_S\right]\mathrm{d}\eta\,\mathrm{d}t\\
&+\int_0^{t_f}\delta\mathfrak{p}_B^{\top}\int_\eta\left[\dot{\mathbf{p}}_B+\tilde{\boldsymbol{\omega}}_B\mathbf{p}_B-\bar{\mathbf{f}}_B\right]\mathrm{d}\eta\,\mathrm{d}t\\
&+\int_0^{t_f}\delta\boldsymbol{\varphi}_B^{\top}\int_\eta\left[\left(\frac{\mathrm{d}}{\mathrm{d}t}+\tilde{\boldsymbol{\omega}}_B\right)(\mathbf{h}_B+\tilde{\mathbf{r}}_B\mathbf{p}_B)+\tilde{\mathbf{v}}_B\mathbf{p}_B+\overline{\mathbf{m}}_B+\tilde{\mathbf{r}}_B\bar{\mathbf{f}}_B\right]\mathrm{d}\eta\,\mathrm{d}t\\
&=\left\{\int_\eta\left[\delta\mathbf{r}_B^{\top}\mathbf{R}_{BS}\mathbf{p}_S+\delta\boldsymbol{\phi}_S^{\top}\mathbf{h}_S\right]\mathrm{d}\eta+\delta\mathfrak{p}_B^{\top}\int_\eta\mathbf{p}_B\,\mathrm{d}\eta+\delta\boldsymbol{\varphi}_B^{\top}\int_\eta(\mathbf{h}_B+\tilde{\mathbf{r}}_B\mathbf{p}_B)\,\mathrm{d}\eta\right\}\Bigg|_0^{t_f}
\end{aligned}
\tag{2.11}
$$

2.2 Finite element equations of motion

To solve Equation 2.11 we now introduce a spatial discretisation that reduces the problem to a finite number of degrees of freedom. The procedure is well established in literature [146] and hence followed here. From before we have alluded to the choice of displacements and rotations to parametrise the flexible beam dynamics, the latter specifically by the use of the Cartesian rotation vector. That requires, first of all, the substitution of all kinematic and dynamic quantities in Equation 2.11, with positions and rotations, and their derivatives, along the reference line. After which, the structure is partitioned into finite elements, and the unknown fields are approximated between the nodes using appropriate shape functions. In the implementation we have elected to use 3-noded beam elements with quadratic shape functions $N(\eta)$. Hence the displacements and rotations along the beam are independently approximated as

$$
\begin{pmatrix}\mathbf{r}(\eta,t)\\ \boldsymbol{\psi}(\eta,t)\end{pmatrix}=\begin{bmatrix}N(\eta) & 0\\ 0 & N(\eta)\end{bmatrix}\boldsymbol{\xi}
\tag{2.12}
$$

where $\boldsymbol{\xi}$ includes all nodal structural dynamics degrees of freedom which are reordered to include firstly, all nodal displacements, and then all nodal rotations. Note the same shape function is used for both fields. These interpolations are then used to evaluate the spatial integrals in Equation 2.11 on an element-by-element basis, which are subsequently assembled into a set of nonlinear algebraic equations in terms of the nodal coordinates, rotations, and their time derivatives, that can be solved at each time step. The discretised form of the beam equations in generalised variables $\mathbf{x}$ for the whole beam assembled can be written as

$$\mathbf{M}(\mathbf{x})\ddot{\mathbf{x}} + \mathfrak{f}_{gyr}(\mathbf{x},\dot{\mathbf{x}}) + \mathfrak{f}_{stiff}(\mathbf{x}) = \mathfrak{f}_{ext}(\mathbf{x},\dot{\mathbf{x}}) \tag{2.13}$$

or in the constituent DoFs, and introducing $\boldsymbol{\beta} = \begin{bmatrix} \boldsymbol{v} \\ \boldsymbol{\omega} \end{bmatrix}$, as [191]

$$\mathbf{M}(\boldsymbol{\xi}) \begin{pmatrix} \ddot{\boldsymbol{\xi}} \\ \dot{\boldsymbol{\beta}} \end{pmatrix} + \begin{pmatrix} \mathfrak{f}^S_{gyr} \\ \mathfrak{f}^R_{gyr} \end{pmatrix} + \begin{pmatrix} \mathfrak{f}^S_{stif} \\ 0 \end{pmatrix} = \begin{pmatrix} \mathfrak{f}^S_{ext} \\ \mathfrak{f}^R_{ext} \end{pmatrix}. \tag{2.14}$$

Time evolution of quaternions are described by

$$\dot{\chi} = \frac{1}{2} \begin{bmatrix} 0 & -\boldsymbol{\omega}_A^\top \\ \boldsymbol{\omega}_A & -\tilde{\boldsymbol{\omega}}_A \end{bmatrix} \chi. \tag{2.15}$$

Noting the dependencies of the quaternion in time on beam rigid body motion in Equation 2.15, in conjunction with Equation 2.14 we can finally describe the beam's rigid-body and flexible motion, with the linearisation as described in [192]

$$\underbrace{\begin{bmatrix} \mathrm{M}_{\xi\xi} & \mathrm{M}_{\xi\beta} & 0 \\ \mathrm{M}_{\beta\xi} & \mathrm{M}_{\beta\beta} & 0 \\ 0 & 0 & I_{4\times4} \end{bmatrix}}_{\mathrm{M}} \begin{pmatrix} \Delta\ddot{\xi} \\ \Delta\dot{\beta} \\ \Delta\dot{\chi} \end{pmatrix} + \underbrace{\begin{bmatrix} \mathrm{C}^t_{\xi\xi} & \mathrm{C}^t_{\xi\beta} & 0 \\ \mathrm{C}^t_{\beta\xi} & \mathrm{C}^t_{\beta\beta} & 0 \\ 0 & \mathrm{C}^t_{\chi\beta} & \mathrm{C}^t_{\chi\chi} \end{bmatrix}}_{\mathrm{C}^t} \begin{pmatrix} \Delta\dot{\xi} \\ \Delta\beta \\ \Delta\chi \end{pmatrix} + \underbrace{\begin{bmatrix} \mathrm{K}^t_{\xi\xi} & 0 & 0 \\ \mathrm{K}^t_{\beta\xi} & 0 & 0 \\ 0 & 0 & 0 \end{bmatrix}}_{\mathrm{K}^t} \begin{pmatrix} \Delta\xi \\ 0 \\ 0 \end{pmatrix} = \underbrace{\begin{pmatrix} r_\xi \\ r_\beta \\ r_\chi \end{pmatrix}}_{r}, \tag{2.16}$$

which condensed for one beam takes the form

$$\mathbf{M}\boldsymbol{\Delta}\ddot{\mathbf{x}} + \mathbf{C}^t\boldsymbol{\Delta}\dot{\mathbf{x}} + \boldsymbol{K}^t\boldsymbol{\Delta}\mathbf{x} = \boldsymbol{r}. \tag{2.17}$$

2.3 Validation: Rigid and flexible crossbeam

We apply the coupled rigid body-flexible beam equations to a benchmark problem as described in [193]. This is with the aim to validate the coupled rigid body and structural dynamics formulation against an inertia relief framework coupled with a commercial-off-the-shelf nonlinear finite element solver. Two different test cases were conducted in the literature with this model shown in Figure 2.2. The first test involved a sinusoidal, vertical force of 0.5 N at 2 Hz applied at the clamping point. The second test was designed to achieve larger structural displacements by reducing the crossbeam's Young's modulus 20-fold. The sinusoidal force was reduced to 0.1 N in this case. Due to the symmetries in the system, the inputs are only expected to excite the vertical rigid body and flexible beam modes. Model parameters are as given in Table 2.1. Temporal and spatial discretisation parameters are given in Table 2.2.

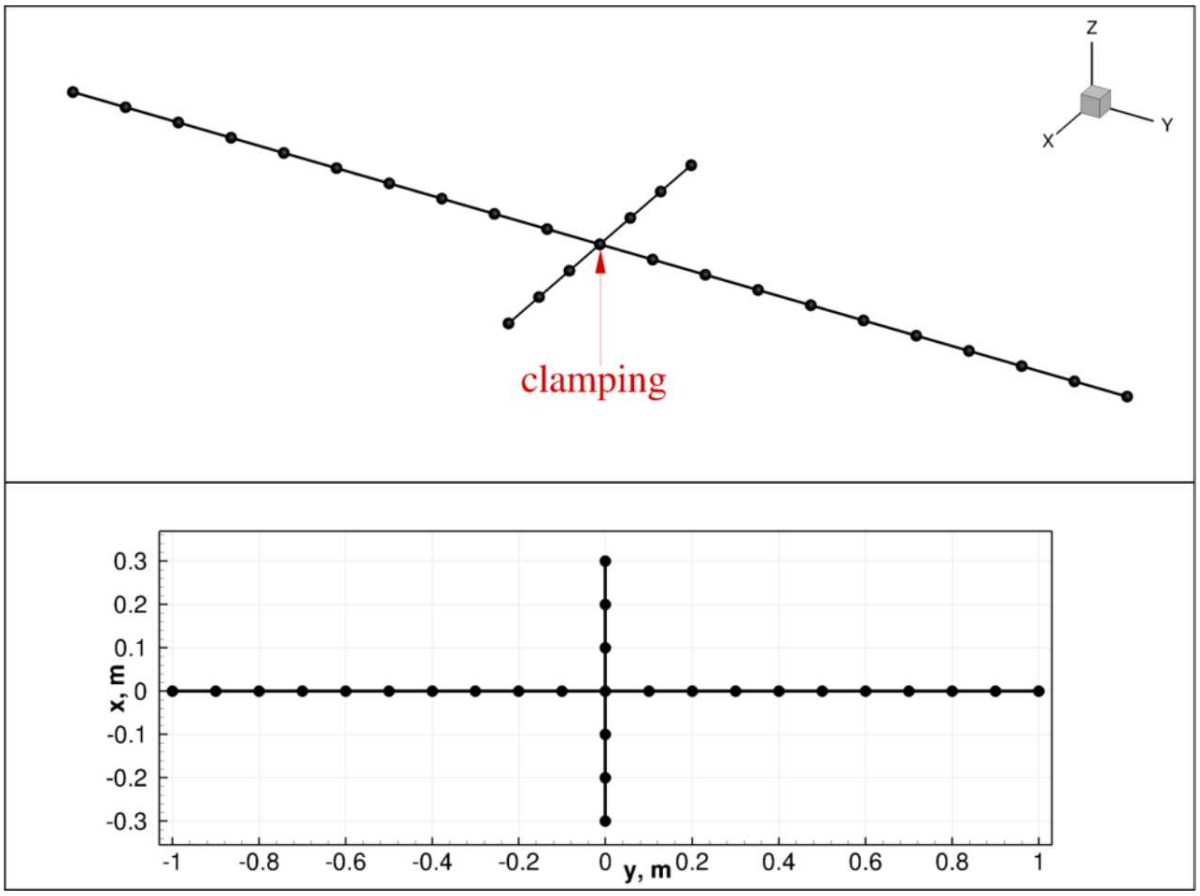


Figure 2.2: Generic crossbeam FE model used for validation, reproduced from [193]

Hilger's approach couples a nonlinear finite-element solver (MSC Nastran SOL400) with flight dynamics equations via a inertial-relief formulation, with implicit BDF time integration for the rigid body part of the solution. Results from our implementation is compared with the published results in Figures 2.3 and 2.4 and shows generally good agreement, barring mismatch in high-frequency content in the acceleration time histories more notable in the flexible case, speculated to be of numerical origin.

Table 2.1: Crossbeam parameters for rigid and flexible cases

Parameter	**Symbol**	**Rigid**	**Flexible**	**Unit**
Mass	m	0.13	0.13	kg
Young's Modulus	E	2×10^{11}	1×10^{10}	N/m^2
Cross-sectional area	A	1×10^{-5}	1×10^{-5}	m^2
Moment of inertia	I_{zz}	5×10^{-11}	5×10^{-11}	m^4
Density	ρ	5000	5000	kg/m^3
Forcing amplitude	f_{amp}	0.5	0.1	N
Forcing frequency	f_{freq}	2.0	2.0	Hz

Table 2.2: Simulation parameters for crossbeam in Hilger [193] and SHARPy

Parameters	Hilger [193]	SHARPy
Longer half-beam discretisation	10 CBEAM	21 nodes, 10 elements
Shorter half-beam discretisation	3 CBEAM	7 nodes, 3 elements
Simulation time step [s]	0.001	0.0005

2.4 Flexible multibody formulation with Lagrange multipliers

To obtain the overall structural system of equations we assemble the relevant equation of motion for each generalised DoF $\mathbf{x}$, consisting, for each of the beams within the multibody structure, the global attitude, rigid body velocities, and the flexible deformations described by displacements and rotations at the grid nodes of the beam elements, which is consistent in nomenclature as in Equation 9.4 in [46]. The constraints are then appended as functions of one or several of the DoFs in the formulation. To represent the connections between different nodal DoFs and/or to address the fact that we have not explicitly chosen the DoFs to be linearly independent, we introduce extra constraint equations $\boldsymbol{g}$ which are itemised in Section 2.4.1. Multiplying with Lagrange multipliers $\boldsymbol{\lambda}$ defines an augmented Lagrangian for the system, from which we arrive at the general form of the multibody problem as

$$\begin{cases} \mathbf{M}(\mathbf{x})\ddot{\mathbf{x}} + \mathbf{B}^{\top}(\mathbf{x}, \dot{\mathbf{x}}, t)\boldsymbol{\lambda} = \mathfrak{f}(\mathbf{x}, \dot{\mathbf{x}}, t) = \mathfrak{f}_{ext}(\mathbf{x}, \dot{\mathbf{x}}) - \mathfrak{f}_{gyr}(\mathbf{x}, \dot{\mathbf{x}}) - \mathfrak{f}_{stiff}(\mathbf{x}), \\ \boldsymbol{g}(\mathbf{x}, \dot{\mathbf{x}}, t) = \mathbf{B}(\mathbf{x}, \dot{\mathbf{x}}, t)\dot{\mathbf{x}} + \boldsymbol{g}_0 = 0 \end{cases} \tag{2.18}$$

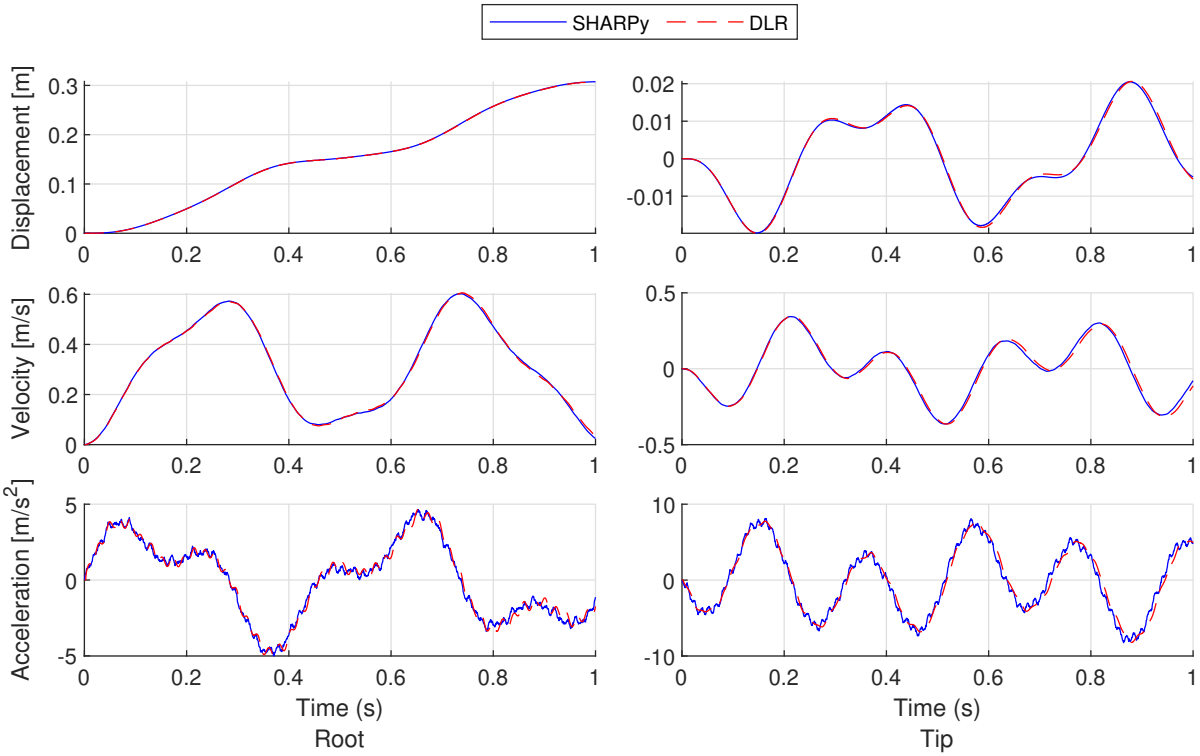


Figure 2.3: Crossbeam vertical kinematic quantities at root and tip for rigid case in time

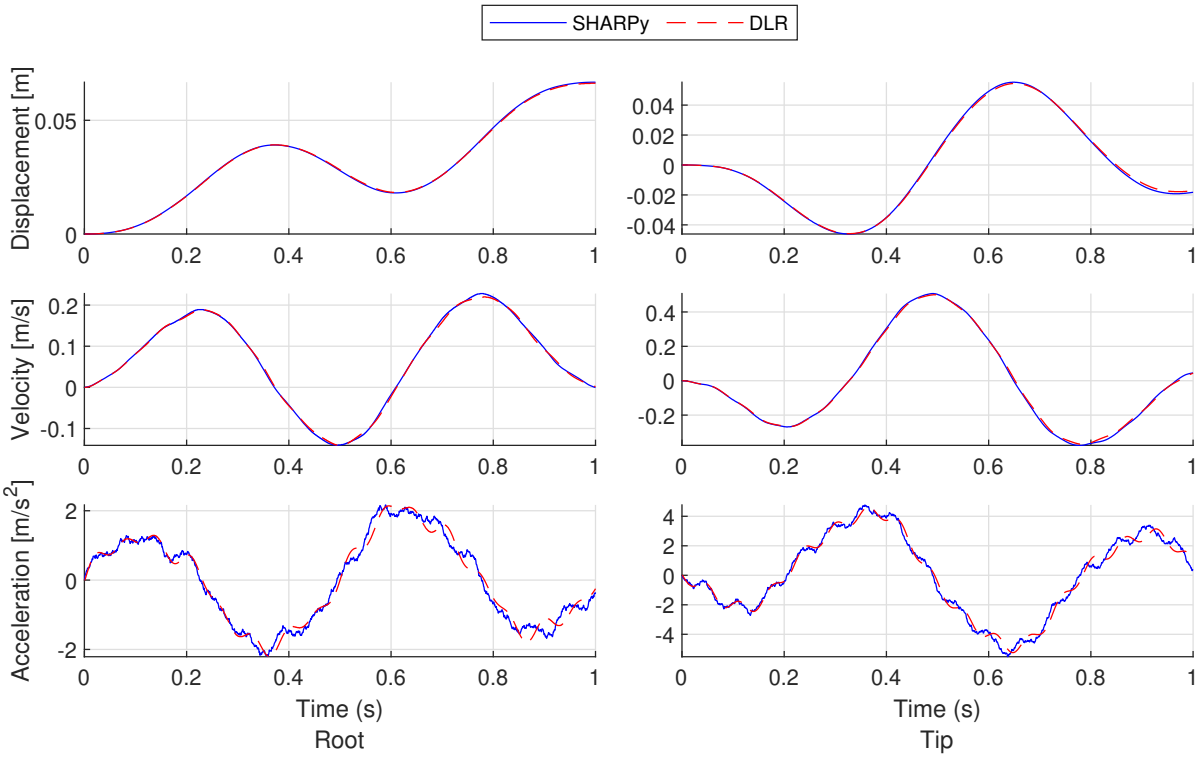


Figure 2.4: Crossbeam vertical kinematic quantities at root and tip for flexible case in time

in which $\mathbf{M}$ is the mass matrix and $\mathfrak{f}$ includes the external, gyroscopic, and stiffness forces respectively, and $\mathbf{B} = \frac{\partial \boldsymbol{g}}{\partial \mathbf{x}}$ is the Jacobian of the constraints. [194] In the problems of interest, specifically with flexible hinged wing tips, $\mathfrak{f}_{ext}$ is given by a co-simulation with a UVLM solver [187, 195] to give the aerodynamic forcing $\mathfrak{f}_{aero}$. If we then write Equation (2.18) in incremental form and recast we obtain

$$\begin{bmatrix} \mathbf{M} & 0 \\ 0 & 0 \end{bmatrix} \begin{pmatrix} \Delta\ddot{\mathbf{x}} \\ \Delta\dot{\boldsymbol{\lambda}} \end{pmatrix} + \begin{bmatrix} \mathbf{C} & \mathbf{B}^\top \\ \mathbf{B} & 0 \end{bmatrix} \begin{pmatrix} \Delta\dot{\mathbf{x}} \\ \Delta\boldsymbol{\lambda} \end{pmatrix} + \begin{bmatrix} \mathbf{K} & 0 \\ 0 & 0 \end{bmatrix} \begin{pmatrix} \Delta\mathbf{x} \\ 0 \end{pmatrix} = \begin{pmatrix} \mathfrak{r}^\circ \\ -\boldsymbol{g}^\circ \end{pmatrix} + \text{H.O.T.} \tag{2.19}$$

where the tangent damping and stiffness matrices $\mathbf{C}$ and $\mathbf{K}$, as well as the residual vector $\mathfrak{r}^\circ$ are given as

$$\begin{cases} \mathbf{C} = \underbrace{\dfrac{\partial \mathbf{B}^\top \boldsymbol{\lambda}}{\partial \dot{\mathbf{x}}}}_{\overline{\boldsymbol{C}}} - \dfrac{\partial \mathfrak{f}}{\partial \dot{\mathbf{x}}}, \\ \mathbf{K} = \dfrac{\partial (\mathbf{M}\ddot{\mathbf{x}})}{\partial \mathbf{x}} + \underbrace{\dfrac{\partial \mathbf{B}^\top \boldsymbol{\lambda}}{\partial \mathbf{x}}}_{\overline{\mathbf{K}}} - \dfrac{\partial \mathfrak{f}}{\partial \mathbf{x}}, \\ \mathfrak{r}^\circ = \mathfrak{f} - \mathbf{M}\ddot{\mathbf{x}} - \mathbf{B}^\top \boldsymbol{\lambda} \end{cases} \tag{2.20}$$

evaluated at the reference point. We determine $\mathbf{B}$ for the common lower pair joints that we are interested in, then, reminding ourselves of the Newmark-β formulation for a generalised state variable, incorporating DoFs $\mathbf{x}$ for all beams, as well as the Lagrange multipliers $\boldsymbol{\lambda}$, as $\boldsymbol{q}$,

$$\begin{cases} \boldsymbol{q}_{n+1} = \boldsymbol{q}_n + \dot{\boldsymbol{q}}_n \Delta t + (\frac{1}{2} - \beta_T)\ddot{\boldsymbol{q}}_n \Delta t^2 + \beta_T \ddot{\boldsymbol{q}}_{n+1} \Delta t^2 + \mathcal{O}(\Delta t^3), \\ \dot{\boldsymbol{q}}_{n+1} = \dot{\boldsymbol{q}}_n + (1 - \gamma_T)\ddot{\boldsymbol{q}} \Delta t_n + \gamma_T \ddot{\boldsymbol{q}}_{n+1} \Delta t^2 + \mathcal{O}(\Delta t^3). \end{cases} \tag{2.21}$$

Equations (2.19) and (2.21) define a well-posed linear problem, which is used to iteratively update the nonlinear equations in (2.18), using a predictor-corrector algorithm to accelerate convergence.

For aeroelastic problems, the nodal displacements are used to deform the lifting surfaces on which the aerodynamics solver computes nodal loads [196], which is in turn passed onto the multibody solver for the next time step in a classical FSI coupling scheme.

2.4.1 Multibody constraints for the hinged wing tip

Equation (2.18) describes the coupling of a generic flexible multibody structure; this formulation has been applied previously on other multibody systems such as wind turbines. [197] For a hinge connection between 2 beams, we require three and two equations for the linear and angular velocities respectively to allow only for one degree of freedom, which is the rotation about the hinge axis. They are derived next.

Linear velocity constraint

We begin by placing the condition of same linear velocity at frames G and H. Equating the velocities across the connection, in H frame gives

$$\boldsymbol{v}_H^H = \mathbf{R}_{HB}\left(\dot{\boldsymbol{r}}_B^G + \boldsymbol{v}_B^B + \widetilde{\boldsymbol{\omega}}_B^B \boldsymbol{r}_B^G\right), \tag{2.22}$$

which when written as a constraint in matrix form in the inertial frame E, and following the notation in Equation (2.18), is

$$\boldsymbol{g}_1 = \begin{bmatrix} -\mathbf{R}_{EB}(\chi^B) & -\mathbf{R}_{EB}(\chi^B) & \mathbf{R}_{EB}(\chi^B)\widetilde{\boldsymbol{r}}_B^G & \mathbf{R}_{EH}(\chi^H) \end{bmatrix} \begin{bmatrix} \dot{\boldsymbol{r}}_B^G \\ \boldsymbol{v}_B^B \\ \boldsymbol{\omega}_B^B \\ \boldsymbol{v}_H^H \end{bmatrix} = \mathbf{B}_1(\dot{\mathbf{x}}, \mathbf{x}, t)\dot{\mathbf{x}} = 0, \tag{2.23}$$

where in these expressions $\widetilde{\bullet}$ or $skew(\bullet)$ is the cross product operator. Apart from introducing the constraint as an extra equation in the system, we would also have to update the residual $\mathfrak{r}^\circ$, and evaluate $\overline{\mathbf{C}}$ in Equation (2.20). The only non-zero terms in the full-rank matrix $\overline{\mathbf{C}}$ are the submatrices

$$\begin{aligned} \overline{\mathbf{C}}_{\dot{\boldsymbol{r}}_B^G, \chi^B} &= -\frac{\partial}{\partial \chi^B}\left((\mathbf{R}_{EB}(\chi^B))^\top \boldsymbol{\lambda}\right), \\ \overline{\mathbf{C}}_{\boldsymbol{v}_B^B, \chi^B} &= -\frac{\partial}{\partial \chi^B}\left((\mathbf{R}_{EB}(\chi^B))^\top \boldsymbol{\lambda}\right), \\ \overline{\mathbf{C}}_{\boldsymbol{\omega}_B^B, \chi^B} &= \frac{\partial}{\partial \chi^B}\left((\mathbf{R}_{EB}(\chi^B))^\top \left(\widetilde{\boldsymbol{r}}_B^G \boldsymbol{\lambda}\right)\right), \\ \overline{\mathbf{C}}_{\boldsymbol{v}_H^H, \chi^H} &= \frac{\partial}{\partial \chi^H}\left((\mathbf{R}_{EB}(\chi^H))^\top \boldsymbol{\lambda}\right). \end{aligned} \tag{2.24}$$

Likewise the only non-zero contribution to the full-rank matrix $\overline{\mathbf{K}}$ is the submatrix

$$\overline{\mathbf{K}}_{\boldsymbol{\omega}_B^B, \boldsymbol{r}_B^G} = -\mathbf{R}_{EB}(\chi^B)\widetilde{\boldsymbol{\lambda}}. \tag{2.25}$$

Angular velocity constraint

To apply the angular velocity constraint, in practice we restrict any two pairs of corresponding points on the vectors to always have the same linear velocity. Choosing the origins of the vectors in Figure 2.1b as the first pair gives Equation (2.22), and additionally choosing two points along the vectors give their common linear velocity in the H frame as

$$\boldsymbol{v}_H^H + \widetilde{\boldsymbol{\omega}}_H^H \boldsymbol{e_H} = \mathbf{R}_{HB}\left(\dot{\boldsymbol{r}}_B^G + \boldsymbol{v}_B^B + \widetilde{\boldsymbol{\omega}}_B^B \boldsymbol{r}_B^G\right) + \mathbf{R}_{HG}(\text{skew}(\mathbf{T}^{GB}\dot{\boldsymbol{\psi}}_B^G + \mathbf{R}_{GB}\boldsymbol{\omega}_B^B)\boldsymbol{e_B}), \tag{2.26}$$

where $\mathbf{T}$ is the tangential rotational operator described in Appendix C of [46], from which Equation (2.22) is eliminated to give

$$\widetilde{\boldsymbol{\omega}}_H^H \boldsymbol{e_H} = \mathbf{R}_{HG}(\text{skew}(\mathbf{T}^{GB}\dot{\boldsymbol{\psi}}_B^G + \mathbf{R}_{GB}\boldsymbol{\omega}_B^B)\boldsymbol{e_B}), \tag{2.27}$$

which is transformed to G frame and recast in matrix form as

$$\boldsymbol{g}_2 = \begin{bmatrix} \widetilde{\boldsymbol{e}}_B\mathbf{R}_{GB}(\boldsymbol{\psi}_B^G) & \widetilde{\boldsymbol{e}}_B\mathbf{T}^{GB}(\boldsymbol{\psi}_B^G) & -\mathbf{R}_{GB}(\boldsymbol{\psi}_B^G)\mathbf{R}_{BE}(\chi^B)\mathbf{R}_{EH}(\chi^H)\widetilde{\boldsymbol{e}}_H \end{bmatrix} \begin{bmatrix} \boldsymbol{\omega}_B^B \\ \dot{\boldsymbol{\psi}}_B^G \\ \boldsymbol{\omega}_H^H \end{bmatrix} = \mathbf{B}_2(\dot{\mathbf{x}}, \mathbf{x}, t)\dot{\mathbf{x}} = 0. \tag{2.28}$$

We then follow a similar procedure as in Section 2.4.1 to obtain $\overline{\mathbf{C}}$ and $\overline{\mathbf{K}}$,

$$\begin{aligned}
\overline{\mathbf{K}}_{\boldsymbol{\omega}_B^B, \boldsymbol{\psi}_B^G} &= -\frac{\partial(\mathbf{R}_{GB}(\boldsymbol{\psi}_B^G))^\top}{\partial \boldsymbol{\psi}_B^G}(\widetilde{\boldsymbol{e}}_B\boldsymbol{\lambda}), \\
\overline{\mathbf{K}}_{\dot{\boldsymbol{\psi}}_B^G, \boldsymbol{\psi}_B^G} &= -\frac{\partial(\mathbf{T}(\boldsymbol{\psi}_B^G))^\top}{\partial \boldsymbol{\psi}_B^G}(\widetilde{\boldsymbol{e}}_B\boldsymbol{\lambda}), \\
\overline{\mathbf{K}}_{\boldsymbol{\omega}_H^H, \boldsymbol{\psi}_B^G} &= \widetilde{\boldsymbol{e}}_H\mathbf{R}_{HE}(\chi^H)\mathbf{R}_{EB}(\chi^B)\frac{\partial(\mathbf{R}_{BG}(\boldsymbol{\psi}_B^G))}{\partial \boldsymbol{\psi}_B^G}\boldsymbol{\lambda}, \\
\overline{\mathbf{C}}_{\boldsymbol{\omega}_H^H, \chi^B} &= \widetilde{\boldsymbol{e}}_H\mathbf{R}_{HE}(\chi^H)\frac{\partial \mathbf{R}_{EB}(\chi^B)}{\partial \chi^B}(\mathbf{R}_{BG}(\boldsymbol{\psi}_B^G)\boldsymbol{\lambda}), \\
\overline{\mathbf{C}}_{\boldsymbol{\omega}_H^H, \chi^H} &= \widetilde{\boldsymbol{e}}_H\frac{\partial \mathbf{R}_{HE}(\chi^H)}{\partial \chi^H}(\mathbf{R}_{EB}(\chi^B)\mathbf{R}_{BG}(\boldsymbol{\psi}_B^G)\boldsymbol{\lambda}).
\end{aligned} \tag{2.29}$$

The formulation above can be further simplified with alternative choices for the rotation parametrisation - in particular, one could consider $\mathbf{R}_{GH}$ with a 1D dependency in the fold angle, for the third term in $\mathbf{B}_{n2}$. Here, we opted to express equivalence in the body-attached frame both to accommodate the existing solver structure and to keep the formulation general for future additional kinematic constraints.

2.5 Validation: Rigid double pendulum

By deriving the system of equations from first principles for a rigid double pendulum using Lagrangian mechanics, this will serve to verify the formulation and implementation of the multibody solver.

Consider a rigid double pendulum - Newtonian and Lagrangian mechanics would lead to different forms of the system of equations, describing the same dynamics, with different complexity. Both formulations are mathematically equivalent or transformable into one another, as expected from consistent physical formulations. In this particular problem, a Newtonian approach would require the explicit derivation of the internal tension connecting the two rigid bodies, increasing the complexity. The Lagrangian approach, on the other hand, bypasses the direct computation of these internal forces by leveraging generalised coordinates contributing to energy terms - in the set of constraints for an ideal, frictionless hinge connection the constraint forces do not perform work. Here the system of equations is derived, again with the Lagrangian approach. [178]

The Lagrangian $\mathcal{L}$ is defined, for a generalised particle system, in the absence of other sources and sinks of energy, as the difference between the kinetic energy $\mathcal{T}$ and potential energy $\mathcal{U}$ of a system:

$$\mathcal{L} = \mathcal{T} - \mathcal{U}, \tag{2.30}$$

where if the system described is parametrised by a set of independent, constraint-free *generalised coordinates* q_i, and here considering rigid pendulums imply the kinetic energy maps to the generalised velocities, and potential energy in this case to the gravitational field. Hence the dependencies are laid out explicitly as

$$\mathcal{L}(q_i, \dot{q}_i, t) = \mathcal{T}(q_i, \dot{q}_i, t) - \mathcal{U}(q_i, t). \tag{2.31}$$

The action $\mathcal{S}$, a scalar, is the integral of the Lagrangian, given as

$$\mathcal{S}[q_i(t)] = \int_{t_1}^{t_2} \mathcal{L}(q_i, \dot{q}_i, t)\, dt. \tag{2.32}$$

Hamilton's principle of least action requires the action to be stationary for the actual path taken by a system between two specified times t_1 and t_2 to give

$$\delta\mathcal{S} = \delta \int_{t_1}^{t_2} \mathcal{L}(q_i, \dot{q}_i, t)\, dt = 0, \tag{2.33}$$

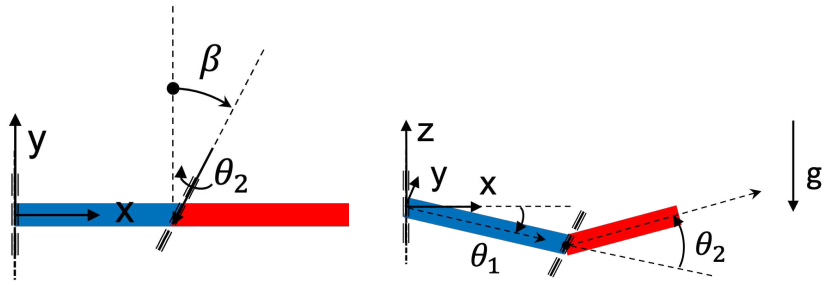
which when we take the partial derivative becomes

$$\begin{aligned} 0 &= \int_{t_1}^{t_2} \left(\frac{\partial \mathcal{L}}{\partial q_i} \delta q_i + \frac{\partial \mathcal{L}}{\partial \dot{q}_i} \delta \dot{q}_i \right) dt \\ &= \int_{t_1}^{t_2} \left(\frac{\partial \mathcal{L}}{\partial q_i} - \frac{d}{dt} \frac{\partial \mathcal{L}}{\partial \dot{q}_i} \right) \delta q_i \, dt. \end{aligned} \tag{2.34}$$

For the equality to hold true with any arbitrary δq_i the expression within the brackets must vanish, and hence we arrive at the Euler–Lagrange equations:

$$\frac{d}{dt} \left(\frac{\partial \mathcal{L}}{\partial \dot{q}_i} \right) - \frac{\partial \mathcal{L}}{\partial q_i} = 0 \quad \text{for } i = 1, 2, \ldots, n. \tag{2.35}$$

Now for our double pendulum parametrised as two constant density beams each of length l_n, mass m_n, without loss of generality with a square cross section of width w_n for $n = 1$ or 2 choosing the fold angles θ_1 and θ_2 gives us the set of constraint-free generalised coordinates, their derivatives as generalised velocities, required to describe the system dynamics. The acceleration due to gravity is g. Note this can be extended to pendulums with non-perpendicular hinges, for which motion is no longer limited in a 2D plane, with relative ease, we can describe the trajectories and hence the energies and Lagrangian of the resultant system as functions of the flare angle β. When $\beta = 0$ we then recover the 2D double pendulum, and when $\beta = 90°$ the system is effectively reduced to a single swinging pendulum.



(a) Top view at t=0 (b) 3D view at t>0

Figure 2.5: Setup of the rigid-body model

Hence we arrive at analytical expressions for the locations of the centre of mass of the two pendulums $\boldsymbol{r}_{1_{mid}}$ and $\boldsymbol{r}_{2_{mid}}$ as

$$\boldsymbol{r}_{1_{mid}} = \begin{bmatrix} x_{1_{mid}} \\ y_{1_{mid}} \\ z_{1_{mid}} \end{bmatrix} = \begin{bmatrix} l_1 \cos(\theta_1)/2 \\ 0 \\ -l_1 \sin(\theta_1)/2 \end{bmatrix}, \text{ and } \boldsymbol{r}_{2_{mid}} = \begin{bmatrix} x_{2_{mid}} \\ y_{2_{mid}} \\ z_{2_{mid}} \end{bmatrix} = \begin{bmatrix} 2x_{1_{mid}} + l_2 x_{2_{rot}}/2 \\ 2y_{1_{mid}} + l_2 y_{2_{rot}}/2 \\ 2z_{1_{mid}} + l_2 z_{2_{rot}}/2 \end{bmatrix}, \tag{2.36}$$

where

$$\begin{bmatrix} x_{2_{rot}} \\ y_{2_{rot}} \\ z_{2_{rot}} \end{bmatrix} = \begin{bmatrix} \cos(\theta_1) & 0 & \sin(\theta_1) \\ 0 & 1 & 0 \\ -\sin(\theta_1) & 0 & \cos(\theta_1) \end{bmatrix} \begin{bmatrix} \left(\sin(\beta)\sin(\beta) + \frac{\cos(\beta)(1+\cos(2\beta))}{\sqrt{2+2\cos(2\beta)}}\right)\cos(\theta_2) \\ \left(\sin(\beta)\cos(\beta) - \frac{\cos(\beta)\sin(2\beta)}{\sqrt{2+2\cos(2\beta)}}\right)\cos(\theta_2) \\ -\sin(\theta_2)\cos(\beta) \end{bmatrix}, \tag{2.37}$$

in which the last term of $\boldsymbol{r}_{2_{rot}}$ is the location of a point in Cartesian coordinates along the base of the cone by θ_2 with a half cone angle of $(\pi - \beta)$, since in the frame of the tip of rigid pendulum 1, the mid point of pendulum 2 makes the locus of a cone.

The Lagrangian of the system is hence a function of the derivatives of $\boldsymbol{r}_{1_{mid}}$ and $\boldsymbol{r}_{2_{mid}}$, as well as other constants, expressed as

$$\begin{aligned} \mathcal{L} = &\Bigg(\frac{m_1}{2} \left| \frac{d\boldsymbol{r}_{1_{mid}}}{dt} \right|^2 + \frac{m_2}{2} \left| \frac{d\boldsymbol{r}_{2_{mid}}}{dt} \right|^2 \\ &+ \frac{I_{1_y}}{2} \left| \frac{d\theta_1}{dt} \right|^2 + \frac{I_{2_y}}{2} \left| \cos(\beta)\frac{d\theta_2}{dt} + \frac{d\theta_1}{dt} \right|^2 + \frac{I_{2_x}}{2} \left| \sin(\beta)\frac{d\theta_2}{dt} \right|^2 \Bigg) \\ &- \left(m_1 g z_{1_{mid}} + m_2 g z_{2_{mid}} \right), \end{aligned} \tag{2.38}$$

where the first row is the translational kinetic energy, second row the rotational kinetic energy, and finally the gravitational potential energy. The mass inertias I_n are given, assuming square cross sections, as

$$I_{n_x} = \frac{1}{12} m_n \left(l_n^2 + w_n^2 \right), \text{ and}$$

$$I_{n_{y,z}} = \frac{1}{12} m_n \left(w_n^2 + w_n^2 \right) = \frac{1}{6} m_n w_n^2,$$

for rotations about the selected axes.

Now we can go forward and substitute the expression for the Lagrangian into the Euler-Lagrange equations using a symbolic mathematics package. The fully expanded set of 2 equations can be found in Appendix A.1. The equations of motion can be presented in the standard structure where

$$\mathbf{M}(\mathbf{q})\,\ddot{\mathbf{q}} + \mathbf{C}(\mathbf{q}, \dot{\mathbf{q}})\,\dot{\mathbf{q}} + \mathbf{K}(\mathbf{q}) = \mathbf{0} \tag{2.39}$$

where $\mathbf{q} = [\theta_1, \theta_2]^T$ is the generalised coordinate vector. $\mathbf{M}(\mathbf{q})$ entails the system's rotational inertia and couples the angular accelerations $\ddot{\theta}_1$ and $\ddot{\theta}_2$. $\mathbf{C}(\mathbf{q}, \dot{\mathbf{q}})$ captures centrifugal and Coriolis effects that arise from the nonlinear coupling of the rotating links. $\mathbf{K}(\mathbf{q})$ contains all gravitational restoring forces that act to bring the system back toward equilibrium.

2.5.1 Reference slanted-hinge double pendulum results

For such a intricate-looking system luckily this is rather straightforward to numerically march in time. The structural parameters of our reference pendulum is as tabulated.

Table 2.3: Reference pendulum parameters

Parameters	Description	Values	Units
l_x	Axial length	0.5	m
l_d	Cross-sectional side length	0.02	m
ρ	Material density	2700	kg m^{-3}
I_y	Moment of inertia w.r.t. y axis	1.127E-02	kg m
I_x	Moment of inertia w.r.t. x axis	3.600E-05	kg m
g	Gravity	9.81	m s^{-2}
θ_{1_0}	Initial value for θ_1	0	deg
θ_{2_0}	Initial value for θ_2	0	deg
t	Simulation time	2	s

Notice of course the non-zero y-coordinate for the tip position of the double pendulum as we time step the system in Figure 2.6 - the out of pendulum (x-z) plane motion is a result of the flare angle. For the first swing the out-of-plane excursion remains relatively small, reflecting weak initial excitation of this mode. Since the system is governed by nonlinear, coupled equations of motion, the lateral response can become increasingly sensitive to the initial conditions and pendulum parameters. Over time or at higher energies it can evolve into the familiar chaotic regime where the out-of-plane motion becomes larger and strongly aperiodic, analogous to the planar double pendulum.

From the derivation of the systems of equation for the rigid slanted-hinge double pendulum in the previous section, it can be observed that even with just two degrees of freedom, the complexity of the symbolic description of the resultant system quickly grows. With more degrees of freedom required to model the double pendulum as flexible beams themselves, the analytical problem becomes intractable.

2.6 Validation: Flexible double pendulum

The rigid results given in 2.5.1 are compared with two flexible models, one from SHARPy, one from MSC NASTRAN. For the latter, to model the slanted hinge, two CBUSH elements of sufficient stiffness ($1.00 \times 10^{12}\,\mathrm{kg\,m^{-1}\,s^{-2}}$) were placed, enforcing coincidence of two RBE2

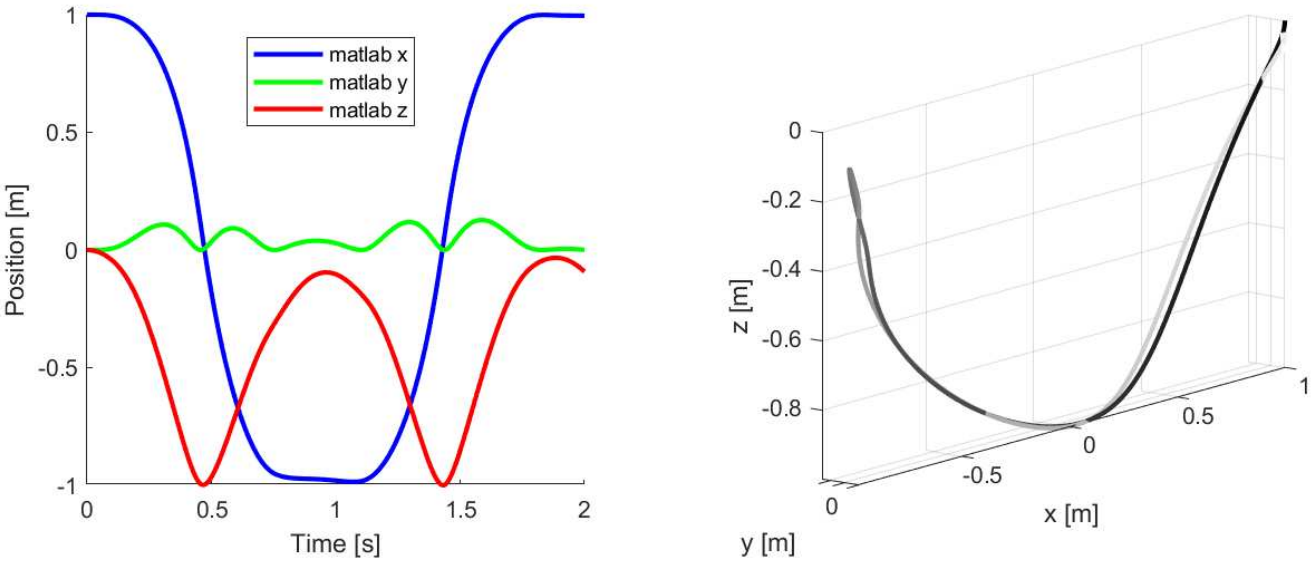


Figure 2.6: Tip position for the rigid double pendulum with 45° flare angle. Left: Time histories. Right: Trajectory in 3D.

elements, consisted of two pairs of GRID points, along the hinge line as described in Section 2.4.1. NASTRAN SOL400 was used to perform nonlinear multibody analysis.

The common parameters of the three different models at baseline rigidity $\sigma = 1$ are tabulated in Table 2.4. σ as the non-dimensionalised rigidity of the double pendulum will be varied in the series of verification and validation cases to examine the accuracy and robustness of the structural multibody formulation.

Table 2.4: Common model parameters for rigidity ratio $\sigma = 1$

Parameters	Description	Values	Units
l_x	Axial length	0.5	m
l_d	Cross-sectional side length	0.02	m
ρ	Material density	2700	kg m^{-3}
I_y	Moment of inertia w.r.t. y axis	1.127×10^{-2}	kg m
I_x	Moment of inertia w.r.t. x axis	3.600×10^{-5}	kg m
EA	Axial rigidity	2.800×10^{7}	kg m s^{-2}
GA	Shear rigidity	1.037×10^{7}	kg m s^{-2}
EI	Flexural rigidity	9.333×10^{2}	kg m^3 s^{-2}
GJ	Torsional rigidity	6.914×10^{2}	kg m^3 s^{-2}
g	Gravity	9.81	m s^{-2}

Three cases ($\beta = 0, 45°, 90°$) are investigated, corresponding to three very different sets of dynamics in play. All cases are initialised with θ_{1_0} and θ_{2_0} at 0°. A simulation time of 2 seconds used, which is very close to the period of the pendulum motion. Correspondingly Δt for each of the MATLAB, MSC NASTRAN, and SHARPy model is 3.54×10^{-3} s, 2.00×10^{-4} s, and 2.00×10^{-3} s respectively. 5 elements are used with the SHARPy model, and 10 CBEAM elements with MSC NASTRAN. Note that NASTRAN CBEAM elements are 2-noded, whereas SHARPy beam elements are 3-noded.

Case $\beta = 0$

This is equivalent to the case when we have a planar double pendulum. As expected, the motion is entirely contained in the x-z plane, and we only start to see deviations in the NASTRAN solution from the rigid MATLAB result after almost a period when chaotic effects are more prone to kicking in.

Case $\beta = 90°$

This is equivalent to the case when we effectively have a single planar pendulum, a problem to which an analytical solution exists. As this is not computationally demanding at all, and also likely as the rotation about the axial direction have not caused numerical issues, we have not observed any meaningful deviation from the rigid result.

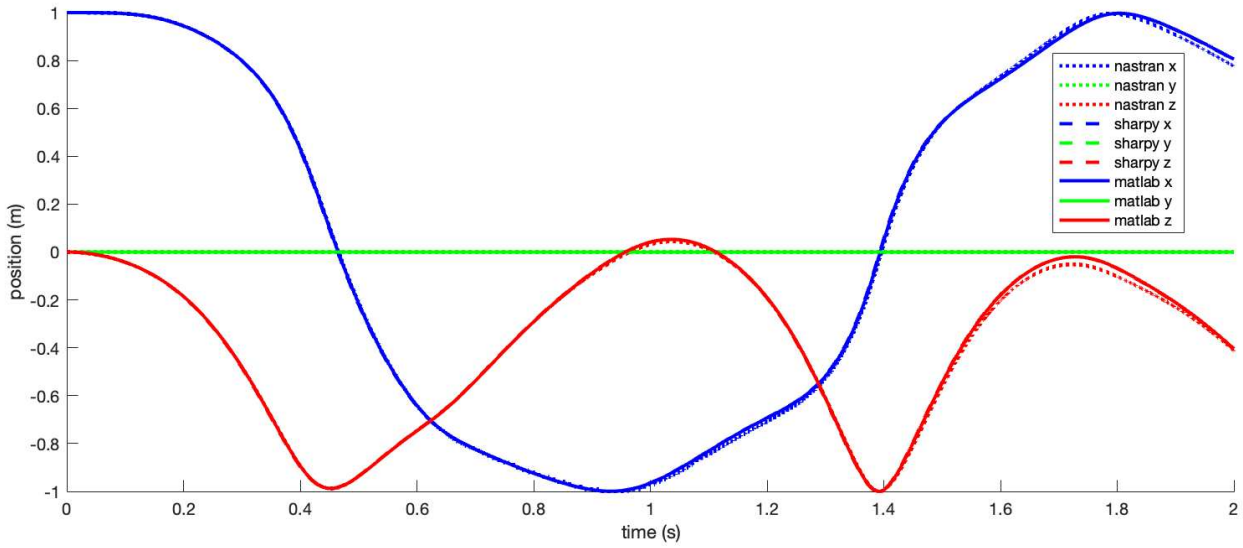


Figure 2.7: $\boldsymbol{r}_{2_{tip}}$ time histories for $\beta = 0$, $\sigma = 1$

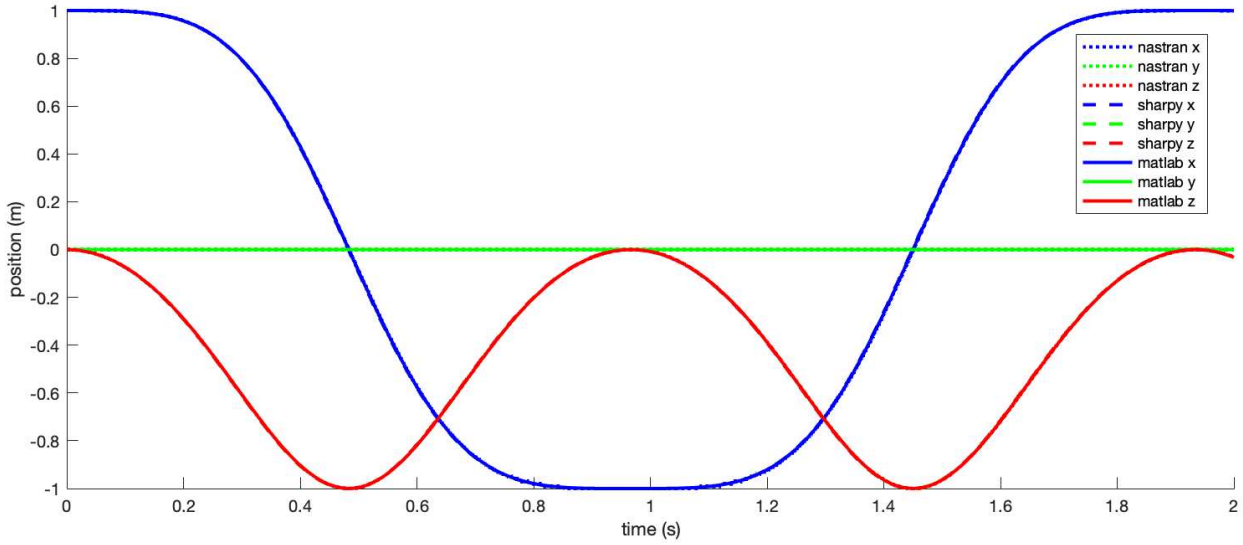


Figure 2.8: $\boldsymbol{r}_{2_{tip}}$ time histories for $\beta = 90$, $\sigma = 1$

Case $\boldsymbol{\beta = 45°}$

The slanted double pendulum undergoes translation and rotation in the 3D space, as evidenced by the non-zero $y_{2_{tip}}$ values. The flexible (SHARPy and NASTRAN) results shows significant deviations from the rigid comparison during the second swing, when the elastic modes of the system is energised, supported by the fact that the flexible results are almost coincident.

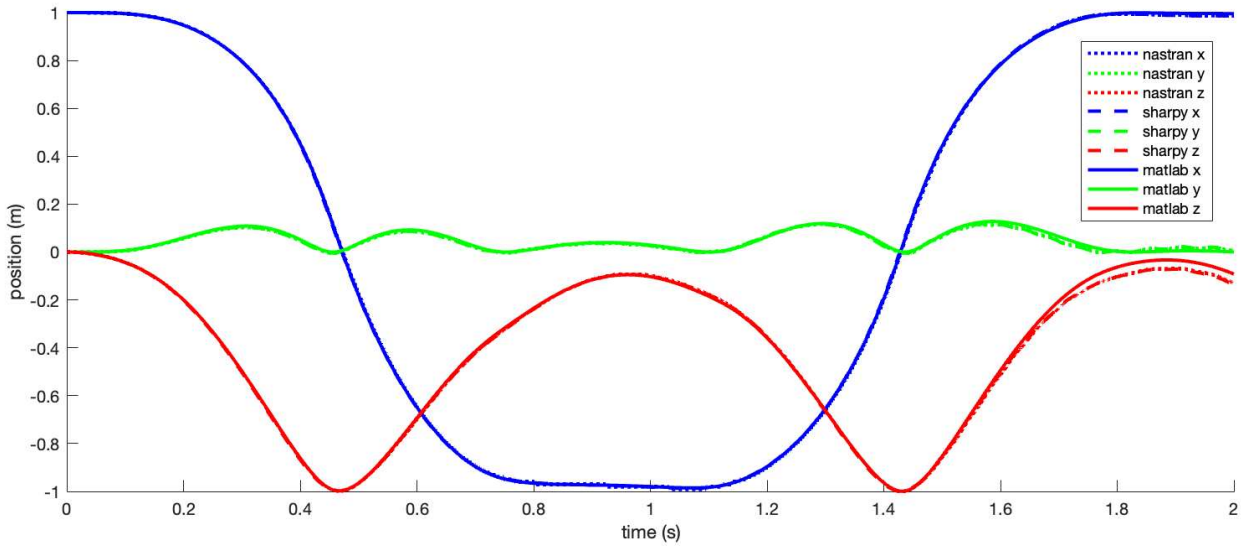


Figure 2.9: $\boldsymbol{r}_{2_{tip}}$ time histories for $\beta = 45$, $\sigma = 1$

To further investigate the robustness of the SHARPy implementation we have reduced the rigidity in all directions by ten-fold. Notice now the two swings are significantly less symmetric, and that NASTRAN results deviate from SHARPy to assume another trajectory.

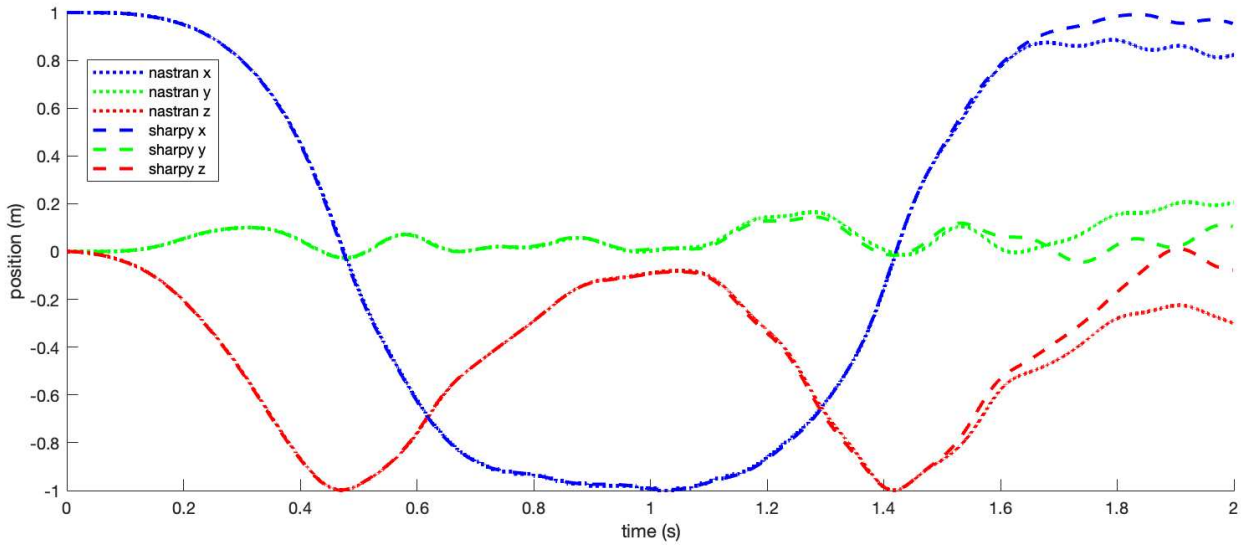


Figure 2.10: $\boldsymbol{r}_{2_{tip}}$ time histories for $\beta = 45$, $\sigma = 0.1$

We have then refined the discretisation five-fold for both the models to see if that would improve the accuracy of the NASTRAN results. With a total of 100 CBEAM elements convergence was only slightly improved, since the chaotic nature of the system meant small deviations are readily propagated to push the system on an alternate path.

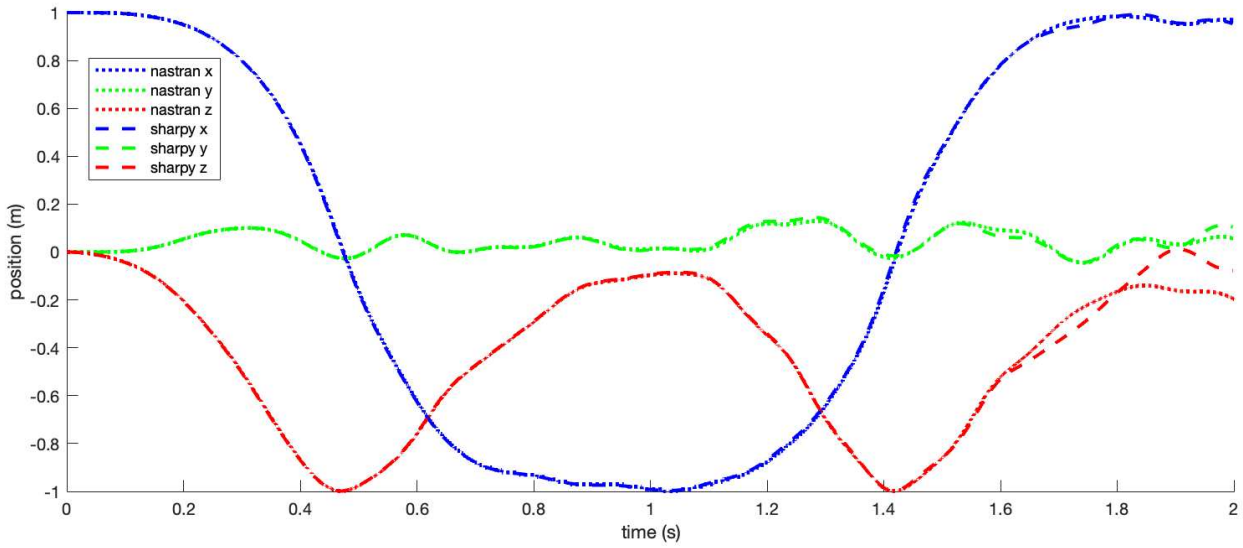


Figure 2.11: $\boldsymbol{r}_{2_{tip}}$ time histories for $\beta = 45$, $\sigma = 0.1$, 10 $\times$ more elements

By reducing the rigidity of the system by a further ten-fold the role of the rigid body motion at the hinge is masked by the flexible deformations of the beams. Hence even with the original discretisation we recover good agreement between SHARPy and NASTRAN results. These tests have established the validity and robustness of the SHARPy hinge condition across various stiffness regimes, geometry, and initial conditions over existing methods.

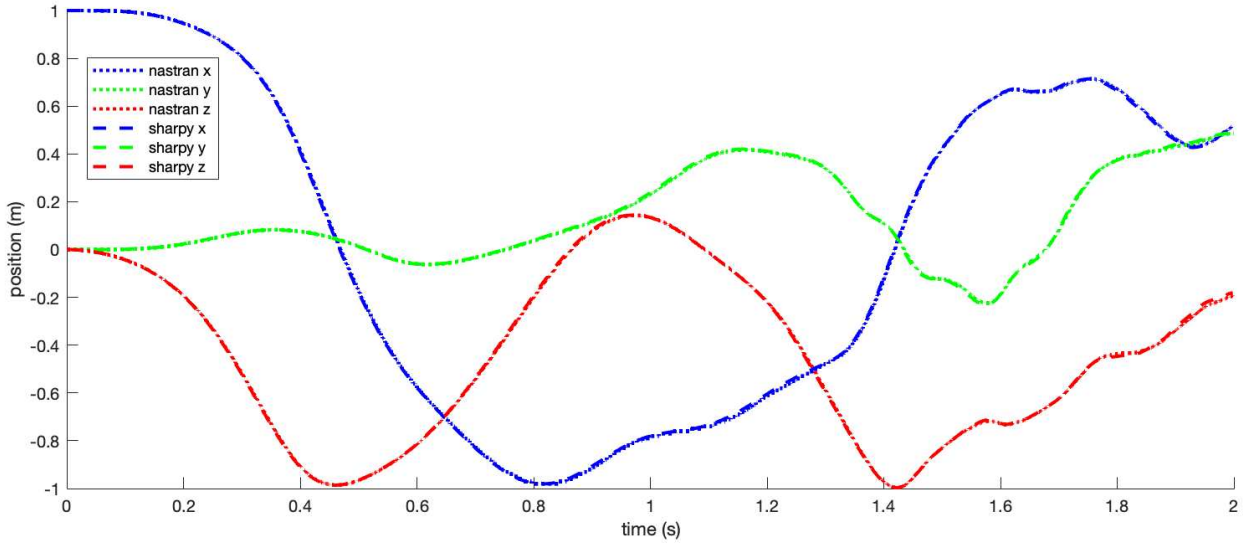


Figure 2.12: $\boldsymbol{r}_{2_{tip}}$ time histories for $\beta = 45$, $\sigma = 0.01$

2.7 Validation: Multibody dynamics across beam formulations and implementations

Here we have selected some results from code-to-code validation of the multibody beam formulation completed. For the same double pendulum verified in Section 2.6, results from [198] are given in Figure 2.13 as reproduced from the paper. We compare against ANCF because it is a well-established approach for flexible multibody beam modelling, and recent work by Otsuka and coauthors [174, 175] has applied ANCF to hinged-wing and deployable-wing dynamics. The multibody ANCF method produces indistinguishable time histories compared to the SHARPy implementation, indicating that neither the more involved constraint definition in SHARPy nor the poorer convergence of ANCF reported in the literature reduce accuracy in this case.

In [199], the dynamic response of a flexible planar double pendulum is simulated to validate different solvers' ability to capture significant geometric nonlinearities. The geometric and stiffness properties for the links are detailed in Table 2.5, with a sufficiently high shear modulus (G) applied to minimise shear deformation. Figure 2.14 presents the time history of the horizontal tip displacement, comparing the results from the displacement-based [187, 200], intrinsic [201], and strain-based [164, 202, 203] beam formulations. All three methods show excellent agreement throughout the simulation, even as high-frequency content emerges near the end of the swing period.

Table 2.5: Model parameters for flexible planar pendulum in [199]

Parameters	Description	Values	Units
l_x	Axial length	0.5	m
l_d	Cross-sectional side length	0.02	m
ρA	Mass per unit length	2.88	kg m^{-1}
ρI_{yy}	Rotational inertia w.r.t. y axis	9.60×10^{-5}	kg m
ρI_{xx}	Rotational inertia w.r.t. x axis	1.92×10^{-4}	kg m
EA	Extensional stiffness	8000	N
EI	Bending stiffness	0.2667	N m^2
g	Gravity	9.8	m s^{-2}

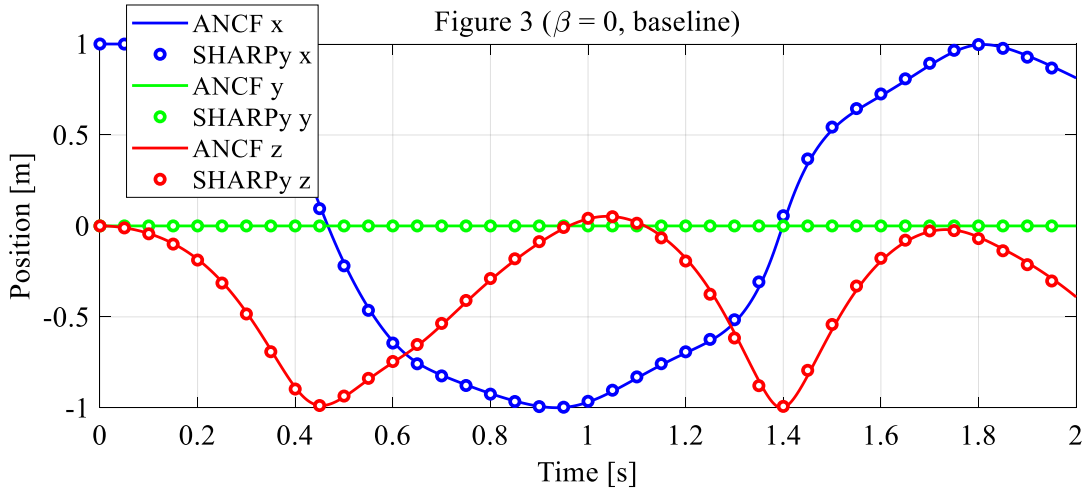


Figure 3 ($\beta = 0$, baseline)

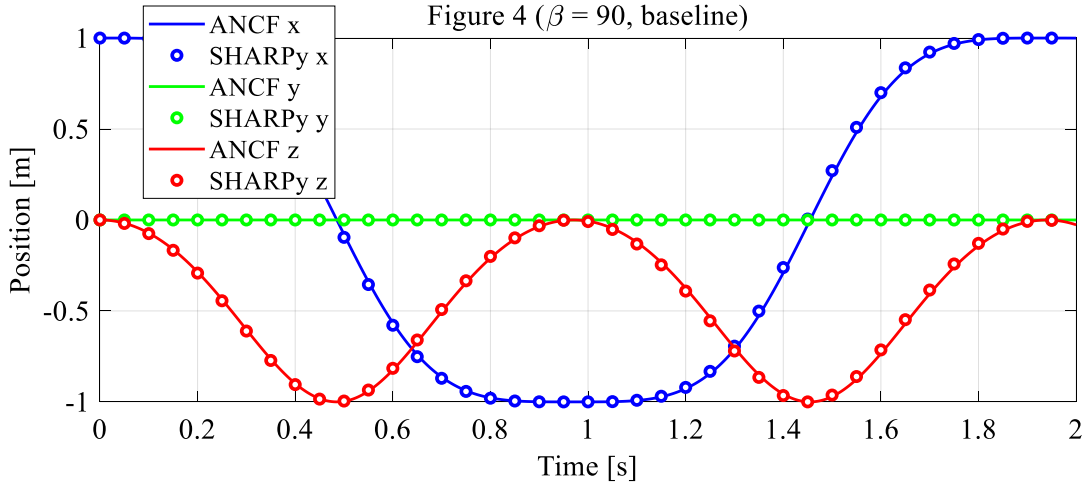


Figure 4 ($\beta = 90$, baseline)

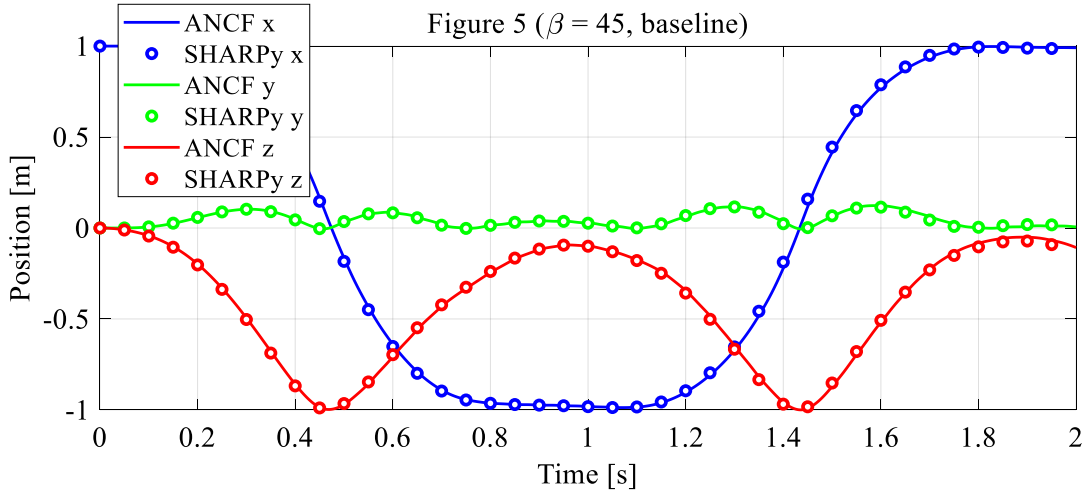
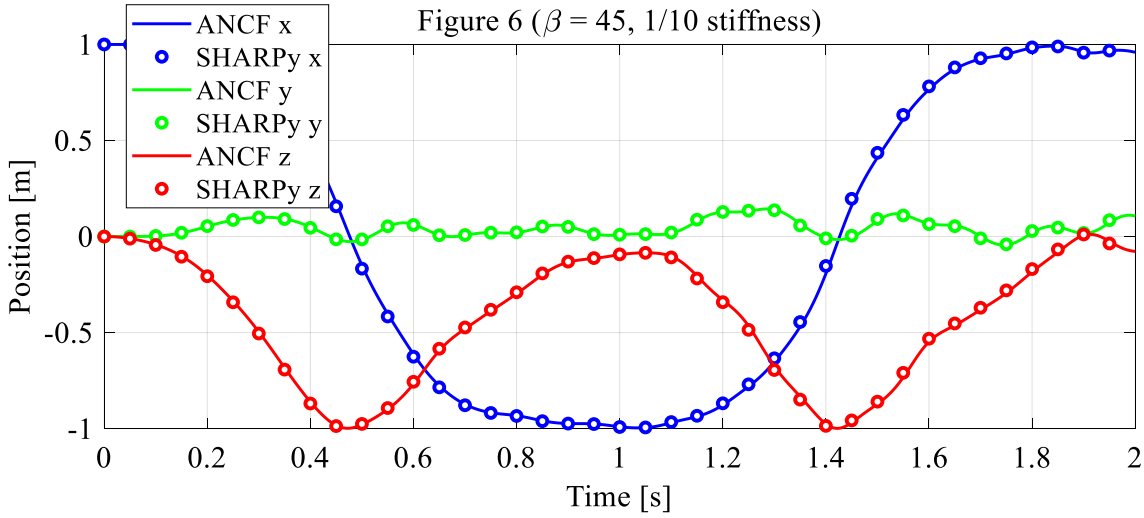
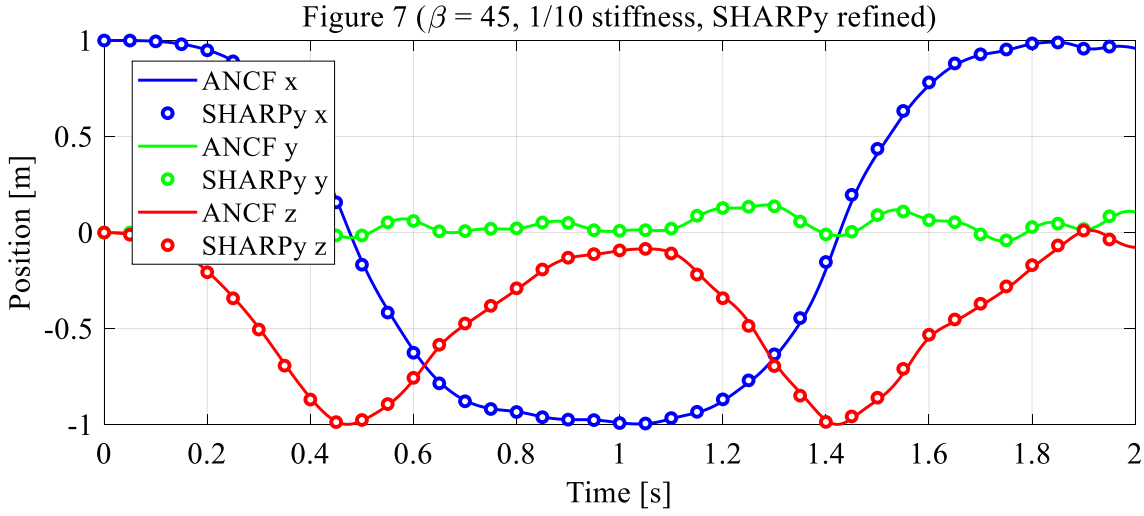


Figure 5 ($\beta = 45$, baseline)





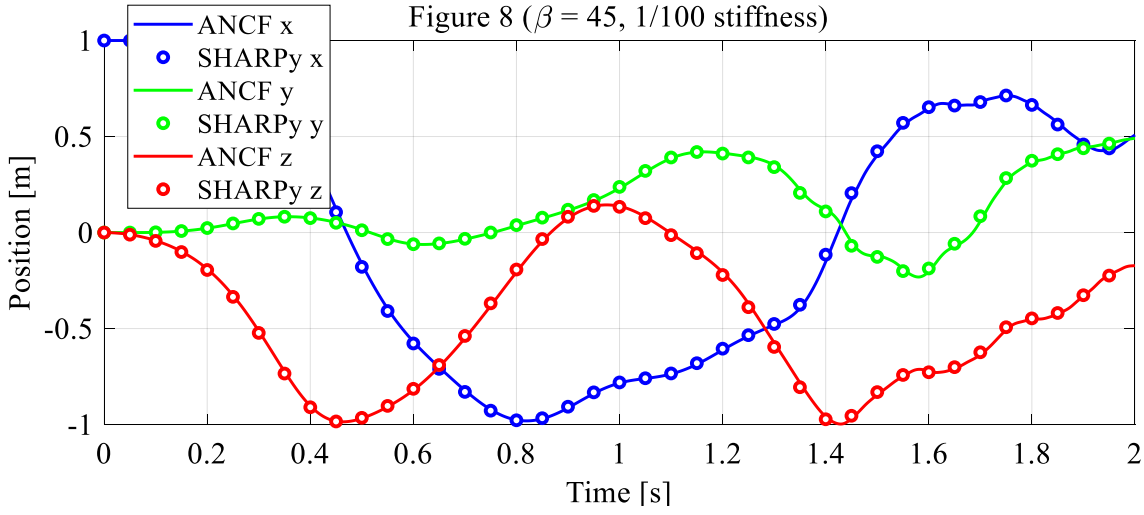


Figure 2.13: Time histories of free-end coordinates of double pendulum, reproduced from [198]

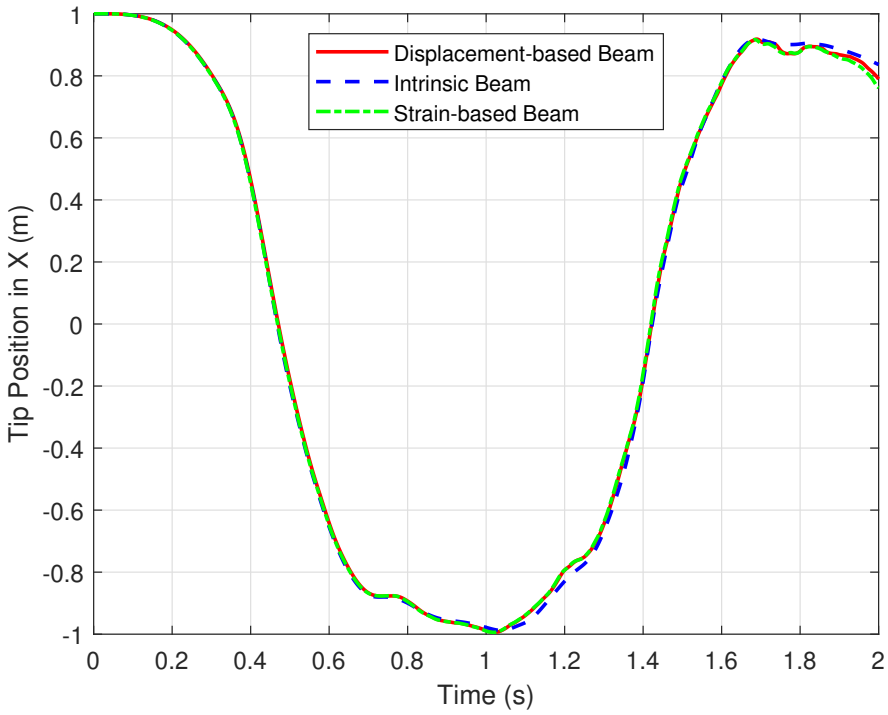


Figure 2.14: Time history comparison of the horizontal tip position for the flexible double pendulum, reproduced from [199]

2.8 Summary

Thus we have laid out the core building blocks of a coupled structural and multibody dynamics framework, with a geometrically-exact beam augmented with multibody kinematics to represent a wing–wingtip assembly. The implementation is verified against various benchmarks in literature, showing good agreement. This enables our work to model very flexible aircraft that requires coupling the said framework with unsteady aerodynamics for time-domain simulations.

Chapter 3

Modelling aeroelastic multibody systems

Building on the flexible multibody structural dynamics formulation introduced and verified in the previous chapter, we couple that with unsteady aerodynamic modelling to capture the aeroelastic behaviour of the system. Unsteady aerodynamics is particularly important in aeroelasticity because phenomena like flutter and limit-cycle oscillations (LCOs) depend on the phase-lagged, history-dependent aerodynamic load response to structural motion. The structural displacements and rotations computed from the geometrically-exact beam and multibody dynamics deform the aerodynamic lifting surfaces, which in turn affect the aerodynamic load distribution. The aerodynamic forces are computed via the Unsteady Vortex Lattice Method (UVLM), with corrections to be detailed, and are fed back to the structural solver at each time step in a strongly coupled scheme.

3.1 Unsteady potential flow aerodynamics

For aeroelastic problems, the nodal displacements are used to deform the lifting surfaces on which the aerodynamics solver computes nodal loads [196], which is in turn passed onto the multibody solver for the next time step in a classical FSI coupling scheme.

Here a brief overview of the method is given, with particular focus on two aspects of the implementation that is most relevant to the accurate modelling of the physics involved in wings with hinged wing tips.

The UVLM is based on the assumption of potential flow, that the fluid is considered incompressible, inviscid, and irrotational. For incompressible flow with constant density ρ,

the continuity equation reduces to the divergence-free condition

$$\nabla \cdot \mathbf{u} = 0, \tag{3.1}$$

where $\mathbf{u}$ is the velocity field. The lack of viscous drag predictions does not prejudice the dynamic predictions of the aeroelastic multibody system, as will be shown later. Neglecting viscosity eliminates the viscous stress terms in the Navier-Stokes equations, reducing them to the Euler equations. The resulting dynamics are governed only by inertia and pressure forces, with no shear stresses or vorticity diffusion. If the flow is also irrotational, that's equivalent to the curl of the velocity field being the zero vector,

$$\nabla \times \mathbf{u} = \mathbf{0}, \tag{3.2}$$

and there exists a scalar velocity potential ϕ such that

$$\mathbf{u} = \nabla\phi. \tag{3.3}$$

Substituting $\mathbf{u} = \nabla\phi$ into the incompressibility condition gives

$$\nabla \cdot \mathbf{u} = \nabla \cdot (\nabla\phi) = \nabla^2\phi = 0, \tag{3.4}$$

which is Laplace's equation for the velocity potential. The velocity potential is subjected to the boundary conditions as described - firstly, in nearfield on the surface of the lifting body we enforce the non-penetration condition, expressed as the normal derivative of the potential along the surface normal vector $\mathbf{n}$, or as a dot product of the velocity at the surface $\mathbf{u}_{surf}$, as a result of superposition with the background flow field with disturbances, $\mathbf{v}$,

$$\left(\frac{\partial\phi}{\partial\mathbf{n}} + \mathbf{v}\right) \cdot \mathbf{n} = \mathbf{u}_{surf} \cdot \mathbf{n} = 0. \tag{3.5}$$

Next, we have the farfield condition that requires the potential changes caused by the body and wake to vanish at infinity,

$$\lim_{|\mathbf{x}|\to\infty} \phi(\mathbf{x}, t) = \phi_\infty(\mathbf{x}), \tag{3.6}$$

where ϕ_∞ is the potential of the undisturbed freestream flow, and $\mathbf{x}$ represents a position vector in the fluid domain with origin at the body.

With the UVLM, Equation 3.4, being linear in nature, is solved by the superposition of vortices, an elementary solution to the partial differential equation, with a collocation method in the time domain. Firstly, the lifting surface (with zero thickness as modelled) along the wing camber line, is discretised spanwise and chordwise into N and M_b quadrilateral panels,

each of which consists of a control point at the centre, where the non-penetration condition is enforced, and a set of 4 bounded vortex segments of equal strength, integrated along the closed. The 4 endpoints of each of the $\mathrm{NM_b}$ panels are collected into $\boldsymbol{\zeta}_b$.

This alone is not sufficient to model lift on the wing, as circulation as the closed-loop integral of vorticity along the wing must be non-zero to give lift. The Kutta condition is imposed at the trailing edge panels, where wake vorticity shed into the first corresponding panels of the wake (hence of same spanwise number of panels N) is equal and opposite to the instantaneous change in circulation on the airfoil. This satisfies Kelvin's theorem that total circulation is conserved in time considering both the body and wake surfaces. The wake is discretised chordwise with more panels $\mathrm{M_w}$ than the body - since the wake keeps the history of all past circulation changes on the wing, but also because the forces and moments acting on the all lifting surfaces are functions of the shape of the wake, discretised similarly as the 4 endpoints of each of the $\mathrm{NM_w}$ panels in time as $\boldsymbol{\zeta}_w$.

The discrete time-marching solution procedure is explicit, first-order, and goes as follows: at time step 0 we initialise the wake by some informed guesswork - we choose an initial spatial configuration for $\boldsymbol{\zeta}_w$ with circulation Γ_w set to zero - for the problems of interest we usually lay subsequent wake panels downstream in a straight wake, of panel length $u_\infty \Delta t$. At time step t we take the converged body panel displacements and velocities $\boldsymbol{\zeta}_b$ and $\dot{\boldsymbol{\zeta}}_b$, considering all of the vortices in the fluid domain, no matter bound on body or free in wake, will induce a flow velocity at the collocation points on the body panels, where we enforce the non-penetration boundary condition from Equation 3.5, which we generalise to describe a non-stationary body with potentially large geometry changes, giving rise to $\mathrm{NM_b}$ equations of form

$$\mathbf{K}_c(\boldsymbol{\zeta}_b^n, \boldsymbol{\zeta}_b^n)\boldsymbol{\Gamma}_b^n + \mathbf{K}_c(\boldsymbol{\zeta}_b^n, \boldsymbol{\zeta}_w^n)\boldsymbol{\Gamma}_w^n + \mathbf{W}_c(\boldsymbol{\zeta}_b^n)(u_b^n - \dot{\boldsymbol{\zeta}}_b^n) = \mathbf{0} \tag{3.7}$$

,

where $\mathbf{K}_c(\boldsymbol{\zeta}_b, \boldsymbol{\zeta}_b)$ is a discrete kernel matrix derived from the Biot–Savart law, representing the velocity induced at the collocation points by the bound circulation, $\mathbf{K}_c(\boldsymbol{\zeta}_b, \boldsymbol{\zeta}_w)$ for the same by the wake circulation, $\mathbf{W}_c(\boldsymbol{\zeta}_b)$ for interpolates the structural velocity from the lattice vertices to the collocation points and projects it onto the local normal vector, u_b^{n+1} for background flow velocity at the bound lattice vertices at t_{n+1}. This reflects the elliptical nature of the Laplace equation - disturbances in the flow field propagate instantaneously throughout the entire domain, precisely by the non-penetration equations.

Here it is appropriate to lay out the discrete form of the Biot-Savart law, implemented as

$$\mathbf{u}_{\text{ind}}(\mathbf{x}) = \frac{1}{4\pi} \sum_k \sum_l \frac{\mathbf{r}_{0l}^\top \left(\frac{\mathbf{r}_{1l}}{|\mathbf{r}_{1l}|} - \frac{\mathbf{r}_{2l}}{|\mathbf{r}_{2l}|} \right) \tilde{\mathbf{r}}_{1l} \mathbf{r}_{2l}}{|\tilde{\mathbf{r}}_{1l} \mathbf{r}_{2l}|^2} \mathbf{\Gamma}_k \tag{3.8}$$

where $\mathbf{\Gamma}_k$ is the circulation strength of the k-th vortex ring, k runs through all vortex rings (both bound and wake), l iterates over the segments of the k-th vortex ring, $\mathbf{r}_{0l}$, $\mathbf{r}_{1l}$, and $\mathbf{r}_{2l}$ are segment vectors related to the geometry of the l-th segment and the target point $\mathbf{x}$. The expression containing the vector ratios and the cross product ($\tilde{\mathbf{r}}_{1l}\mathbf{r}_{2l}$) defines the discrete kernel that maps the circulation $\mathbf{\Gamma}_k$ to the induced velocity. The cross product as implemented has a lower bound of a minimum vortex core radius, to avoid the expression for induced velcoity being singular.

The NM_w equations each for wake circulations and panel locations are described next - they follow naturally from the convection of circulation downstream of the trailing edge, and the induced velocity of the bound and wake circulation on the wake panels.

The convection is described as a linear combination of two effects, namely,

$$\mathbf{\Gamma}_w^{n+1} = \mathbf{C}_{\Gamma b} \mathbf{\Gamma}_b^n + \mathbf{C}_{\Gamma w} \mathbf{\Gamma}_w^n \quad , \tag{3.9}$$

where the first effect is captured by $\mathbf{C}_{\Gamma b}$, a sparse constant matrix that introduces the Kutta–Joukowski condition at the trailing edge, linking the bound circulation to the first row of wake vortex rings (shedding circulation), and the second by $\mathbf{C}_{\Gamma w}$, a sparse constant matrix that shifts the wake circulation downstream on streamwise row at every time step, based on the discretisation of the convection equation. For simplicity we usually assume a Courant-Friedrichs–Lewy number CFL of 1 where $\text{CFL} = u_\infty \Delta t / \Delta \zeta$. This in effect describes the wake convection as a chordwise downstream transfer of historic shed circulation, where $\mathbf{\Gamma}_k^{t+1} = \mathbf{\Gamma}_{k-1}^t$, and k is a chordwise coordinate not at the trailing edge.

If we neglect the induced velocity of the bound and wake circulation on the wake panels, that reduces the description of the instantaneous wake panel locations $\boldsymbol{\zeta}_w$ to the historical location of the trailing edge, where each new wake panel created from shed circulation in each time step, following a $\text{CFL} = 1$ discretisation, is offset for $u_\infty \Delta t$ from the instantaneous trailing edge location. That is what is described as a *prescribed* wake - by which wake-wake-body interactions and self-interactions (giving the characteristic wing tip wake roll up effects) are not considered.

Instead if we consider also the induced velocities, the full expression is given as

$$\boldsymbol{\zeta}_w^{n+1} = \mathbf{C}_{\zeta b}\boldsymbol{\zeta}_b^{n+1} + \mathbf{C}_{\zeta w}\boldsymbol{\zeta}_w^{n} + \Delta t\dot{\boldsymbol{\zeta}}_w^{n} \tag{3.10}$$

where $\mathbf{C}_{\zeta b}$ is a sparse matrix relating the coordinates at the trailing edge ($\boldsymbol{\zeta}^{n+1}b$) to those on its downstream wake, and $\mathbf{C}_{\zeta w}$ is a sparse matrix that shifts the wake lattice downstream along the streamwise row at every time step.

Equations 3.7, 3.9, and 3.10 describe an explicit first order time-stepping scheme for the UVLM system for low-speed flight, implemented in SHARPy. At each time step we return the aerodynamic forces to the structural solver, by considering both quasi-steady lift from Joukowski's theorem, and unsteady lift from the added mass effect. The quasi-steady component, acting on each of the 4 vortex segment centre at a panel, is given as the cross product of the circulation and the local flow velocity, scaled by the fluid density,

$$\boldsymbol{f}_{\text{steady}} = \rho\Gamma_s\left(\overline{\boldsymbol{v}}_s \times \boldsymbol{l}_s\right) \tag{3.11}$$

where the subindex s iterates through each vortex segment, $\overline{\boldsymbol{v}}_s$ is the relative segment-fluid velocity, and l the segment vector.

The unsteady component is instead calculated at the collocation point as a pressure force due to the acceleration of the vortex segment,

$$\boldsymbol{f}_{\text{unsteady}} = \rho S_k \boldsymbol{n}_k \dot{\Gamma}_k \tag{3.12}$$

where $\boldsymbol{n}$ again is the normal vector at the collocation point, and S is the panel area.

The variable wake discretisation described, implemented, and verified by Muñoz et al. [204] is utilised to reduce computational cost while, as confirmed by refinement studies, preserving the accuracy of the original scheme.

3.1.1 Panelling at the hinge line

As mentioned above, the unsteady aerodynamics are modelled by the UVLM. This approach easily accommodates the wingtip kinematics. The UVLM grid boundary at the hinge is skewed by the hinge axis along the flare angle, as shown in Figure 3.1. This ensures as the structure rotates about the hinge axis there is no ambiguity of the aero-structural force-displacement interface, as discussed in Ref. [205]. Here, all UVLM grid nodes along the same chord-wise line are controlled by the displacements and rotations of the corresponding beam

node. The careful choice of span-wise discretisation is hence crucial to avoid a self-intersecting UVLM grid.

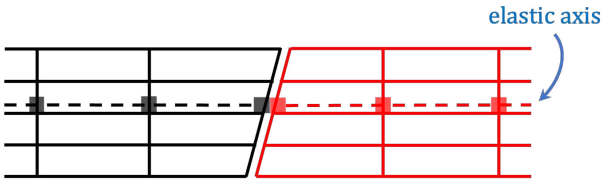


Figure 3.1: UVLM grid boundaries with beam nodes near the hinge

3.1.2 Sectional polar correction

While UVLM is effective for low-subsonic aeroelastic applications involving thin lifting surfaces with attached flow, it does not inherently account for viscous effects, compressibility, or non-lifting body interactions. This is problematic in two aspects, specially in the case of dynamic hinged wing tips. Firstly, the wing tips when unlocked tend to fly at larger range of flow incidence angles, requiring a more realistic lift curve slope to be referenced when time-marching the system to predict the correct dynamics. Also, where interactions between lifting bodies are relevant, UVLM tends to overestimate the induced forces primarily due to the lack of stall modelling, leading to wrong aeroelastic predictions.

The process for sectional polar force correction as implemented in SHARPy is the work of Goizueta (Chapter 4.1.1) [206] and Düssler (Chapter 2.3.3) [186]. Relevant parts of the formulation are included next for completeness.

Fundamentally the corrections are obtained by the estimation of the local angle of attack at each airfoil section, then the interpolation of 2D airfoil polar data provided for the corrected steady lift, drag, and moment coefficients. The effective local angle of attack of any point along the beam, dependent on the instantaneous coupled multibody and structural kinematics, is not tracked in the formulation given in Chapter 2, and hence here we rely on the seen sectional lift coefficient computed by the UVLM, $C_{l,i}$ at each section i as

$$C_{l,i} = \frac{\boldsymbol{f}_A^\top \boldsymbol{e}_{A,z}}{0.5\rho \left|\boldsymbol{u}_{\mathrm{rel}_{E_i}}\right|^2 |\boldsymbol{c}_i|\,|\boldsymbol{b}_i|}, \tag{3.13}$$

where in the numerator the projection of $\boldsymbol{f}_A$, the aerodynamic force in the aerodynamic frame A along the unit vector $\boldsymbol{e}_{A,z}$ for scalar lift is computed, and in the denominator, ρ is the fluid density, $|\boldsymbol{c}_i|$ is the chord, $|\boldsymbol{b}_i|$ is the spanwise distance to the adjacent node, and $\left|\boldsymbol{u}_{\mathrm{rel}_{E_i}}\right|$ denotes the relative flow velocity in Earth frame E, as a function of the both external

flow velocity and the coupled structural-rigid-body dynamics, at the corresponding beam node in material frame S at each section i, given further as,

$$\boldsymbol{u}_{\mathrm{rel}_{E_i}} = \overline{\boldsymbol{U}}_{\infty_{E,i}} - \mathbf{R}_{EB}(\chi^B)\left(\dot{\boldsymbol{r}}_{S_i} + \boldsymbol{v}_B + \tilde{\boldsymbol{\omega}}_B \boldsymbol{r}_{S_i}\right), \tag{3.14}$$

where for the ease of implementation the average external velocity $\overline{\boldsymbol{U}}_{\infty_{E,i}}$ across all UVLM lattice vertices at the section is taken, and hence justifying another approximation in the kinematics by leaving out the local rotation term $(\mathrm{skew}(\mathbf{T}\,\dot{\boldsymbol{\psi}}^S_B)\,\boldsymbol{c}_i)$, as found in Equation 2.26.

Potential flow theory for an infinite thin wing with camber gives $C_{l,i}$ as

$$C_{l,i} = 2\pi(\alpha_{\text{effective}} - \alpha_{0,\text{ camber}}), \tag{3.15}$$

where the zero-lift angle of attack $\alpha_{0,\text{ camber}}$ can be supplied or approximated to calculate the effective angle of attack $\alpha_{\text{effective}}$.

This is then used to look up the polar data, which provides corrections to the lift, drag, and moment, $\boldsymbol{f}_L = \boldsymbol{f}_A^\top \boldsymbol{e}_{A,z}$, $\boldsymbol{f}_D = \boldsymbol{f}_A^\top \boldsymbol{e}_{A,x}$, $\boldsymbol{m}$ through the coefficients, $C_{l,i}$, $C_{d,i}$, $C_{m,i}$, respectively as follows, with $\hat{\bullet}$ denoting corrected quantities.

$$\hat{\boldsymbol{f}}_L = 0.5\rho \left|\boldsymbol{u}_{\mathrm{rel}\ E_i}\right|^2 |\boldsymbol{c}_i|\,|\boldsymbol{b}_i|\,C_{l,\text{ polar}}\left(\alpha_{\text{effective}}\right) \tag{3.16}$$

$$\hat{\boldsymbol{f}}_D = \boldsymbol{f}_D + 0.5\rho \left|\boldsymbol{u}_{\mathrm{rel}_{E_i}}\right|^2 |\boldsymbol{c}_i|\,|\boldsymbol{b}_i|\,C_{d,\text{ polar}}\left(\alpha_{\text{effective}}\right) \tag{3.17}$$

$$\hat{\boldsymbol{m}} = \boldsymbol{m} + \boldsymbol{m}_{\text{polar}}\left(C_m\left(\alpha_{\text{effective}}\right)\right) + \left|\tilde{\boldsymbol{r}}_A \boldsymbol{f}_{D_{\text{polar}}}\right| \tag{3.18}$$

Note in Equation 3.17 the supplied drag polar is assumed to only consist of viscous contribution, whereas the lift-induced drag is included in the UVLM computed drag, and in Equation 3.18 the last term captures the contribution of the viscous drag to the moment by way of the beam axis offset described by the moment arm $\boldsymbol{r}_A$.

The corrected aerodynamic forces and moments are now fed back into the structural subsystem with the coupling shown in the next section.

3.2 Coupling of the aeroelastic solution

The aerodynamic and structural subsystems are strongly coupled using a block Gauss-Seidel algorithm - a common choice among multiphysics simulation frameworks since it preserves modularity and reusability of discipline-level subsolvers, as well as providing iterative convergence to capture strong nonlinear coupling effects.

In this framework the multibody constraints are enforced in the structural subsolver, consistent with the approach described in Chapter 2.4. The aero subsolver sees the combined action of rigid-body motions and flexible deformations as an aggregate displacement field, and returns a corresponding external forcing distribution. When solving the structural subsystem for the next time step, the Lagrange constraints modifies the internal forces, especially between the bodies, so that the final displacement field reflects both flexible deformation and rigid-body kinematics.

3.2.1 Structure to aerodynamic coupling

The goal here is to obtain the aerodynamic panel displacements and velocities $\boldsymbol{\zeta_b}$ and $\dot{\boldsymbol{\zeta}}_{\boldsymbol{b}}$ from the structural rigid body and flexible degrees of freedom $\boldsymbol{v}$, $\boldsymbol{\omega}$ and $\mathbf{r}$, $\boldsymbol{\psi}$. In the current implementation, no interpolation in the mapping[1] between the aerodynamic lattice grid vertices and structural nodes is required, as one beam node corresponds to one chordwise row of bound aerodynamic panel edges, which makes the approach conservative. This is a deliberate design choice: also conveniently at each time step, a new aerodynamic lattice is generated by placing pre-twisted and pre-swept chordwise lattice coordinates in the material frame, then transforming to the Earth, inertial frame.

$$\begin{aligned}\boldsymbol{\zeta}_b(t) &= \boldsymbol{x}_E(t) + \mathbf{R}_{EB}\left(\boldsymbol{r}_B + \mathbf{R}_{BS}\boldsymbol{X}_S\right)\\ \dot{\boldsymbol{\zeta}}_b(t) &= \mathbf{R}_{EB}\dot{\boldsymbol{\zeta}}_B = \mathbf{R}_{EB}\left(\boldsymbol{v}_B + \tilde{\boldsymbol{\omega}}_B\boldsymbol{r}_B + \dot{\boldsymbol{r}}_B + \mathbf{R}_{BS}\cdot\mathrm{skew}(\boldsymbol{T}\dot{\boldsymbol{\Psi}} + \mathbf{R}_{SB}\boldsymbol{\omega}_B)\boldsymbol{X}_S\right)\end{aligned} \tag{3.19}$$

with $\boldsymbol{X}_S$ denoting the chordwise lattice vortex coordinates in the material frame. $\boldsymbol{X}_S$ is calculated by first placing the chordwise lattice in the y-direction of the material frame - then using the extrinsic rotation convention (rotation axis are inertial), we first perform twist of Θ about the fixed x axis to apply washout, then perform sweep of ϕ about the fixed

[1] Here we only consider a matching fluid-structure interface. For more general cases, the interface mapping must be handled carefully to enforce kinematic compatibility and to transfer tractions/loads in a conservative, ideally work/energy consistent, manner [207, 208]

z axis to align chordwise panel direction to freestream (taking into account direction of the material frame y axis), or prescribe panel direction for example to model the flared hinge line. The order is chosen such that the twist and sweep angle are as thus defined.

$$\mathbf{R}_{\text{twist}} = \begin{bmatrix} 1 & 0 & 0 \\ 0 & \cos\Theta & -\sin\Theta \\ 0 & \sin\Theta & \cos\Theta \end{bmatrix}, \quad \mathbf{R}_{\text{sweep}} = \begin{bmatrix} \cos\phi & -\sin\phi & 0 \\ \sin\phi & \cos\phi & 0 \\ 0 & 0 & 1 \end{bmatrix} \tag{3.20}$$

$$\boldsymbol{X}_S = c\mathbf{R}_{\text{sweep}}\mathbf{R}_{\text{twist}} \begin{bmatrix} 0 & \cdots & 0 \\ -1+\iota_{\text{ea}} & \cdots & \iota_{\text{ea}} \\ 0 & \cdots & 0 \end{bmatrix} \tag{3.21}$$

where c is the chord length at that particular spanwise location, and ι_{ea} is the location of the elastic axis of the beam as % of chord, and the matrix has as many columns as the bound chordwise discretisation $\mathrm{M_b}$.

3.2.2 Aerodynamic to structure coupling

The goal here is to obtain the force acting on each of the structural nodes, from the steady plus unsteady aerodynamic forcing $\boldsymbol{f}$ acting on the aerodynamic lattice locations. $\boldsymbol{f}_{\text{steady}}$ are linearly interpolated from the vortex segment centres, $\boldsymbol{f}_{\text{unsteady}}$ are linearly interpolated from the collocation point, to each of the lattice panel corners. In the current implementation as the fluid-structural interface is conforming with clear dependencies as laid out in the previous section, total force and moment acting on a spanwise structural node i is the sum of the contributions from each chordwise lattice corner j, given as

$$\boldsymbol{f}_{S_i} = \mathbf{R}_{SE_i} \sum_{j=1}^{N_j} \boldsymbol{f}_{i,j}, \tag{3.22}$$

$$\boldsymbol{m}_{S_i} = \boldsymbol{R}_{SE_i} \sum_{j=1}^{N_j} \widetilde{\boldsymbol{r}}(\boldsymbol{\zeta}_b)\boldsymbol{f}_{i,j} \tag{3.23}$$

where $\boldsymbol{r}(\boldsymbol{\zeta}_b)$ is a function of the bound panel locations describing the moment arm, along the cornerwise direction, of the aerodynamic force from the lattice location to the beam node location.

3.3 Validation: A multibody aeroelastic wing assembly

In this section, aeroelastic simulations are carried out for a flexible flared hinged wing configuration. [198] The geometry is derived from a high–aspect ratio wing with a total span of 16 m. The wing root is clamped at the origin, while the flared hinge line separates the wing into inner and outer wing. The structural and aerodynamic properties of the wing are summarised in Table 3.1, with the simulation setup and discretisation parameters listed in Table 3.2.

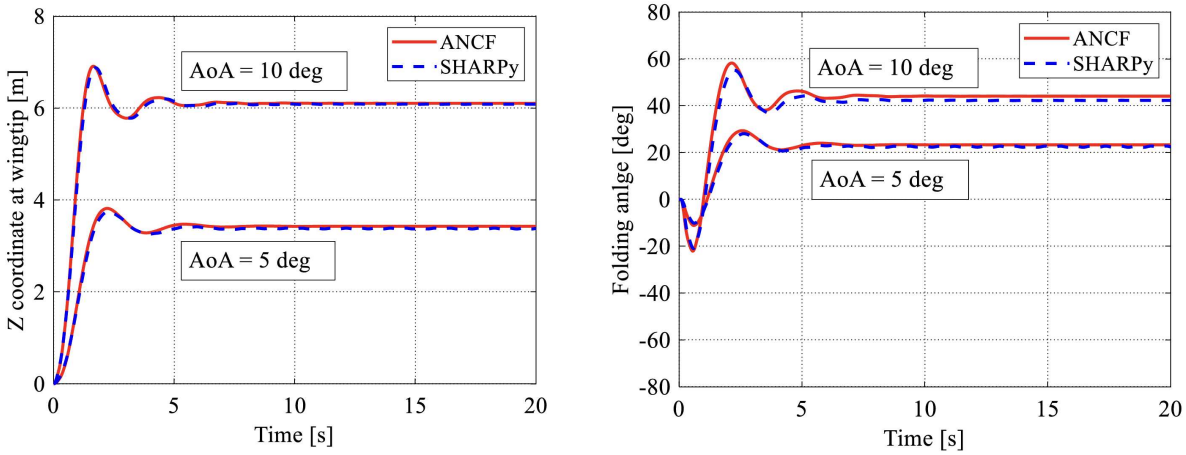
The transient problem involves both aerodynamic and gravitational excitations, which are both activated on an undeformed wing at $t = 0$. Figure 3.2 presents the resulting time histories of the wing tip vertical displacement and the fold angle for angles of attack of 5° and 10°. A comparison between the ANCF-UVLM coupled framework used and SHARPy (using a geometrically-exact beam formulation) shows good agreement with vertical displacements reaching over one-third of the semispan, and wing tip hinge fold angle exceeding 60° in the 10° case, confirming that the present multibody aeroelastic formulation successfully captures the coupled dynamics of a highly flexible flared hinged wing.

Table 3.1: Parameters of flared hinge wing

Parameter	**Symbol**	**Value**	**Unit**
Total length (semispan)	L	16	m
Inner wing length	L_1	12	m
Outer wing length	L_2	4	m
Chord length	C	1	m
Linear density	ρA	0.75	kg/m
Rotational inertia about x axis	ρI_{xx}	0.10	kg·m
Rotational inertia about y axis	ρI_{yy}	0.01	kg·m
Rotational inertia about z axis	ρI_{zz}	0.09	kg·m
Extensional stiffness	EA	1×10^7	N
Torsional stiffness	GJ	1×10^4	N·m^2
Bending stiffness about y axis	EI_{yy}	2×10^4	N·m^2
Bending stiffness about z axis	EI_{zz}	5×10^6	N·m^2
Shear stiffness	GA	5×10^6	N·m^2

Table 3.2: Common simulation parameters

Parameter	Symbol	Value	Unit
Simulation time	t_{end}	20	s
Time step	Δt	0.01	s
Gravity constant	g	9.8	m/s^2
Air density	ρ_a	0.0889	kg/m^3
Airflow speed	U	25	m/s
Angle of attack	AoA	5 / 10	deg
Flare angle	β	10	deg
Time integration method	Implicit generalised-α method		
Number of finite element nodes	13 (inner wing), 5 (outer wing)		
Number of spanwise panels	24 (inner wing), 8 (outer wing)		
Number of chordwise panels	4 (inner and outer wing)		
Number of streamwise wake panels	40		



(a) Z coordinate at tip (b) Folding angle

Figure 3.2: Time histories of released wing transient response

3.4 Validation: Code-to-code-to-experiment comparison

This test case is a flexible full wing with flared hinged wing tips. It is set up with similar structural complexity as the flared double pendulum model in Section 2.6. Experimental and numerical results are those of [113], [116], and [112]. To capture the main viscous

aerodynamic effects we apply sectional corrections as detailed in [196, 195] based on the lift and drag polars for the NACA0015 airfoil at Re = 200000. Selected properties of the wing assembly as well as simulation inputs are presented in Table 3.3. Figure 3.3 shows the single tracked variable (symmetric across the global x axis) as the fold angle θ - with the three coloured regions with varied stiffness and crosses denoting lumped masses and inertias, as per the structural layout of the numerical model described in [113].

Table 3.3: Key Parameters for flexible slender prismatic wing with wing tip

Parameters	Values	Units
Air density	1.225	kg/m^3
Half-span	1.0	m
Wingtip span	0.345	m
Chord	0.15	m
Flare angle β	10	deg
Angle of attack	2.5, 5.0, 7.5, 10.0	deg
Freestream velocity	12 to 28 (in 2 increments)	m s^{-1}
Gravity	9.81	m s^{-2}

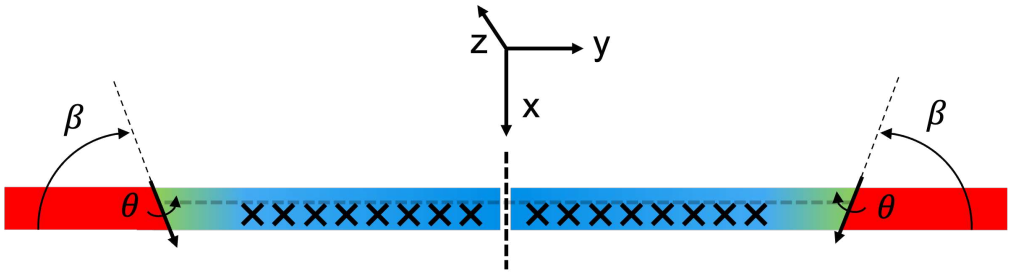


Figure 3.3: Wing assembly with flared hinged wing tips

Referring to Figure 3.4, the numerical model [113] is an iterative aeroelastic solution process partly leveraging NASTRAN routines to model follower aerodynamic loads on the deformed structure, solving for, and at the converged fold angle for each input condition. The secondary effects of inner-wing flexibility, and local changes in AoA and sideslip due to the flare angle are not considered. At certain angle of attack and velocity combinations in the time-domain SHARPy multibody aeroelastic simulations there exist stable dynamic equilibrium fold angles - those are denoted with triangles. Where a particular combination of input conditions give limit cycle oscillations, the mean fold angle is calculated as the average of the maximum and minimum fold angles seen in the time histories of the sustained LCO -

those are denoted with asterisks.

At lower angles of attack, SHARPy predicts the experimental data points similarly to the model in [113]. In this case, the nonlinearities present in the aeroelastic modelling are relatively small. At higher angles of attack we see a slightly better alignment with experimental results versus [113] towards higher velocities - where the large main wing deformations start to influence and interact with the wingtip dynamics, and its effect captured by the nonlinear coupled model in SHARPy natively. The experimental flutter boundary of this wing assembly as quoted in [113] is indicated in Figure 3.4, which is just beyond all available quoted experimental data points in circles. The SHARPy stability boundary can be estimated from time-domain simulation and compares well with the experiments. Sectional polar corrections applied to lift and pitching moment have been found necessary to obtain good agreement with experimental cases at higher angles of attack and velocity.

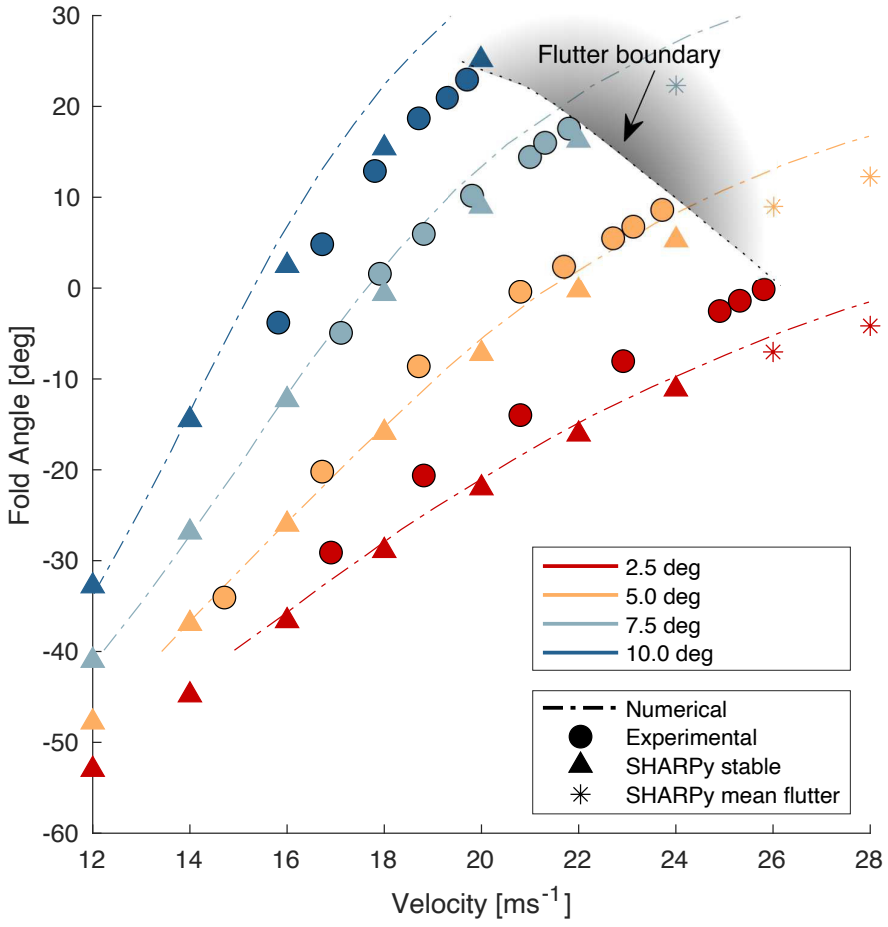


Figure 3.4: SHARPy equilibrium and mean LCO fold angle θ for various velocity and angle of attack combinations, overlaid on numerical and experimental data from [113]

At $\alpha = 2.5°$ and $u_\infty = 26.8ms^{-1}$ we compare LCO response of the wing assembly at the same flare angle of $\beta = 10°$, in Figure 3.5. An extra velocity point beyond the flutter boundary in Figure 3.4 was computed at $u_\infty = 26.8ms^{-1}$ on the $\alpha = 2.5°$ curve to give the SHARPy results. As for the reference, a different numerical aeroelastic model is used [116] coupling unsteady strip theory with an Euler-Bernoulli beam with a rigid wingtip attachment (the structural solver does not model the hinge flare angle, i.e. the wingtip is along a perpendicular hinge line against the spanwise direction). Broadly speaking the response predictions are good by both formulations - the slight differences in the prediction are thought to be due to the secondary effects by the flare angle on the geometric nonlinearities, and the differences in spanwise distribution of lift and stall from the aerodynamic nonlinearities. The initiation of the dynamic response into a fully developed LCO is different in each of the setup in Figure 3.5.

We have established the multibody aeroelastic formulation as implemented in SHARPy produces results that are largely in line with those reported in the literature for a representative flared hinged wing assembly.

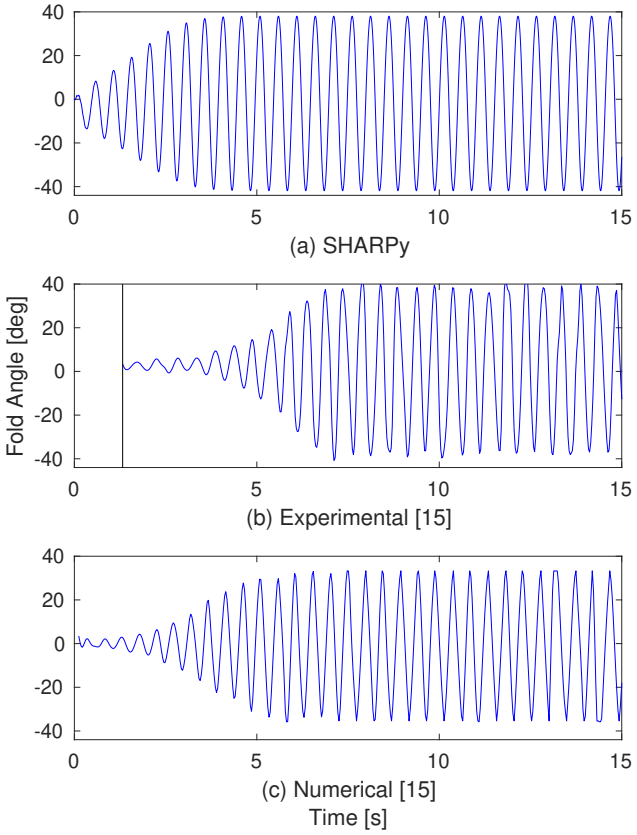


Figure 3.5: SHARPy LCO fold angle θ for $u_\infty = 26.8\,\mathrm{m\,s^{-1}}$ and $\alpha = 2.5°$, against numerical and experimental data from [116]

3.5 Trim strategies for free-flying configurations

In general, a flexible aircraft is trimmed by subsequent static computations of deformed geometry and load subjected to control inputs, which are given by a gradient-based method as a function of previous total forces and moments on the system. Loosely speaking, when dealing with the relatively simple case of longitudinal trim, we can associate input-output systems of primary importance by physical arguments - lift is mostly influenced by angle of attack, drag by thrust, and pitching moment by elevator deflection.

When considering a flexible aircraft with flared hinged wing tips, we augment the above static approach by adding another single input-single output system for hinge bending moment by fold angle, for when the hinge is locked. Zero hinge bending moment produced by a locked wing tip making a particular fold angle with respect with the inner wing in the quasi-steady sense means, that fold angle recorded is the equilibrium fold angle if the hinge lock is released. The uniqueness of the solution for fold angle in the domain (-π to π) is not guaranteed. The static method furthermore makes no distinction between the stability of the solutions given - whether a particular aircraft trim configuration is on a reachable path is unknown, and can only be determined by inspection or time-stepping of the nonlinear aeroelastic multibody system. Nonetheless, the availability of a static solution might be beneficial for narrowing down further efforts for more costly dynamic analysis.

For that we have laid out the algorithm as implemented below. Note that the coupled static aeroelastic solver runs, especially at cases with high flexibility and nonlinearity, will benefit from the gradual application of loads in substeps. We could very easily adapt this process to find out the equilibrium fold angle at prescribed conditions.

Note the total resultant forces and moments, here for longitudinal trim are total x-direction force F_x, summing from nodal contributions, total z-direction force F_z, total pitching moment M including contributions from sectional airfoil moments and the cross product of location vector and nodal force, and the hinge moment HM being, of course, the internal moment about the hinge axis.

Algorithm 1 Static Trim Loop

Initialise variables: α (angle of attack), δ (control surface deflection), T (thrust), θ (fold angle) with initial guesses
for $i = 1$ to max_iter **do**
  Initialise new undeformed single-body structure with current inputs (α, δ, T, θ)
  Run coupled static aeroelastic solver to get outputs: (F_z, M, F_x, HM)
  Compute gradient estimates for each input variable with finite differences
  Evaluate convergence:
  if $|F_z| < \epsilon_{F_z}$ **and** $|F_x| < \epsilon_{F_x}$ **and** $|M| < \epsilon_M$ **and** $|HM| < \epsilon_{HM}$ **then**
    Return trimmed solution (α, δ, T, θ)
  end if
  for each input variable (α, δ, T, θ) **do**
    if corresponding output is not converged **then**
      Update input variable using previous gradient and relaxation factor
    end if
  end for
end for
Raise exception: Maximum iterations reached without convergence

At times, particularly when initial guesses are far from the target equilibrium or near singular configurations where hinge aerodynamic stiffness provided by the flare angle becomes small, the static nonlinear equilibrium solver can become ill-conditioned and fail to converge reliably. An alternative method is required to obtain (otherwise unobtainable from the static approach) dynamic equilibria of the multibody system. By replacing the gradient based approach with independent single-input single-output (SISO) control systems loosely coupled by the nonlinear aeroelastic dynamics, we provide the multibody system with natural damping to promote convergence when time-stepping the solution, where the fold angle θ is now dynamic, akin to a free-flying wing tip subjected to the coupled multibody aeroelastics and flight dynamics, and taken out of the control loop. In the case of longitudinal trim, we have clamped the otherwise free-flying aircraft except the pitching degree of freedom (as it is the only necessary DoF), and set up three separate SISO PID controllers for lift-angle of attack, drag-thrust, pitching moment-elevator relationships for zero targets $r(t)$ for all measured forces and moments, regulated through the coupled aeroelastic system, as demonstrated in Figure 3.6.

The algorithm is described below. Note that each iteration is now tied to a certain number of time steps in the dynamic coupled aeroelastic multibody solver. Regarding the

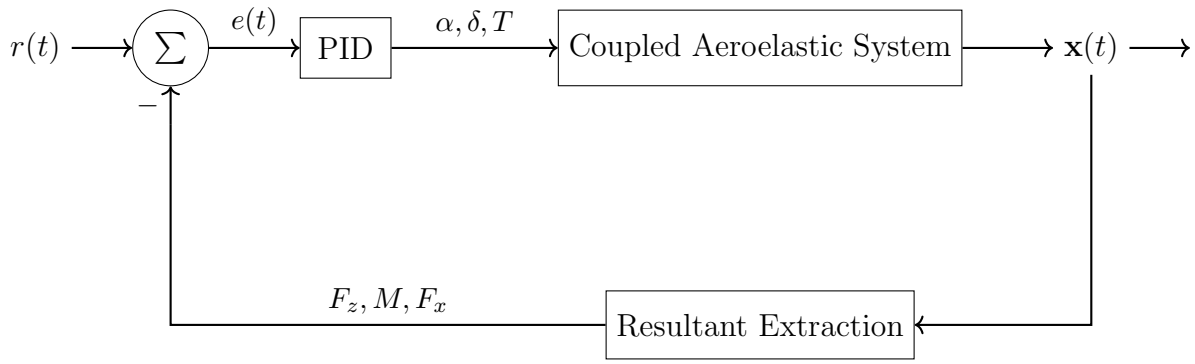


Figure 3.6: Closed-loop feedback control architecture for each time step in longitudinal dynamic trim

PID controllers, the proportional gains are chosen by physical argument - for example, in the alpha-Fz system, we choose the proportional gain to give alpha in the range of approximately $\pm 10^\circ$ by using the dynamic pressure, planform area, and a thin-plate lift curve slope of 2π as a back of the envelop estimate.

Algorithm 2 Dynamic Trim Loop

1: Initialise inputs: α (angle of attack), δ (control surface deflection), T (thrust) using guesses or previous trim values
2: **for** $i = 1$ to max_iter **do**
3: Let dynamic PID controllers choose current guesses of (α, δ, T)
4: Advance dynamic coupled aeroelastic multibody solver (Equation 2.18) for n time steps then retrieve outputs: F_z, M, F_x
5: Check convergence for each output:
6: **if** $|F_z| < \epsilon_{F_z}$ **and** $|M| < \epsilon_M$ **and** $|F_x| < \epsilon_{F_x}$ **then**
7: **Return** trimmed solution (α, δ, T)
8: **end if**
9: Feed PID controllers with input and output history
10: **end for**
11: Exception: maximum iterations reached

These two approaches are equivalent in the quasi-steady state and forms the toolbox at our disposal for the determination of trim state of flexible multibody assemblies such as those incorporating flared hinged wing tips. They are deployed individually or in combination in Sections 4.2 and 5.2.

Chapter 4

Nonlinear aeroelasticity of a HALE aircraft with flared hinged wingtips

With our verified formulation, we now shift our focus to the modelling and analysis of a representative High-Altitude Long-Endurance (HALE) T-tail-configured aircraft, which has previously served as a basis for investigating dynamic aeroelasticity in reduced-order modelling, nonlinear control, wake vortex encounters, and manoeuvres. [185, 209] This chapter sets up the comparison for hinge dynamics by investigating three configurations: the conventional HALE aircraft with fixed dihedral wing tips (HALE-d00 and HALE-d90), and the Hinged-HALE ($\mathrm{H^2}$ALE) with freely-flapping wing tips. We will investigate how parametrised versions of the aircraft respond to both sweeps in vertical and lateral gusts. Here, the 1-cos discrete gust profile is chosen, not just because it is the standard certification gust input [210], but also since it is easily parametrised by length and amplitude to excite the nonlinear coupled system across the range of rigid-body and flexible modes, and provides a set of reproducible aircraft responses that will aid future validation and development efforts.

We here define L_g and $\bar{L}_g$, in units meters and seconds respective, as the dimensional and normalised gust lengths; and U_g and $\bar{U}_g$, the former in meters per second, as the dimensional and normalised-with-freestream gust intensities. Wing root bending and torsional moment values, where quoted, are nondimensionalised by the product of aircraft weight and one-eighth span length.

4.1 Definition of the hinged (H^2ALE) and rigidly-connected (HALE) configurations

In the subsequent analyses we have not applied any sectional corrections to the forces and moments obtained from the UVLM solution. For the low cruise speed of the HALE considered here, at near-stall effective angles of attack induced by high gust intensities this mainly leads to an over-prediction of sectional loads and, consequently, structural displacements, which can be regarded as conservative in a static sense. However, in flapping and other strongly unsteady aeroelastic regimes, increased lift is typically associated with increased aerodynamic damping, so over-predicting lift might not necessarily yield conservative predictions of system dynamics. The aeroelastic stability and dynamic response presented in this chapter should therefore be interpreted with this limitation in mind, which is justified as the role of geometric nonlinearities in the coupled structural and flight dynamics is explored starting from the baseline and reaching stretch cases in parametric sweeps.

The HALE aircraft, as shown in Figure 4.1, is configured with a constant-chord, unswept wing of aspect ratio of 32 and a T-tail, powered by a constant thrust force in the material frame forward direction at $\pm 1m$ spanwise from the wing/fuselage intersection, and trimmed for longitudinal flight by means of an elevator deflection input. The flexible wing weighs 24 kg; the rest of the structure weighs 54.25 kg, 50 kg of which is a lumped mass at the wing-fuselage intersection. The numerical model is made parametric with respect to the dihedral angle of the wing tips, with versions denoted as HALE-dXX where XX is the dihedral angle in degrees. More details on the architecture of the model can be found in [211].

Based on the HALE aircraft model we have also built the Hinged-HALE, or H^2ALE, by replacing the dihedral seen at the outboard sections of the wings with a pair of flared hinged wing tips, where they are flush with the inner wing at 0 fold angle. The wing tips are allowed to flap freely and constitute one-fourth of the total span, which should be more than sufficient for the wing-wingtip interactions to be evident. [69] The numerical model is made parametric with respect to the flare angle, with versions denoted as H^2ALE-fXX where XX is the flare angle β in degrees. Figure 4.2 shows the H^2ALE aircraft in steady level flight, where as the flare angle increases, the equilibrium fold angle decreases, while bending/twisting of the main wing increases, where Figure 4.3 shows the H^2ALE-f10 in free flight, 2 seconds post a very large gust encounter from trim. The results are very likely non-physical, as in a huge gust onset the UVLM fails to capture separation, stall, and damping from viscous forces, all contributing to reduction of the peak loads experienced. This is thought to be beneficial in

this case to demonstrate the robustness of the solvers and hence framework at extreme load conditions.

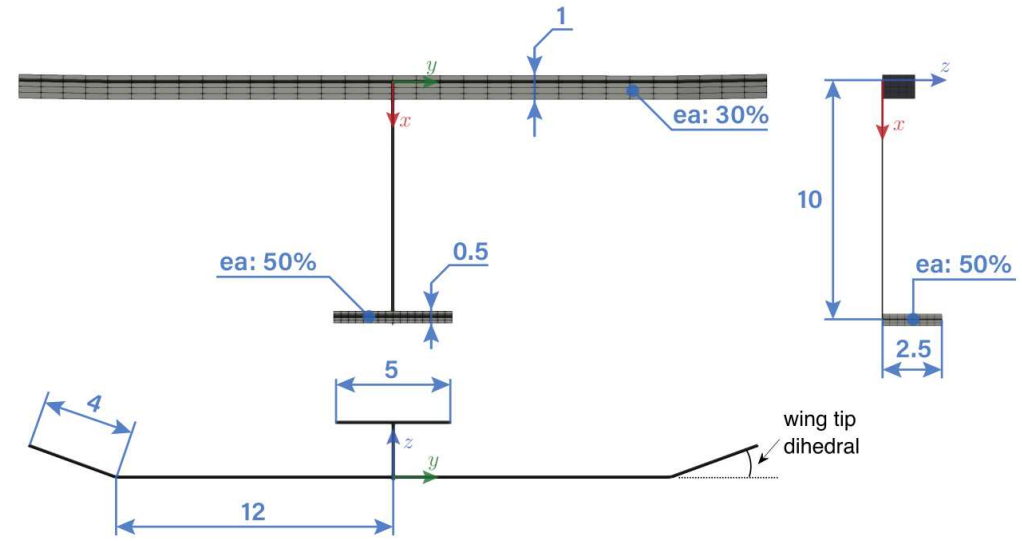


Figure 4.1: Geometric definition of the T-tail HALE model with all units in meters as in [211]



Figure 4.2: H²ALE aircraft, with flared hinged wing tips coloured in increasing flare, at trim. Note where flare angle increases, trim fold angle decreases.

We have first selected the HALE-d00 and the HALE-d90, to compare with the H²ALE-f10 - it is thought that the former configurations would be good proxies of the latter with the flared hinged wing tips locked. A small flare angle of 10 degrees is shown to be enough practically for ensuring the dynamic stability of the hinged wing tips, while having a larger flare angle would extend the stability boundary with respect to sideslip angle [109], but lead to lower damping in the hinge flapping mode. Fundamentally, the H²ALE will have the locked, extended (HALE-d00) and upturned (HALE-d90) configurations as limit cases - its dynamics is shown in subsequent sections to mostly fall in between that of the two references.

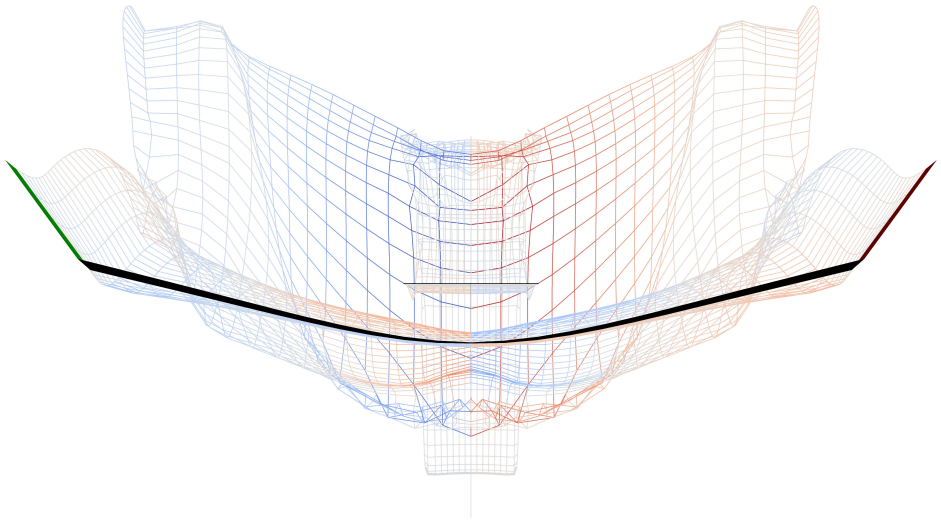


Figure 4.3: Snapshot of H^{2}ALE-f10 with force-free UVLM wake grid coloured by circulation intensity, response to 1-cos gust with $\bar{L}_g = 1.5$ s and $\bar{U}_g = 1.6$, 2 seconds post gust encounter

4.2 Aeroelastic trim and equilibrium state

We first trim all three aircraft at a flow velocity of $10\,\mathrm{m\,s^{-1}}$. respectively, using the algorithm described in Section 3.5. Figure 4.4 shows the time histories of the control inputs and the relevant states. Note that more steps are required to trim the H^{2}ALE-f10.

The longitudinal trim values are given in Table 4.1. We have nondimensionalised the pitching moment and lift by weight multiplied by chord, and weight, respectively. Do note the residual induced drag here, as percentage of thrust, is secondary to the elevator and angle of attack inputs - the thrust only ensures the aircraft is in equilibrium longitudinally. Both the HALE-d90 and H^{2}ALE-f10 requires a slightly higher angle of attack for longitudinal trim - that is thought to be a result of the partial loss in lift outboard of the hinge, resulting in a higher angle of incidence at the main wing to generate the same overall lift. Elevator and thrust input is likewise higher in magnitude to counteract the extra pitching moment and induced drag due to the higher angle of attack. The tiny residuals in the pitching moment and lift in H^{2}ALE-f10 are due to the less aggressive action of the PI controllers, and at less than 1%, the impact on the time histories of the aircraft are not evident in the short gust timescales we are subjecting the aircraft to.

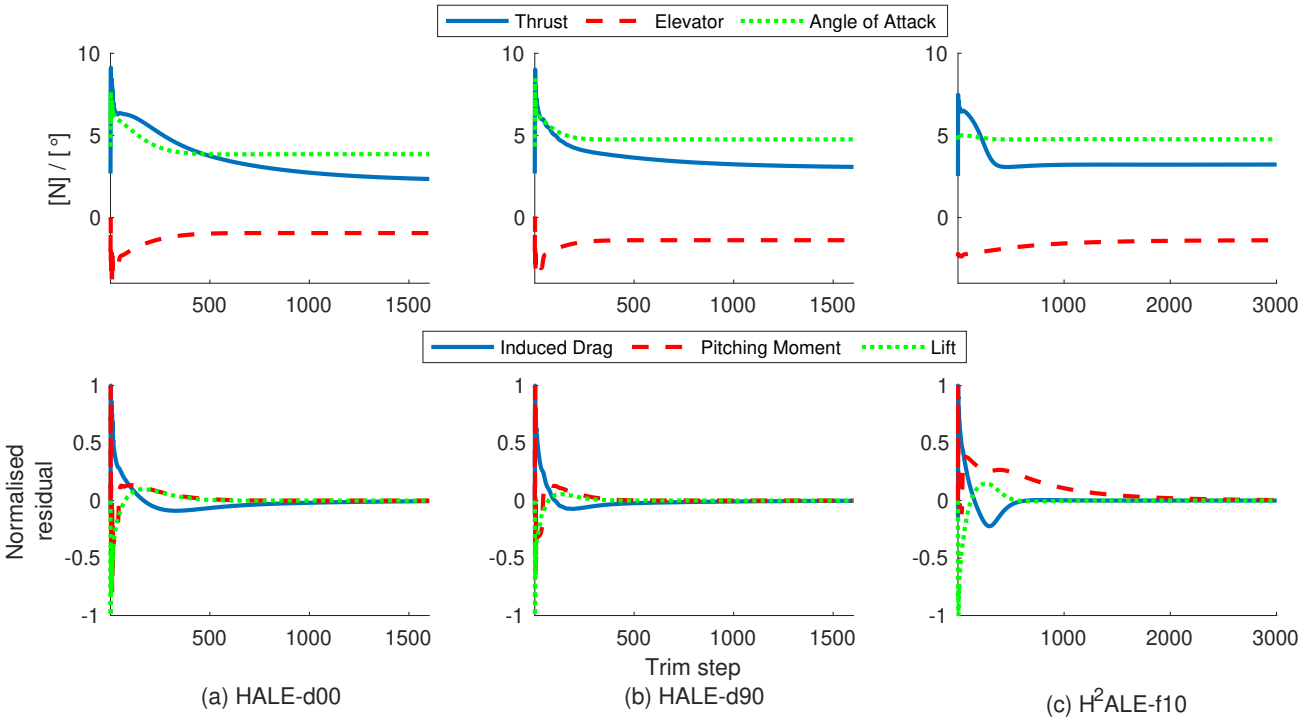


Figure 4.4: Trim histories of control input versus corresponding states

Table 4.1: Comparison of trimmed values for HALE and H^{2}ALE

Values at trim	HALE-d00	HALE-d90	H^{2}ALE-f10
Thrust [N]	2.35	3.08	3.23
Residual Induced Drag [%]	13.1	4.10	0.27
Elevator [deg]	-0.95	-1.38	-1.39
Residual Pitching Moment [%]	0.00	0.00	0.14
Angle of attack [deg]	3.86	4.76	4.76
Residual Lift [%]	0.00	0.00	0.03

4.3 Vertical gust response

To understand more about the coupled flight dynamics and aeroelastics, we have performed a gust length sensitivity analysis by subjecting each of the three aircraft, from their respective trim state defined in Section 3.5, to 1-cos gusts across an order of magnitude in length centred around the vehicle length (10 m), and constant intensity of $\bar{U}_g = 0.5$. This gust will then excite a combination of aeroelastics and flight dynamics at different length and time scales, allowing for a comparison of the responses. The tracked variable, wing root

bending moment (WRBM), is chosen because it is thought to be the most critical in a vertical gust encounter. It is nondimensionalised using the product of the aircraft weight and one-eighth span length (4 m). A sequential search - first over gust length and then over intensity - can miss the worst-case WBRM; that limitation is acceptable here because the objective is to isolate the influence of gust length alone on the maximum response of coupled flight dynamics and aeroelastics under a fixed intensity; once that is identified, intensity can then be swept at that fixed length to assess whether additional nonlinear effects are triggered.

As shown in Figure 4.5, the H^{2}ALE-f10 has a trim wing root bending moment (WRBM) between the two HALE configurations as predicted, with value much closer to that of HALE-d90 - that implies with the free flared hinge we can almost recover the best case scenario of vertical winglets in terms of alleviating the bending loads at the root. In terms of the sensitivities, the HALE configurations show a early peak in response, both at the 7.5 m ($\bar{L}_g = 0.75$ s) mark, where the H^{2}ALE-f10 peaks at 15 m ($\bar{L}_g = 1.5$ s), suggesting different mechanisms in play especially after the first WRBM peak in response to the gust. We have chosen to compare the gust intensity sweep, from 0 to $\bar{U}_g = 1.6$, of the three configurations at each of the identified gust lengths. We have intentionally chosen high values for the gust intensity, both to examine the dynamics of the very flexible aircraft configurations at extreme geometric nonlinearities, and to demonstrate robustness of the numerical implementation. Note that no stall model is included.

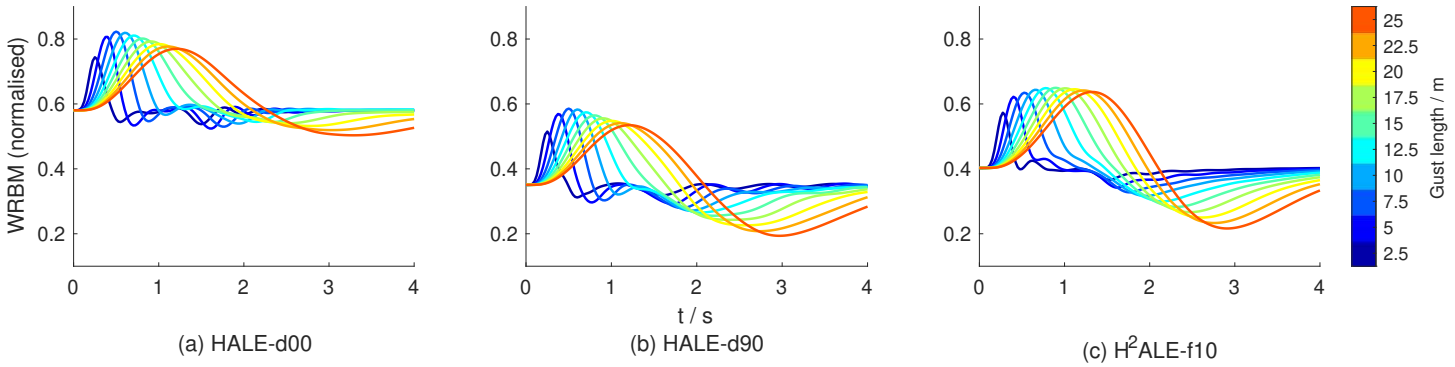


Figure 4.5: Time histories of wing root bending moment, normalised by the product of aircraft weight and one-eighth span length, at various gust lengths, $\bar{U}_g = 0.5$

4.3.1 Results for different gust lengths

For subsequent analysis we focus on each of the two critical gust length identified, starting with $\bar{L}_g = 0.75$ s, then $\bar{L}_g = 1.5$ s. We will examine the time histories of WRBM, WRTM, relative vertical displacement as a proxy for wing out of plane bending, aircraft pitch angle,

and hinge fold angle, to gain a better understanding of the coupled flight dynamics and aeroelasticity of the HALE vs H^{2}ALE aircraft in the time domain.

$\bar{L}_g = 0.75$ s

As this is the most sensitive gust length for the HALE configurations, it is perhaps unsurprising that comparing across most gust intensities, both the HALE-d00 and HALE-d90 experience higher maximum transient WRBM than the H^{2}ALE-f10 at the highest gust intensity of $\bar{U}_g = 1.6$, as evidenced in Figure 4.6, where in the first row the time histories from trim of the normalised WRBM are shown, and in the second row, the increments in WRBM from the trim case, normalised by the gust intensity, are plotted, with the trends near the first peak included in the inset. Apart from a lower first peak at higher intensities than the HALE-d90, the transient oscillations are more damped than the HALE-d00 with the H^{2}ALE, suggesting the hinge is helpful in this particular setup and conditions to alleviate both the peak and subsequently oscillating gust loads. An example of configuration and conditions where the oscillations are less damped after the peak load is reduced can be seen in [69]. It is worth noting that the WRBM increments as plotted do not exactly coincide as the gust intensity increases - this is because of the geometric nonlinearities captured in the formulation. A close inspection of the first peak would reveal that as we increase the gust intensities, the very presence of the hinges brings about less increment in WRBM per gust intensity unit - suggesting perhaps the additional wingtip flapping motion is extracting more aerodynamic damping to reduce transient loads.

Examining the wing root torsional and bending moment plotted against each other in Figure 4.7 reveals a few trends - first of all, that the H^{2}ALE-f10 shares similar correlation of bending to torsional loads with the HALE-d00, and that they are much less coupled than in HALE-d90, where the fixed vertical wing tips act as unbalanced masses promoting bending-twisting coupling. In terms of the magnitude of loads experienced, the H^{2}ALE sees loads comparable to the HALE-d90 and significantly smaller than HALE-d00.

In determining the overall load envelope of a particular aircraft configuration Figure 4.7 demonstrates why it is important to consider the nonlinear dynamics - for the H^{2}ALE-f10, and to a lesser extent the HALE-d90, the largest gust intensity case does not define the entire load envelope.

In addition to the zero moment transfer, a second mechanism of wing root bending moment relief is seen for the H^{2}ALE. At gust onset the inner wing tends to fly up and flex

up, and through the hinge by inertia and aerodynamic damping the wing tips tend to fold negatively (seen in Figure 4.8) - that leads to higher effective angle of attack on the wing tips due to the downwards flapping motion, and higher geometric angle of attack on the wing tips due to flare. All this combined gives upwards (restoring) lift on the wing tips, and hence a downwards (dampening) force is exerted through the hinge on the inner wing, reducing the flex up tendency, itself a self-regulating cycle which in time dampens any transient flexible and hinge motion, as evidenced by Figure 4.9. Note also the WRBM and z-location of the dihedral / hinge point, respectively in Figures 4.6 and 4.9, are almost always in phase, suggesting one is a good proxy for the other, in this largely inertia-driven wingtip assembly.

With this mechanism the momentum of the rigid body motion is converted to the flapping of the wing tips, which is readily dissipated by the aerodynamic forcing - we see marginally higher net vertical position of the hinge, relative to the root (which scales with structural deformation) in exchange for massively reduced rigid body vertical displacement, and improvement in WBRM. This scales well with increasing gust intensity, as aerodynamic damping is predominantly quadratic with respect to increasing velocity.

$\bar{L}_g = 1.5$ s

This is the most sensitive gust length for the H^{2}ALE-f10 - as evidenced by Figure 4.10, where the transient WRBM increment due to the longitudinal gust is consistently higher than the HALE configurations. There is a silver lining to this, since the hinge mechanism results in progressively less WRBM when increasing gust intensity, i.e. nonlinear load relief - something which is not seen in the gust length = 7.5 m case. Torsional and bending moments in Figure 4.11 shows the same trends.

When we examine the flexible vertical deflection in Figure 4.13 we recognise the same higher initial peak. Subsequently, and more visibly than with the previous gust length, in terms of the flexible deformation the H^{2}ALE-f10 enjoys the best of both worlds - quicker to settle to equilibrium shape than the HALE-d00, and much more damped oscillations than the HALE-d90, likely due to the dissipative flapping identified earlier. Regarding the fold angle time histories in Figure 4.12, as the gust intensity increases the higher frequency flapping modes become less damped - becoming a potential source of LCO in the wing assembly.

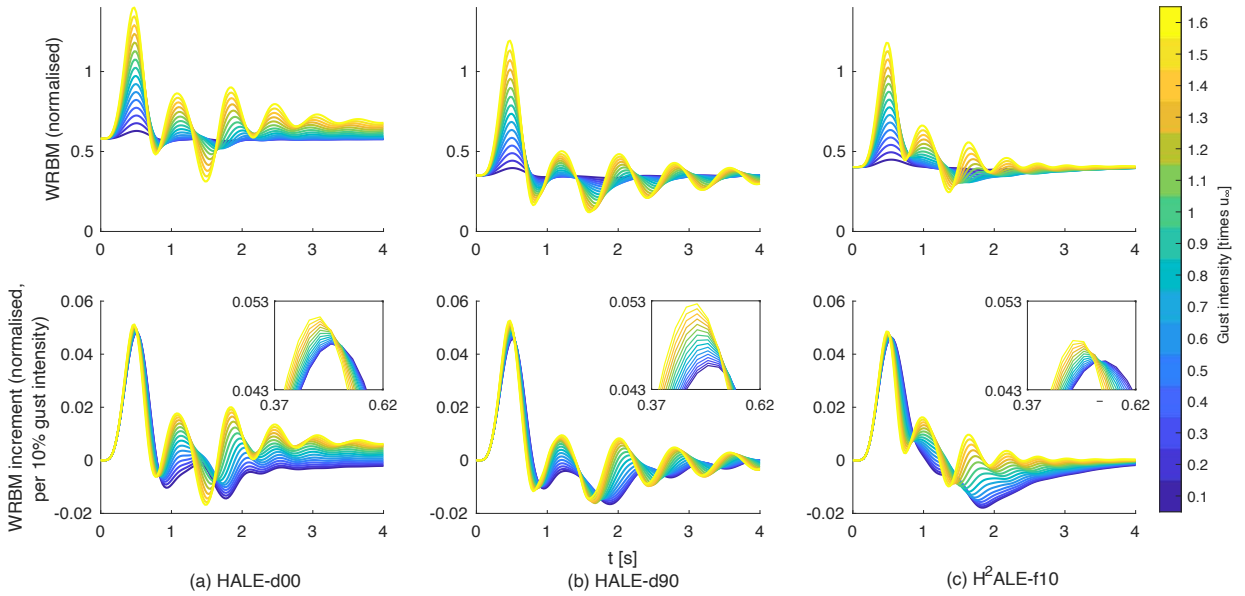


Figure 4.6: Time histories of normalised and incremental WRBM over a range of gust intensities, $\bar{L}_g = 0.75$ s. Moment increment plots include inset with values near the first peak.

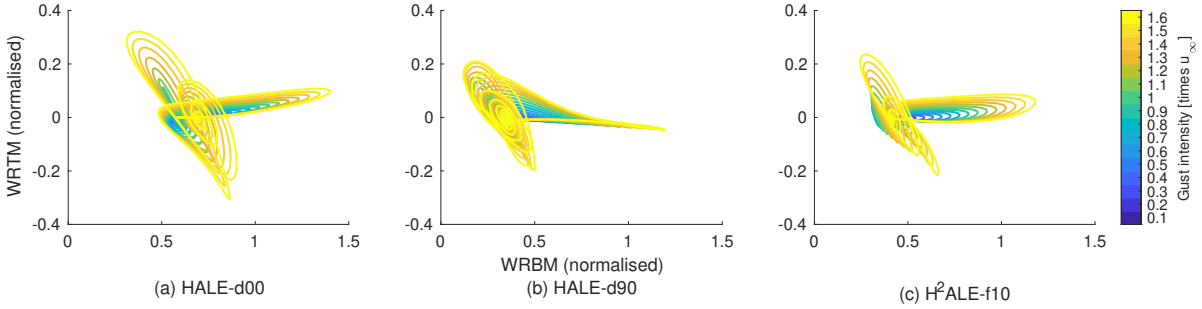


Figure 4.7: Instantaneous values of normalised wing root bending and torsional moment over a range of gust intensities, $\bar{L}_g = 0.75$ s

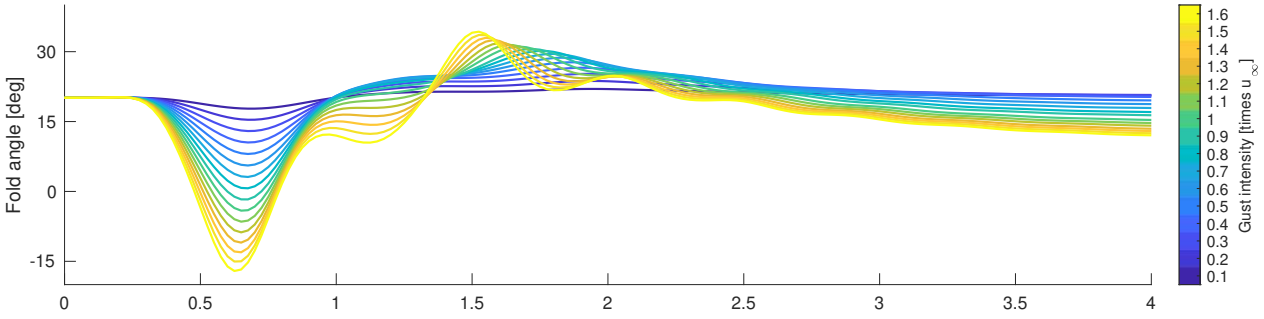


Figure 4.8: Time histories of hinge fold angle for the H^{2}ALE-f10, $\bar{L}_g = 0.75$ s

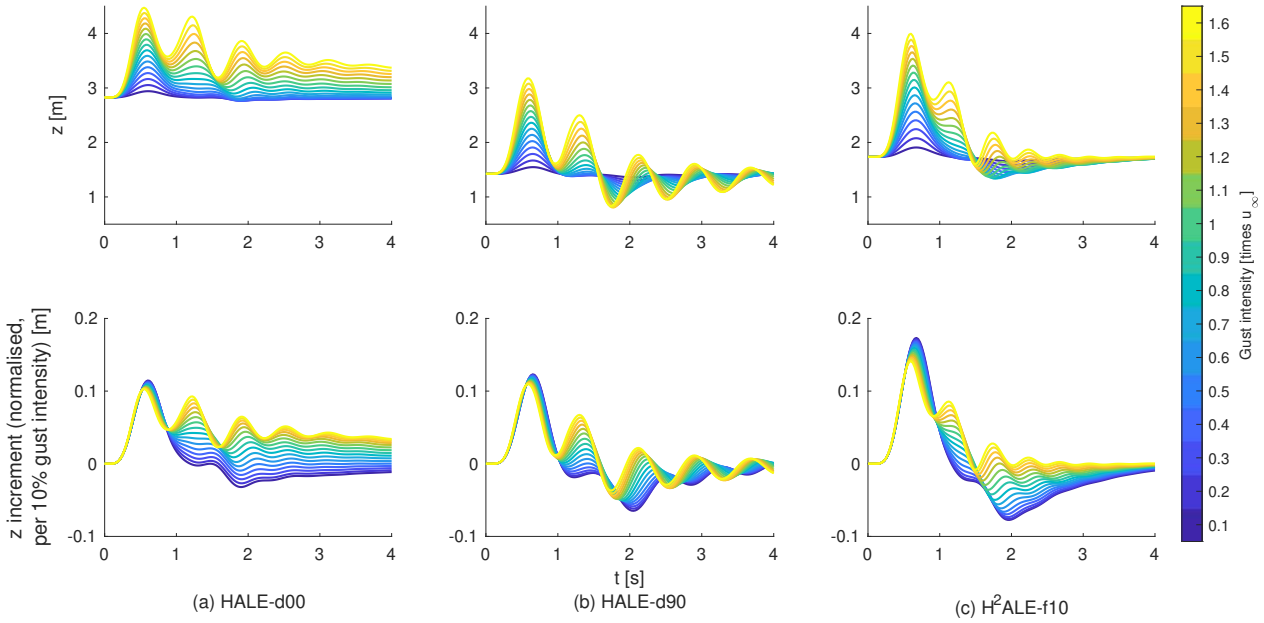


Figure 4.9: Time histories of wing dihedral/hinge vertical position relative to root over a range of gust intensities, $\bar{L}_g = 0.75$ s

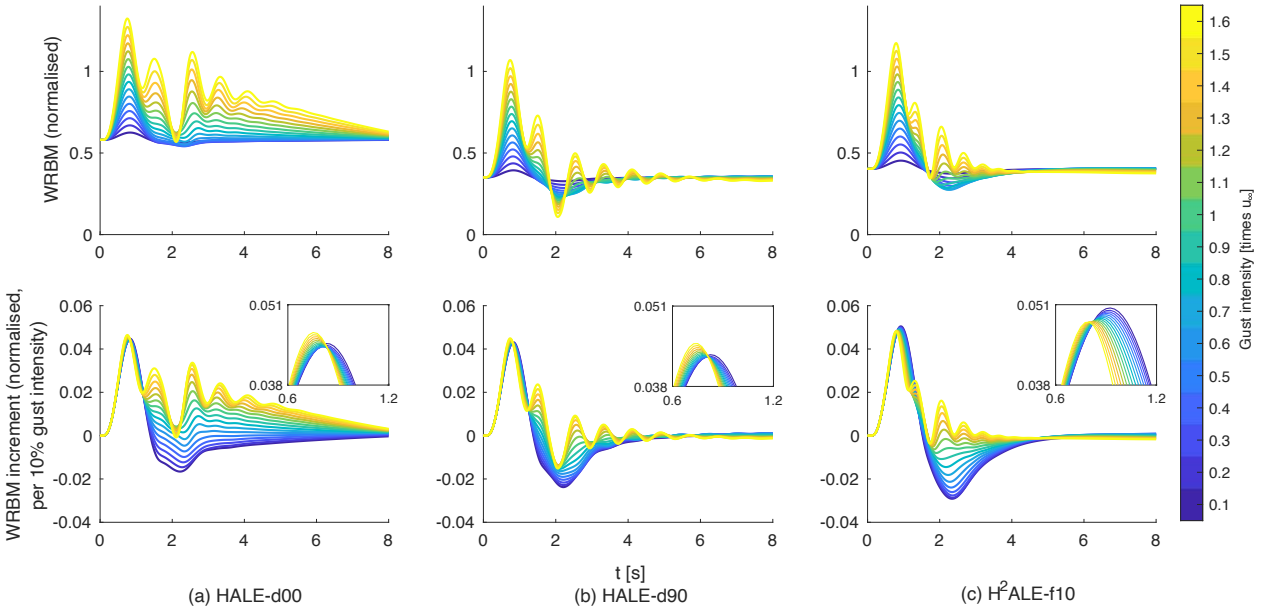


Figure 4.10: Time histories of normalised and incremental WRBM over a range of gust intensities, $\bar{L}_g = 1.5$ s. Moment increment plots include inset with values near the first peak.

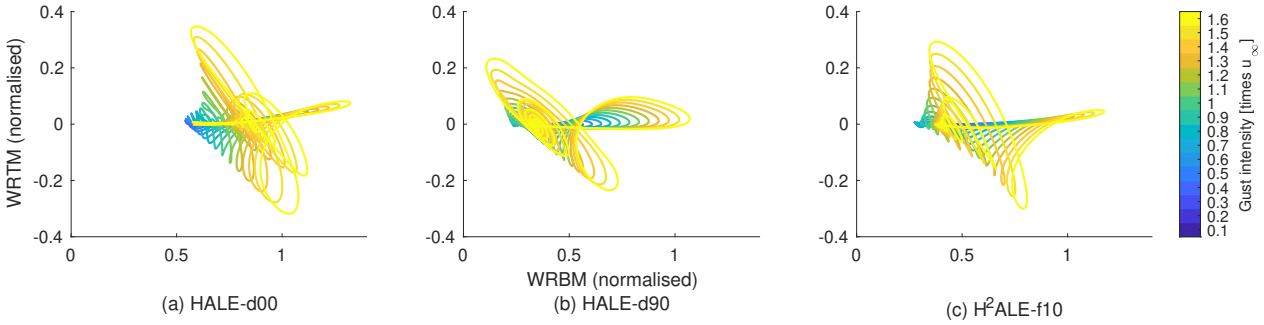


Figure 4.11: Instantaneous values of normalised wing root bending and torsional moment over a range of gust intensities, $\bar{L}_g = 1.5$ s

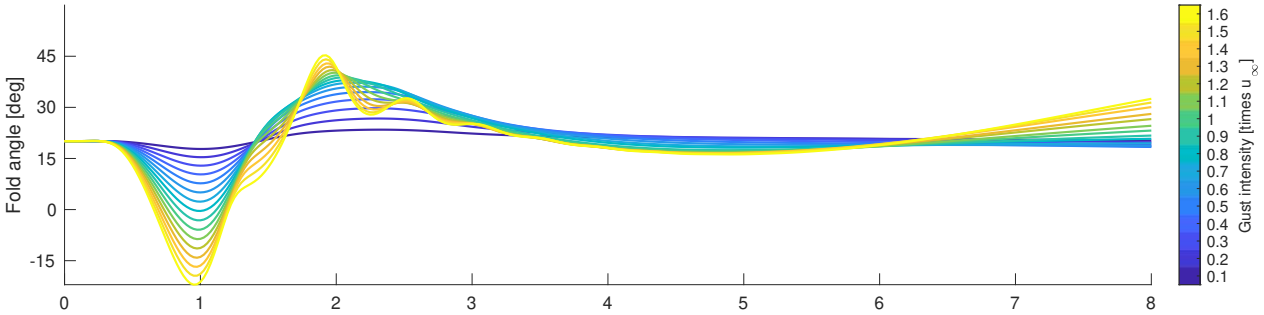


Figure 4.12: Time histories of hinge fold angle for the H^{2}ALE-f10, $\bar{L}_g = 1.5$ s

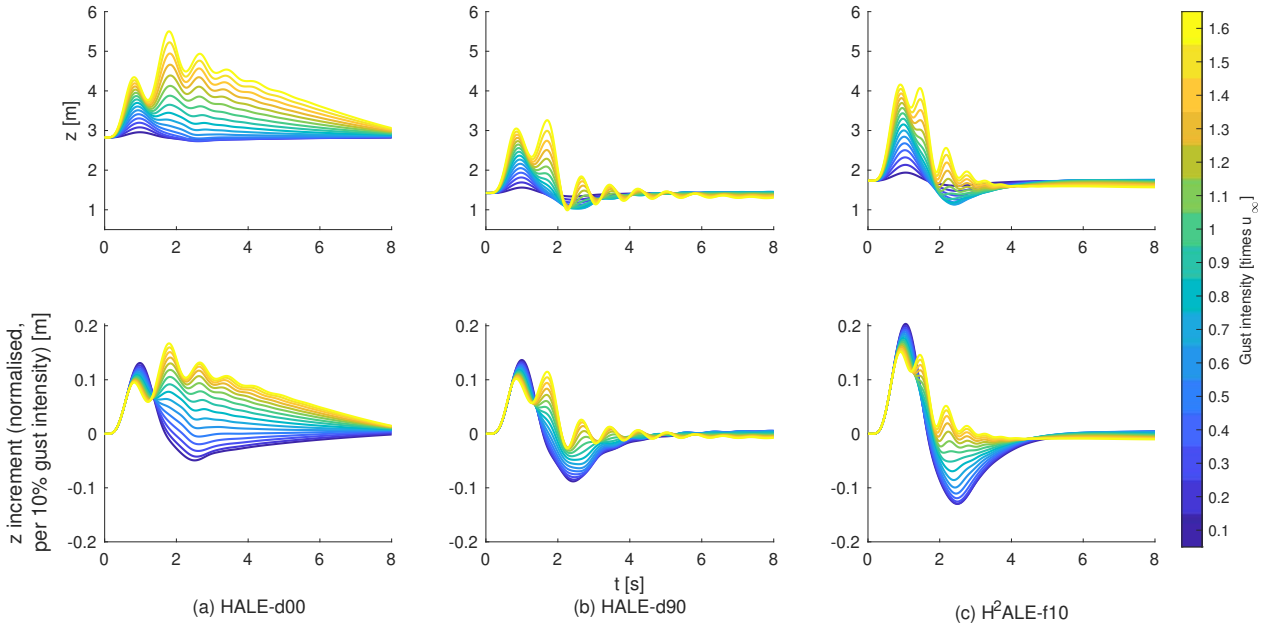


Figure 4.13: Time histories of wing dihedral/hinge vertical position relative to root over a range of gust intensities, $\bar{L}_g = 1.5$ s

4.3.2 Effect of flare

Returning to the physics of the hinges that no moment parallel to the axis are transferred, it is then evident that non-zero flare angles at the hinge would slightly increase trim WRBM, as shown in Figure 4.14. This penalty is secondary to the presence of the hinge itself. However, maximum penalty occurs at around $\beta = 10°$, then slightly decreases at higher flare angles for the trim WRBM - the effect can be attributed to the steady-state decreasing bending contribution of the lift by the rotated wingtip aerodynamic surface.

For the peak WRBM experienced during the gust encounter, there is a gradual hike from zero flare to again around around $\beta = 10°$, followed by a slight increase towards higher flare angles. The increasing trend is explained by the transient transfer of moment not parallel to the axis - the bending contribution of that increases with the increasingly slanted hinge axis.

Both of the progressively tapering trends towards higher flare angles can be explained by cross-referencing the fold angle and z flex displacements in Figure 4.15 in time. They coalesce towards higher flare angles, indicating a similar equilibrium shape leading to a largely similar loading.

It is worth noting that at $\beta = 0$, where the hinge axis is exactly perpendicular to the spanwise direction, we do not experience the theorised loss of stability in the wing tip from a linear analysis [70] - that is due to the bending/twisting coupling of the very flexible wing changing the effective flare angle seen by the flow. It is also remarkable that the amplitude of the hinge motion is largely constant with flare angle, suggesting a weak relationship with the induced geometric angle of attack due to flare in a vertical gust encounter.

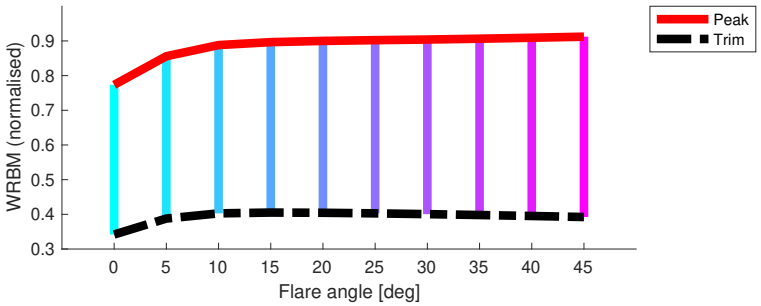


Figure 4.14: Range of trim-peak WRBM for H^{2}ALE with varying flare angle, $\bar{L}_g = 1.5$ s, $\bar{U}_g = 1.0$

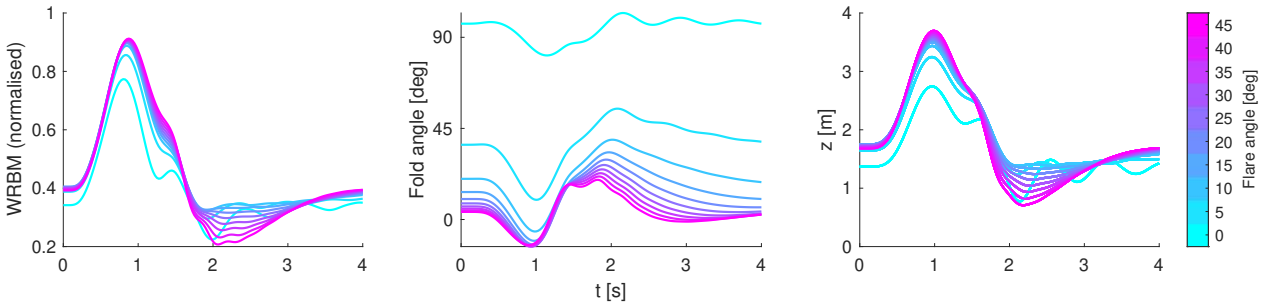


Figure 4.15: Time histories of key quantities for H^{2}ALE with varying flare angle, $\bar{L}_g = 1.5$ s, $\bar{U}_g = 1.0$

4.3.3 Effect of negative flare

Since for this particular straight wing configuration we have seen that a zero-flare configuration can still produce stable trim shapes, we turn our attention to negative flare angles, i.e. a hinge axis towards the wing tips downstream, to complete the discussion. Wing tips with the hinge axis pointed in the aforementioned direction is previously thought to be inherently dynamically unstable, at least from a static analysis point of view. [70]

Figure 4.16 shows at $\beta = -35°$ there exists a stable dynamic equilibrium with fold angle close to $-180°$, meaning the wing tips are folded inwards. Conceptually a dynamically stable equilibrium is possible at a negative flare angle with inward-folding wing tips since higher lift on the wing tips mean it folds in even more, where then the flare angle means the geometrical angle of attack is reduced, providing a restoring force. The trim values for WRBM and vertical flexing largely follows the same trend - that they are both larger than the zero flare value. They are however bigger in magnitude than the positive-flare variants, suggesting an inward-folding wing tip configuration is much less efficient.

Examining the gust encounter time history of the fold angle at $\beta = -35°$ reveals a limitation of the model - that the wing tips have actually exceeded the negative 180° physical limit - which in real life would mean the wing tips are in collision with the main wing. This is the only case within this work where this happens - all other cases shown features dynamics that respects this limit.

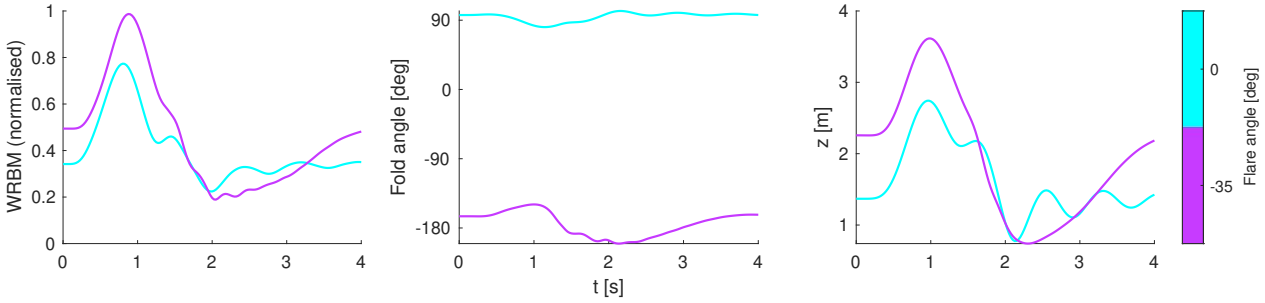


Figure 4.16: Time histories of key quantities for H^{2}ALE with $\beta = 0, -35°$, $\bar{L}_g = 1.5$ s, $\bar{U}_g = 1.0$

4.3.4 Effect of vehicle properties

Effect of mass distribution

The wing tips in the H^{2}ALE configurations are 25% of total span - given also there's no taper in the wing, and it having constant material properties, it can be considered quite a heavy tip, resulting in what is thought to be more inertia-driven dynamics in the past Sections. To address that we have also set up an alternative model with half of the wingtip mass removed and added to the lumped mass at the root, to keep the total wing assembly mass constant.

The gust response in Figure 4.17 are largely similar in terms of the time histories - except there has been a constant offset at the trim value, and we no longer have a turning point in WRBM vs flare angle as in Figure 4.15. This explains the secondary WRBM mechanism discussed in Section 4.3.2, that increasing flare brings about an additional WRBM penalty, is predominantly an effect due to the mass distribution of the wing and wingtip assembly. In fact, it is perhaps surprising that with less mass at the wing tip more WRBM is seen - that would be down to the extent bending-torsion coupling is active in the aeroelastic case that changes the spanwise distribution of lift on the wing.

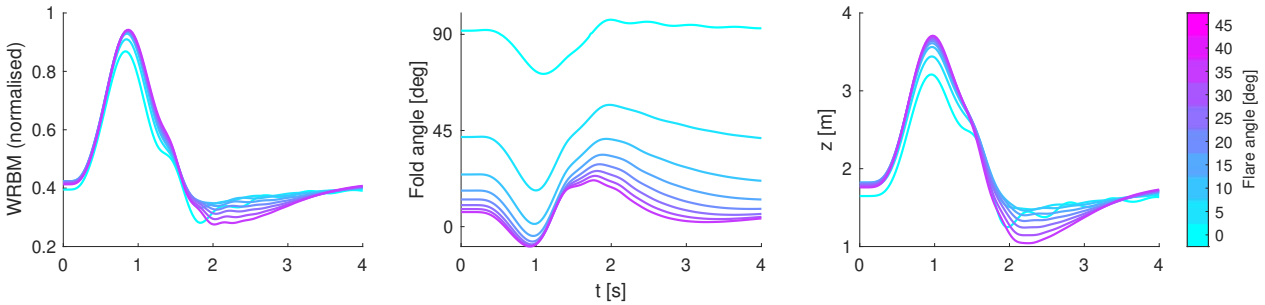


Figure 4.17: Time histories of key quantities for H^{2}ALE with varying flare angle (redistributed mass), $\bar{L}_g = 1.5$ s, $\bar{U}_g = 1.0$

Other results involving also the HALE remain closely aligned with the original mass configuration and hence will be included instead in the accompanying online repository.

Effect of stiffness

In an effort to attribute the load alleviation effects seen in Section 4.3, we have prepared yet another set of alternative HALE and H^{2}ALE models, this time with five times the original stiffness in all directions. With a much stiffer wing assembly we see a clean single cycle response to the 1-cos vertical gust in the WRBM and z-deflection, where subsequent transient fluctuations decay quickly. This can be best explained by the reduced deflections and rotations due to the higher stiffness; hence geometric nonlinearities and aeroelastic mode coupling that could otherwise sustain oscillations are more limited. It is also worth noting that the peak values across all configurations are much higher in Figure 4.18 than in Figure 4.10 - indicating that the flexible modes do take away energy from the rigid body response, resulting in a substantial load alleviation, which is evident also in Figure 4.21. It is also evident that in terms of the first peak, as gust intensities increase, the H^{2}ALE-f10 loses its comparative effectiveness in reducing transient WRBM (we also lose the nonlinear load relief identified earlier) - that the hinge itself, and flexibility in the main wing, are both necessary for any load alleviation mechanism identified. The fold angle time histories in Figure 4.20 compared to Figure 4.12 indicates the same; that the first negative peak of the fold angle is reduced compared to the flexible model, which is because the main wing flexes much less with the gust encounter and causes less of a inertial downswing of the wing tips.

From Figure 4.19 we can identify that the H^{2}ALE-f10 sees a larger range of WRBM, where the coupling with the torsional component bears resemblance to both the HALE-d00 and HALE-d90 - more so to the HALE-d00 at lower bending loads (where presumably the dynamics mimic a cantilever wing), and to the HALE-d90 otherwise (where the higher bending loads encourage the wing tip to flap - behaving more like a out of plane mass as in the HALE-d90).

When sweeping through the various variants with different flare angles for H^{2}ALE, the same general trend in higher loads and deflections are identified in Figure 4.22. The fold angle time history for $\beta = 0$ is perhaps interesting - since the wing tips are pointing almost vertically upwards, and the main wing flexes much less, it is seen that the fold angle range is smaller than the other β cases.

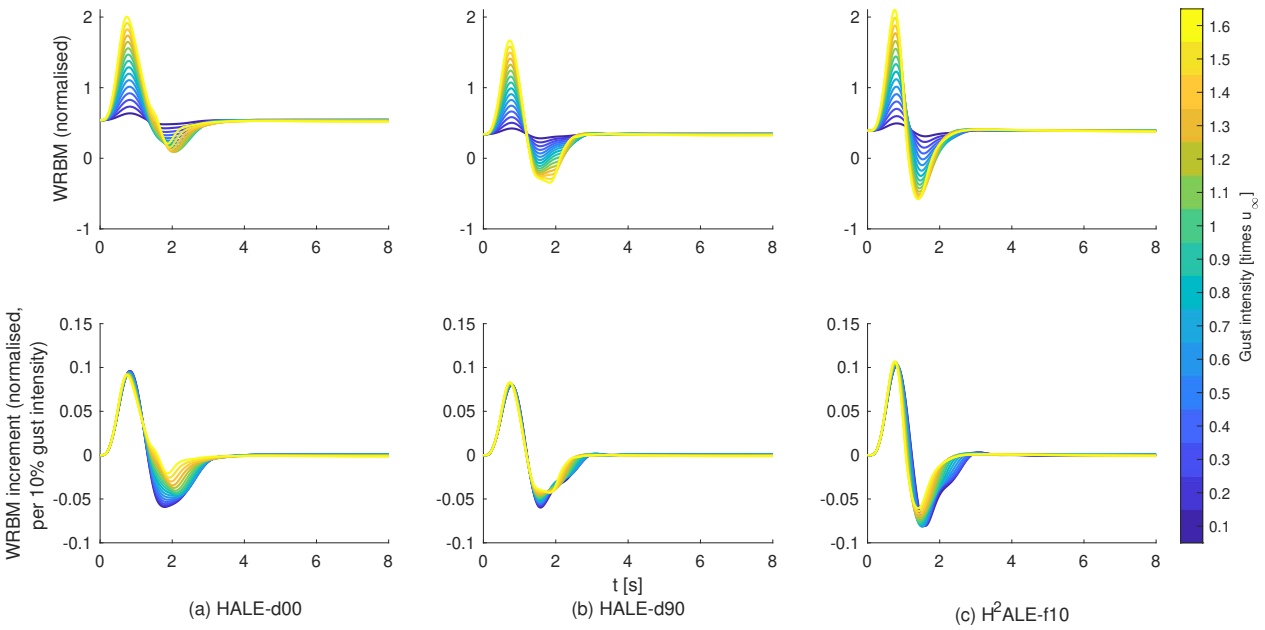


Figure 4.18: Time histories of normalised and incremental WRBM over a range of gust intensities, $\bar{L}_g = 1.5$ s, stiffened wing assembly

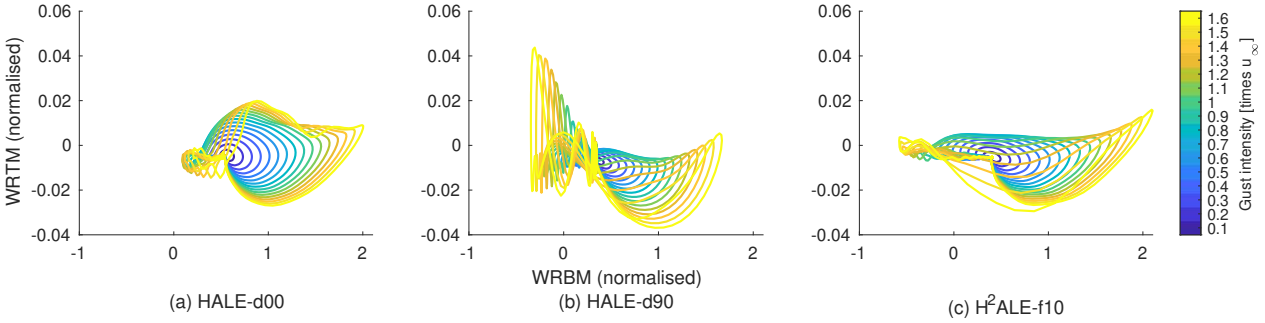


Figure 4.19: Instantaneous values of normalised wing root bending and torsional moment over a range of gust intensities, $\bar{L}_g = 1.5$ s, stiffened wing assembly

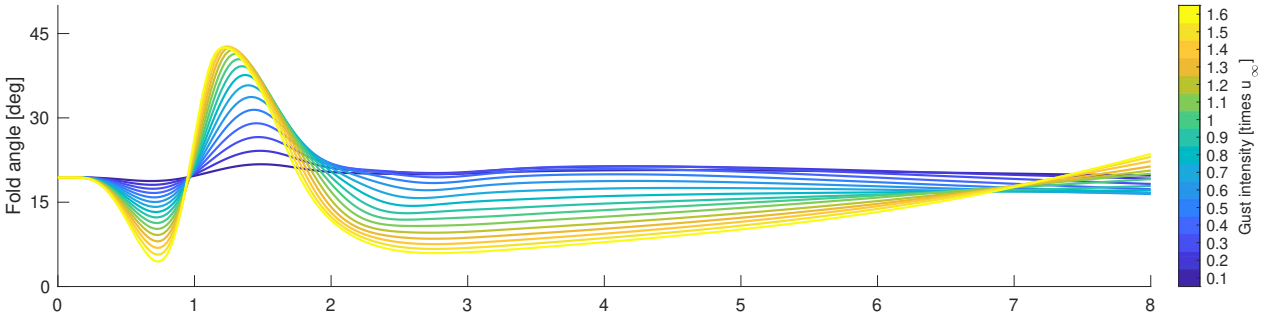


Figure 4.20: Time histories of hinge fold angle for the H^{2}ALE-f10, $\bar{L}_g = 1.5$ s, stiffened wing assembly

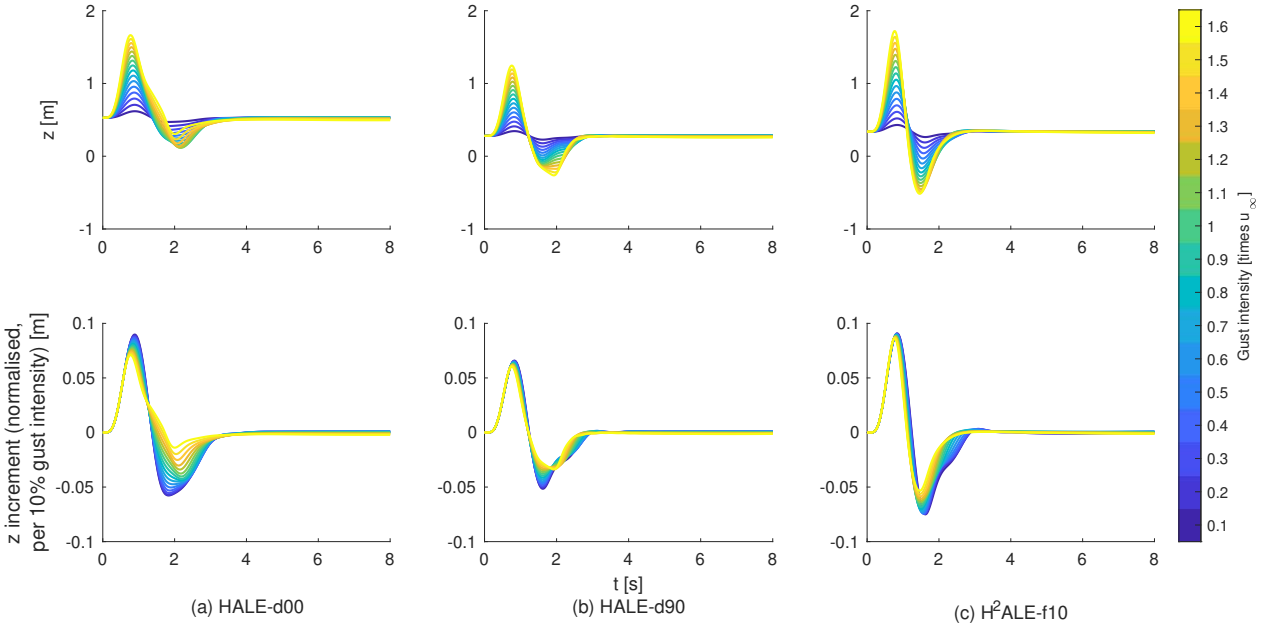


Figure 4.21: Time histories of wing dihedral/hinge vertical position relative to root over a range of gust intensities, $\bar{L}_g = 1.5$ s, stiffened wing assembly

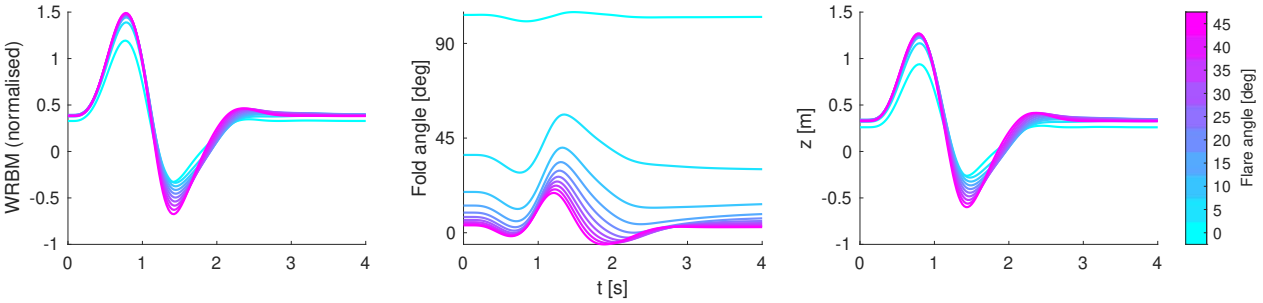


Figure 4.22: Time histories of key quantities for H^{2}ALE with varying flare angle (stiffened), $\bar{L}_g = 1.5$ s, $\bar{U}_g = 1.0$

4.4 Lateral gust response

The lateral gust response, particularly for the H^{2}ALE, is driven by quite different physics when compared to the vertical gust response. A 1-cos lateral gust to the right (starboard) wing is introduced in all the configurations. For this problem, the wingtip collision at fold angle = $\pm 180°$ is used as the sizing case rather than wing root moments, since the wing moment increments due to a lateral gust are much smaller than the manoeuvre loads. Hence, in Figure 4.23 we plot the evolution of the fold angles and roll angle with gust length.

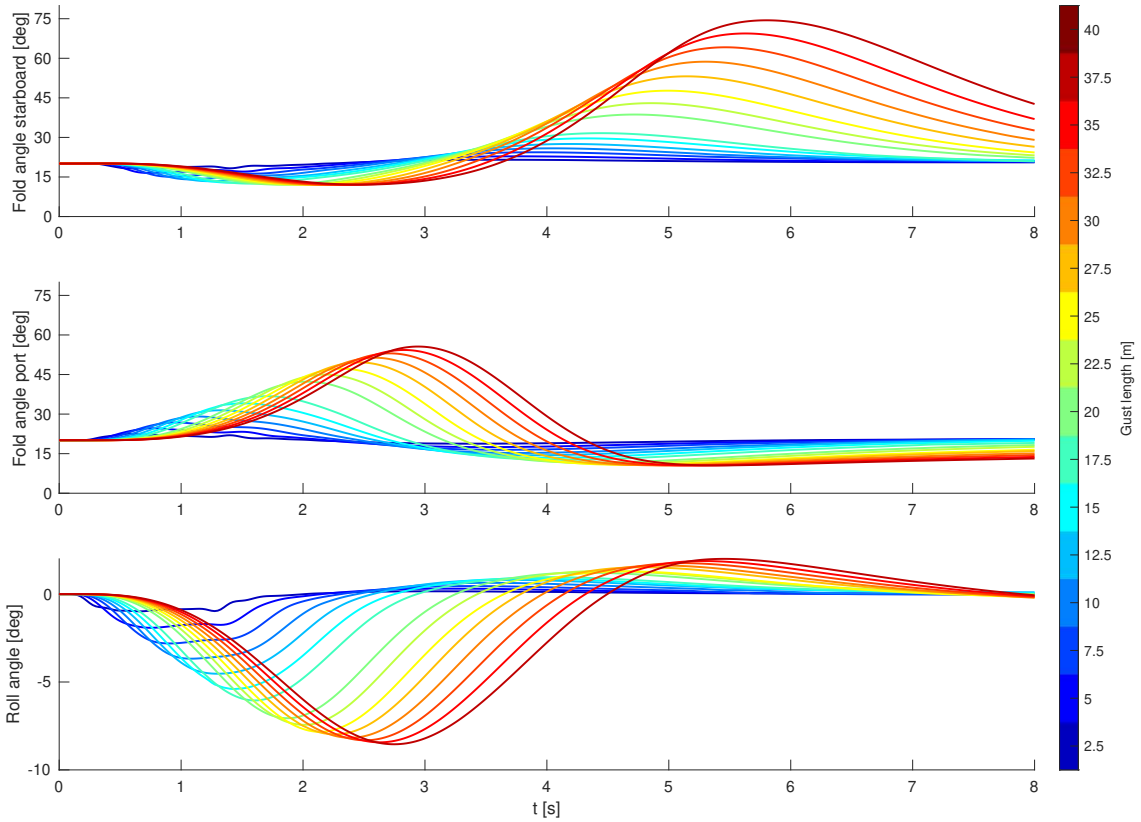


Figure 4.23: Time histories of hinge fold angle port and starboard at various lateral gust lengths, $\bar{U}_g = 0.5$

As it can be seen, roughly for the first 4 seconds after gust onset, the starboard wing tip settled at a smaller fold angle than trim which does not scale with gust length, while the port wing tip promptly increases largely linearly with gust length. The opposite occurs in the subsequent 4 seconds, after which the fold angle on both wing tips approaches the trim value. From the roll angle subplot we recognise for the first 4 seconds after gust onset the aircraft rolls to the right and back, and for the subsequent 4 seconds the roll angle remains almost zero. We have chosen $\bar{L}_g = 1.5$ s as before for a reasonable range of fold angle, as well as a good mix of wing tip and rigid body driven flight dynamics. For subsequent analyses the intensity sweep is limited to a maximum of $\bar{U}_g = 0.6$ to prevent unwanted wake defects causing numerical issues in the time marching simulations.

We have plotted all the Euler angles (roll Φ, pitch Θ, and yaw Ψ) and their time derivatives in Figure 4.24 - as the aircraft is in steady level flight before the gust hits all parameters other than Θ begin at 0, and that Θ at trim is dependent on the aircraft configuration. Comparing the roll angle response we find the HALE-d90 has the highest roll stability out of the three, whereas the HALE-d00 reached the highest roll angle. The roll rates follow a

different evolution: for the first peak the H^{2}ALE-f10 showed the lowest angular roll velocity across gust intensity levels amongst the three configurations, indicating a higher roll damping, similar to the vertical gust scenario where there are lower increments in WRBM with increasing gust intensity. These can both be attributed to the flapping motion allowing for dissipation. The pitch angle and the time derivative show a similar trend where H^{2}ALE-f10 has smaller magnitudes than the HALE-d00. The HALE-d90 demonstrates fundamentally different physics - as the aircraft rolls there is a tendency to pitch down rather than up, and it yaws in the different direction (right wing aft) as the plane banks right, which indicates the worsening spiral mode characteristics with the fixed-upwards wing tips. Time histories of the yaw angle and its derivative remains constant across HALE-d00 and H^{2}ALE-f10, suggesting in the flight dynamics timescale the free wing tips has a negligible impact at least in the directional flight characteristics. From the time histories of the port and starboard fold angles in Figure 4.26, it is perhaps interesting to see the fold angle histories are approximately in the same timescale as the roll angle history. Hence the wing tips in H^{2}ALE-f10 are the first to react to the gust, and is subsequently driven by the inertial of the wing tips and flight dynamics. At the gust encounter, the positive-y forcing on the each of the wing tips pushes the starboard tip down and port tip up, and because the hinge moment imparted by the aerodynamic force increase with fold angle up to $\pm 90^\circ$ due to geometry, port fold angle magnitudes are higher. They then reverse direction as the restoring motion from the flight dynamic modes dominate. The two phases are identified and differentiated also by looking at the hinge vertical position history in Figure 4.25; during the first 3 seconds when the port fold angle increases, the aircraft is rolling to the starboard side and back due to the gust excitation, and the subsequent restoring wing tip dynamics with higher starboard fold angle at almost no roll.

The same effect is then seen with a sweep in flare, as shown in Figure 4.27 at zero flare, fold angles are amplified due to the larger moment arm. Only a reasonably small (¡15°) flare angle is needed to keep the working range of the fold angle small, much like the vertical gust analysis. With a flexible aircraft configuration, there exists a trade-off between higher fold angles in lateral gust, and higher WRBM in vertical gust, when selecting an appropriate flare angle.

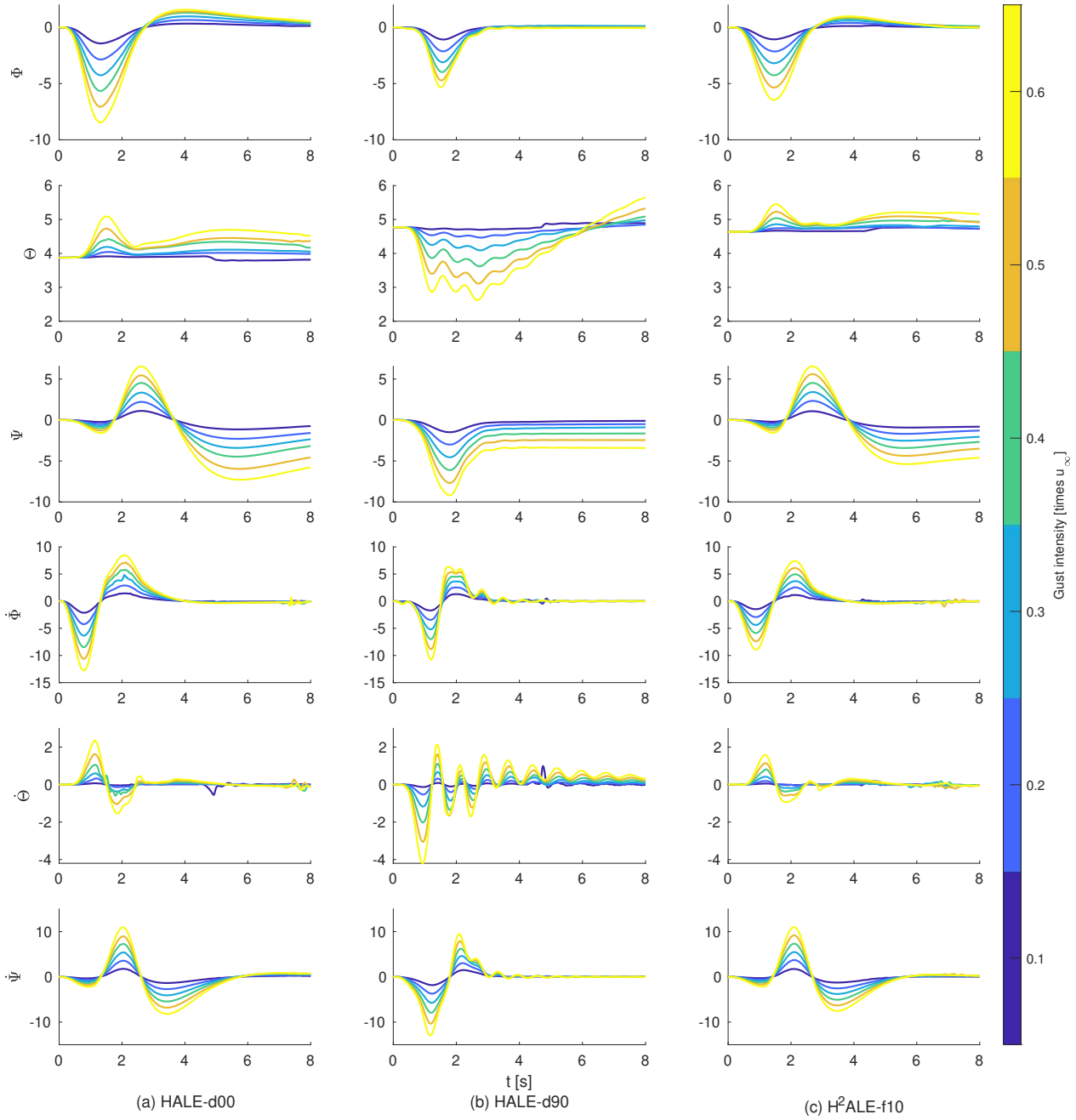


Figure 4.24: Time histories of Euler angles in degrees and their derivatives (deg / s) at the wing root, over a range of gust intensities for lateral $\bar{L}_g = 0.5$ s

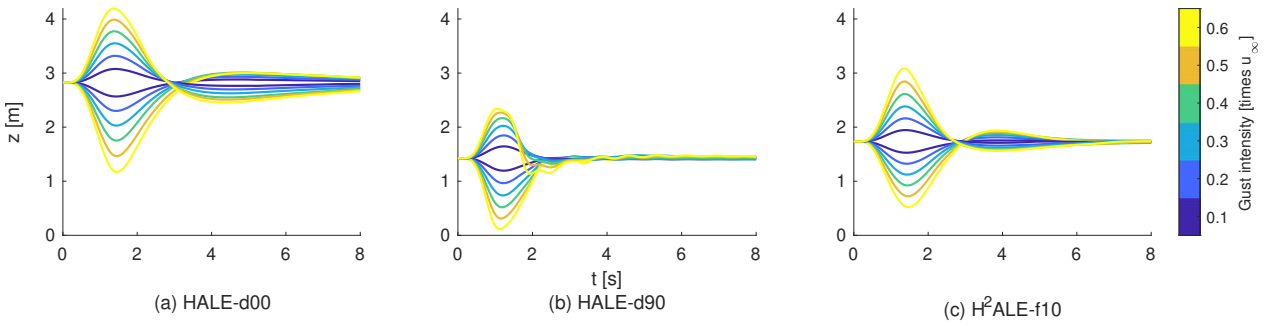


Figure 4.25: Time histories of wing dihedral/hinge vertical positions port and starboard, relative to root, over a range of gust intensities, lateral $\bar{L}_g = 0.5$ s

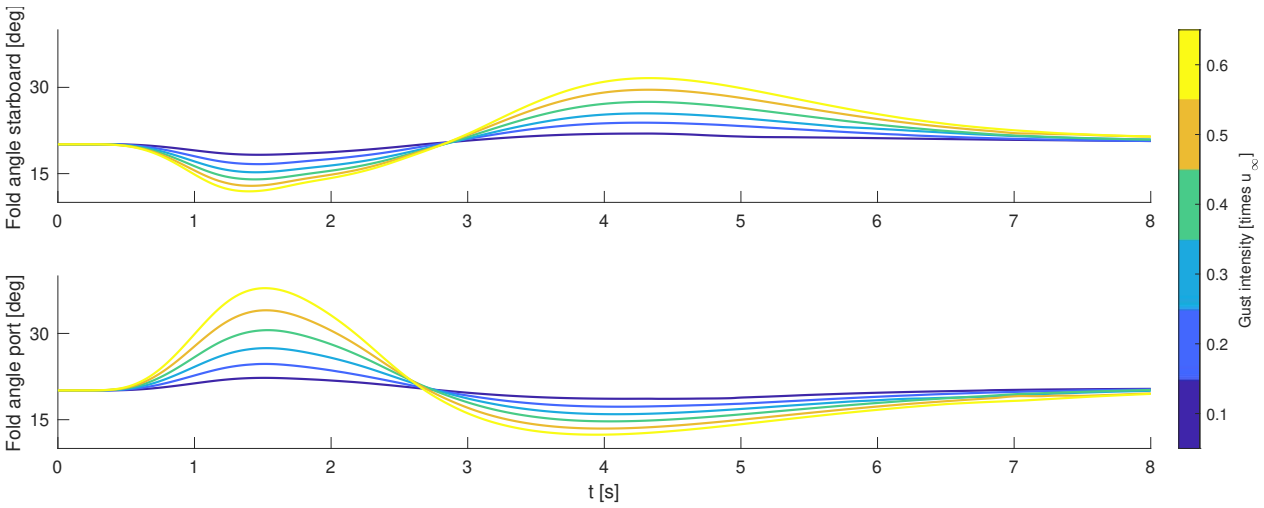


Figure 4.26: Time histories of hinge fold angle for H^{2}ALE-f10 port and starboard, relative to root, over a range of gust intensities, lateral $\bar{L}_g = 0.5$ s

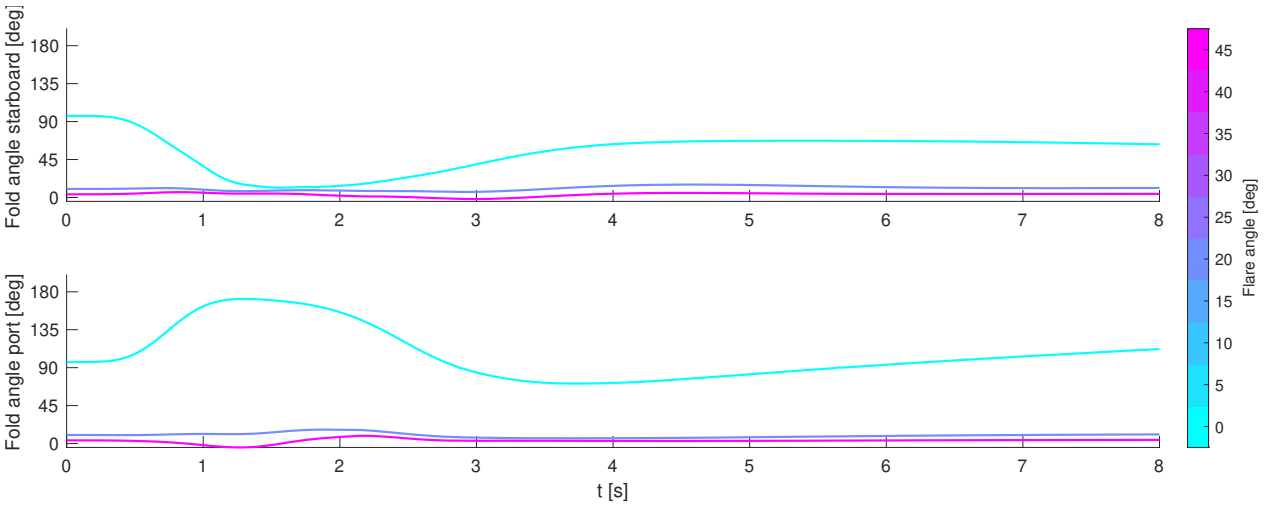


Figure 4.27: Time histories of hinge fold angle port and starboard, for various flare angle, lateral $\bar{L}_g = 0.5$ s, lateral $\bar{U}_g = 0.5$

4.5 Discussion

It must be noted before we further discuss the observations on the multiple HALE vs H^{2}ALE configurations that these aircraft are by nature highly flexible and nonlinear, and are designed for very different objectives than most of the current candidate models for commercial transport aircraft featuring flared hinged wing tips. However, the observations made will underscore the ability of the formulation to model and predict the coupled dynamics involved,

giving confidence to future applications on heavier and stiffer configurations.

In terms of the static wing root bending load alleviation in vertical gust, this is shown to be primarily a feature of the hinge mechanism - and is a weak function of all other variables. Notably, the WRBM of all H^{2}ALE subconfigurations closely approach the HALE-90, i.e. the fixed upturned wing tip case, demonstrating exceptional efficiency. Across increasing flare angle, there is a turning point of maximum WRBM at around $\beta = 15°$, implying opposing mechanisms of load alleviation at different flare angle regimes. A negative flare angle, while is shown to be stable at $\beta = -35°$, drastically increases static WRBM and hence is not desirable for this particular configuration. Lower ratio of wing tip versus root mass actually encourages the coalescence of WRBM at the higher value across flare angles. It is thought that in this case the weight of the wingtip mass helped attenuate lift-induced bending.

As in the dynamic load alleviation in vertical gust, the HALE is most sensitive to the shorter gust length 7.5 m, while the H^{2}ALE the longer 15 m. At higher gust lengths the incremental H^{2}ALE response can be the most severe out of the three compared configurations, but the 1g+gust response remains bounded by the HALE-d00 and the HALE-d90, a trend which is seen across different variables investigated. A comparison of the first positive (wing tip up) peak increment loads normalised by gust intensity shows cases where the increment on H^{2}ALE is slightly larger than the HALE cases, but at both gust lengths there are nonlinear effects at higher gust intensities that the H^{2}ALE only can leverage to reduce the increments. In terms of flare angle, peak WRBM get slightly higher for increasingly positive flare angles, and much like the static load alleviation, much higher for negative flare. For a stiffened wing assembly, dynamic loads get worse - the loss of flexibility i.e. elastic potential energy as a sink for the energies in excited rigid-body modes affects the H^{2}ALE-f10 more so than the two HALE comparisons, since the incremental gust loads outpaces the savings in the static 1g load. The first negative peak is masked by flexibility likewise, but especially in the H^{2}ALE-f10 - in the stiffened case the main wing of the H^{2}ALE-f10 gradually transitions into bending downwards transiently with increasing gust intensity.

The performance of H^{2}ALE in lateral gusts is constrained by the maximum fold angle, as one seeks to avoid the wing tips flipping and striking the main wing. Across gust intensities in a lateral gust encounter the H^{2}ALE-f10 shows maximum instantaneous roll angle attained as proxy for roll stability between the two HALE configurations, and maximum time derivative of roll angle as proxy for roll damping the highest amongst the three configurations. The roll dynamics are mostly coupled with pitching, where yaw seen in H^{2}ALE-f10 seems unaffected at all by the addition of the hinge and is virtually identical to that of HALE-d00, whilst a

fundamentally different response is seen in the HALE-d90.

The H^{2}ALE has demonstrated qualitatively higher damping across all the flare angles investigated. They also tend to return to the equilibrium value fastest, where generally in the HALE-d00 the steady-state error takes time to dissipate, and in the HALE-d90 oscillations are under-damped. Rolling characteristics in lateral gust showed mixed results, with slightly impeded roll performance in exchange for a similar gain in stability. At higher gust intensities, from the inspection of fold angle histories, there is the risk of exciting the higher frequency modes which might escalate into an LCO.

Overall, it is shown that statically the inertia of the wing tip determines the maximum possible WRBM savings in vertical gust, which is leveraged by a careful choice of flare angle with the hinged wing tips. Dynamically the actual WRBM savings achieved is a strong function of wing flexibility, and weaker functions of flare angle, gust length and intensity. These act as sources of nonlinear effects in the vertical and lateral gust responses alike that complicate the coupled aeroelastics and flight dynamics.

We have not included a stall model on the aerofoil polars, a major source of aerodynamic nonlinearity. This is due to its role, in the gust problem considered thus far, of providing extra attenuation of loads. Finally, considerable effort was dedicated to determining the trim state of the system, by exploring suitable gain values for the PI controllers for angle of attack, elevator deflection, and thrust, as functions of the geometrical and inertial properties of the aircraft. The challenge is for them to enable sufficient control authority, while not inducing unsteady system dynamics particularly by large displacements in the UVLM grid. The derivative control, which would provide artificial numerical damping, did little to influence the performance of the trim routine and hence has been left out.

The difficulty of solving a stiff numerical system comprising dynamics across scales in flight dynamics, aeroelasticity, and multibody dynamics is overcome with the careful choice of the time-integration scheme, extra numerical structural damping, appropriate scaling of the equations, and relaxation across the fluid-structural solutions. In cases where the Lagrange multipliers do not converge readily, in particular when the hinge is experiencing high transient excitation loads, it is discovered that errors propagate to the geometrical definition (location and rotation) of the hinge nodes, and subsequently skews the instantaneous hinge axis, giving rise to incorrect aerodynamic forcing, eventually leading to numerical divergence. This issue is largely mitigated by posing an additional constraint that the hinge nodes each take the averaged location in the Earth frame, and hence are exactly coincident at every time step.

That minimises the constraint force to achieve the hinge constraint and hence encourages convergence of the Lagrange multipliers.

Chapter 5

Nonlinear aeroelasticity of a representative flexible aircraft with flared hinged wingtips

Here we present another case study, building on the previous attempt to explore the qualitative trends in coupled aeroelasticity and flight dynamics, identified in the HALE aircraft variants. In determining whether the observations extrapolate well onto a more representative flexible aircraft we turn to the SuperFLEXOP model [212, 186, 195], based on the T-FLEX demonstrator developed within the FLEXOP project [213], later featured also as the test platform for the FLiPASED project. [214] In contrast to the HALE's rectangular wing, which is optimised for solar panel placement and exhibits relatively low wing loading, the SuperFLEXOP features tapered, swept wings designed to demonstrate aeroelastic phenomena. The trailing edge is nearly entirely fitted with control surfaces, and the wing loading exceeds that of the HALE by more than 10 times. We will begin with the details of the configuration of the model in SHARPy and the necessary adaptations for new wings with flared hinged wingtips, then apply the coupled multibody aeroelasticity and flight dynamics framework to investigate vertical gust encounters. We then introduce the additional aerodynamic nonlinearity of a stall model, first in isolation, then with a new set of trim inputs to better compare the differences in dynamics exhibited.

5.1 SuperFLEXOP and the Hinged-SuperFLEXOP

The representative flexible aircraft is used to demonstrate the aforementioned coupled multibody aeroelastic framework, based on a modified version of the T-FLEX UAV in the FLEXOP project, which has undergone extensive flight testing and numerical validation. [215, 216,

217, 218, 219, 220, 221] Düssler et al. [186] analysed the model and found the wings stiff; wing tip displacements are 2.27% of half-span at trim. Hence they applied a scaling factor of 0.3 to all stiffness constants, and referred to the resultant configuration as the Super-FLEXOP, weighing 64.8 kg. Preston et al. [222] in benchmarking for the performance of variable sweep wingtips, extended the SuperFLEXOP with multibody configurations and developed the multibody FLEXOP.

In this work the SuperFLEXOP will be compared with the Hinged-SuperFLEXOP at the cruise speed of $45\,\mathrm{m\,s^{-1}}$. For the Hinged-SuperFLEXOP, as in [222], a pair of flared hinged wingtips with zero hinge stiffness and/or damping are installed at 70% span at a flare angle of 10 degrees. Spatial and temporal discretisation parameters are set out in Table 5.1, with the reference geometry plotted in 5.1. A snapshot of the aircraft model in SHARPy during a very large gust encounter is shown in Figure 5.2.

Table 5.1: Simulation parameters for SuperFLEXOP and Hinged-SuperFLEXOP

Parameters	SuperFLEXOP	Hinged-SuperFLEXOP
Wing body panel discretisation, $\mathrm{N} \times \mathrm{M_b}$	54×8	
Tail body panel discretisation, $\mathrm{N} \times \mathrm{M_b}$	22×4	
Wake panel discretisation, $\mathrm{M_w}$	20	
Simulation time step [s]	0.972×10^{-3}	

Following the notation in Chapter 4, we have L_g and $\bar{L}_g$, in units meters and seconds respectively, as the dimensional and normalised gust lengths; and U_g and $\bar{U}_g$, the former in meters per second, as the dimensional and normalised-with-freestream gust intensities. Wing root bending and torsional moment values, where quoted, are nondimensionalised by the product of aircraft weight and one-eighth span length.

5.2 Aeroelastic trim and equilibrium state

In anticipation of the vertical gust encounter the aircraft are trimmed for cruise conditions at $45\,\mathrm{m\,s^{-1}}$ and sea level density of $1.225\,\mathrm{kg\,m^{-3}}$, using the algorithms described in Section 3.5. The trimmed inputs for a force-free UVLM wake (that will be used throughout) are presented in Table 5.2.

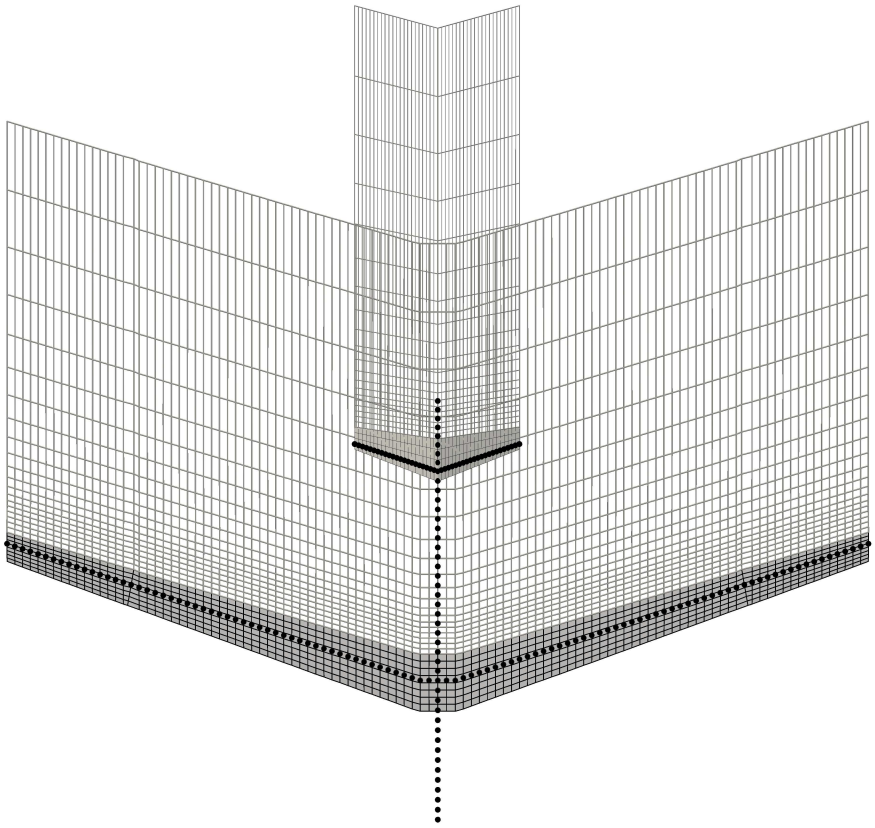


Figure 5.1: Reference geometry of the Hinged-SuperFLEXOP

Table 5.2: Comparison of trimmed values for SuperFLEXOP and Hinged-SuperFLEXOP

Values at trim	SuperFLEXOP	Hinged-SuperFLEXOP
Thrust [N]	2.29	4.06
Elevator [deg]	0.23	0.71
Angle of attack [deg]	0.24	0.27

For the Hinged-SuperFLEXOP, a two-step approach is used for trim - the static trim loop uses the Newton-Raphson Method to quickly find trim inputs for a candidate aeroelastic state that resolves to zero resultant forces and moments (which despite the name of the routine does not guarantee static stability). The preliminary trim inputs are passed on to the dynamic trim loop, where close to a candidate trim aeroelastic state it uses SISO PI controllers, with the help of numerical damping, in time domain drives the solution closer to zero. This hybrid approach strikes a balance between speed and accuracy arriving at a physical equilibrium point.

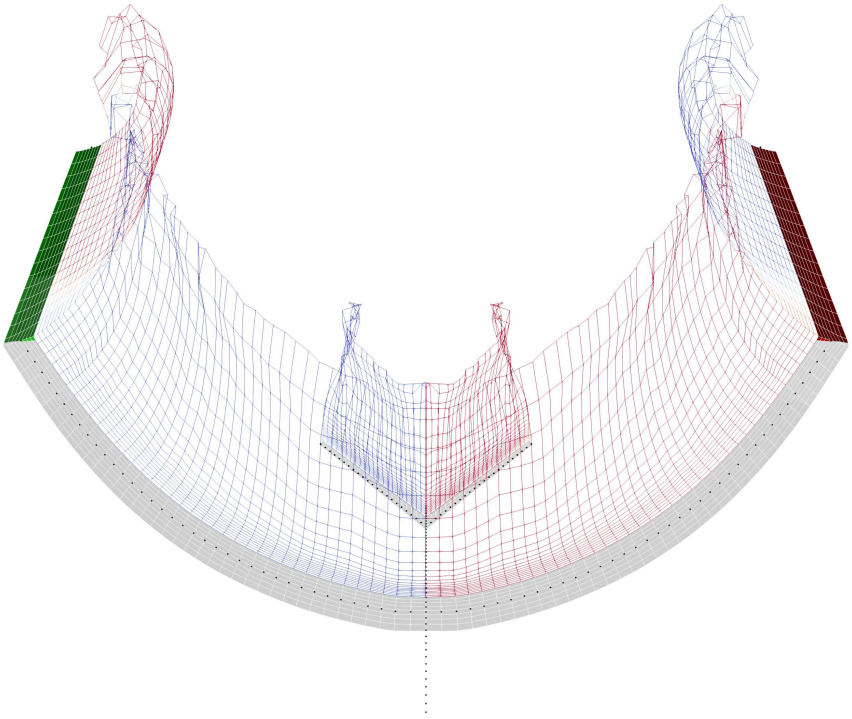


Figure 5.2: Snapshot of Hinged-SuperFLEXOP with force-free UVLM wake grid coloured by circulation intensity, response to 1-cos gust of $\bar{L}_g = 0.225$ s and a very large gust of $\bar{U}_g = 1$, 0.17 seconds post encounter

Some selected trim spanwise quantities are plotted in 5.3. Notice how, as expected, with 30% of span 'lost' to the free wingtips, the Hinged-SuperFLEXOP requires a slightly higher trim angle of attack with the effect of shifting lift inboard, and achieving much lower wing root bending moment at trim. The slightly different span-wise discretisation near root of the SuperFLEXOP means certain panels are wider and hence generate more dimensional lift than the rest of the panels; that should not be interpreted as a local spike in lift per span. As a result of the lower bending moment throughout in the Hinged-SuperFLEXOP, flexible deformations from 70% span to centre compares very favourably to the SuperFLEXOP. The equilibrium fold angle is 10.6°.

With the trim inputs and states defined we proceed to examine the open-loop vertical gust response of the SuperFLEXOP and Hinged-SuperFLEXOP.

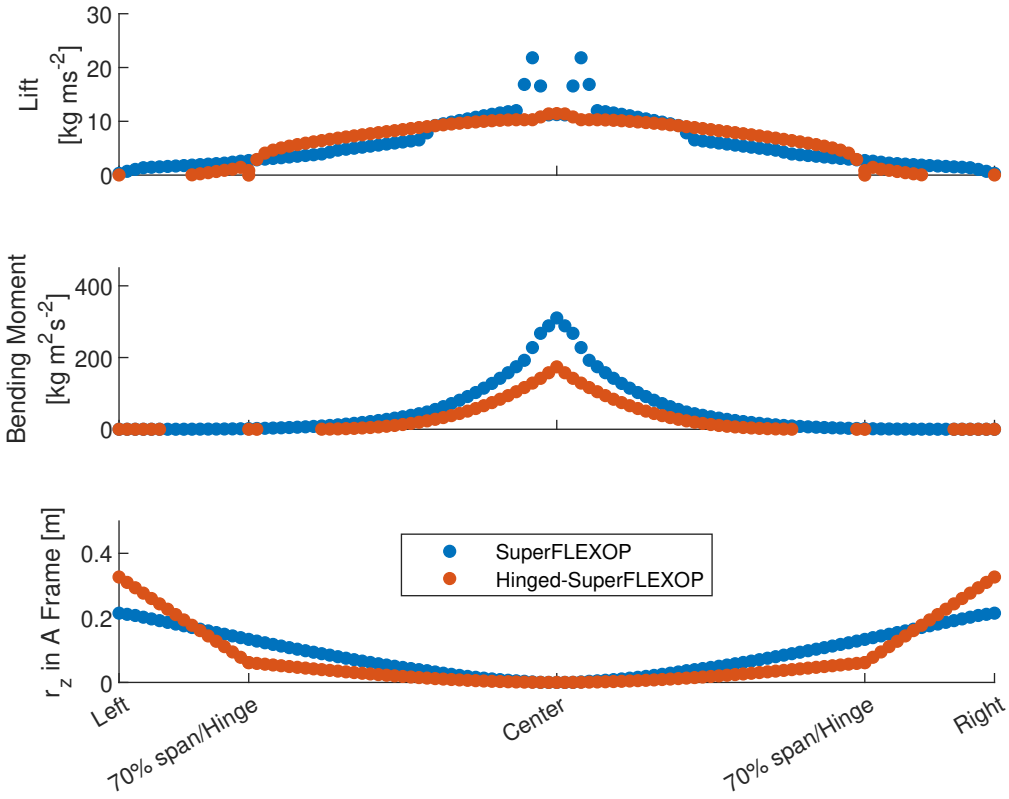


Figure 5.3: Trim spanwise quantities for the SuperFLEXOP and Hinged-SuperFLEXOP

5.3 Vertical gust response

We begin again with a sweep across a range of gust lengths, to better understand the time scales and responses of the SuperFLEXOP and Hinged-SuperFLEXOP to vertical 1-cos gust encounters from trim. The gust lengths are chosen to probe a large range of frequencies; they range from $\bar{L}_g = 0.01$ s, corresponding to 0.45 m, compared to the root chord of 0.471 m, in increments up to $\bar{L}_g = 0.5$ s, corresponding to 22.5m which is more than 10 times the distance between the wing and tailplane (1.976 m). Apart from the WRBM measure which is the biggest driver for load alleviation and hence performance here, we will also examine the excited dynamics in the flexible multibody mechanism, as well as the rigid-body pitch and heave. The results are as presented in Figure 5.4, where we have used a constant gust intensity of $\bar{U}_g = 0.1$ throughout to focus on the effects of the gust length instead.

There is a sizeable difference in trim wing root bending moment at $t = 0$, driven by the shifting of lift inboard, in line with what we identified for the HALE vs H^{2}ALE. Indeed if we consider also the dynamic response to the (small) gust intensity response, across all gust lengths investigated here, the Hinged-SuperFLEXOP has a lower maximum wing root

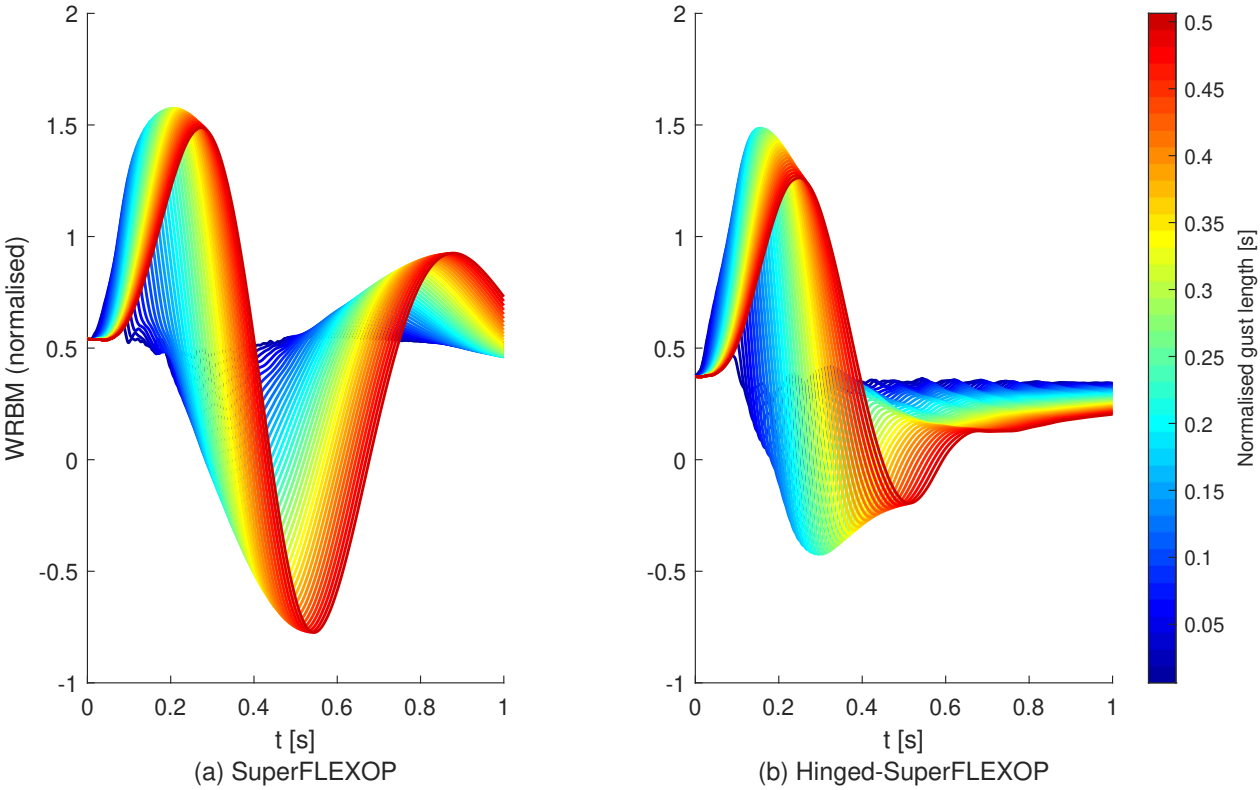


Figure 5.4: Time histories of normalised wing root bending moment at various gust lengths, $\bar{U}_g = 0.1$

bending moment in both directions, positive and negative, the former of which is driven by the lower trim WRBM, demonstrating the potential for gust load alleviation.

With that we can identify in terms of the sensitivities, that the Hinged-SuperFLEXOP shows the earlier peak in response at the $\bar{L}_g = 0.225$ s mark, where the SuperFLEXOP peaks at $\bar{L}_g = 0.3125$ s, with no stall model included. This is opposite from the behaviour seen in the HALE in Chapter 4, in which the multibody version sees a peak response at a gust length longer than the cantilever-winged aircraft.

5.3.1 Results for different gust length

For subsequent analysis we focus on each of the two critical gust length identified, starting with $\bar{L}_g = 0.225$ s, then $\bar{L}_g = 0.3125$ s. We will examine the time histories of WRBM, WRTM, relative vertical displacement as a proxy for wing out of plane bending, aircraft pitch angle, and hinge fold angle, to gain a better understanding of the coupled flight dynamics and aeroelasticity of the SuperFLEXOP vs Hinged-SuperFLEXOP in the time domain.

$\bar{L}_g = 0.225$ s

Since this is the most sensitive gust length for the Hinged-SuperFLEXOP configuration, as expected from Figure 5.5 we are seeing similar WRBM dynamically as we increase the gust intensity from $\bar{U}_g = 0.02$ to $\bar{U}_g = 0.76$, the latter representing a staggering 34.2 m s^{-1} gust intensity over a little more than 10 meters. As before, the first row shows the time histories from trim of the normalised WRBM are shown, and in the second row, the increments in WRBM from the trim case, normalised by the gust intensity, are plotted, with the trends near the first peak included in the inset. The Hinged-SuperFLEXOP, despite the marginally higher WRBM at higher gust intensities, is successful in removing the second positive peak in WRBM completely, when comparing the response to the original SuperFLEXOP. The nonlinearities captured here are at least two-faceted; firstly, the WRBM increments both for the SuperFLEXOP and the Hinged-SuperFLEXOP do not coincide exactly, but both indicate significant load relief, due to large deflections (as in Figure 5.7) leading to geometric stiffening, which grows with gust intensity, upon a close inspection of the first peak. Secondly, we can identify the emerging high frequency response in WRBM at higher gust intensities that is present in both of the models, indicating common emerging nonlinear behaviour, to be unpacked in more detail, driven by large excitations.

Looking at the relationship of the wing root torsional and bending moment as plotted in Figure 5.6 we have a few observations. Here to avoid clutter we have only extracted the time histories corresponding to the first positive and negative peaks from $t = 0$ s to $t = 0.4$ s. For the SuperFLEXOP on the left, at higher gust intensities (yellow), the trajectory simply expands along a similar shape, meaning stronger gusts scale up both bending and torsion without radically changing their relationship, aside from some higher-frequency wiggles at the most negative WRBM. For the Hinged-SuperFLEXOP, the overall envelope in the upper-right (positive WRBM, positive WRTM) is similar, meaning peak positive bending and torsion still correlates with gust intensity. However, in the negative-WRBM region the trajectories become much more criss-crossing, reflecting high-frequency modes superposed on the global bending-torsion response. A final note here, being that similar to the HALE, nonlinear dynamics should be considered in the analysis because the largest gust intensity case, more prominently for the Hinged-SuperFLEXOP, does not define the entire load envelope as well, i.e. the convex hull from one single high load case is not sufficient.

Examining the time histories of wing 70% span position (N.B. for Hinged-SuperFLEXOP this is exactly where the hinged wing tips begins) relative to the root (Figure 5.7), aircraft pitch (Figure 5.8), and hinge fold angle (Figure 5.9) for the Hinged-SuperFLEXOP, gives us

a better idea of the coupled flight dynamics and aeroelasticity in different time scales from gust onset. Immediately after gust onset, the motion for both of the aircraft is dominated by an inertia-driven response: the wing flexes upwards relative to the root, giving a positive peak in Figure 5.7, while the aircraft pitches slightly nose-up throughout the duration of the gust (from $t = 0$ to $\bar{L}_g = 0.225$ s). During this same interval the wing tips begin to fold, initially towards negative angles due to the lag of the tip masses to the flexing up of the wings, partly due to the main wing seeing the gust first due to the sweep angle. Very quickly, now still within the gust field, the wing tip sees massively increased local angle of attack both due to the downwards motion and the gust velocity vector, reversing the downward swing and overshooting the main wing in wing tip rotation as a proxy to vertical deflection, in search for a new equilibrium. The fold angles in higher intensity cases approach and in some cases overshoot 90°; this is reflected, due to post processing the relative rotation between two CRVs near the singularity, as a slight dip from 90° at around $t = \bar{L}_g$.

Past the gust velocity field at $t > \bar{L}_g$ the behaviour of the two aircraft start to diverge. The SuperFLEXOP completes another period of a coupled pitch-bending mode, as evidenced by the WRBM, relative wing deflection, and pitch staying in phase, extrapolating to a gradual return to a trimmed equilibrium with sizeable aerodynamic damping. The Hinged-SuperFLEXOP, however, seeks a new equilibrium far from the trim conditions; the most telling of which is that the fold angle, after a strong downwards flap from the near vertical position, seems to have provided too much pitching moment to send the aircraft in strong nose-down pitch, at that point the fold angle for zero hinge moment moves to the negative region, where it stabilises towards to end of simulation time range. This nonlinear behaviour driven by large gust excitation is captured by the formulation, and remains to be investigated further to examine whether other nonlinearities would change this behaviour.

$\bar{L}_g = 0.3125$ s

Now we switch tracks to the longer gust length of $\bar{L}_g = 0.3125$ s. This is the most sensitive gust length for the SuperFLEXOP instead, but when examining the WRBM time histories in Figure 5.10 and comparing to the shorter gust length the overall trends remains unchanged. The WRBM increments per 2% gust intensity at the first positive peak for the Hinged-SuperFLEXOP are now reduced and very much in line with that of the SuperFLEXOP. Torsional and bending moments in Figure 5.11 shows the same trends as discussed previously.

Other trends identified with increasing gust intensity in flexible deformations (Figure 5.12), aircraft pitch (Figure 5.13), and fold angle (Figure 5.14) appear to be relatively insen-

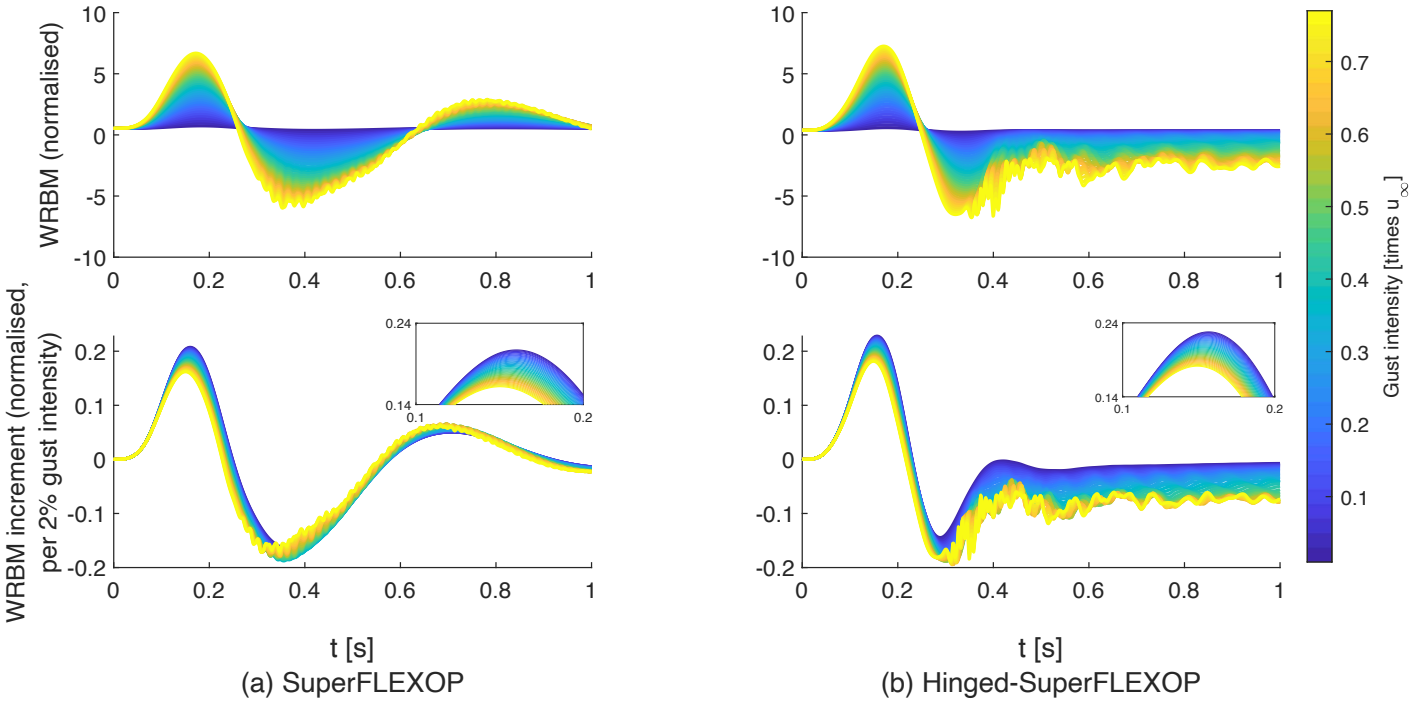


Figure 5.5: Time histories of normalised and incremental WRBM over a range of gust intensities, $\bar{L}_g = 0.225$ s. Moment increment plots include inset with values near the first peak.

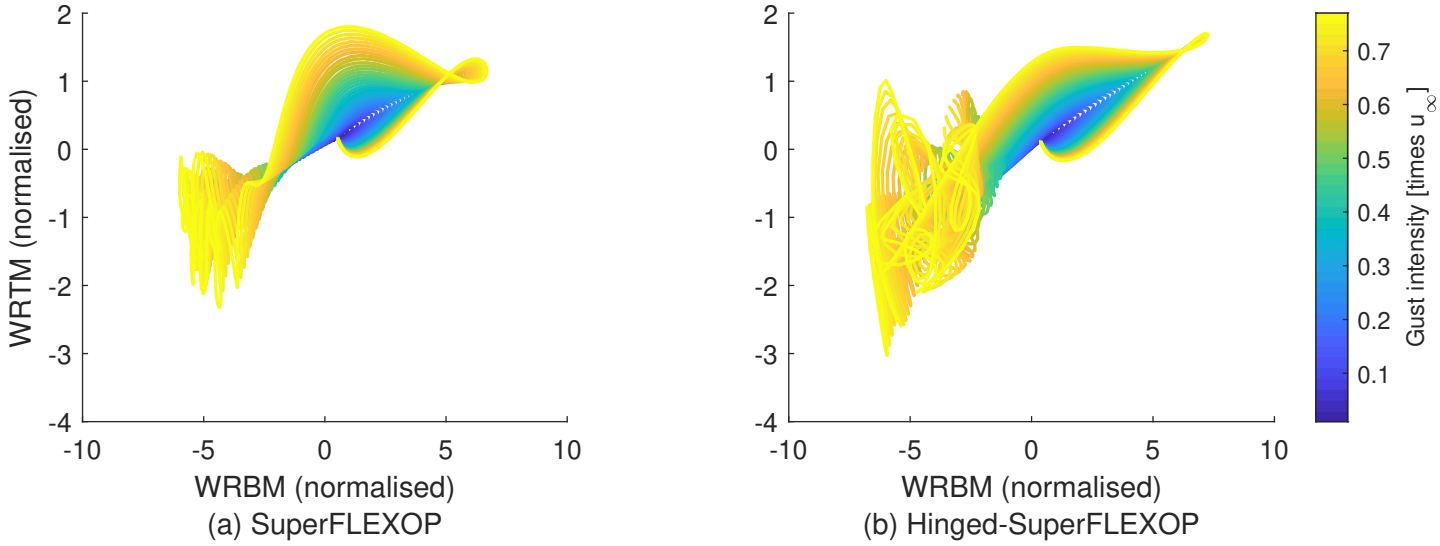


Figure 5.6: Instantaneous values of normalised wing root bending and torsional moment over a range of gust intensities, $\bar{L}_g = 0.225$ s.

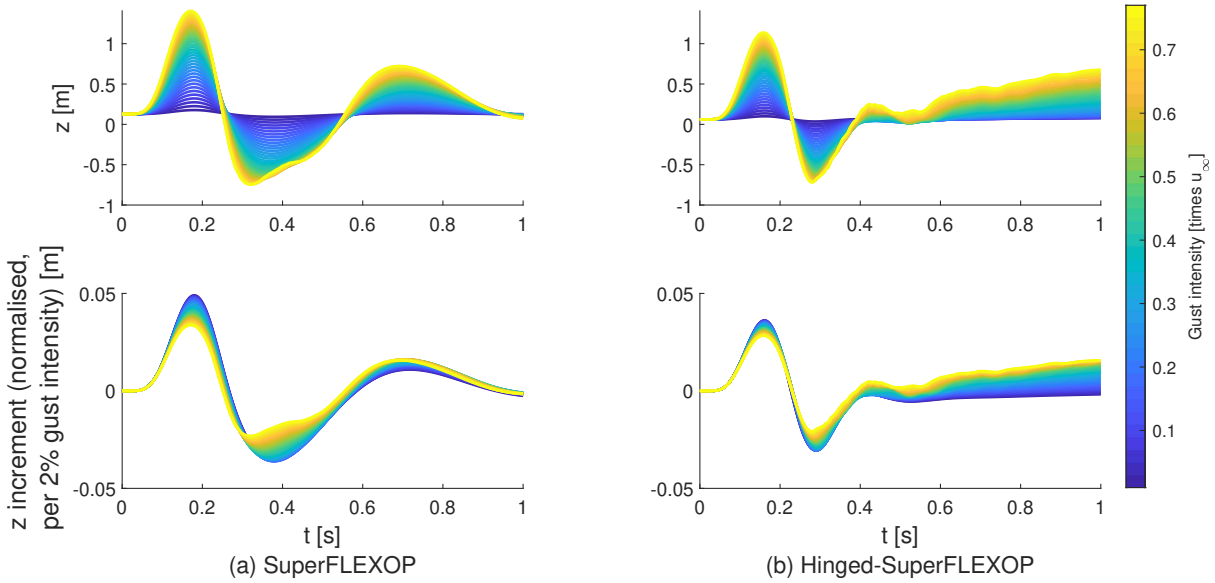


Figure 5.7: Time histories of vertical displacement at the 70% span station relative to the root over a range of gust intensities, $\bar{L}_g = 0.225$ s

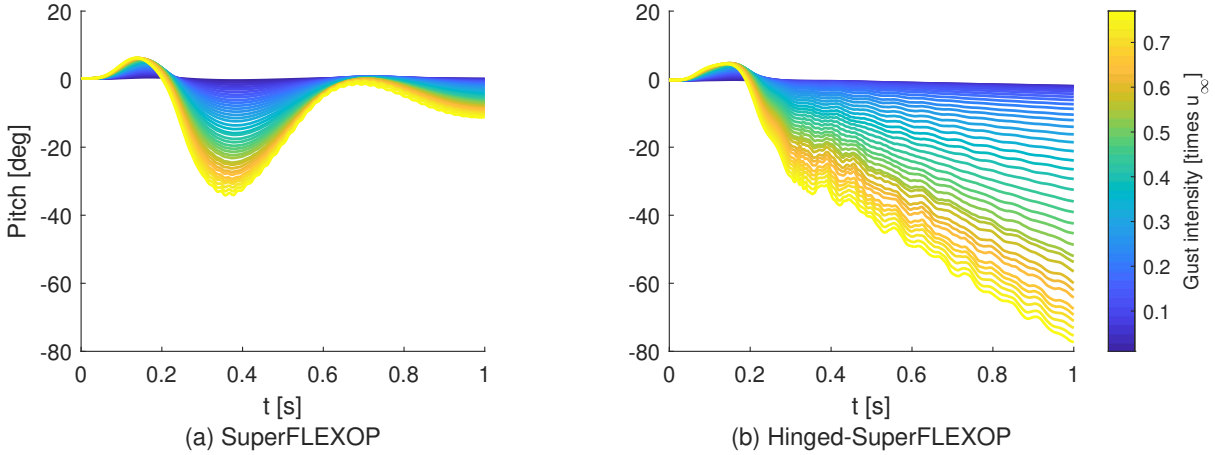


Figure 5.8: Time histories of aircraft pitch angle over a range of gust intensities, $\bar{L}_g = 0.225$ s

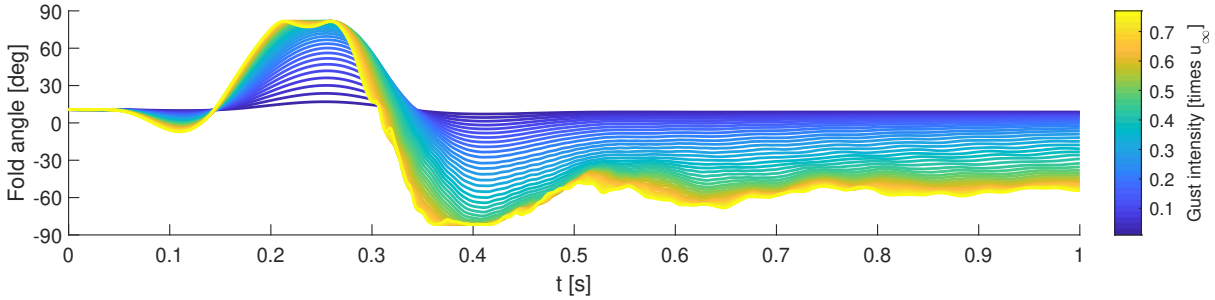


Figure 5.9: Time histories of hinge fold angle for the Hinged-SuperFLEXOP over a range of gust intensities, $\bar{L}_g = 0.225$ s

sitive to changes in gust length at this scale, which suggests that a similar dynamic response is being excited regardless of the exact gust length within this regime. Henceforth we will present only the results for the shorter $\bar{L}_g = 0.225$ s, since that being the critical gust length for the Hinged-SuperFLEXOP should represent the conservative case for loads and dynamics.

5.3.2 Effect of even higher gust intensities

In the previous open loop vertical gust encounters, the maximum gust intensities shown are at $\bar{U}_g = 0.76$, since beyond which, we do not have consistent convergence of the time domain solution at every time step. A stall model and the associated aerodynamic nonlinearity is not included in this set of results as before; findings should be interpreted with this in mind. Note that at $\bar{U}_g = 0.76$, U_g is more than twice the gust velocity at sea level required ($17.07\,\mathrm{m\,s^{-1}}$) for a CS-25 certified aircraft [223], not to mention the Hinged-SuperFLEXOP's low cruise velocity compounding any adverse impact by gusts. Here we present those results from $\bar{U}_g = 0.7$ to $\bar{U}_g = 1.0$ for $\bar{L}_g = 0.225$ s, where missing gust intensity entries due to non-convergence of the solver are identified from the colour bar. This is to demonstrate the onset of highly nonlinear behaviour in the gust response; a higher gust intensity is analogous to a lower effective wing stiffness during the transient phase. The highest gust intensity at which we have a converged results for the SuperFLEXOP is $\bar{U}_g = 0.86$, for the Hinged-SuperFLEXOP results are available inconsistently up to the maximum range investigated of $\bar{U}_g = 1$.

We begin with the time histories of the WRBM and WRTM; in Figure 5.16 showing the first 0.4 seconds post gust encounter the bending and torsion response for the Hinged-SuperFLEXOP for the emerging higher gust intensity group of curves in yellow is qualitatively similar to that of the blue, relatively lower gust intensity group. Closer examination at the time histories of the WRBM post 0.4 seconds in Figure 5.15 reveals a different story; the time histories for the yellow group, despite the high frequency content that is consistent with the richness of the response expected at such high disturbances, takes a different path than the lower intensities blue curves, eventually approaches the baseline WRBM at $t = 1$, very much mimicking the response of the SuperFLEXOP.

To understand the drastic difference in quasi-steady behaviour we turn to the monitored rigid body and aeroelastic quantities in time. In line with the WRBM, the flexible deformation post higher gust intensity encounters in yellow in Figure 5.17 approaches its initial value after the gust encounter, diverging from the lower gust intensity group post the first negative

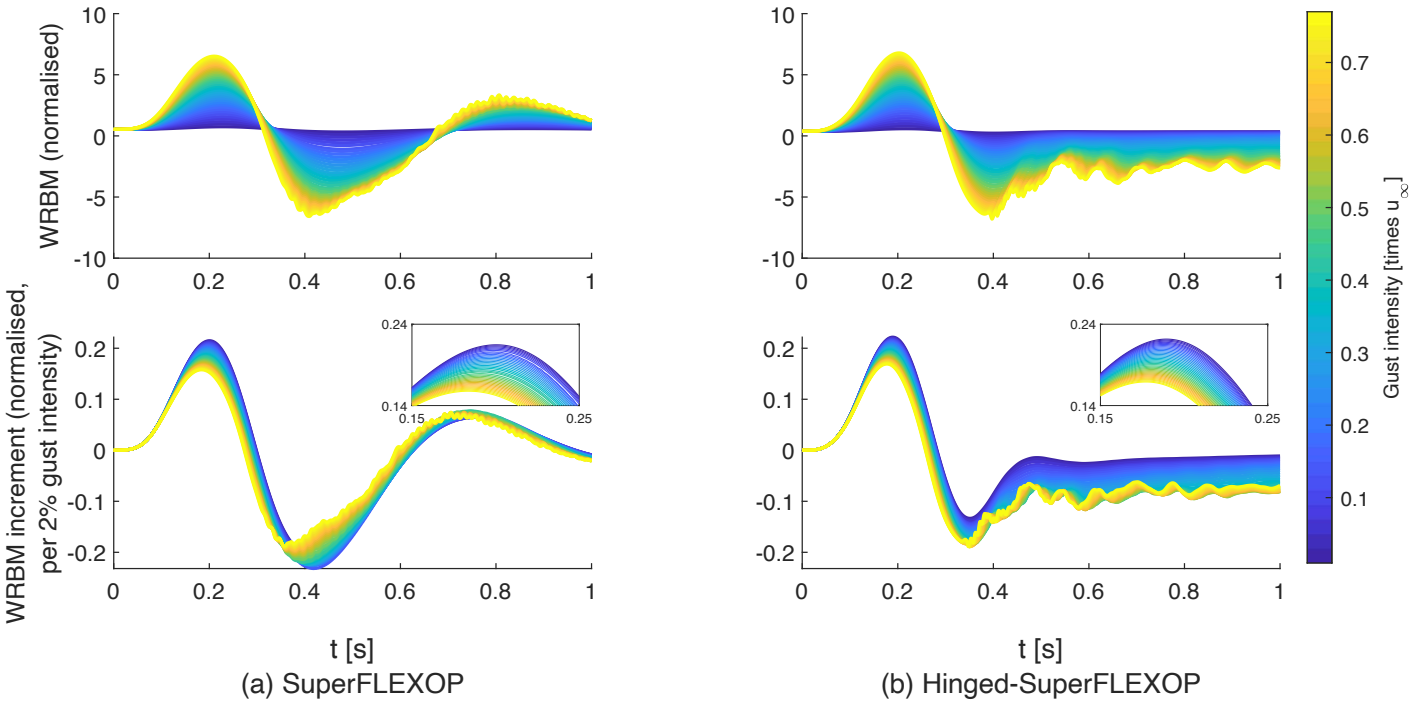


Figure 5.10: Time histories of normalised and incremental WRBM over a range of gust intensities, $\bar{L}_g = 0.3125$ s. Moment increment plots include inset with values near the first peak.

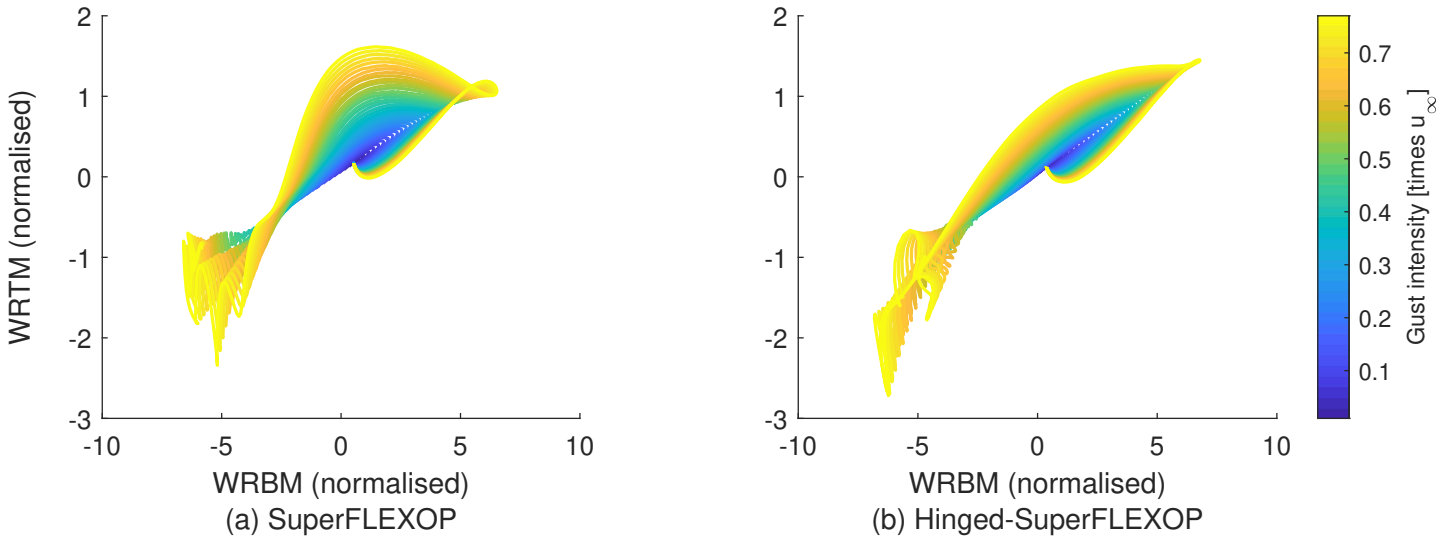


Figure 5.11: Instantaneous values of normalised wing root bending and torsional moment over a range of gust intensities, $\bar{L}_g = 0.3125$ s

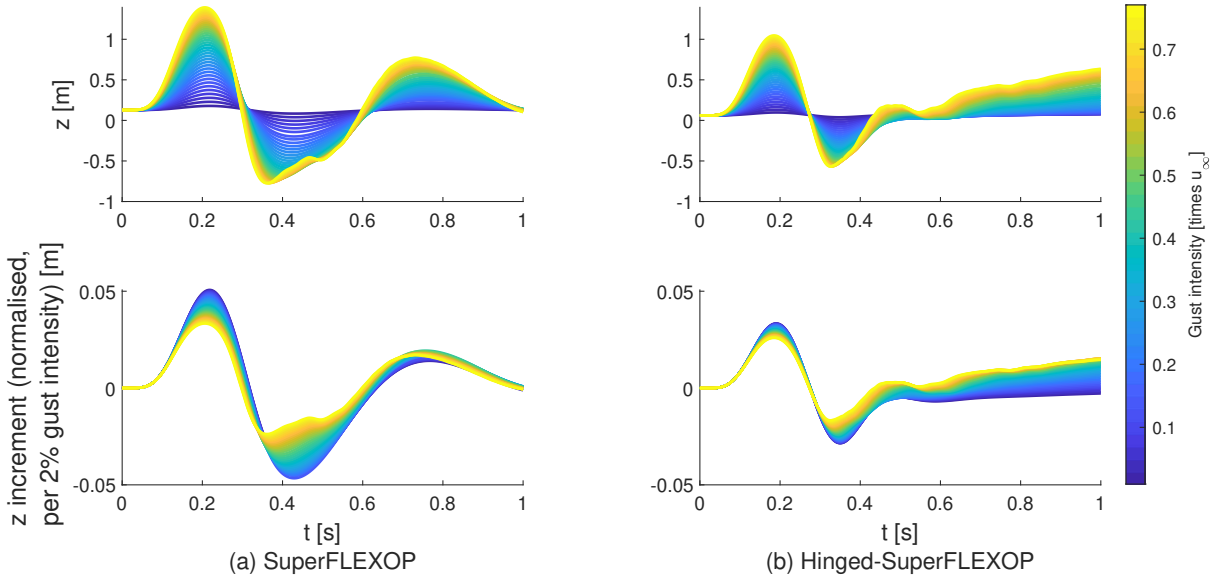


Figure 5.12: Time histories of vertical displacement at the 70% span station relative to the root over a range of gust intensities, $\bar{L}_g = 0.3125$ s

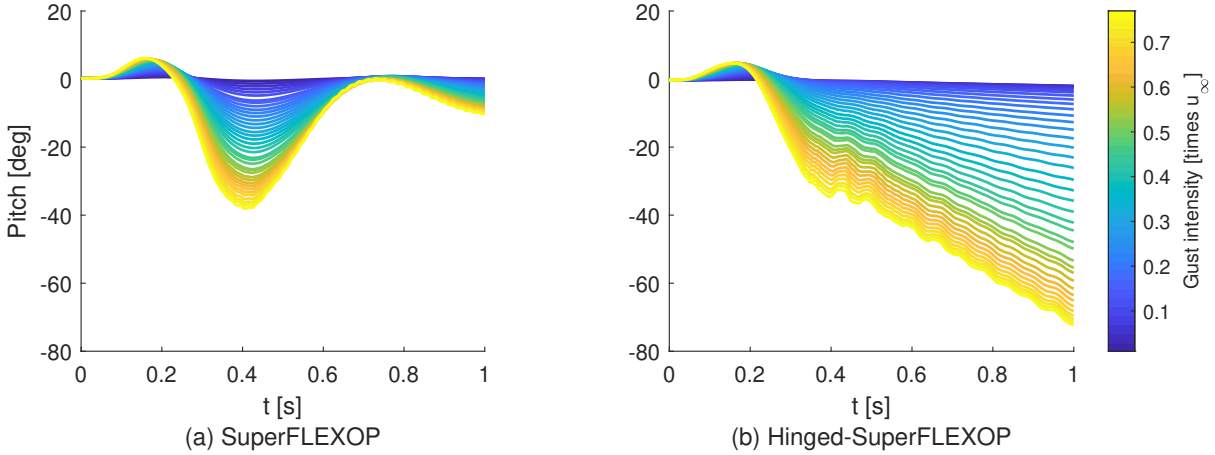


Figure 5.13: Time histories of aircraft pitch angle over a range of gust intensities, $\bar{L}_g = 0.3125$ s

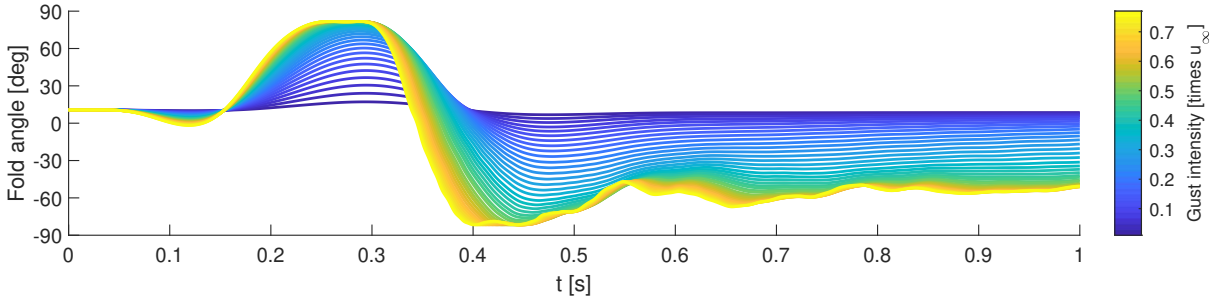


Figure 5.14: Time histories of hinge fold angle for the Hinged-SuperFLEXOP over a range of gust intensities, $\bar{L}_g = 0.3125$ s

peak, indicating a return to the relatively unstretched trim configuration as in Figure 5.3. This is best put in context by the next plot in Figure 5.18, showing the same oscillations resembling a short period pitch oscillation (SPPO) mode, but about different equilibrium; where the higher gust intensity group of cases have pitch close to 0, the other group with seemingly a loss of pitch stability. We can speculate the cause of this apparent bifurcation identified from the fold angle history; in Figure 5.19, we identify a bifurcation in fold angle at $t = 0.3$. At higher gust intensities, instead of the big swing from vertically up to down as we've seen that is common to the lower intensity cases, we see high frequency flapping that could reasonably be attributed to coupling with the beam modes in the main wing. Such flapping decays in the now more modest downwards flap at $t = 0.5$ as the fold angle completes another half-swing to approach the cruise equilibrium post gust encounter.

A spectral analysis performed on the normalised WRBM is presented in Figure 5.20; note the expanded colour bar now represents a sweep from the lowest to the highest gust intensities tested on the aircraft. A discontinuity is identified in the gust intensity sweep as before - the two distinct regimes of coupled aircraft response are now clearly separated; where at the lowest gust intensity the WRBM response is dominated by the first spectral peak at ~ 4 Hz, towards higher intensities the extra peaks likely reflect the broadband content of the 1-cos gust activating several extra aeroelastic modes, rather than nonlinear harmonic generation which would have been shown at multiples of the fundamental frequency.

Across the jump there is significant redistribution of spectral content in the response, which is a stark departure from the mostly linear growth, as evidenced also by the time domain responses presented upfront. The bifurcation is characterised by the new dominant slightly-lower-frequency peak with elevated amplitude, as well as the consolidation and strengthening of higher-frequency content. The former corresponds to branch-switch behaviour suggesting qualitative changes in the coupled response not explained by linear scaling. The latter may be explained with nonlinear interactions contributing to harmonic content, which is best confirmed by phase-coupling and strengthened by applying the same analysis across multiple coupled signals.

If further runs with perturbed initial conditions consistently settle onto the same response region at a fixed gust intensity, that would strongly support nonlinear branching (multiple attractors) rather than numerical artefacts. That would also explains the missing cases in the gust intensity sweep; near a transition, one branch can be unstable, so time marching may not settle within the simulated window and jump to another stable branch. This study is however beyond the scope of this work, and would confirm a bifurcation, with the exact

type to be further determined.

5.3.3 Effect of sectional polar corrections

In an attempt to explore the dynamics of the aircraft and throw another nonlinear spanner in the works, we introduce sectional polar corrections using the method as described in Section 3.1.2 to both aircraft. Consistent with the limitations of the UVLM method we opt not to introduce viscous drag corrections. This is justified for cruise conditions where unsteady lift and induced drag, rather than viscous dissipation, dominates the response to vertical gusts. The lift and moment coefficient curves applied are given in Figure 5.21, with the data given in [212, 186]. Details of the custom airfoil for the wing root can be found in [220], whereas the tail uses a standard NACA0012 symmetric airfoil. For both airfoils the polar corrections introduce a static lift deficiency at very high angles of attack near the onset of stall, and a slight corresponding pitching moment correction. For the root airfoil there is an offset of the zero-lift angle of attack to $-3.28°$.

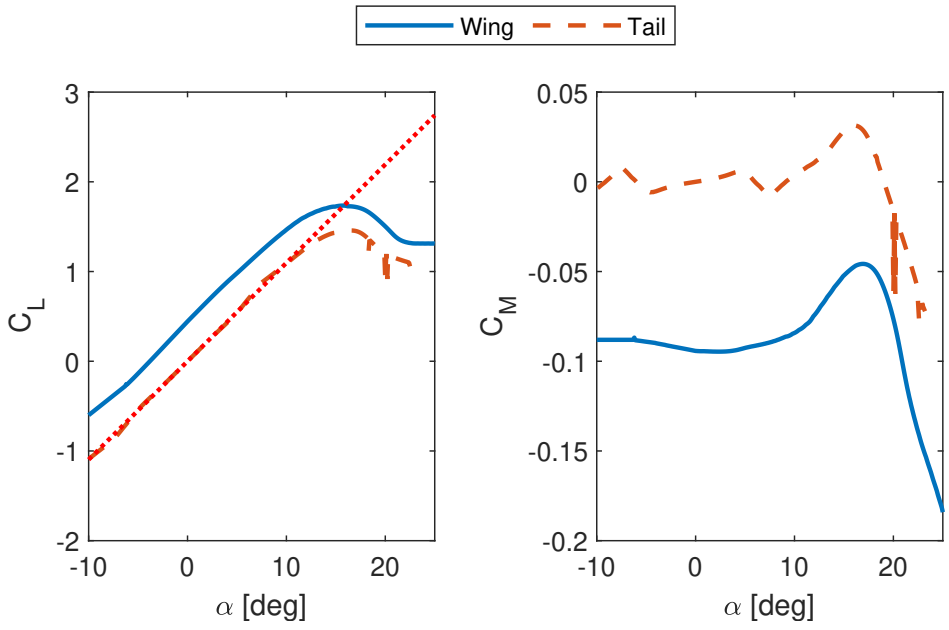


Figure 5.21: Lift and moment coefficient curves of the wing and tail airfoil for $\mathrm{Re} = 1.3 \times 10^6$

Primarily due to this offset to account for this asymmetric airfoil used in the wing, at same trim inputs as in Section 5.3.1 we are generating more lift on the wings. We have not retrimmed the aircraft to provide a like-for-like comparison to attribute differences in

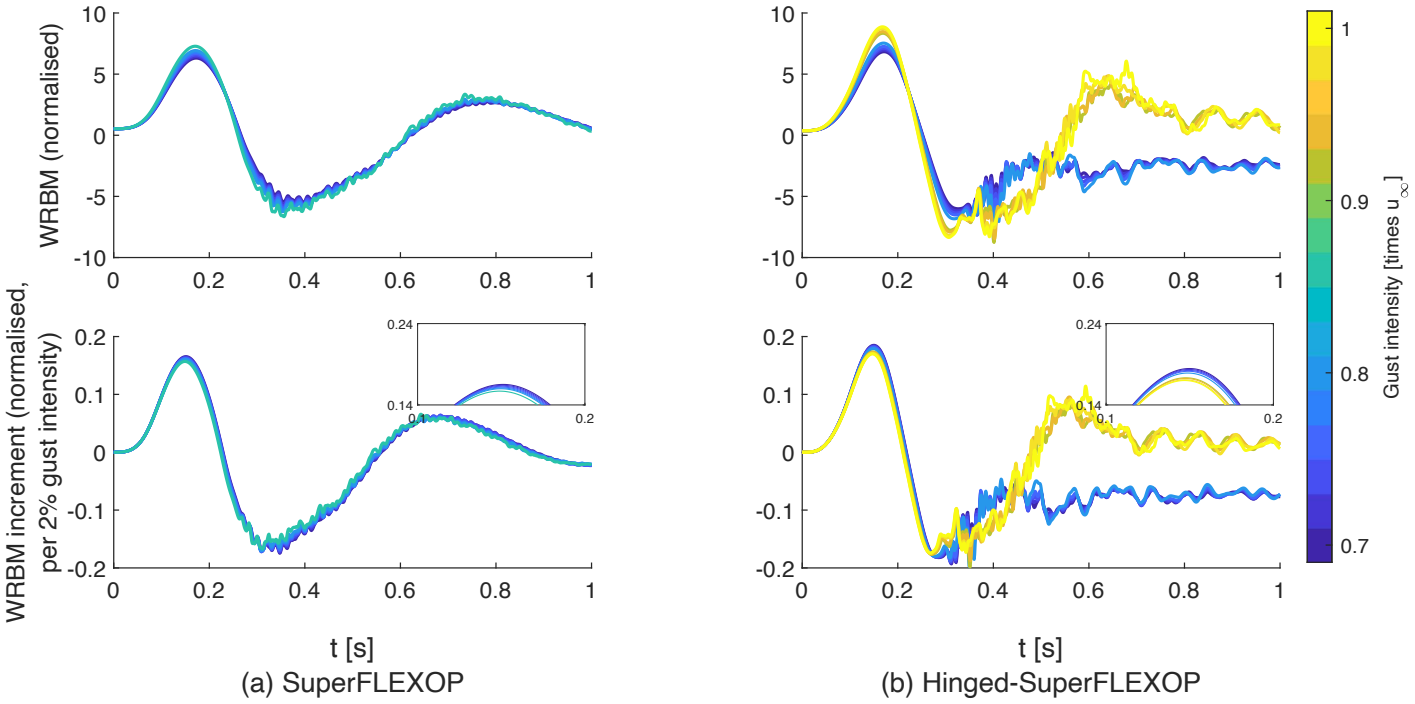


Figure 5.15: Time histories of normalised and incremental WRBM over a range of high gust intensities, $\bar{L}_g = 0.225$ s. Moment increment plots include inset with values near the first peak.

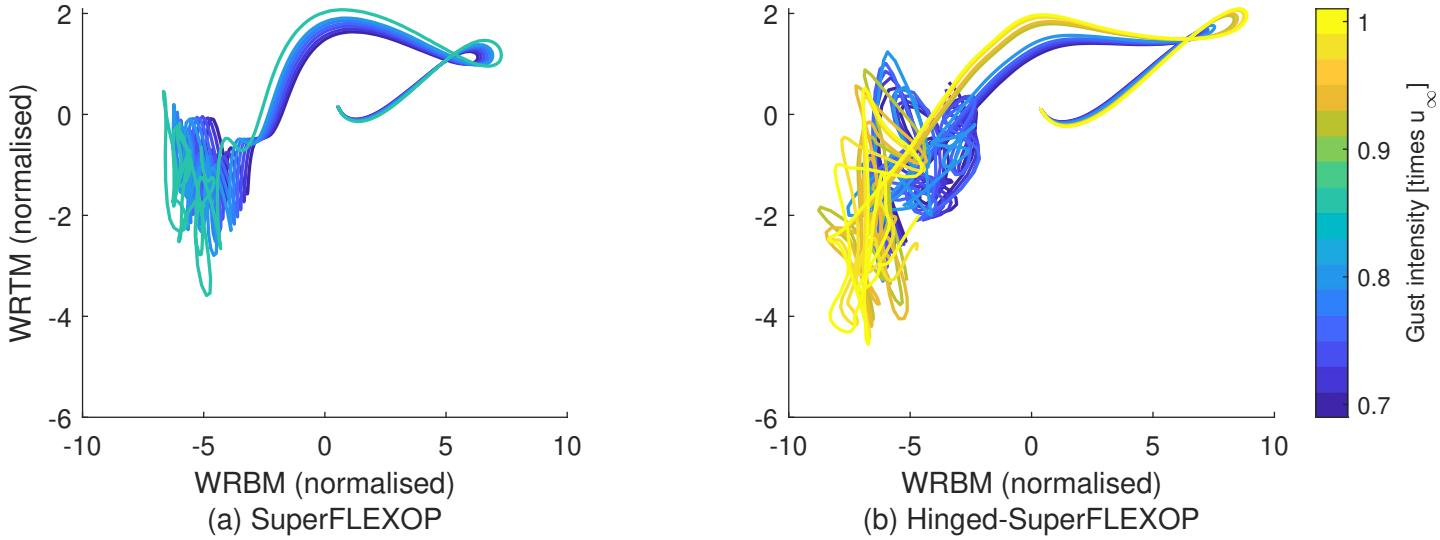


Figure 5.16: Instantaneous values of normalised wing root bending and torsional moment over a range of high gust intensities, $\bar{L}_g = 0.225$ s

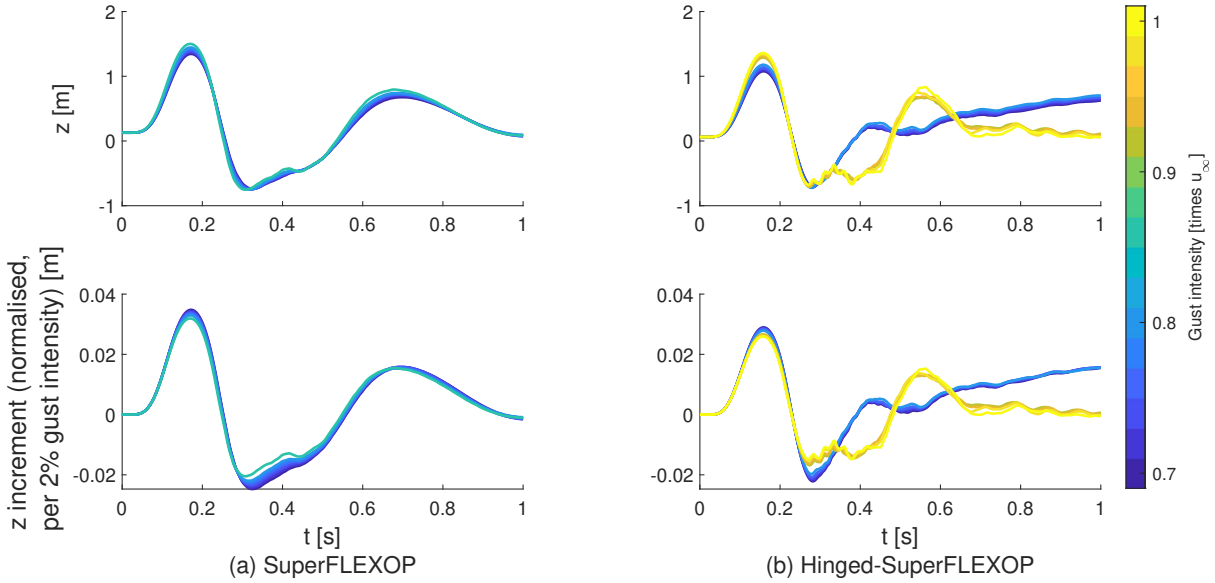


Figure 5.17: Time histories of vertical displacement at the 70% span station relative to the root over a range of high gust intensities, $\bar{L}_g = 0.225$ s

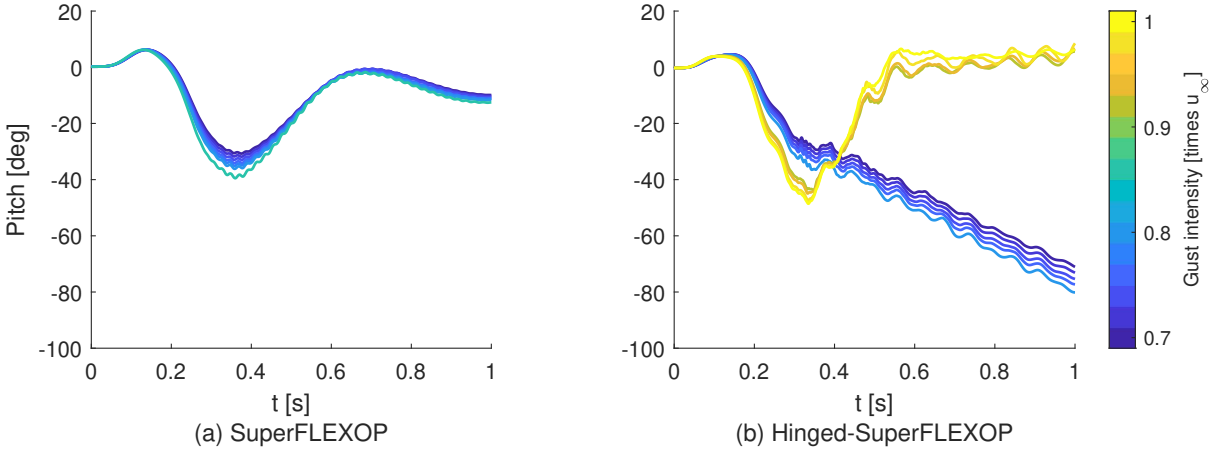


Figure 5.18: Time histories of aircraft pitch angle over a range of high gust intensities, $\bar{L}_g = 0.225$ s

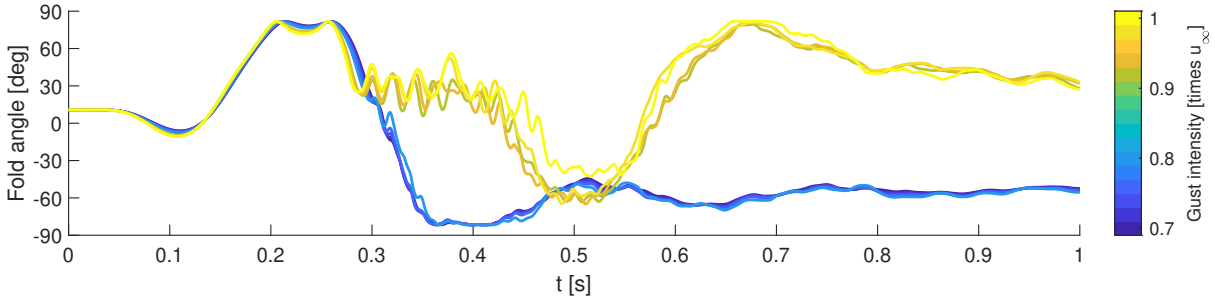


Figure 5.19: Time histories of hinge fold angle for the Hinged-SuperFLEXOP over a range of high gust intensities, $\bar{L}_g = 0.225$ s

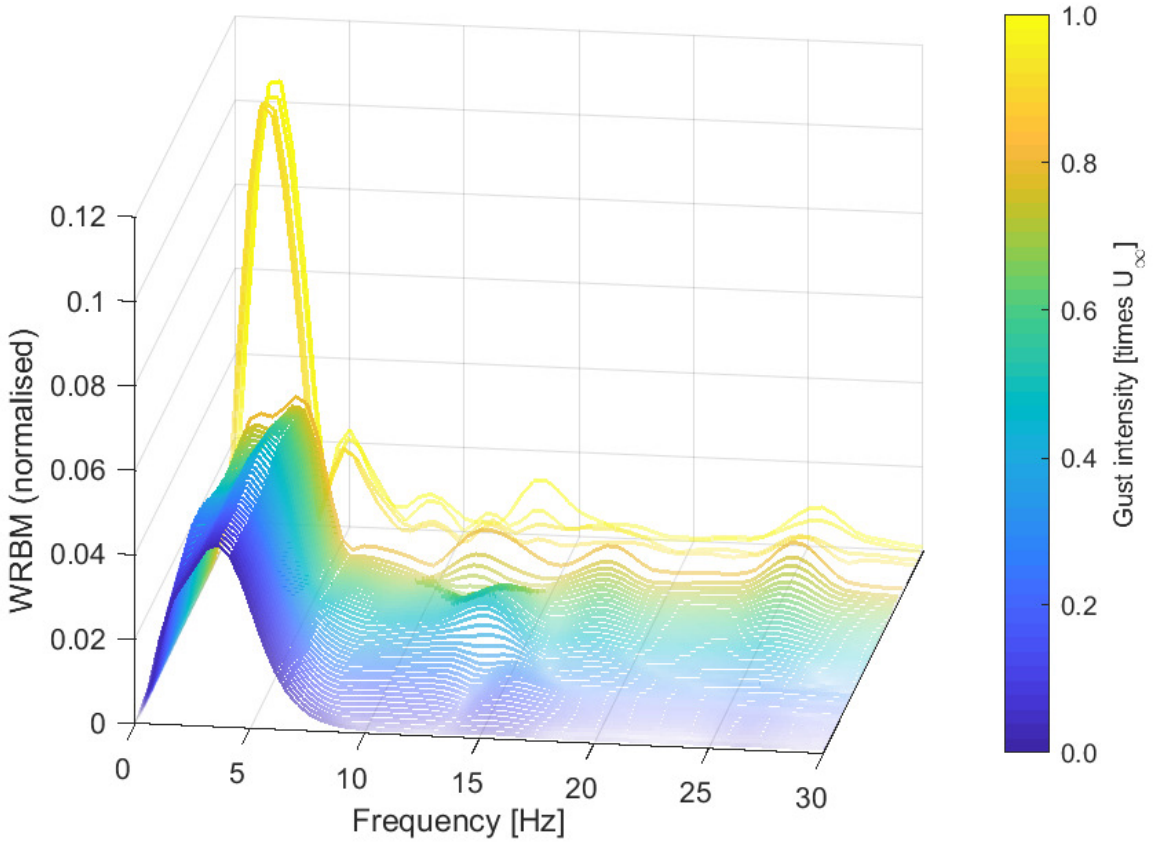


Figure 5.20: Single-sided amplitude spectrum of normalised WRBM for the Hinged-SuperFLEXOP over the full range of gust intensities, $\bar{L}_g = 0.225$ s. The jump at low frequencies occurs between $\bar{U}_g = 0.8$ and $\bar{U}_g = 0.92$

dynamics identified. The updated spanwise quantities are as given in Figure 5.22.

Inspecting the resultant plots reveals a vastly reduced number of cases presented, this time only up to $\bar{U}_g = 0.18$. This is due to the continuous pitching as identified earlier bringing the local angle of attack beyond the upper range of the tail airfoil polars provided. In Figure 5.23, the qualitative trends as identified in lower intensity cases in Section 5.3.1 are preserved, with the notable exception of lower WRBM increments for the Hinged-SuperFLEXOP, presumably due to the reduced shear load from the wingtips experience less lift, with the static stall model in operation at large swings of the wing tips. This is confirmed in Figure 5.27, where both the first positive and negative fold angle peaks are reduced compared to without the polar corrections applied. It is worth pointing out that the existence of each of the lines imply even at large magnitudes of fold angles, the local angle of attack remains within the range of the wing airfoil polars provided, precluding the highly nonlinear post stall and deep

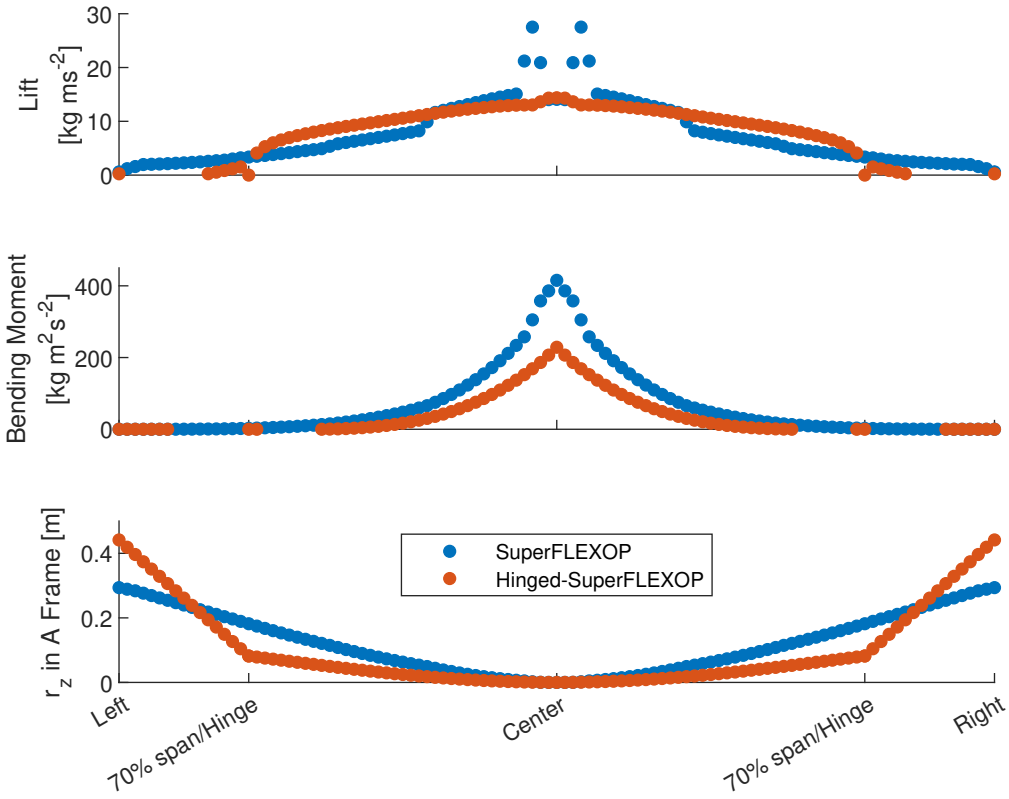


Figure 5.22: Spanwise quantities with polar corrections at gust onset for the SuperFLEXOP and Hinged-SuperFLEXOP

stall regions.

The elevated lift generated prior to the gust onset due to a negative wing zero-lift angle of attack manifests itself in the coupled rigid-body and aeroelastic response, more notably in the Hinged-SuperFLEXOP. Both of the aircraft has a tendency to flex downwards post gust onset as in Figure 5.25, and to pitch nose-up as in Figure 5.26, with the magnitude of both trends higher in the hinged variant. Closer inspection leads to the observation that increasing gust intensities, at least in the vicinity of the local equilibrium, leads to more flex up and pitch down behaviour, consistent with previous observations.

5.3.4 Effect of new trim inputs

For completeness we have also performed the same analysis with polar corrections, this time with new trim inputs duly computed. They are tabulated here in Table 5.3, alongside an update of the spanwise quantities in Figure 5.28. Compared with the original trim inputs presented in Table 5.2, the zero-lift angle of attack is now negative, reducing the trim angle of

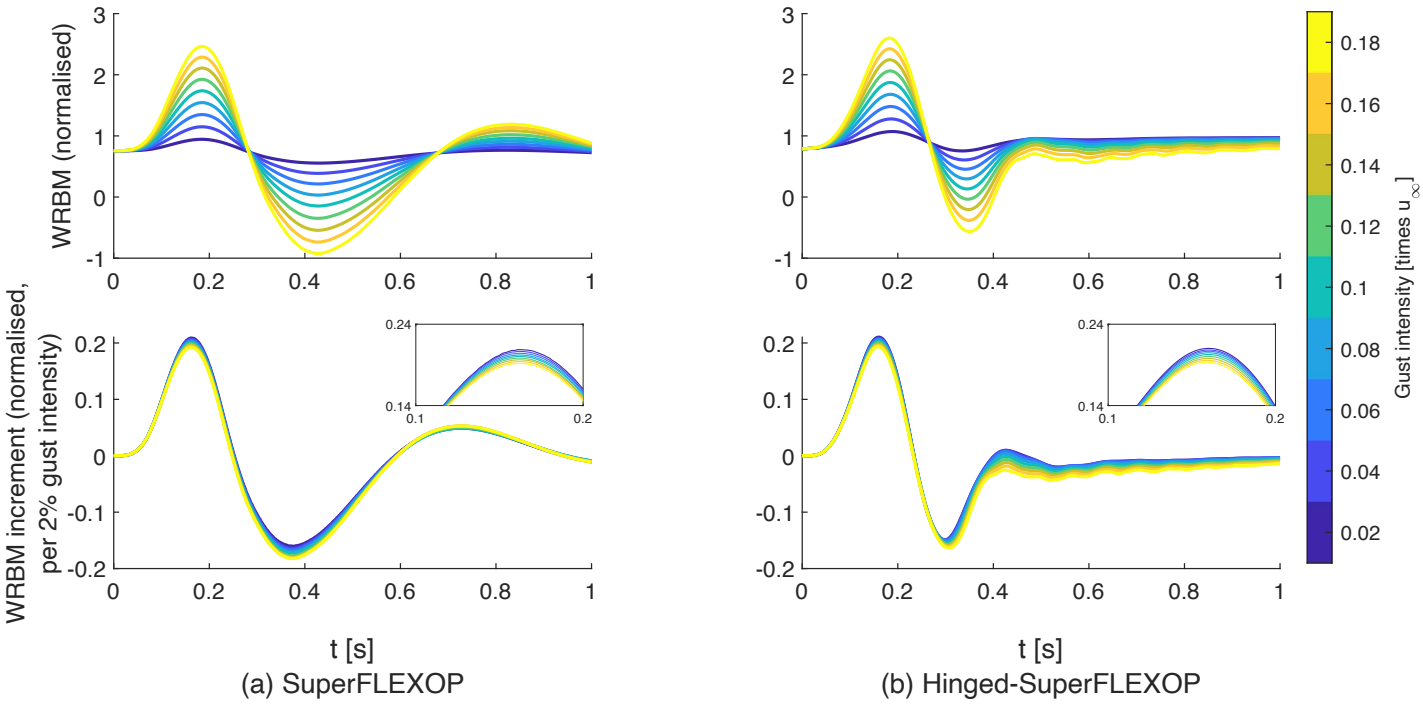


Figure 5.23: Time histories of normalised and incremental WRBM over a range of gust intensities with polar corrections, $\bar{L}_g = 0.225$ s. Moment increment plots include inset with values near the first peak.

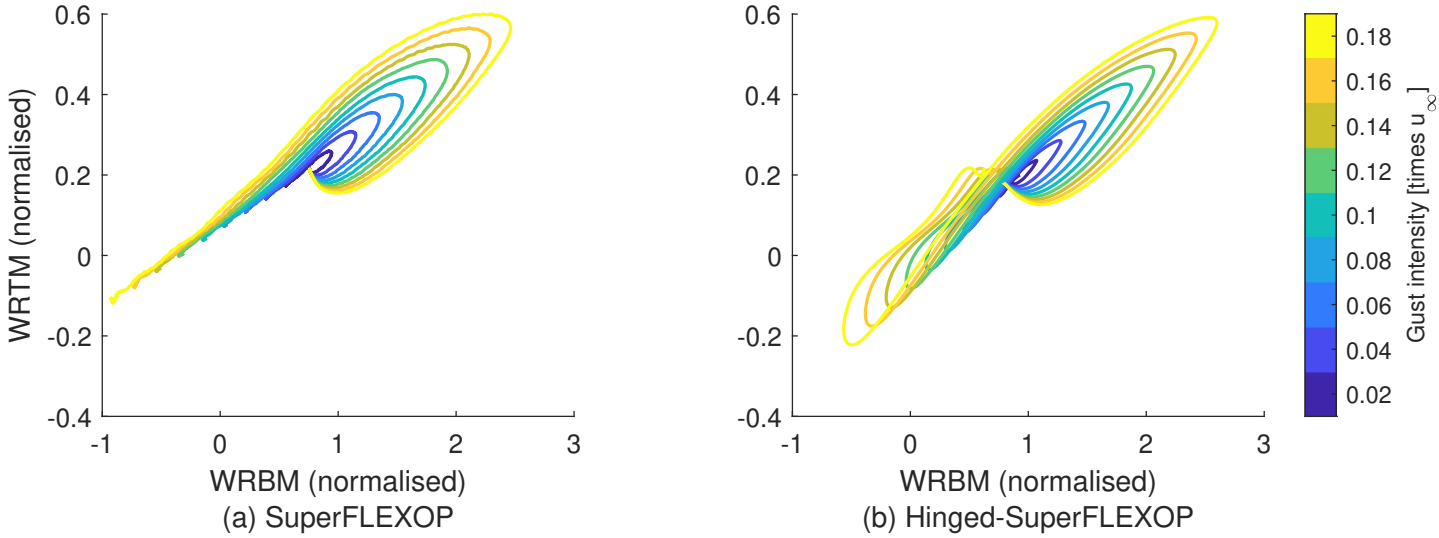


Figure 5.24: Instantaneous values of normalised wing root bending and torsional moment over a range of gust intensities with polar corrections, $\bar{L}_g = 0.225$ s

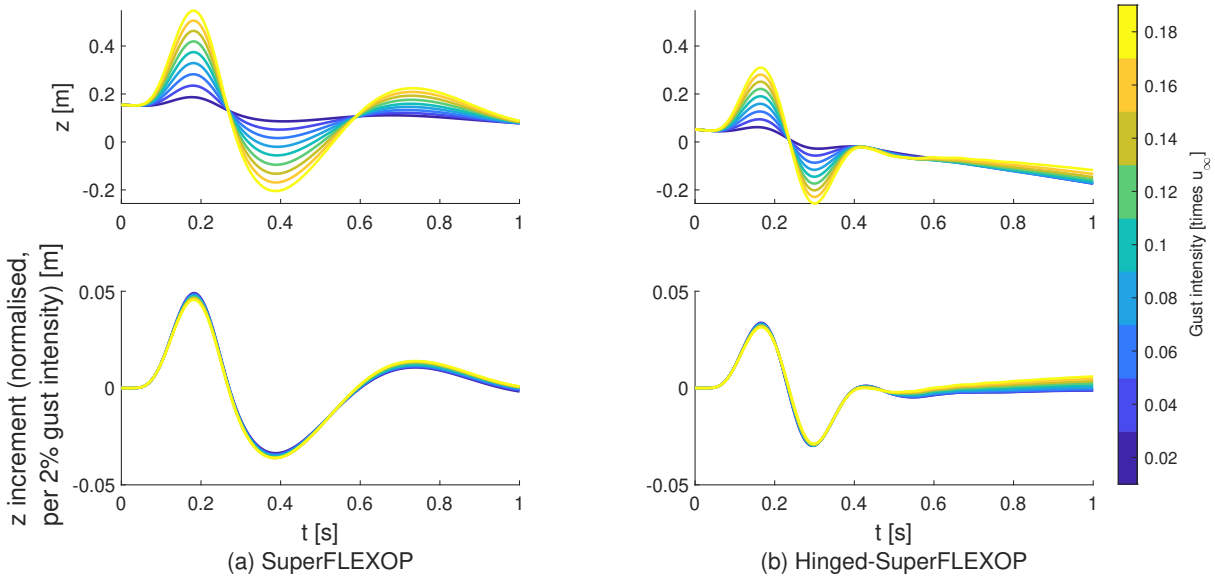


Figure 5.25: Time histories of vertical displacement at the 70% span station relative to the root over a range of gust intensities with polar corrections, $\bar{L}_g = 0.225$ s

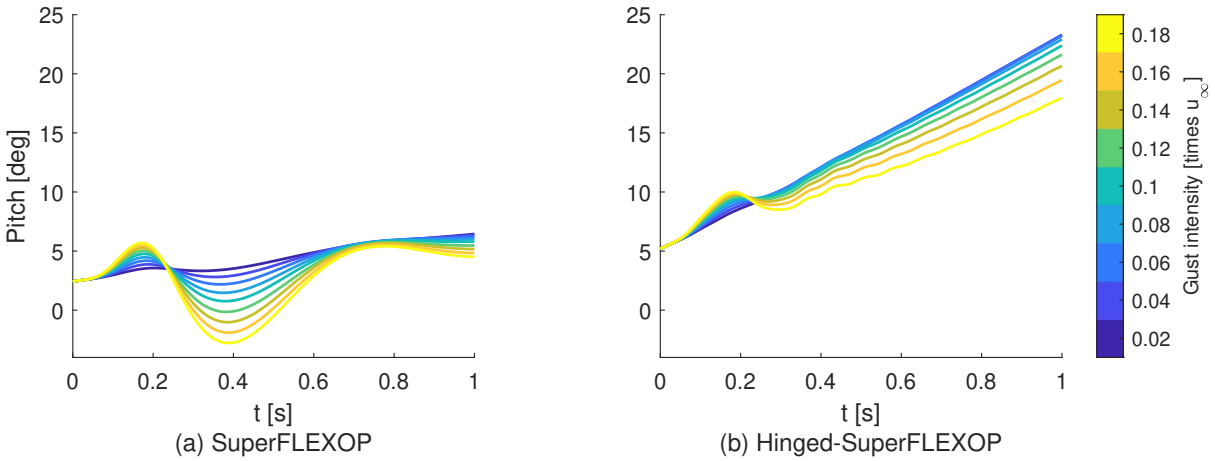


Figure 5.26: Time histories of aircraft pitch angle over a range of gust intensities with polar corrections, $\bar{L}_g = 0.225$ s

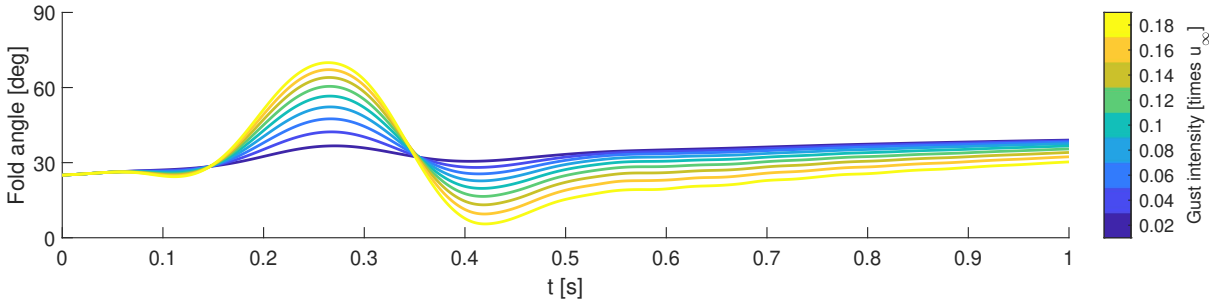


Figure 5.27: Time histories of hinge fold angle for the Hinged-SuperFLEXOP over a range of gust intensities with polar corrections, $\bar{L}_g = 0.225$ s

attack; the thrust required to balance the induced drag has increased, but remains negligible compared to the vertical lift-weight forcing and hence dynamics.

Table 5.3: Comparison of new trim inputs for SuperFLEXOP and Hinged-SuperFLEXOP with polar corrections

Values at trim	SuperFLEXOP	Hinged-SuperFLEXOP
Thrust [N]	28.7	30.1
Elevator [deg]	0.54	1.40
Angle of attack [deg]	-0.54	-0.54

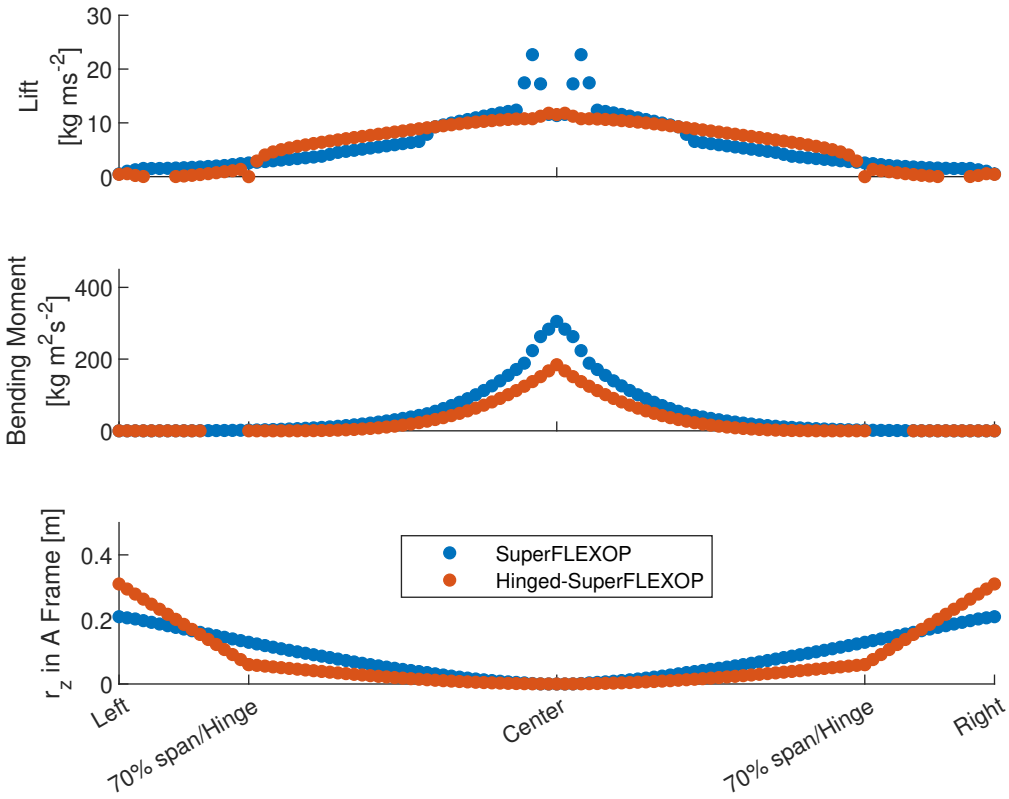


Figure 5.28: Spanwise quantities with polar corrections and new trim inputs at gust onset for the SuperFLEXOP and Hinged-SuperFLEXOP

Trends here to look for include a return of more gust intensity cases; the saturation of the interpolation range for the tail airfoil happens at higher intensities. The sensitivity of the WRBM increments in Figure 5.29 to initial conditions before trim is also noted; unlike in Section 5.3.3, here we see a return of higher increments for the Hinged-SuperFLEXOP.

As expected the flexing with time in the SuperFLEXOP is almost entirely eliminated in Figure 5.31, while that of the Hinged-SuperFLEXOP carries on to represent a developing non steady-level-flight behaviour. Perhaps curiously the quasi-steady pitching of the two aircraft diverges in sign; short-period oscillations are identified in pitch in the Hinged-SuperFLEXOP only. Otherwise polar corrections do not invite further nonlinear behaviour other than those already identified.

5.4 Concluding remarks

In trying to draw generalisations across the dynamics seen in the SuperFLEXOP configurations, either versus the HALE / H^{2}ALE, or more broadly for flexible aircraft featuring wings with flared, hinged wing tips, one has to be very cautious. Taking the former comparison as an example, despite the similar weight, the wing loading of the SuperFLEXOP is more than 10 times over the HALE, combining that with the wing sweep and taper, that leads to completely different qualitative behaviour of the wingtips during and after gust onset. However, commenting on the vehicle specific nonlinear dynamics identified will hopefully give confidence towards the framework, to be applied on the analysis of more industrially-relevant next generation aircraft.

The static bending moment reduction still is evident at trim for the SuperFLEXOP, but is quickly overshadowed by the dynamic gust induced loads and deflection which can be an order of magnitude higher at higher gust intensities. Due to the small trim loads WRBM increments for increasing gust intensities are often beneficial with geometric stiffening. Bending and torsional loads are highly correlated particularly at the first positive peak which is to be expected on a swept and tapered wing, mostly driven by lift from unsteady aerodynamics, with inertial effects taking over as we time march the system. On this aircraft the outsized forces and moments during gust encounters drives big swings in fold angles, unlike in the HALE / H^{2}ALE where large geometrical changes in a slender unswept rectangular wing meant after the first negative peak in fold angles, the washout induced is sufficient to damp the subsequent positive fold angle peak. For the SuperFLEXOP the impact of the wing tips dynamics on the aircraft level is secondary compared to the reciprocal effect, that keeps true with the introduction of sectional polar corrections as another source of nonlinearity, with the noted exception at higher gust intensities, of driving the coupled multibody system across a bifurcation point, triggering a jump to a distinct equilibrium branch. While the actual mechanism is not ascertained, the ability to model this at the current level of fidelity speaks volumes to the need for nonlinear analysis.

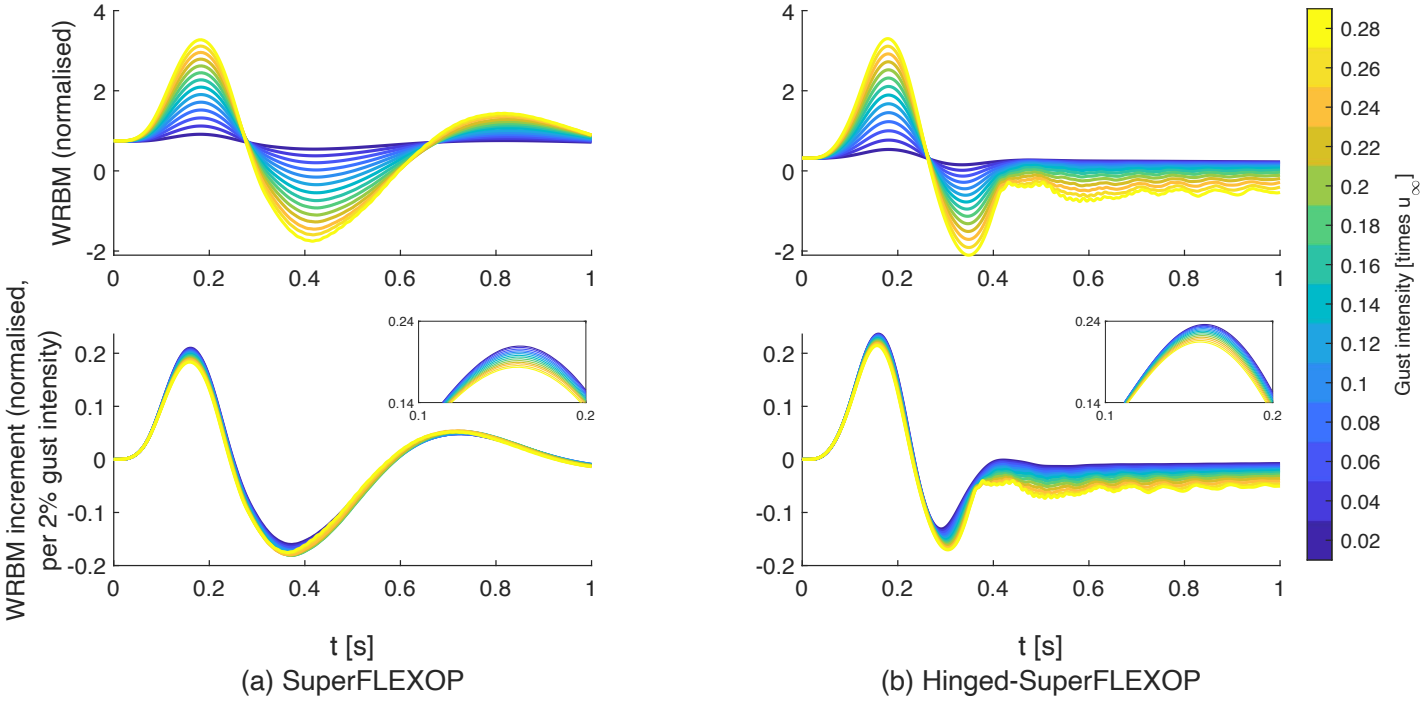


Figure 5.29: Time histories of normalised and incremental WRBM over a range of gust intensities with polar corrections at new trim inputs, $\bar{L}_g = 0.225$ s. Moment increment plots include inset with values near the first peak.

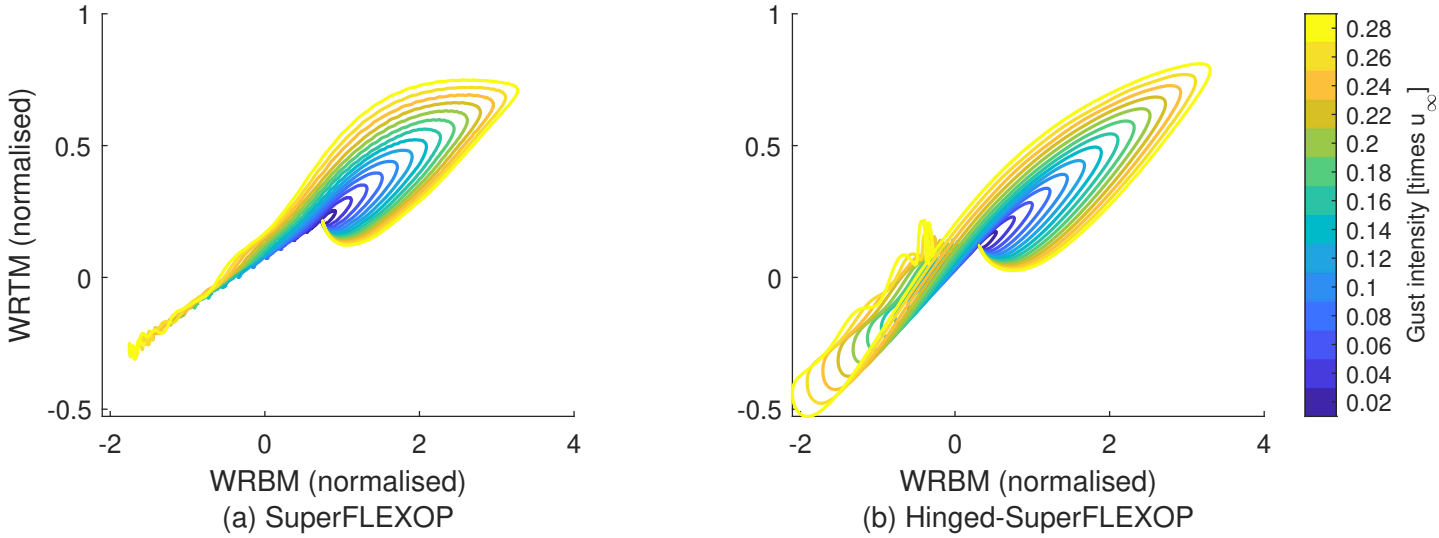


Figure 5.30: Instantaneous values of normalised wing root bending and torsional moment over a range of gust intensities with polar corrections at new trim inputs, $\bar{L}_g = 0.225$ s

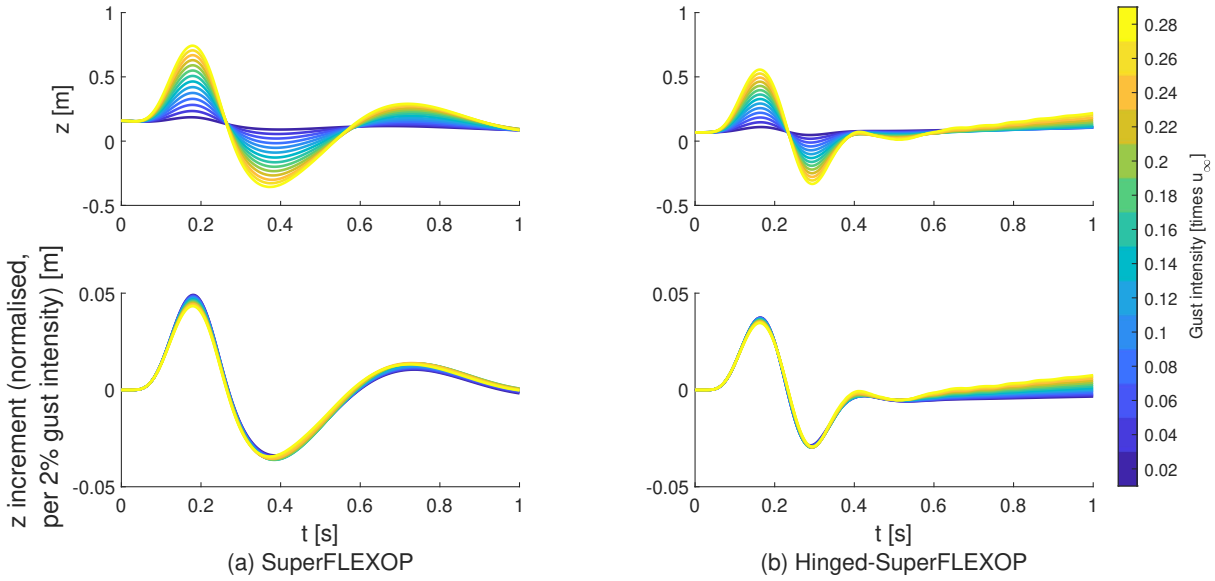


Figure 5.31: Time histories of vertical displacement at the 70% span station relative to the root over a range of gust intensities with polar corrections at new trim inputs, $\bar{L}_g = 0.225$ s

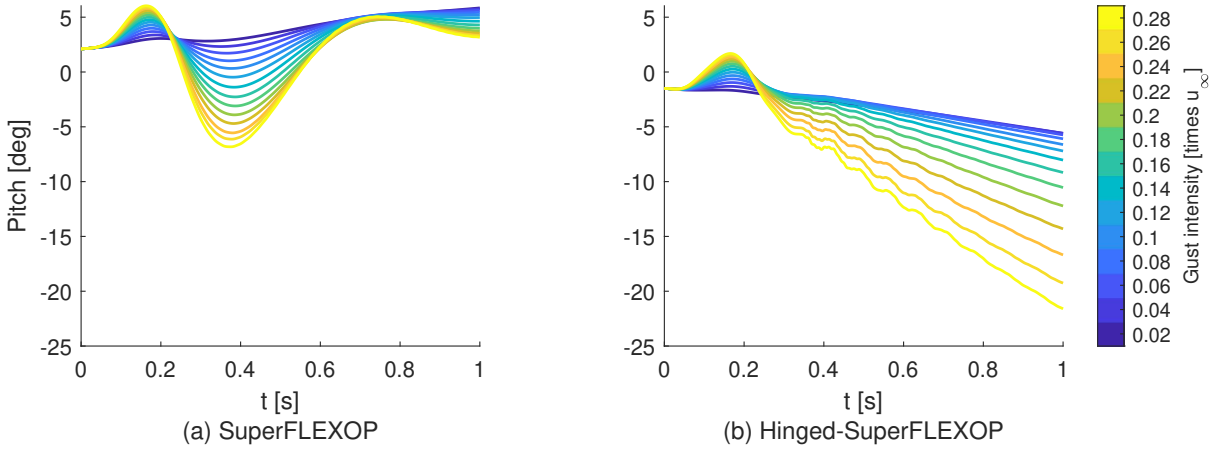


Figure 5.32: Time histories of aircraft pitch angle over a range of gust intensities with polar corrections at new trim inputs $\bar{L}_g = 0.225$ s

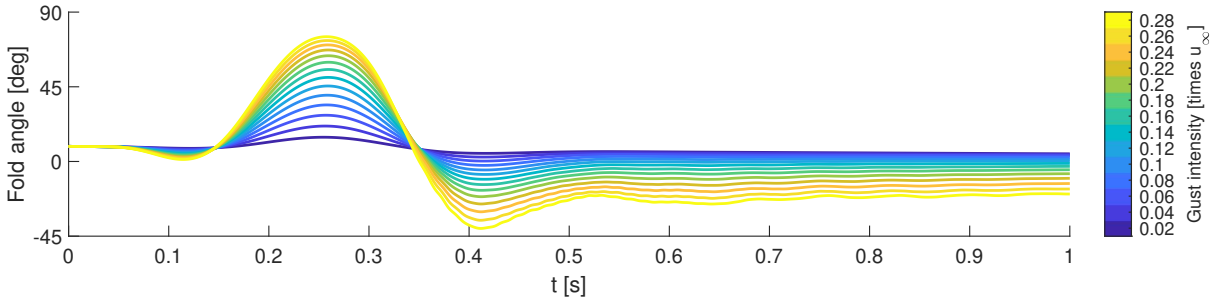


Figure 5.33: Time histories of hinge fold angle for the Hinged-SuperFLEXOP over a range of gust intensities with polar corrections at new trim inputs, $\bar{L}_g = 0.225$ s

The SuperFLEXOP is also very flexible at higher loads; at peak gust encounter deflections at 70% span / hinge position exceeds 30% at the highest gust intensities. The role of the hinge as a local discontinuity in stiffness on a already-flexible representative aircraft was explored by comparing the SuperFLEXOP with the Hinged-SuperFLEXOP; it is found that the wingtip response, moderated by the flare angle, in time domain and out of phase with the wing response, can be critical to the expected load alleviation characteristics.

The study described in this Chapter demonstrates the applicability of the developed coupled aeroelastic formulation on a representative next-generation platform, revealing an emergent pitchfork bifurcation as gust intensity increases. Whereas vehicle-specific understanding of resultant coupled dynamics might not be transferable to a given industrially-relevant design, the various assumptions in modelling of the coupled physics, in UVLM unsteady aerodynamics for lower-speed flight points, nonlinear multibody beam theory for large constrained deflections and rotations, and rigid-body flight dynamics coupling would hold. Future work should examine the physics expected with the specific aircraft configuration at targeted design conditions, and reconcile that with the appropriate selections, based on fidelity and modelling assumptions, for subdiscipline solvers, with enhancements in architecture enabling upstream and downstream propagation of multiphysics simulation in the design cycle.

Chapter 6

Conclusion

This final chapter will wrap up this thesis and to summarise the work that has been presented, mark the key contributions, and to provide recommendation for future work. We started off with the drive towards net-zero and the role of aeroelasticity in the pursuit, then the methods and advancements enabling the analysis of flexible aircraft with multibody mechanisms, converging on verification and validation studies for the flared hinged wingtips, and aircraft level evaluation of coupled aeroelasticity and flight dynamics in various configurations that pushes the boundaries of nonlinear modelling.

6.1 Summary

Chapter 1 has established the context for this thesis by first motivating the paradigm shift towards novel aircraft configurations, specifically high aspect-ratio wings equipped with flared hinge wingtips, to meet the aviation sector's net-zero 2050 commitments. Through a literature review spanning the historical evolution and renewed relevance of these biomimetic designs, we highlight their functional imperative of gate-width compliance and potential in passive gust load alleviation. Subsequently, the implications of such designs on numerical modelling are addressed, underscoring the necessity of geometrically nonlinear frameworks. This leads to an assessment of state-of-the-art methods for resolving coupled aeroelasticity and flight dynamics in time-domain simulations. Gaps in existing simulation capabilities for free-flying, flexible multibody wings are identified, informing the research objectives involving the integrated nonlinear coupled aeroelastic solver presented in this work.

Chapter 2 then has taken on the task to establish the theoretical foundations for a flexible multibody formulation that employs geometrically-exact composite beam theory and La-

grange multipliers to capture nonlinear structural dynamics in the time domain. The flared hinge connection is modelled with linear and angular velocity constraints, allowing rotation about the specified hinge axis as the only degree of freedom. The staged validation process begins with idealised test cases, such as the rigid double pendulum, and systematically progresses to flexible benchmark problems and comparisons against established commercial codes. Through these benchmarks, the framework demonstrates robustness across a range of structural configurations even in highly flexible regimes, providing a platform on which unsteady aerodynamics are coupled for analysing relevant flexible aircraft architectures.

Chapter 3 has further presented and validated a strongly coupled aeroelastic formulation integrating flexible multibody structural dynamics with unsteady aerodynamics through the Unsteady Vortex Lattice Method (UVLM), to capture time-domain aeroelastic behaviour in next-generation aircraft featuring large structural deformations and complex hinge kinematics. Specifics of the implementation address challenges to modelling, including a skewed UVLM grid boundary at the flare-angled hinge line to maintain the aero-structural interface during wingtip rotations, as well as static and dynamic trim strategies to determine the equilibria of flexible multibody wing assemblies. Validation through simulations of a highly flexible flared hinged wing demonstrates successful capture of the relevant dynamics, while comparisons against existing numerical and experimental data confirm the model's ability to accurately predict equilibrium quantities and limit cycle oscillations, paving the way to full aircraft level analysis.

Chapter 4 has applied the verified nonlinear flexible multibody aeroelastic formulation to model and analyse the coupled flight dynamics and aeroelasticity of a representative High-Altitude Long-Endurance aircraft equipped with flared hinged wingtips, demonstrating through time-domain simulations with multi-parameter sweeps that the hinge mechanism achieves substantial static wing root bending load alleviation in vertical gust encounters, where in all cases computed they are comparable to fixed upturned wing tip configurations, i.e., the increase in span with the free wing tips do not come with a wing root bending moment penalty. In addition, dynamic load alleviation capabilities are exhibited particularly in longer gust encounters through wingtip flapping motion that introduces aerodynamic damping. Sensitivity analyses confirm the strong dependence of dynamic wing root bending moment savings on wing flexibility, with stiffening severely diminishing load alleviation benefits and revealing that both main wing flexibility and the hinge mechanism are necessary, while design parameters such as wingtip inertia and flare angle influence loads with a maximum bending moment turning point. The analysis for lateral gust confirmed increased roll damping in the hinged configuration, bearing in mind these trends are highly specific to this

ultra-high-aspect-ratio aircraft.

Chapter 5 has showcased the application of the flexible multibody aeroelastic framework to a derivative model of a representative next-generation platform previously verified, tested and flown. The SuperFLEXOP and Hinged-SuperFLEXOP configurations demonstrates the framework's capability to model highly flexible aircraft subject to complex, nonlinear dynamics under extreme gust loading, with the hinged variant exhibiting substantial reduction in static wing root bending moment at trim through inboard lift shifting and confirming dynamic gust load alleviation potential as evidenced by lower maximum positive and negative bending moments across various gust lengths and successful removal of the second positive peak at critical gust length. Geometric stiffening and the resultant load relief is identified as the probable mechanisms driving load alleviation. Vehicle-specific nonlinear dynamics are uncovered including a bifurcation point at gust intensities above a critical threshold, where the coupled multibody system suddenly transitions to a distinct quasi-steady equilibrium branch resuming steady level flight, diverging from coupled rigid-elastic behaviour at lower intensities. Incorporation of sectional polar corrections as an additional nonlinearity confirms the qualitative trends identified are not a strong function of moderate aerodynamic nonlinearities, although the impact of the highly nonlinear post-stall region is out of the scope of the analysis. The numerical framework developed in this work proves to be efficacious for the analysis and design maturation of next-generation aircraft featuring flared hinged wingtips, lifting the veil on the nonlinear aeroelastic behaviour to be understood, for progress in sustainable aircraft design.

6.2 Key contributions

Implementation and validation of the flexible multibody aeroelastic formulation

The core contribution of this work is the implementation, validation, and demonstration of a flexible multibody aeroelastic formulation. This framework addresses the need for nonlinear analysis of next-generation sustainable aircraft configurations, such as aircraft with flared hinged wingtips with which complex aeroelastic phenomena driven by large displacements and rotations render standard linear tools insufficient. To the best of the author's knowledge, the flexible multibody time-domain aeroelastic formulation within the open-source SHARPy simulation toolbox contributes to the state-of-the-art. Specifically for simulations on aircraft with flared hinged wings, the UVLM implementation with a force-free wake allows for native cross-coupling of unsteady effects in the wings, wingtips and tailplane, whereas the coupled nonlinear rigid-body-structural formulations allows for large deflections and rotations. A

hybrid trim approach allows for direct comparisons of the gust response of the continuous cantilever and hinged aircraft layouts, effectively isolates the nonlinearities under investigation.

The formulation is put to test with a hierarchical validation process, confirming its validity across varying stiffness regimes. This is first verified against the equations of motion for a rigid slanted-hinge double pendulum. By testing across flare angles bounded by the special cases of $\beta = 0°$ (double planar pendulum) to $\beta = 90°$ (single pendulum), the work demonstrated exact agreement with analytical Lagrangian mechanics. The framework was also put to test with a published flexible crossbeam. In the final stage, the fully coupled aeroelastic model was tested against literature for flexible flared hinged wing assemblies. The model accurately predicted the nonlinear dynamics present, including static equilibrium fold angles and limit-cycle oscillations. This can be readily deployed, with the appropriate pre- and post-processing, on industrial models to better support multibody aircraft design decisions.

Characterisation of load alleviation mechanisms

The second principal contribution of this work pertains to the characterisation of load alleviation mechanisms arising from the interaction between structural flexibility and multibody kinematics in aircraft featuring flared hinged wingtips. Through parametric studies conducted using the developed computational framework, this research reveals the nonlinear relationships between wing design parameters, flight conditions, and the resulting dynamics experienced during gust encounters. These findings inform the physical mechanisms responsible for load alleviation, which will feed into the selection of design parameters to optimise performance across multiple objectives including but not limited to structural efficiency, stability, and handling qualities.

The HALE aircraft studies demonstrate that the presence of flared hinged wingtips alters both the static and dynamic load distribution along the wing. In steady level flight trim conditions, the introduction of free-to-rotate wingtips with even modest flare angles results in reductions in wing root bending moment, compared to a baseline configuration with rigidly attached wingtips. This static load alleviation effect stems from the equilibrium fold angle, which positions the wingtip aerodynamic surfaces at reduced effective angles of attack relative to the freestream. The spanwise redistribution of lift that accompanies this shifts the centre of pressure inboard, thereby reducing the moment arm of aerodynamic forces about the wing root. The magnitude of this effect is found to be a function of the hinge flare angle, with positive flare angles (hinge axis towards inboard-aft) slightly degrading load re-

lief up to a threshold value, beyond which further increases in flare angle produce only a modest improvement, indicating a near-saturation in performance. Importantly, this static load alleviation is achieved passively, without requiring active control inputs, exploiting the natural equilibrium of aerodynamic forces and geometric constraints imposed by the hinge mechanism.

When subjected to transient disturbances such as discrete vertical gusts, the aircraft with hinged wingtips exhibit dynamic load alleviation characteristics that differ from those of baseline configuration. The dynamic response is a result of inertial effects, elastic deformations, and multibody constraints acting across multiple time scales. Immediately following gust encounter, the wing assembly undergoes rapid upward bending driven by the sudden increment in aerodynamic loading. The wingtip masses initially lag behind this bending motion due to their inertia, causing transient fold angle excursions that temporarily alter the geometric angle of attack distribution along the outboard wing sections. As the wing reaches its peak upward deflection, the wingtips experience significant forcing that drives them towards increased fold angles, flapping upwards relative to the main wing. The restoring moment provided by the flare geometry eventually reverses the upward flapping motion, leading to oscillatory wingtip dynamics that gradually decay through aerodynamic damping. This sequence of events results in a characteristic time history of wing root bending moment featuring an attenuated first positive peak, followed by more complex transient behaviour involving interactions between structural bending modes, wingtip flapping modes, and rigid-body longitudinal dynamics.

The effectiveness of dynamic load alleviation is found to depend on several configuration parameters and gust characteristics. More flexible configurations generally exhibit greater load relief due to geometric stiffening effects, and the ability of elastic deformations to couple with and dissipate energy from excited rigid-body modes through phase-delayed aerodynamic transfer. Conversely, stiffer wings tend to respond in a nearly rigid fashion, where the benefits of wingtip articulation are diminished because the main wing does not undergo sufficient deformation to produce favourable coupling with the multibody degrees of freedom. The ratio of wingtip mass to total wing mass also influences the dynamic response, with lighter wingtips reacting more quickly to changes in aerodynamic loading but potentially introducing higher-frequency oscillations that can complicate the coupled dynamics. Heavier wingtips, while exhibiting more sluggish initial response, provide inertial damping that can attenuate subsequent transient oscillations. The hinge flare angle affects dynamic load alleviation in a more nuanced manner than its influence on static loads. While positive flare angles remain beneficial overall, there exists a trade-off where larger flare angles provide stronger restoring

moments that limit maximum fold angle reached during a transient perturbation, but also increase the coupling between bending and torsional loads that can lead to higher torsional moments at the wing root. Negative flare angles, i.e., with the hinge axis oriented outboard-aft, are found to produce unfavourable dynamics characterised by an inward-folding wingtip equilibrium position that exacerbates rather than alleviating wing root loads.

The SuperFLEXOP-based studies extend these findings to a configuration more representative of unmanned aerial vehicles designed for aeroelastic research. The SuperFLEXOP model, with its scaled-down stiffness properties, exhibits coupled aeroelastic and flight dynamic behaviour that differs from the HALE configuration in several respects. Introduction of flared hinged wingtips at seventy percent span produces the anticipated reduction in wing root bending moment at trim, though the relative magnitude of this benefit is quite smaller than observed for the HALE case. Dynamic gust response analysis reveals that the Hinged-SuperFLEXOP exhibits peak sensitivity at a shorter relative normalised gust length than its HALE counterpart. The coupled pitch and bending dynamics are more pronounced in the SuperFLEXOP configuration, with gust-induced pitch excursions in the open-loop bringing the aircraft to a stall / dive.

Assessment of nonlinearities in full aircraft dynamic response

The nonlinearities appear as non-proportional changes in loads and motion as hinge geometry, structural flexibility, mass distribution, and gust characteristics vary, as described under the preceding header.

When perturbations about a steady operating point are modelled in a fully coupled, multidisciplinary nonlinear framework, the response typically departs from a linear "scaled-baseline" prediction and instead exhibits richer, strongly time-dependent behaviour. Cross-disciplinary interactions introduce feedback pathways that modify the effective loads and the instantaneous dynamics; these effects depend on the combined influence of design variables, geometry, mass distribution, and material properties, and are therefore difficult to isolate. Increased structural flexibility (where multibody mechanisms like hinges function as local discontinuities in stiffness) generally amplifies these interactions by strengthening aeroelastic coupling, promoting larger deformation-induced changes in loading, and enabling energy exchange between modes. Nevertheless, this work makes a best-faith effort to isolate individual effects where feasible and to attribute the governing physical mechanisms as seen in Chapters 4 and 5.

An important observation emerging from both case studies is the presence of nonlinear effects that manifest at higher gust intensities. As deflections and fold angles increase, geometric nonlinearities associated with the large-rotation kinematics of the beam formulation become significant, leading to stiffening behaviours that cause the incremental load per unit gust intensity to decrease rather than remain constant. Additionally, interactions between the deformed wake geometry and the lifting surfaces introduce aerodynamic nonlinearities that influence the pressure distribution in ways not captured by linearised theories. These nonlinear mechanisms can be beneficial from a structural loads perspective, as they provide extra margins of safety that becomes active when loads approach critical values. An example of which comes to be the bifurcation in wing tip dynamics observed at higher gust intensities in the Hinged-SuperFLEXOP. At elevated gust intensities, the aforementioned loss in pitch stability gives way to a new equilibrium branch of returning to steady level flight. However, they also complicate the design process by annulling extrapolation from low-gust-intensity cases, thereby necessitating high-fidelity nonlinear analyses of the type enabled by the present framework.

Aerodynamic nonlinearities associated with viscous effects were also explored by enabling sectional polar corrections; this is necessarily because the underlying UVLM formulation represents unsteady, incompressible inviscid flow. Such polar-based corrections can introduce lift decrements near stall onset (and associated moment changes) and can influence predicted dynamics, as seen in the accurate prediction of the LCO response in Section 3.4, or more generally when large effective angles of attack occur.

In the full aircraft simulations, however, the qualitative time-domain trends identified without polar corrections were largely preserved: the dominant differences remained driven by the coupled rigid-body–flexible dynamics and the hinge-mediated multibody response, rather than by additional aerodynamic nonlinearity. Modest quantitative shifts such as reduced WRBM increments and reduced fold-angle peak magnitudes have not translated into nonlinear paradigm shifts, i.e., new nonlinear behaviour beyond that already observed in the baseline nonlinear coupled response, which remain to be explored in future work.

6.3 Future work

Incorporation of aeroelastic considerations early in the design cycle

The current framework operates primarily as an analysis tool for evaluating aircraft configurations that have already been defined through conventional design processes. To unlock the full potential of the hinged wingtip paradigm, aeroelastic considerations must be integrated into design decisions at the conceptual and preliminary design stages, where major trades between wing geometry, stiffness, mass distribution, and hinge parameters are established. This requires continuous improvement and optimisation of the runtime of the core nonlinear aeroelastic multibody solver within a comprehensive multidisciplinary design and optimisation (MDO) environment. An example of the state-of-the-art can be found here [224].

The path toward MDO integration involves several checkpoints. Firstly, sensitivity analysis capabilities could be implemented to enable computation of gradients relating design outputs (such as wing root bending moments, deflections, and flutter margins) to design variables. Secondly, reduced-order models and surrogate approaches should be developed to accelerate design iterations, allowing sweeping of the design spaces without the computational burden of many fully nonlinear transient simulations. Methods like Gaussian process surrogates, polynomial response surfaces, or neural network models could support rapid design trades and optimisation. Thirdly, automated workflows can codify the process of translating aircraft specifications (target wing loading, cruise altitude, payload requirements) into detailed aeroelastic models compatible with the simulation framework, eliminating the manual overhead that currently restricts design study frequency. SHARPy benefits from a compartmentalised approach to discipline solvers and mature data-passing interfaces to couple with other tools. Through these developments, the hinged wingtip can be optimised monolithically alongside other design variables, enhancing structural efficiency and aerodynamic performance.

Manoeuvre loads and edges cases

While the thesis focuses on low-speed steady-level flight conditions, comprehensive aircraft design and certification demands analysis right to the edge cases of loading conditions. The nonlinear multibody framework should be extended to model the physics at those boundaries that drive structural design and must be considered during certification.

Manoeuvre analysis to certification requirements requires assessment of aircraft response

to aggressive control inputs, such as maximum control deflection pulls and lateral-directional manoeuvres that establish critical design loads. For hinged wingtip configurations, manoeuvre loading is even more important because control inputs that command large attitude changes induce inertial loads that drive geometric nonlinearities and large rotations in fold angle, with conflicting literature [118, 119, 225] on the influence of wingtips on for example roll dynamics of the aircraft.

Beyond standard manoeuvres, edge cases including flutter / LCO onset, hinge mechanism failure / delay in release, landing, et cetera, should be characterised across the flight envelope. The nonlinear nature of the coupled system means that flutter boundaries may exhibit dependence on amplitude, hinge deflection state, resulting in some cases subcritical LCOs. Traditional linear flutter analysis may fail to capture phenomena such as flutter-triggering gust encounters or complex bifurcations in the nonlinear dynamics. Future work could employ continuation methods and bifurcation analysis to map the full nonlinear stability landscape, identifying regions where the hinged wingtip mechanism induces unexpected instabilities or benefits. Flutter and limit cycle oscillations should be characterised to establish safe operating regions and understand the limits of safety of the flexible hinge mechanism.

Inclusion of more unsteady aerodynamic nonlinearities across the flight regime

While the current UVLM formulation with sectional polar corrections performs well for low-speed and high-altitude long-endurance (HALE) applications, most next-generation aircraft operate in the transonic regime where the static stall model and CFD-derived lift, drag, and moment curve corrections are not sufficient. Future work should extend aerodynamic fidelity with

- Compressibility corrections: Implementation of compressibility corrections (e.g., Prandtl-Glauert, or Laitone rule) to the UVLM would extend the validity of predictions, conservatively to aircraft cruising up to around Mach 0.5. This will not be valid for transonic regimes where shock-induced flow separation and shock-boundary layer interactions become dominant physical phenomena that cannot be captured by potential flow methods.

- Dynamic stall model: The UVLM can be improved by incorporating semi-empirical stall models to better capture time-dependent aerodynamic forces during unsteady motion. When coupled with dynamic stall corrections (such as Beddoes-Leishman or ONERA models), UVLM improves predictive accuracy for rapid manoeuvres and gust encounters. While useful for preliminary design and aeroelastic analysis, inviscid

methods fundamentally cannot resolve viscous separation physics in aggressive post-stall regimes.

- Higher-fidelity aerodynamic coupling: For configurations where viscous effects, separation, or transonic phenomena dominate, coupling with higher-fidelity aerodynamic solvers (vortex particle methods with CFD-informed kernel functions, or reduced-order CFD models) would be warranted. The coupling framework could support multi-fidelity approaches where regions of the design space prone to separation, e.g. near the hinge axis, or closer to the tip of the wingtips, could invoke higher-fidelity aerodynamic analysis while regions of well-attached flow use the computationally efficient UVLM.

- Wind Tunnel and CFD Validation: The current validation efforts should be extended to include wind tunnel data and CFD comparisons, particularly for configurations with large hinge deflections and rates where nonlinear aerodynamic effects become significant. Experimental validation of sectional polars used in corrections would also strengthen confidence in polar-corrected UVLM predictions.

Linearisation at nonlinear equilibrium for quick characterisation of dynamics

Whilst nonlinear simulation provides time-accurate predictions of aircraft response to specific gust encounters and/or manoeuvres, the frequency-domain perspective offered by linear analysis remains invaluable for physical insight. Future work should develop procedures to linearise the coupled multibody-aerodynamic system about nonlinear equilibrium conditions, enabling linear modal and frequency response analysis that captures how equilibrium state influences stability and dynamic response characteristics.

At each operating point, eigenvalue analysis of the linearised system would reveal how natural frequencies, mode shapes, and damping characteristics evolve as aircraft configuration and flight conditions change. This linearisation approach would be particularly insightful for understanding how the hinged wingtip modes interact with primary wing modes; for example in determining how effective hinge aerodynamic stiffness and damping influence coupled mode frequencies, and whether frequency separation requirements established by certification standards can be met across the envelope. Frequency response functions computed from linearised models could reveal whether resonance phenomena or adverse frequency interactions might emerge that would be missed by time-domain simulations. In particular, linearisation enables the separation of frequency content that is observed in time-domain responses as seen in the Hinged-SuperFLEXOP, allowing for a more detailed diagnosis of the system's dynamic behaviour and the resultant mechanism for bifurcation. This linearisation capability bridges

the gap between design-stage frequency-based analyses (where flutter margins and handling qualities are traditionally assessed) and the nonlinear time-domain framework, enabling design teams to employ familiar frequency-domain perspectives while retaining confidence that nonlinear equilibrium effects have been properly accounted for.

6.4 Data statement

This work is supported by contributions from the wider aeroelastics community, whose shared numerical and experimental datasets, along with collaborative verification and validation activities, enable continued improvement in the tools and results presented here. The author is committed to making all the advancements presented in this thesis open-source, in the same spirit of openness and transparency that allowed this work to build upon the contributions of the many dedicated and talented SHARPy researchers.

The simulations scripts, SHARPy codebase, as well as post-processing are made available under a BSD 3-Clause License, with details in Table 6.1.

Table 6.1: Repositories containing research contributions in the context of this thesis

Repository	URL
SHARPy	https://github.com/ImperialCollegeLondon/sharpy
HALE	https://github.com/ImperialCollegeLondon/sharpy_cases/tree/main/HALE
H^2ALE	https://github.com/ImperialCollegeLondon/sharpy_cases/tree/main/H2ALE
Results & post-processing	https://github.com/kccwing/SHARPy_flared_hinged_wing_tips

London, December 2025.

Bibliography

[1] Jean-Jacques Hublin et al. "New fossils from Jebel Irhoud, Morocco and the pan-African origin of Homo sapiens". In: *Nature* 546.7657 (June 2017), pp. 289–292. ISSN: 0028-0836. DOI: 10.1038/nature22336.

[2] Matilda Brindle, Catherine F. Talbot, and Stuart West. "A comparative approach to the evolution of kissing". In: *Evolution and Human Behavior* (Nov. 2025), p. 106788. ISSN: 10905138. DOI: 10.1016/j.evolhumbehav.2025.106788.

[3] Jasen Kin-Fung Leung, Martin Chi-Sang Wong, and Eliza Lai-Yi Wong. "Unseen Threats of Chronic Diseases among the Middle-Aged: Examining the Feasibility of Well-Defined Healthcare Vouchers in Encouraging Uptake of General Checkups". In: *International Journal of Environmental Research and Public Health* 19.18 (Sept. 2022), p. 11751. ISSN: 1660-4601. DOI: 10.3390/ijerph191811751.

[4] NASM. *1903 Wright Flyer*. 2013. URL: https://airandspace.si.edu/collection-objects/1903-wright-flyer/.

[5] James R. Hansen. "Aviation History in the Wider View". In: *Technology and Culture* 30.3 (July 1989), p. 643. ISSN: 0040165X. DOI: 10.2307/3105965.

[6] IATA. *Airline Industry Economic Performance; 2015 Mid Year Tables*. 2015. URL: https://www.iata.org/en/iata-repository/publications/economic-reports/airline-industry-economic-performance---2015-mid-year---tables/.

[7] IATA. *Airline Industry Economic Performance; December 2018 Tables*. 2018. URL: https://www.iata.org/en/iata-repository/publications/economic-reports/airline-industry-economic-performance---december-2018---tables/.

[8] IATA. *Airline Industry Economic Performance; June 2020 Data Tables*. 2020. URL: https://www.iata.org/en/iata-repository/publications/economic-reports/airline-industry-economic-performance-june-2020-data-tables/.

[9] IATA. *Industry Statistics*. 2024. URL: https://www.iata.org/en/iata-repository/pressroom/fact-sheets/industry-statistics/.

[10] IATA Sustainability and Economics. *Global Outlook for Air Transport; Protectionism on the rise*. 2025. URL: https://www.iata.org/en/iata-repository/publications/economic-reports/global-outlook-for-air-transport-june-2025/.

[11] World Bank Group. *Population, Total*. 2025. URL: https://data.worldbank.org/indicator/SP.POP.TOTL%20https://databank.worldbank.org/source/population-estimates-and-projections.

[12] United Nations. *World Population Prospects 2024*. 9. 2024. URL: https://population.un.org/wpp/.

[13] Jongrim Ha, M. Ayhan Kose, and Franziska Ohnsorge. "One-stop source: A global database of inflation". In: *Journal of International Money and Finance* 137 (2023). ISSN: 02615606. DOI: 10.1016/j.jimonfin.2023.102896.

[14] Prospects Group World Bank. *A Global Database of Inflation*. 2025. URL: https://www.worldbank.org/en/research/brief/inflation-database.

[15] Shibo Jiang, Lanying Du, and Zhengli Shi. "An emerging coronavirus causing pneumonia outbreak in Wuhan, China: calling for developing therapeutic and prophylactic strategies". In: *Emerging Microbes & Infections* 9.1 (Jan. 2020), pp. 275–277. ISSN: 2222-1751. DOI: 10.1080/22221751.2020.1723441.

[16] Joyce E.. Penner et al. *Aviation and the global atmosphere : a special report of IPCC Working Groups I and III in collaboration with the Scientific Assessment Panel to the Montreal Protocol on Substances that Deplete the Ozone Layer*. Cambridge University Press, 1999, p. 373. ISBN: 9780521664042.

[17] William Stanley. Jevons. *The coal question : an inquiry concerning the progress of the nation, and the probable exhaustion of our coal-mines*. Macmilan, 1865, p. 349. URL: https://books.google.co.uk/books?id=VxNEAIFRQD0C.

[18] Antony Evans and Andreas Schäfer. "The rebound effect in the aviation sector". In: *Energy Economics* 36 (Mar. 2013), pp. 158–165. ISSN: 01409883. DOI: 10.1016/j.eneco.2012.12.005.

[19] United Nations. *Adoption of the Paris Agreement*. 2015. URL: https://unfccc.int/resource/docs/2015/cop21/eng/l09r01.pdf.

[20] ICAO. *Global SAF Accounting Framework based on Robust Chain of Custody Approaches: A Must-have for Sustainable Aviation Fuel (SAF) Deployment and its Commercial Viability*. 2024. URL: https://www.icao.int/sites/default/files/

EURNAT/Documents/EUR%20and%20Nat%20Docs/EURNAT-DGCA%20Meetings/EURNAT-DGCA%202024/EURNATDGCA2024-IP05-IATA-SAF-Accounting.pdf.

[21] Dave Gandy. *Font Awesome 5*. 2021. URL: http://fontawesome.io.

[22] IATA. *Annual Report 2010 - IATA*. 2010. URL: https://www.iata.org/contentassets/c81222d96c9a4e0bb4ff6ced0126f0bb/iataannualreport2010.pdf.

[23] International Air Transport Association. *Resolution on the Industry's Commitment to Reach Net Zero Carbon Emissions By 2050*. 2021. URL: https://www.iata.org/contentassets/d13875e9ed784f75bac90f000760e998/iata-agm-resolution-on-net-zero-carbon-emissions.pdf.

[24] ATAG. *Commitment to Fly Net Zero 2050*. 2021. URL: https://aviationbenefits.org/media/167501/atag-net-zero-2050-declaration.pdf.

[25] ICAO. *Environmental Technical Manual - Volume IV - Procedures for demonstrating compliance with the Carbon Offsetting and Reduction Scheme for International Aviation (CORSIA)*. 2023. URL: https://elibrary.icao.int/product/446973.

[26] International Civil Aviation Organization. *Consolidated statement of continuing ICAO policies and practices related to environmental protection — Carbon Offsetting and Reduction Scheme for International Aviation (CORSIA)*. 2022. URL: https://www2023.icao.int/environmental-protection/CORSIA/Documents/Resolution_A41-22_CORSIA.pdf.

[27] Liang Jing et al. "Understanding variability in petroleum jet fuel life cycle greenhouse gas emissions to inform aviation decarbonization". In: *Nature Communications* 13.1 (Dec. 2022), p. 7853. ISSN: 2041-1723. DOI: 10.1038/s41467-022-35392-1.

[28] Jörgen Larsson et al. "International and national climate policies for aviation: a review". In: *Climate Policy* 19.6 (July 2019), pp. 787–799. ISSN: 1469-3062. DOI: 10.1080/14693062.2018.1562871.

[29] Benoit Mayer and Zhuoqi Ding. "Climate Change Mitigation in the Aviation Sector: A Critical Overview of National and International Initiatives". In: *Transnational Environmental Law* 12.1 (Mar. 2023), pp. 14–41. ISSN: 2047-1025. DOI: 10.1017/S204710252200019X.

[30] Stefan Gössling, Andreas Humpe, and Ya-Yen Sun. "Are emissions from global air transport significantly underestimated?" In: *Current Issues in Tourism* 28.5 (Mar. 2025), pp. 695–708. ISSN: 1368-3500. DOI: 10.1080/13683500.2024.2337281.

[31] IATA. *Aviation Net-Zero CO2 Transition Pathways: Comparative Review*. Apr. 2024. URL: https://www.iata.org/contentassets/8d19e716636a47%20c184e7221c77563c93/nz-roadmaps.pdf.

[32] Joosung Lee and Jeonghoon Mo. "Analysis of Technological Innovation and Environmental Performance Improvement in Aviation Sector". In: *International Journal of Environmental Research and Public Health* 8.9 (Sept. 2011), pp. 3777–3795. ISSN: 1660-4601. DOI: 10.3390/ijerph8093777.

[33] ICAO. *ICAO Environmental Report 2022*. 2022. URL: https://www.icao.int/sites/default/files/environmental-protection/Documents/EnvironmentalReports/2022/ENVReport2022_Art27.pdf.

[34] G Lachmann. "The span as a fundamental factor in airplane design". In: *Technical Memorandums, National Advisory Committee for Aeronautics* (1928).

[35] Ludwig Prandtl. *Applications of Modern Hydrodynamics to Aeronautics*. Tech. rep. NACA Report No 116, 1922.

[36] Ludwig Prandtl. "Über tragflügel kleinsten induzierten widerstandes". In: *Zeitschrift für Flugtecknik und Motorluftschiffahrt* (1933).

[37] William Bailey Oswald. *General Formulas and Charts for the Calculation of Airplane Performance*. Tech. rep. NASA, 1933.

[38] W.F. Phillips, D.F. Hunsaker, and J.D. Taylor. "Minimising induced drag with weight distribution, lift distribution, wingspan, and wing-structure weight". In: *The Aeronautical Journal* 124.1278 (Aug. 2020), pp. 1208–1235. ISSN: 0001-9240. DOI: 10.1017/aer.2020.24.

[39] Team J2mcL. *J2mcL Sailplanes Database (extracted 2022)*. 2022. URL: https://www.j2mcl-planeurs.net.

[40] Lucie Morichon. *Selected Statistics in Aircraft Design*. Tech. rep. 27 May. Hochschule für angewandte Wissenschaften, 2006. URL: https://www.fzt.haw-hamburg.de/pers/Scholz/arbeiten/AbstractMorichon.html.

[41] Guy. Norris and Mark. Wagner. *Boeing 787 Dreamliner*. Zenith Press, 2009, p. 160. ISBN: 9781616732271.

[42] Rebecca Slayton and Graham Spinardi. "Radical innovation in scaling up: Boeing's Dreamliner and the challenge of socio-technical transitions". In: *Technovation* 47 (Jan. 2016), pp. 47–58. ISSN: 01664972. DOI: 10.1016/j.technovation.2015.08.004.

[43] Raymond L.. Bisplinghoff, Holt. Ashley, and Robert L.. Halfman. *Aeroelasticity*. Dover Publications, 2013, p. 1577. ISBN: 9780486132433.

[44] Dewey H. Hodges and G. Alvin Pierce. *Introduction to Structural Dynamics and Aeroelasticity*. Cambridge University Press, Aug. 2011. ISBN: 9780521195904. DOI: 10.1017/CBO9780511997112.

[45] Jan R. Wright and Jonathan E. Cooper. *Introduction to Aircraft Aeroelasticity and Loads: Second Edition*. 2015. DOI: 10.1002/9781118700440.

[46] Rafael Palacios and Carlos E. S. Cesnik. *Dynamics of Flexible Aircraft*. Cambridge University Press, June 2023. ISBN: 9781108354868. DOI: 10.1017/9781108354868.

[47] Tobias F. Wunderlich et al. "Global aerostructural design optimization of more flexible wings for commercial aircraft". In: *Journal of Aircraft* 58.6 (2021). ISSN: 15333868. DOI: 10.2514/1.C036301.

[48] Airbus. *Airbus reveals new zero-emission concept aircraft*. 2020. URL: https://www.airbus.com/en/newsroom/press-releases/2020-09-airbus-reveals-new-zero-emission-concept-aircraft.

[49] Jerry T. Callaghan and Robert H. Liebeck. "Some Thoughts on the Design of Subsonic Transport Aircraft for the 21st Century". In: Sept. 1990. DOI: 10.4271/901987.

[50] R. H. Liebeck. "Design of the Blended Wing Body Subsonic Transport". In: *Journal of Aircraft* 41.1 (Jan. 2004), pp. 10–25. ISSN: 0021-8669. DOI: 10.2514/1.9084.

[51] Paul Okonkwo and Howard Smith. "Review of evolving trends in blended wing body aircraft design". In: *Progress in Aerospace Sciences* 82 (Apr. 2016), pp. 1–23. ISSN: 03760421. DOI: 10.1016/j.paerosci.2015.12.002.

[52] Boeing. *Boeing Flies Blended Wing Body Research Aircraft*. 2007. URL: https://boeing.mediaroom.com/2007-07-26-Boeing-Flies-Blended-Wing-Body-Research-Aircraft.

[53] Delta. *Delta, JetZero partner to design the future of air travel by advancing first-of-its-kind, 50% more fuel-efficient aircraft for domestic and international routes*. 2025. URL: https://news.delta.com/delta-jetzero-partner-design-future-air-travel.

[54] Airbus UpNext. *Imagine travelling in this blended wing body aircraft; the Airbus MAVERIC demonstrator is pushing innovative aircraft design to the limit*. 2020. URL: https://www.airbus.com/en/newsroom/stories/2020-11-imagine-travelling-in-this-blended-wing-body-aircraft.

[55] Airbus. *These new Airbus concept aircraft have one thing in common; Airbus ZEROe puts hydrogen at the heart of future aircraft*. 2020. URL: https://www.airbus.com/en/newsroom/stories/2020-09-these-new-airbus-concept-aircraft-have-one-thing-in-common.

[56] Eytan J. Adler and Joaquim R. R. A. Martins. "Blended Wing Body Configuration for Hydrogen-Powered Aviation". In: *Journal of Aircraft* 61.3 (May 2024), pp. 887–901. ISSN: 0021-8669. DOI: 10.2514/1.C037582.

[57] European Commission. *ENABLing cryogEnic Hydrogen based CO2 free air transport (ENABLEH2)*. Tech. rep. Sept. 2018. DOI: 10.3030/769241.

[58] Stanislav Karpuk, Yiyuan Ma, and Ali Elham. "Design Investigation of Potential Long-Range Hydrogen Combustion Blended Wing Body Aircraft with Future Technologies". In: *Aerospace* 10.6 (June 2023), p. 566. ISSN: 2226-4310. DOI: 10.3390/aerospace10060566.

[59] Oi Ching Vanessa Chung et al. "Design of Hydrogen Solid Oxide Fuel Cells in Blended-Wing–Body Aircraft". In: *Journal of Aircraft* 62.4 (July 2025), pp. 816–834. ISSN: 0021-8669. DOI: 10.2514/1.C038174.

[60] NASA. *Sustainable Flight Demonstrator Project*. 2025. URL: https://www.nasa.gov/directorates/armd/iasp/sfd/.

[61] NASA Langley Research Center. *Subsonic Ultra Green Aircraft Research*. Tech. rep. 2011. URL: https://ntrs.nasa.gov/citations/20110011321.

[62] Neal Harrison et al. *Subsonic Ultra Green Aircraft Research: Phase IV Final Report – Volume I Mach 0.80 Transonic Truss-Braced Wing High Speed Design Report*. Tech. rep. 2023. URL: https://ntrs.nasa.gov/api/citations/20220016017/downloads/NASA-CR-20220016017%20Volume%201.pdf.

[63] NASA. *NASA Issues Award for Greener, More Fuel-Efficient Airliner of Future*. 2023. URL: https://www.nasa.gov/news-release/nasa-issues-award-for-greener-more-fuel-efficient-airliner-of-future/.

[64] NASA. *NASA, Boeing, Consider New Thin-Wing Aircraft Research Focus*. 2025. URL: https://www.nasa.gov/aeronautics/nasa-boeing-new-thin-wing-aircraft/.

[65] Manav Bhatia, Rakesh K. Kapania, and Raphael T. Haftka. "Structural and Aeroelastic Characteristics of Truss-Braced Wings: A Parametric Study". In: *Journal of Aircraft* 49.1 (Jan. 2012), pp. 302–310. ISSN: 0021-8669. DOI: 10.2514/1.C031556.

[66] Imon Chakraborty et al. "Comparative Assessment of Strut-Braced and Truss-Braced Wing Configurations Using Multidisciplinary Design Optimization". In: *Journal of Aircraft* 52.6 (Nov. 2015), pp. 2009–2020. ISSN: 0021-8669. DOI: 10.2514/1.C033120.

[67] Douglas Wells et al. "NASA Transonic Truss-Braced Wing Studies". In: *34th Congress of the International Council of the Aeronautical Sciences, ICAS 2024*. 2024.

[68] Neal Harrison, David Akiyama, and Gregory Gatlin. "Transonic Truss-Braced Wing Maturation". In: *7th UTIAS International Workshop on Aviation and Climate Change*. 2021. URL: http://goldfinger.utias.utoronto.ca/IWACC5/IWACC7/Harrison.pdf.

[69] Jonathan E. Cooper et al. "CS2-THT U-HARWARD Project: Final Assessment and Project Outcomes Evaluation". In: *AIAA SCITECH 2024 Forum*. Reston, Virginia: American Institute of Aeronautics and Astronautics, Jan. 2024. ISBN: 978-1-62410-711-5. DOI: 10.2514/6.2024-2111. URL: https://arc.aiaa.org/doi/10.2514/6.2024-2111.

[70] A. Castrichini et al. "Preliminary investigation of use of flexible folding wing tips for static and dynamic load alleviation". In: *The Aeronautical Journal* 121.1235 (Jan. 2017), pp. 73–94. ISSN: 0001-9240. DOI: 10.1017/aer.2016.108.

[71] Thomas Wilson et al. "Aeroelastic Behaviour of Hinged Wing Tips". In: *International Forum on Aeroelasticity and Structural Dynamics, IFASD 2017*. Como, Italy, 2017.

[72] Taras Skavinskyy. *Arc de Triomphe Paris in 1912*. 2014. URL: https://histolines.com/timeline_event.php?eventId=728643%20https://pbs.twimg.com/media/B31uBZqIYAANnnq.jpg.

[73] Jean-Pierre Harrison. *The Cierva Autodynamic Rotor*. Tech. rep. NASA/TP—2015–218714, 2015. URL: https://ntrs.nasa.gov/citations/20180007693.

[74] The Royal Naval Air Service. *Aircraft of the Royal Naval Air Service 1912 - 1918*. 1913. URL: https://www.iwm.org.uk/collections/item/object/205027633.

[75] C. H.. Barnes and Derek N.. James. *Shorts aircraft since 1900*. Putnam, 1989, p. 560. ISBN: 9780851778198.

[76] Philip. MacDougall. *Short Brothers : the Rochester years*. Fonthill, 2019, p. 176. ISBN: 9781781557303.

[77] Edmond de Marçay and Émile Moonen. *Improvements in and relating to Aeroplanes and other Machines*. 1910. URL: https://patents.google.com/patent/GB191018661A.

[78] "Popular Mechanics". In: *Popular Mechanics* (1912), p. 194. URL: https://wp.oldmagazinearticles.com/magazine-articles/aviation_history/folding_wing_aircraft_de_marcay-mooney_monoplane_1912/%20https://web.archive.org/web/20101126145159/http://oldmagazinearticles.com/pdf/PLANES%20mooney.pdf.

[79] Leonard E.. Opdycke. *French aeroplanes before the Great War, including many rare photos from the Musee de l'Air et de l'Espace*. Schiffer Pub., 1999, p. 288. ISBN: 0764307525.

[80] Boeing. *Cathay Pacific Orders 14 More Boeing 777-9 Passenger Jets*. 2025. URL: https://boeing.mediaroom.com/2025-08-06-Cathay-Pacific-Orders-14-More-Boeing-777-9-Passenger-Jets.

[81] Mark Smith, Michael Renzelmann, and Alan Marx. *Folding wing-tip system*. 1995. URL: https://patents.google.com/patent/US5381986A.

[82] EASA. *EASA Type-certificate Data Sheet No. EASA.IM.A.003 for BOEING 777*. Tech. rep. 2024, Issue: 19.0. URL: https://www.easa.europa.eu/en/downloads/7521/en.

[83] Anatolii Kretov and Dmytro Tiniakov. "Evaluation of the Mass and Aerodynamic Efficiency of a High Aspect Ratio Wing for Prospective Passenger Aircraft". In: *Aerospace* 9.9 (Sept. 2022), p. 497. ISSN: 2226-4310. DOI: 10.3390/aerospace9090497.

[84] Reuters. *Boeing 777X to be delayed to 2027, Bloomberg News reports*. 2025. URL: https://www.reuters.com/business/autos-transportation/boeing-777x-be-delayed-2027-bloomberg-news-reports-2025-10-02/.

[85] FAA Airport Engineering Division. *Engineering Brief #94B; Accommodating the Boeing B-777 Folding Wingtip Airplane onto Airports*. Tech. rep. 2024. URL: https://www.faa.gov/sites/faa.gov/files/arp-eb-94b-B-777-folding-wings.pdf.

[86] Department of Defense. *An air-to-air right rear view of an XB-70 Valkyrie aircraft*. 1960. URL: https://catalog.archives.gov/id/6362754.

[87] Peter E.. Davies, Wiek. Luijken, and Adam. Tooby. *North American XB-70 Valkyrie*. Bloomsbury Publishing Plc, 2018, p. 81. ISBN: 9781472825049.

[88] Graham M.. Simons. *Valkyrie : the north American xb-70*. Pen & Sword Books, 2014. ISBN: 9781783461615.

[89] NASA Dryden Flight Research Center. *NASA Facts; XB-70*. 2003. URL: https://www.nasa.gov/wp-content/uploads/2021/09/121584main_fs-084-dfrc.pdf.

[90] Srinivas Vasista, Liyong Tong, and K. C. Wong. "Realization of Morphing Wings: A Multidisciplinary Challenge". In: *Journal of Aircraft* 49.1 (Jan. 2012), pp. 11–28. ISSN: 0021-8669. DOI: 10.2514/1.C031060.

[91] S. Ameduri and A. Concilio. "Morphing wings review: aims, challenges, and current open issues of a technology". In: *Proceedings of the Institution of Mechanical Engineers, Part C: Journal of Mechanical Engineering Science* 237.18 (2023). ISSN: 20412983. DOI: 10.1177/0954406220944423.

[92] Anna-Maria R. McGowan et al. "Perspectives on Highly Adaptive or Morphing Aircraft". In: *RTO Applied Vehicle Technology Panel (AVT) Symposium* (2009). URL: https://ntrs.nasa.gov/api/citations/20090017845/downloads/20090017845.pdf.

[93] Gaétan X. Dussart et al. "In-flight Wingtip Folding: Inspiration from the XB-70 Valkyrie". In: *International Journal of Aviation, Aeronautics, and Aerospace* (2019). ISSN: 23746793. DOI: 10.15394/ijaaa.2019.1343.

[94] Flight International. "The Le Bourget Fête". In: *Flight International* LX.2215 (1951). URL: https://archive.org/details/sim_flight-international_1951-07-06_60_2215.

[95] R. L. M. F. Rouanet and F. V. Rey. *Aircraft*. 1938. URL: https://patents.google.com/patent/US2186558A.

[96] R Rouanet. "Contribution À L'étude Des Avions À Ailes Déformables". In: *Publications scientifiques et techniques du Ministère de l'air* Bulletins des services techniques 114 (1951).

[97] Anon. "Research Reports and Memoranda". In: *Aircraft Engineering* XXIII.271 (1951). ISSN: 0002-2667. URL: https://cybra.lodz.pl/Content/21530/Aireraft_Engineering_Vol_XXIII_nr_271_1951.pdf.

[98] The Technical Editor. "Techniques Françaises: Notes on Detail Design Seen at Le Bourget". In: *Flight International* 60.2216 (1951). URL: https://archive.org/details/sim_flight-international_1951-07-13_60_2216.

[99] Airbus. *AlbatrossOne: Revolutionising Aircraft Wing Design*. 2019. URL: https://www.youtube.com/watch?v=Rq2poT9pW3w.

[100] Thomas Wilson et al. *An Aircraft Wing With A Moveable Wing Tip Device For Load Alleviation*. 2016. URL: https://patents.google.com/patent/EP3862261B1%20https://patents.google.com/patent/EP3400167B1.

[101] Thomas Wilson et al. *An Aircraft Wing With A Moveable Wing Tip Device For Load Alleviation*. 2016. URL: https://patents.google.com/patent/US11203410B2.

[102] Airbus. *AlbatrossONE - A revolutionary approach to aircraft wing design*. June 2020. URL: https://www.airbus.com/en/innovation/disruptive-concepts/biomimicry/albatrossone.

[103] Thomas Wilson et al. "Small scale flying demonstration of semi aeroelastic hinged wing tips". In: *International Forum on Aeroelasticity and Structural Dynamics 2019, IFASD 2019*. 2019.

[104] Thomas Wilson et al. "Update on AlbatrossONE Semi Aeroelastic Hinge Small Scale Flying Demonstrator Project". In: *Proceedings of the International Forum of Aeroelasticity and Structural Dynamics 2022, IFASD 2022*. 2022.

[105] Paolo Mastracci, Andrea Castrichini, and Thomas Wilson. "Parametric Nonlinear Flutter Analysis of the Semi-Aeroelastic Hinges During Manoeuvres and Gust Encounters". In: *International Forum on Aeroelasticity and Structural Dynamics IFASD 2024*. 2024.

[106] Airbus. *Airbus launches extra high performance wing demonstrator to fortify decarbonisation ambition*. 2021. URL: https://www.airbus.com/en/newsroom/press-releases/2021-09-airbus-launches-extra-high-performance-wing-demonstrator-to-fortify.

[107] Thomas Wilson et al. "Overview of Semi Aeroelastic Hinge Simulation Research at Airbus". In: *AIAA SCITECH 2025 Forum*. Reston, Virginia: American Institute of Aeronautics and Astronautics, Jan. 2025. ISBN: 978-1-62410-723-8. DOI: 10.2514/6.2025-0712.

[108] Airbus. *eXtra Performance Wing demonstrator - Assembly*. 2025. URL: https://www.facebook.com/watch/?v=814312961051951.

[109] Claudio Conti et al. "Quasi-Steady Aeroelastic Analysis of the Semi-Aeroelastic Hinge Including Geometric Nonlinearities". In: *Journal of Aircraft* 58.5 (Sept. 2021), pp. 1168–1178. ISSN: 1533-3868. DOI: 10.2514/1.C036115.

[110] Paolo Mastracci et al. "Unsteady Aeroelastic Analysis of the Semi Aeroelastic Hinge Including Local Geometric Nonlinearities". In: *AIAA Journal* 60.5 (May 2022), pp. 3147–3165. ISSN: 0001-1452. DOI: 10.2514/1.J061108.

[111] Davide Balatti et al. "Experimental and numerical investigation of an aircraft wing with hinged wingtip for gust load alleviation". In: *Journal of Fluids and Structures* 119 (May 2023), p. 103892. ISSN: 08899746. DOI: 10.1016/j.jfluidstructs.2023.103892.

[112] R. C. M. Cheung et al. "Testing of Folding Wingtip for Gust Load Alleviation of Flexible High-Aspect-Ratio Wing". In: *Journal of Aircraft* 57.5 (Sept. 2020), pp. 876–888. ISSN: 1533-3868. DOI: 10.2514/1.C035732.

[113] Fintan Healy et al. "On the Effect of Geometric Nonlinearity on the Dynamics of Flared Folding Wingtips". In: *Journal of Aircraft* 60.2 (Mar. 2023), pp. 368–381. ISSN: 0021-8669. DOI: 10.2514/1.C036877.

[114] Fintan Healy, Djamel Rezgui, and Jonathan E. Cooper. "Experimental Effect of Sideslip Angle on the Dynamic Behaviour of Flared Folding Wingtips". In: *AIAA SCITECH 2023 Forum*. Reston, Virginia: American Institute of Aeronautics and Astronautics, Jan. 2023. ISBN: 978-1-62410-699-6. DOI: 10.2514/6.2023-0376.

[115] Xavier Carrillo Córcoles et al. "Effect of Wing Stiffness and Folding Wingtip Release Threshold on Gust Loads". In: *Journal of Aircraft* (May 2023), pp. 1–20. ISSN: 0021-8669. DOI: 10.2514/1.C037108.

[116] Fintan Healy et al. "Experimental and Numerical Nonlinear Stability Analysis of Wings Incorporating Flared Folding Wingtips". In: *Journal of Aircraft* (July 2023), pp. 1–15. ISSN: 0021-8669. DOI: 10.2514/1.C037167.

[117] Huaiyuan Gu et al. "Aeroelastic Scaling of a High-Aspect-Ratio Wing Incorporating a Semi-Aeroelastic Hinge". In: *AIAA Journal* (Apr. 2024), pp. 1–13. ISSN: 0001-1452. DOI: 10.2514/1.J063646.

[118] Fintan Healy et al. "Folding Wingtips for Improved Roll Performance". In: *Journal of Aircraft* 59.1 (Jan. 2022), pp. 15–28. ISSN: 1533-3868. DOI: 10.2514/1.C036372.

[119] Divya Sanghi, Carlos E. S. Cesnik, and Cristina Riso. "Roll Maneuverability of Transonic High-Aspect-Ratio-Wing Aircraft with Flared Folding Wingtips". In: *Journal of Aircraft* (Feb. 2024), pp. 1–14. ISSN: 0021-8669. DOI: 10.2514/1.C037470.

[120] Eric Tuegel. "The Airframe Digital Twin: Some Challenges to Realization". In: *53rd AIAA/ASME/ASCE/AHS/ASC Structures, Structural Dynamics and Materials Conference
20th AIAA/ASME/AHS Adaptive Structures Conference
14th AIAA*. Reston, Virginia: American Institute of Aeronautics and Astronautics, Apr. 2012. ISBN: 978-1-60086-937-2. DOI: 10.2514/6.2012-1812.

[121] Andrea Pedrioli, Andrea Vaiuso, and Marcello Righi. *MODEL-SI, D-3.1 Report on the main changes required to regulatory materials and standards*. Tech. rep. EASA, 2024. URL: https://elib.dlr.de/136848/1/Paper%20DLRK_01.pdf.

[122] Timothy Mauery et al. "A Guide for Aircraft Certification by Analysis". In: *Nasa/Cr-20210015404* january 2025 (2021). URL: https://ntrs.nasa.gov/api/citations/20210015404/downloads/NASA-CR-20210015404%20updated.pdf.

[123] Rafael Palacios, Joseba Murua, and Robert Cook. "Structural and Aerodynamic Models in Nonlinear Flight Dynamics of Very Flexible Aircraft". In: *AIAA Journal* 48.11 (Nov. 2010), pp. 2648–2659. ISSN: 0001-1452. DOI: 10.2514/1.J050513.

[124] Frederico Afonso et al. *A review on non-linear aeroelasticity of high aspect-ratio wings*. 2017. DOI: 10.1016/j.paerosci.2016.12.004.

[125] M.J. de C. Henshaw et al. "Non-linear aeroelastic prediction for aircraft applications". In: *Progress in Aerospace Sciences* 43.4-6 (May 2007), pp. 65–137. ISSN: 03760421. DOI: 10.1016/j.paerosci.2007.05.002.

[126] I.E. Garrick. "Aeroelasticity-Frontiers and Beyond". In: *Journal of Aircraft* 13.9 (Sept. 1976), pp. 641–657. ISSN: 0021-8669. DOI: 10.2514/3.58696.

[127] Eli Livne. "Future of Airplane Aeroelasticity". In: *Journal of Aircraft* 40.6 (Nov. 2003), pp. 1066–1092. ISSN: 0021-8669. DOI: 10.2514/2.7218.

[128] Weixing Yuan, Rimple Sandhu, and Dominique Poirel. "Fully Coupled Aeroelastic Analyses of Wing Flutter towards Application to Complex Aircraft Configurations". In: *Journal of Aerospace Engineering* 34.2 (Mar. 2021). ISSN: 0893-1321. DOI: 10.1061/(ASCE)AS.1943-5525.0001232.

[129] O. A. Bauchau and J. I. Craig. "Euler-Bernoulli beam theory". In: 2009. DOI: 10.1007/978-90-481-2516-6{_}5.

[130] Andreas Öchsner. "Euler–Bernoulli Beam Theory". In: *Classical Beam Theories of Structural Mechanics*. Cham: Springer International Publishing, 2021, pp. 7–66. DOI: 10.1007/978-3-030-76035-9{_}2.

[131] S.P. Timoshenko. "On the transverse vibrations of bars of uniform cross-section". In: *The London, Edinburgh, and Dublin Philosophical Magazine and Journal of Science* 43.253 (1922). ISSN: 1941-5982. DOI: 10.1080/14786442208633855.

[132] Rafael Palacios and Carlos E.S. Cesnik. "Cross-sectional analysis of nonhomogeneous anisotropic active slender structures". In: *AIAA Journal* 43.12 (2005). ISSN: 00011452. DOI: 10.2514/1.12451.

[133] Carlos E.S. Cesnik and Dewey H. Hodges. "VABS: A new concept for composite rotor blade cross-sectional modeling". In: *Journal of the American Helicopter Society* 42.1 (1997). ISSN: 00028711. DOI: 10.4050/jahs.42.27.

[134] Alvaro Cea and Rafael Palacios. "A non-intrusive geometrically nonlinear augmentation to generic linear aeroelastic models". In: *Journal of Fluids and Structures* 101 (Feb. 2021), p. 103222. ISSN: 08899746. DOI: 10.1016/j.jfluidstructs.2021.103222.

[135] Cristina Riso and Carlos E. S. Cesnik. "Impact of Low-Order Modeling on Aeroelastic Predictions for Very Flexible Wings". In: *Journal of Aircraft* 60.3 (May 2023), pp. 662–687. ISSN: 0021-8669. DOI: 10.2514/1.C036869.

[136] Ariel Drachinsky and Daniella E. Raveh. "Modal Rotations: A Modal-Based Method for Large Structural Deformations of Slender Bodies". In: *AIAA Journal* 58.7 (July 2020), pp. 3159–3173. ISSN: 0001-1452. DOI: 10.2514/1.J058899.

[137] E. Reissner. "On One-Dimensional Large-Displacement Finite-Strain Beam Theory". In: *Studies in Applied Mathematics* 52.2 (June 1973), pp. 87–95. ISSN: 0022-2526. DOI: 10.1002/sapm197352287.

[138] J.C. Simo. "A finite strain beam formulation. The three-dimensional dynamic problem. Part I". In: *Computer Methods in Applied Mechanics and Engineering* 49.1 (May 1985), pp. 55–70. ISSN: 00457825. DOI: 10.1016/0045-7825(85)90050-7.

[139] O. A. Bauchau and C. H. Hong. "Nonlinear Composite Beam Theory". In: *Journal of Applied Mechanics* 55.1 (Mar. 1988), pp. 156–163. ISSN: 0021-8936. DOI: 10.1115/1.3173622.

[140] Dewey Hodges. *Finite rotation and nonlinear beam kinematics*. Tech. rep. NASA, 1987. URL: https://ntrs.nasa.gov/citations/19870047587.

[141] Dewey H.. Hodges. *Nonlinear composite beam theory*. American Institute of Aeronautics and Astronautics, 2006, p. 304. ISBN: 1563478323.

[142] Leonard A Euler. "Formulae Generales Pro Translatione Quacunque Corporum Rigidorum". In: *Novi Commentarii Academiae Scientiarum Imperialis Petropolitanae* 20 (1776).

[143] William Rowan Hamilton. "On a new Species of Imaginary Quantities Connected with a Theory of Quaternions". In: *Proceedings of the Royal Irish Academy* 2.1844 (1844).

[144] John Argyris. "An excursion into large rotations". In: *Computer Methods in Applied Mechanics and Engineering* 32.1-3 (1982). ISSN: 00457825. DOI: 10.1016/0045-7825(82)90069-X.

[145] A. Cardona and M. Geradin. "A beam finite element non-linear theory with finite rotations". In: *International Journal for Numerical Methods in Engineering* 26.11 (Nov. 1988), pp. 2403–2438. ISSN: 0029-5981. DOI: 10.1002/nme.1620261105.

[146] Michel Géradin and Alberto Cardona. *Flexible Multibody Dynamics: A Finite Element Approach*. Chichester [u.a.]: Wiley, 2001. ISBN: 978-0-471-48990-0.

[147] Adnan Ibrahimbegović, François Frey, and Ivica Kožar. "Computational aspects of vector-like parametrization of three-dimensional finite rotations". In: *International Journal for Numerical Methods in Engineering* 38.21 (Nov. 1995), pp. 3653–3673. ISSN: 0029-5981. DOI: 10.1002/nme.1620382107.

[148] Adnan Ibrahimbegovic. "On the choice of finite rotation parameters". In: *Computer Methods in Applied Mechanics and Engineering* 149.1-4 (Oct. 1997), pp. 49–71. ISSN: 00457825. DOI: 10.1016/S0045-7825(97)00059-5.

[149] G. Jelenić and M. A. Crisfield. "Interpolation of rotational variables in nonlinear dynamics of 3D beams". In: *International Journal for Numerical Methods in Engineering* 43.7 (Dec. 1998), pp. 1193–1222. ISSN: 0029-5981. DOI: 10.1002/(SICI)1097-0207(19981215)43:7<1193::AID-NME463>3.0.CO;2-P.

[150] Michael A. Crisfield and Gordan Jelenić; "Objectivity of strain measures in the geometrically exact three-dimensional beam theory and its finite-element implementation". In: *Proceedings of the Royal Society of London. Series A: Mathematical, Physical and Engineering Sciences* 455.1983 (Mar. 1999), pp. 1125–1147. ISSN: 1364-5021. DOI: 10.1098/rspa.1999.0352.

[151] I. Romero and F. Armero. "An objective finite element approximation of the kinematics of geometrically exact rods and its use in the formulation of an energy–momentum conserving scheme in dynamics". In: *International Journal for Numerical Methods in Engineering* 54.12 (Aug. 2002), pp. 1683–1716. ISSN: 0029-5981. DOI: 10.1002/nme.486.

[152] P. Betsch and P. Steinmann. "Frame-indifferent beam finite elements based upon the geometrically exact beam theory". In: *International Journal for Numerical Methods in Engineering* 54.12 (Aug. 2002), pp. 1775–1788. ISSN: 0029-5981. DOI: 10.1002/nme.487.

[153] S.R. Eugster et al. "Director-based beam finite elements relying on the geometrically exact beam theory formulated in skew coordinates". In: *International Journal for Numerical Methods in Engineering* 97.2 (Jan. 2014), pp. 111–129. ISSN: 0029-5981. DOI: 10.1002/nme.4586.

[154] Robert J. Simpson and Rafael Palacios. "Numerical aspects of nonlinear flexible aircraft flight dynamics modeling". In: *54th AIAA/ASME/ASCE/AHS/ASC Structures, Structural Dynamics, and Materials Conference*. Reston, Virginia: American Institute

of Aeronautics and Astronautics, Apr. 2013. ISBN: 978-1-62410-223-3. DOI: 10.2514/6.2013-1634.

[155] Robert J. S. Simpson. "Unsteady aerodynamics, reduced-order modelling, and predictive control in linear and nonlinear aeroelasticity with arbitrary kinematics". PhD thesis. Imperial College London, 2016. DOI: 10.25560/33327. URL: http://hdl.handle.net/10044/1/33327%20https://doi.org/10.25560/33327.

[156] Dewey H. Hodges. "A mixed variational formulation based on exact intrinsic equations for dynamics of moving beams". In: *International Journal of Solids and Structures* 26.11 (1990). ISSN: 00207683. DOI: 10.1016/0020-7683(90)90060-9.

[157] Dewey H. Hodges. "Geometrically exact, intrinsic theory for dynamics of curved and twisted anisotropic beams". In: *AIAA Journal* 41.6 (2003). ISSN: 00011452. DOI: 10.2514/2.2054.

[158] Yinan Wang and Keisuke Otsuka. "Multibody Constraints in the Geometrically Nonlinear Intrinsic Formulation". In: *Journal of Computational and Nonlinear Dynamics* 18.12 (2023). ISSN: 15551423. DOI: 10.1115/1.4063724.

[159] Weihua Su and Carlos E.S. Cesnik. "Strain-based geometrically nonlinear beam formulation for modeling very flexible aircraft". In: *International Journal of Solids and Structures* 48.16-17 (2011). ISSN: 00207683. DOI: 10.1016/j.ijsolstr.2011.04.012.

[160] Christopher M. Shearer and Carlos E. S. Cesnik. "Nonlinear Flight Dynamics of Very Flexible Aircraft". In: *Journal of Aircraft* 44.5 (Sept. 2007), pp. 1528–1545. ISSN: 0021-8669. DOI: 10.2514/1.27606.

[161] Weihua Su and Carlos E. S. Cesnik. "Nonlinear Aeroelasticity of a Very Flexible Blended-Wing-Body Aircraft". In: *Journal of Aircraft* 47.5 (Sept. 2010), pp. 1539–1553. ISSN: 0021-8669. DOI: 10.2514/1.47317.

[162] Weihua Su and Carlos E. S. Cesnik. "Dynamic Response of Highly Flexible Flying Wings". In: *AIAA Journal* 49.2 (Feb. 2011), pp. 324–339. ISSN: 0001-1452. DOI: 10.2514/1.J050496.

[163] Carlos Cesnik and Eric Brown. "Modeling of High Aspect Ratio Active Flexible Wings for Roll Control". In: *43rd AIAA/ASME/ASCE/AHS/ASC Structures, Structural Dynamics, and Materials Conference*. Reston, Virginia: American Institute of Aeronautics and Astronautics, Apr. 2002. ISBN: 978-1-62410-117-5. DOI: 10.2514/6.2002-1719.

[164] Keisuke Otsuka et al. "Strain-Based Geometrically Nonlinear Beam Formulation for Rigid–Flexible Multibody Dynamic Analysis". In: *AIAA Journal* 60.8 (Aug. 2022), pp. 4954–4968. ISSN: 0001-1452. DOI: 10.2514/1.J061516.

[165] A.A. Shabana. "Definition of the Slopes and the Finite Element Absolute Nodal Coordinate Formulation". In: *Multibody System Dynamics* 1.3 (Sept. 1997), pp. 339–348. ISSN: 1384-5640. DOI: 10.1023/A:1009740800463.

[166] Ahmed A. Shabana and Refaat Y. Yakoub. "Three Dimensional Absolute Nodal Coordinate Formulation for Beam Elements: Theory". In: *Journal of Mechanical Design* 123.4 (Dec. 2001), pp. 606–613. ISSN: 1050-0472. DOI: 10.1115/1.1410100.

[167] Refaat Y. Yakoub and Ahmed A. Shabana. "Three Dimensional Absolute Nodal Coordinate Formulation for Beam Elements: Implementation and Applications". In: *Journal of Mechanical Design* 123.4 (Dec. 2001), pp. 614–621. ISSN: 1050-0472. DOI: 10.1115/1.1410099.

[168] Johannes Gerstmayr, Hiroyuki Sugiyama, and Aki Mikkola. "Review on the Absolute Nodal Coordinate Formulation for Large Deformation Analysis of Multibody Systems". In: *Journal of Computational and Nonlinear Dynamics* 8.3 (July 2013). ISSN: 1555-1415. DOI: 10.1115/1.4023487.

[169] Keisuke Otsuka, Kanjuro Makihara, and Hiroyuki Sugiyama. "Recent Advances in the Absolute Nodal Coordinate Formulation: Literature Review From 2012 to 2020". In: *Journal of Computational and Nonlinear Dynamics* 17.8 (Aug. 2022). ISSN: 1555-1415. DOI: 10.1115/1.4054113.

[170] Karin Nachbagauer. "State of the Art of ANCF Elements Regarding Geometric Description, Interpolation Strategies, Definition of Elastic Forces, Validation and the Locking Phenomenon in Comparison with Proposed Beam Finite Elements". In: *Archives of Computational Methods in Engineering* 21.3 (Sept. 2014), pp. 293–319. ISSN: 1134-3060. DOI: 10.1007/s11831-014-9117-9.

[171] Johannes Gerstmayr and Ahmed A. Shabana. "Analysis of Thin Beams and Cables Using the Absolute Nodal Co-ordinate Formulation". In: *Nonlinear Dynamics* 45.1-2 (July 2006), pp. 109–130. ISSN: 0924-090X. DOI: 10.1007/s11071-006-1856-1.

[172] Olivier A. Bauchau et al. "Validation of flexible multibody dynamics beam formulations using benchmark problems". In: *Multibody System Dynamics* 37.1 (May 2016), pp. 29–48. ISSN: 1384-5640. DOI: 10.1007/s11044-016-9514-y.

[173] Ignacio Romero. "A comparison of finite elements for nonlinear beams: the absolute nodal coordinate and geometrically exact formulations". In: *Multibody System Dynamics* 20.1 (Aug. 2008), pp. 51–68. ISSN: 1384-5640. DOI: 10.1007/s11044-008-9105-7.

[174] Keisuke Otsuka et al. "Multifidelity Modeling of Deployable Wings: Multibody Dynamic Simulation and Wind Tunnel Experiment". In: *AIAA Journal* 57.10 (Oct. 2019), pp. 4300–4311. ISSN: 0001-1452. DOI: 10.2514/1.J058676.

[175] Keisuke Otsuka, Yinan Wang, and Kanjuro Makihara. "Versatile Absolute Nodal Coordinate Formulation Model for Dynamic Folding Wing Deployment and Flutter Analyses". In: *Journal of Vibration and Acoustics* 141.1 (Feb. 2019). ISSN: 1048-9002. DOI: 10.1115/1.4041022.

[176] Ahmed A. Shabana. "An overview of the ANCF approach, justifications for its use, implementation issues, and future research directions". In: *Multibody System Dynamics* 58.3-4 (2023). ISSN: 1573272X. DOI: 10.1007/s11044-023-09890-z.

[177] Riko Ogawara, Stefan Kaczmarczyk, and Yoshiaki Terumichi. "Numerical approach for flexible body with internal boundary movement". In: *Scientific Reports* 13.1 (2023). ISSN: 20452322. DOI: 10.1038/s41598-023-32526-3.

[178] J. L Lagrange, William Thomson Kelvin, and William Howie. *Méchanique analitique*. A Paris: Chez la veuve Desaint, 1788. DOI: 10.5479/sil.322586.39088000898585.

[179] Theodore Theodorsen. *General Theory of Aerodynamic Instability and the Mechanism of Flutter, NACA Report 496, 1935*. 1935.

[180] Herbert Wagner. "Über die Entstehung des dynamischen Auftriebes von Tragflügeln". In: *ZAMM - Journal of Applied Mathematics and Mechanics / Zeitschrift für Angewandte Mathematik und Mechanik* 5.1 (1925). ISSN: 15214001. DOI: 10.1002/zamm.19250050103.

[181] Edward Albano and William P. Hodden. "A doublet-lattice method for calculating lift distributions on oscillating surfaces in subsonic flows". In: *AIAA Journal* 7.2 (1969). ISSN: 00011452. DOI: 10.2514/3.5086.

[182] E. H. Atta et al. *Unsteady flow past wings having sharp-edge separation*. Tech. rep. NASA. Langley Res. Center, 1976. URL: https://ntrs.nasa.gov/citations/19760021097.

[183] Joseph Katz and Allen Plotkin. *Low-Speed Aerodynamics*. 2001. DOI: 10.1017/cbo9780511810329.

[184] Nicola Fonzi, Steven L. Brunton, and Urban Fasel. "Data-Driven Modeling for Transonic Aeroelastic Analysis". In: *Journal of Aircraft* 61.2 (Mar. 2024), pp. 625–637. ISSN: 0021-8669. DOI: 10.2514/1.C037409.

[185] Joseba Murua, Rafael Palacios, and J. Michael R. Graham. "Applications of the unsteady vortex-lattice method in aircraft aeroelasticity and flight dynamics". In: *Progress in Aerospace Sciences* 55 (Nov. 2012), pp. 46–72. ISSN: 03760421. DOI: 10.1016/j.paerosci.2012.06.001. URL: https://linkinghub.elsevier.com/retrieve/pii/S0376042112000620.

[186] Stefanie Düssler. "Nonlinear aeroservoelastic modelling for design and performance evaluation of gust load alleviation systems for flexible air vehicles". PhD thesis. Imperial College London, 2024. DOI: 10.25560/115128. URL: http://hdl.handle.net/10044/1/115128%20https://doi.org/10.25560/115128.

[187] Alfonso del Carre et al. "SHARPy: A dynamic aeroelastic simulation toolbox for very flexible aircraft and wind turbines". In: *Journal of Open Source Software* 4.44 (Dec. 2019), p. 1885. ISSN: 2475-9066. DOI: 10.21105/joss.01885. URL: https://joss.theoj.org/papers/10.21105/joss.01885.

[188] Ch. Lunk and B. Simeon. "Solving constrained mechanical systems by the family of Newmark and α-methods". In: *ZAMM - Journal of Applied Mathematics and Mechanics / Zeitschrift für Angewandte Mathematik und Mechanik* 86.10 (Oct. 2006), pp. 772–784. ISSN: 0044-2267. DOI: 10.1002/zamm.200610285.

[189] Martin Arnold and Olivier Brüls. "Convergence of the generalized-α scheme for constrained mechanical systems". In: *Multibody System Dynamics* 18.2 (Aug. 2007), pp. 185–202. ISSN: 1384-5640. DOI: 10.1007/s11044-007-9084-0.

[190] Ahmed A. Shabana. "Flexible Multibody Dynamics: Review of Past and Recent Developments". In: *Multibody System Dynamics* 1.2 (1997), pp. 189–222. ISSN: 13845640. DOI: 10.1023/A:1009773505418.

[191] Henrik Hesse. "Consistent aeroelastic linearisation and reduced-order modelling in the dynamics of manoeuvring flexible aircraft". In: *Imperial College London* Ph.D. Thesis (2013).

[192] Henrik Hesse and Rafael Palacios. "Consistent structural linearisation in flexible-body dynamics with large rigid-body motion". In: *Computers & Structures* 110-111 (Nov. 2012), pp. 1–14. ISSN: 00457949. DOI: 10.1016/j.compstruc.2012.05.011.

[193] Jonathan Hilger. "A Dynamic Nonlinear Inertia Relief Formulation". In: *AIAA SCITECH 2024 Forum*. Reston, Virginia: American Institute of Aeronautics and Astronautics, Jan. 2024. ISBN: 978-1-62410-711-5. DOI: 10.2514/6.2024-2258.

[194] Olivier Andre Bauchau. *Flexible Multibody Dynamics*. Vol. 176. Dordrecht [u.a.]: Springer, 2011. ISBN: 9789400703346.

[195] Stefanie Düssler and Rafael Palacios. "Enhanced Unsteady Vortex Lattice Aerodynamics for Nonlinear Flexible Aircraft Dynamic Simulation". In: *AIAA Journal* 62.3 (Mar. 2024), pp. 1179–1194. ISSN: 0001-1452. DOI: 10.2514/1.J063174.

[196] Stefanie Düssler et al. "Modelling and Numerical Enhancements on a UVLM for Nonlinear Aeroelastic Simulation". In: *AIAA SCITECH 2022 Forum*. Reston, Virginia: American Institute of Aeronautics and Astronautics, Jan. 2022. ISBN: 978-1-62410-631-6. DOI: 10.2514/6.2022-2455.

[197] Arturo Muñoz-Simón. "Vortex-lattice-based nonlinear aeroservoelastic modelling and analysis of large floating wind turbines". PhD thesis. Imperial College London, 2021. DOI: 10.25560/96986.

[198] Keisuke Otsuka, Chi Wing Cheng, and Rafael Palacios. "Absolute Nodal Coordinate Formulation for Nonlinear Multibody Modeling of Flared Hinged Wings". In: *34th Congress of the International Council of the Aeronautical Sciences, ICAS 2024* (2024).

[199] Keisuke Otsuka et al. "Geometrically Nonlinear Beam Model for Slender Multibody Wings". In: *The 22nd International Symposium on Advanced Fluid Information (AFI-2022)*. Sendai, Japan, 2022.

[200] Kelvin Chi-Wing Cheng et al. "Nonlinear Multibody Modeling of Flexible Aircraft with Flared Hinged Wingtips". In: *Journal of Aircraft* 62.4 (July 2025), pp. 929–948. ISSN: 0021-8669. DOI: 10.2514/1.C038094.

[201] Yinan Wang et al. "Aeroelastic Simulation of High-Aspect Ratio Wings with Intermittent Leading-Edge Separation". In: *AIAA Journal* 60.3 (Mar. 2022), pp. 1769–1782. ISSN: 0001-1452. DOI: 10.2514/1.J060909.

[202] Keisuke Otsuka et al. "Consistent Strain-Based Multifidelity Modeling for Geometrically Nonlinear Beam Structures". In: *Journal of Computational and Nonlinear Dynamics* 17.11 (Nov. 2022). ISSN: 1555-1415. DOI: 10.1115/1.4055310.

[203] Keisuke Otsuka, Yinan Wang, and Kanjuro Makihara. "Absolute Nodal Coordinate Formulation With Vector-Strain Transformation for High Aspect Ratio Wings". In: *Journal of Computational and Nonlinear Dynamics* 16.1 (Jan. 2021). ISSN: 1555-1415. DOI: 10.1115/1.4049028.

[204] Arturo Muñoz-Simón, Rafael Palacios, and Andrew Wynn. "Some modelling improvements for prediction of wind turbine rotor loads in turbulent wind". In: *Wind Energy* 25.2 (Feb. 2022), pp. 333–353. ISSN: 1095-4244. DOI: 10.1002/we.2675.

[205] Andrea Castrichini. "Parametric Assessment of a Folding Wing-Tip Device for Aircraft Loads Alleviation". PhD thesis. University of Bristol, 2017. URL: https://www.researchgate.net/publication/318040984_Parametric_Assessment_of_a_Folding_Wing-Tip_Device_for_Aircraft_Loads_Alleviation.

[206] Norberto Goizueta Alfaro. "Parametric reduced-order aeroelastic modelling for analysis, dynamic system interpolation and control of flexible aircraft". PhD thesis. Imperial College London, 2022. DOI: 10.25560/100137. URL: http://hdl.handle.net/10044/1/100137%20https://doi.org/10.25560/100137.

[207] C. Farhat, M. Lesoinne, and P. Le Tallec. "Load and motion transfer algorithms for fluid/structure interaction problems with non-matching discrete interfaces: Momentum and energy conservation, optimal discretization and application to aeroelasticity". In: *Computer Methods in Applied Mechanics and Engineering* 157.1-2 (Apr. 1998), pp. 95–114. ISSN: 00457825. DOI: 10.1016/S0045-7825(97)00216-8.

[208] T. C. S. Rendall and C. B. Allen. "Unified fluid–structure interpolation and mesh motion using radial basis functions". In: *International Journal for Numerical Methods in Engineering* 74.10 (June 2008), pp. 1519–1559. ISSN: 0029-5981. DOI: 10.1002/nme.2219.

[209] Marc Artola et al. "Proof of Concept for a Hardware-in-the-Loop Nonlinear Control Framework for Very Flexible Aircraft". In: *AIAA Scitech 2021 Forum*. Reston, Virginia: American Institute of Aeronautics and Astronautics, Jan. 2021. ISBN: 978-1-62410-609-5. DOI: 10.2514/6.2021-1392. URL: https://arc.aiaa.org/doi/10.2514/6.2021-1392.

[210] Kermit G. Pratt. *A Revised Formula For The Calculation Of Gust Loads*. 1953. URL: https://ntrs.nasa.gov/api/citations/19930084025/.

[211] Alfonso del Carre and Rafael Palacios. "Simulation and Optimization of Takeoff Maneuvers of Very Flexible Aircraft". In: *Journal of Aircraft* 57.6 (Nov. 2020), pp. 1097–1110. ISSN: 1533-3868. DOI: 10.2514/1.C035901.

[212] Stefanie Düssler and Rafael Palacios. *Scripts for the Demonstration of Enhanced Unsteady Vortex Lattice Aerodynamics for Nonlinear Flexible Aircraft Dynamic Simulation*. 2023. DOI: 10.5281/zenodo.8336814.

[213] European Commission. *Flutter Free FLight Envelope eXpansion for ecOnomical Performance improvement*. June 2015. DOI: 10.3030/636307. URL: https://cordis.europa.eu/project/id/636307.

[214] European Commission. *Flight Phase Adaptive Aero-Servo-Elastic Aircraft Design Methods*. Sept. 2019. DOI: 10.3030/815058. URL: https://cordis.europa.eu/project/id/815058.

[215] Yasser M. Meddaikar et al. "Aircraft aeroservoelastic modelling of the flexop unmanned flying demonstrator". In: *AIAA Scitech 2019 Forum*. 2019. DOI: 10.2514/6.2019-1815.

[216] Christian Roessler et al. "Aircraft design and testing of flexop unmanned flying demonstrator to test load alleviation and flutter suppression of high aspect ratio flexible wings". In: *AIAA Scitech 2019 Forum*. 2019. DOI: 10.2514/6.2019-1813.

[217] Christian Roessler et al. "Results of an aeroelastically tailored wing on the flexop demonstrator aircraft". In: *AIAA Scitech 2020 Forum*. Vol. 1 PartF. 2020. DOI: 10.2514/6.2020-1969.

[218] Béla Takarics et al. "Active flutter mitigation testing on the flexop demonstrator aircraft". In: *AIAA Scitech 2020 Forum*. Vol. 1 PartF. 2020. DOI: 10.2514/6.2020-1970.

[219] Jurij Sodja et al. "Ground testing of the flexop demonstrator aircraft". In: *AIAA Scitech 2020 Forum*. Vol. 1 PartF. 2020. DOI: 10.2514/6.2020-1968.

[220] Jurij Sodja, Noud P. M. Werter, and Roeland De Breuker. "Aeroelastic Demonstrator Wing Design for Maneuver Load Alleviation Under Cruise Shape Constraint". In: *Journal of Aircraft* 58.3 (2021). DOI: 10.2514/1.c035955.

[221] Wolf R. Krüger et al. "Application of Aeroelastic Tailoring for Load Alleviation on a Flying Demonstrator Wing †". In: *Aerospace* 9.10 (2022). ISSN: 22264310. DOI: 10.3390/aerospace9100535.

[222] Ben Preston et al. "Multibody Simulation of Flexible Aircraft with Variable-Sweep Wingtips". In: *AIAA Journal* (Nov. 2025), pp. 1–14. ISSN: 0001-1452. DOI: 10.2514/1.J065846.

[223] EASA. *Easy Access Rules for Large Aeroplanes (CS-25)*. Tech. rep. 2023. URL: https://www.easa.europa.eu/en/document-library/easy-access-rules/online-publications/easy-access-rules-large-aeroplanes-cs-25.

[224] Alvaro Cea, Rafael Palacios, and Lucian Iorga. "Near-Real-Time Nonlinear Analysis of Free-Flying Flexible Aircraft on Modern Hardware Architectures". In: *AIAA Journal* (Oct. 2025), pp. 1–14. ISSN: 0001-1452. DOI: 10.2514/1.J065779.

[225] Francesco Sacchi et al. "Effect of Wing Flexibility and Bending-Torsion Coupling on Roll Behavior of Wings Incorporating Flared Folding Wingtips". In: *AIAA SCITECH 2025 Forum*. Reston, Virginia: American Institute of Aeronautics and Astronautics, Jan. 2025. ISBN: 978-1-62410-723-8. DOI: 10.2514/6.2025-0713.

Appendix A

Symbolic expressions for the rigid constant density double pendulum

A.1 Full equations of motion

The equations of motion for the rigid constant density double pendulum with slanted hinge are given below in full, as expanded using a symbolic maths package.

$$
\begin{aligned}
&-\frac{g l_1 m_1 \cos\left(\theta_1(t)\right)}{2} - g l_1 m_2 \cos\left(\theta_1(t)\right) \\
&- \frac{g l_2 m_2 \sin^2\left(\beta\right) \cos\left(\theta_1(t)\right) \cos\left(\theta_2(t)\right)}{2} \\
&+ \frac{g l_2 m_2 \sin\left(\theta_1(t)\right) \sin\left(\theta_2(t)\right) \cos\left(\beta\right)}{2} \\
&- \frac{g l_2 m_2 \cos\left(\beta\right) \cos\left(\theta_1(t)\right) \cos\left(\theta_2(t)\right) \left|\cos\left(\beta\right)\right|}{2} + \frac{l_1^2 m_1 \frac{d^2}{dt^2}\theta_1(t)}{3} \\
&+ l_1^2 m_2 \frac{d^2}{dt^2}\theta_1(t) - l_1 l_2 m_2 \sin^2\left(\beta\right) \sin\left(\theta_2(t)\right) \frac{d}{dt}\theta_1(t) \frac{d}{dt}\theta_2(t) \\
&+ l_1 l_2 m_2 \sin^2\left(\beta\right) \cos\left(\theta_2(t)\right) \frac{d^2}{dt^2}\theta_1(t) \\
&- l_1 l_2 m_2 \sin\left(\theta_2(t)\right) \cos\left(\beta\right) \left|\cos\left(\beta\right)\right| \frac{d}{dt}\theta_1(t) \frac{d}{dt}\theta_2(t) \\
&- \frac{l_1 l_2 m_2 \sin\left(\theta_2(t)\right) \cos\left(\beta\right) \left(\frac{d}{dt}\theta_2(t)\right)^2}{2} \\
&+ l_1 l_2 m_2 \cos\left(\beta\right) \cos\left(\theta_2(t)\right) \left|\cos\left(\beta\right)\right| \frac{d^2}{dt^2}\theta_1(t) \\
&+ \frac{l_1 l_2 m_2 \cos\left(\beta\right) \cos\left(\theta_2(t)\right) \frac{d^2}{dt^2}\theta_2(t)}{2} \\
&- \frac{l_2^2 m_2 \sin^4\left(\beta\right) \sin^2\left(\theta_2(t)\right) \frac{d^2}{dt^2}\theta_1(t)}{2} \\
&- l_2^2 m_2 \sin^4\left(\beta\right) \sin\left(\theta_2(t)\right) \cos\left(\theta_2(t)\right) \frac{d}{dt}\theta_1(t) \frac{d}{dt}\theta_2(t) \\
&+ \frac{l_2^2 m_2 \sin^4\left(\beta\right) \frac{d^2}{dt^2}\theta_1(t)}{2} \\
&- \frac{l_2^2 m_2 \sin^2\left(\beta\right) \sin^2\left(\theta_2(t)\right) \cos\left(\beta\right) \left|\cos\left(\beta\right)\right| \frac{d^2}{dt^2}\theta_1(t)}{2} \\
&+ \frac{l_2^2 m_2 \sin^2\left(\beta\right) \sin^2\left(\theta_2(t)\right) \frac{d^2}{dt^2}\theta_1(t)}{4} \\
&- l_2^2 m_2 \sin^2\left(\beta\right) \sin\left(\theta_2(t)\right) \cos\left(\beta\right) \cos\left(\theta_2(t)\right) \left|\cos\left(\beta\right)\right| \frac{d}{dt}\theta_1(t) \frac{d}{dt}\theta_2(t) \\
&+ \frac{l_2^2 m_2 \sin^2\left(\beta\right) \sin\left(\theta_2(t)\right) \cos\left(\theta_2(t)\right) \frac{d}{dt}\theta_1(t) \frac{d}{dt}\theta_2(t)}{2} \\
&+ \frac{l_2^2 m_2 \sin^2\left(\beta\right) \cos\left(\beta\right) \left|\cos\left(\beta\right)\right| \frac{d^2}{dt^2}\theta_1(t)}{2} \\
&+ \frac{l_2^2 m_2 \sin^2\left(\beta\right) \cos\left(\beta\right) \frac{d^2}{dt^2}\theta_2(t)}{4} - \frac{l_2^2 m_2 \sin^2\left(\beta\right) \left|\cos\left(\beta\right)\right| \frac{d^2}{dt^2}\theta_2(t)}{4} \\
&- \frac{l_2^2 m_2 \sin^2\left(\beta\right) \frac{d^2}{dt^2}\theta_1(t)}{2} + \frac{l_2^2 m_2 \cos\left(\beta\right) \frac{d^2}{dt^2}\theta_2(t)}{12} \\
&+ \frac{l_2^2 m_2 \left|\cos\left(\beta\right)\right| \frac{d^2}{dt^2}\theta_2(t)}{4} + \frac{l_2^2 m_2 \frac{d^2}{dt^2}\theta_1(t)}{3} + \frac{m_1 w_1^2 \frac{d^2}{dt^2}\theta_1(t)}{12} \\
&+ \frac{m_2 w_2^2 \cos\left(\beta\right) \frac{d^2}{dt^2}\theta_2(t)}{12} + \frac{m_2 w_2^2 \frac{d^2}{dt^2}\theta_1(t)}{12} = 0,
\end{aligned}
\tag{A.1}
$$

$$
\begin{aligned}
&\frac{g l_2 m_2 \sin^2(\beta) \sin(\theta_1(t)) \sin(\theta_2(t))}{2} \\
&+ \frac{g l_2 m_2 \sin(\theta_1(t)) \sin(\theta_2(t)) \cos(\beta) |\cos(\beta)|}{2} \\
&- \frac{g l_2 m_2 \cos(\beta) \cos(\theta_1(t)) \cos(\theta_2(t))}{2} \\
&+ \frac{l_1 l_2 m_2 \sin^2(\beta) \sin(\theta_2(t)) \left(\frac{d}{dt}\theta_1(t)\right)^2}{2} \\
&+ \frac{l_1 l_2 m_2 \sin(\theta_2(t)) \cos(\beta) |\cos(\beta)| \left(\frac{d}{dt}\theta_1(t)\right)^2}{2} \\
&+ \frac{l_1 l_2 m_2 \cos(\beta) \cos(\theta_2(t)) \frac{d^2}{dt^2}\theta_1(t)}{2} \\
&+ \frac{l_2^2 m_2 \sin^4(\beta) \sin(\theta_2(t)) \cos(\theta_2(t)) \left(\frac{d}{dt}\theta_1(t)\right)^2}{2} \\
&+ \frac{l_2^2 m_2 \sin^2(\beta) \sin^2(\theta_2(t)) \frac{d^2}{dt^2}\theta_2(t)}{4} \\
&+ \frac{l_2^2 m_2 \sin^2(\beta) \sin(\theta_2(t)) \cos(\beta) \cos(\theta_2(t)) |\cos(\beta)| \left(\frac{d}{dt}\theta_1(t)\right)^2}{2} \\
&- \frac{l_2^2 m_2 \sin^2(\beta) \sin(\theta_2(t)) \cos(\theta_2(t)) \left(\frac{d}{dt}\theta_1(t)\right)^2}{4} \\
&+ \frac{l_2^2 m_2 \sin^2(\beta) \sin(\theta_2(t)) \cos(\theta_2(t)) \left(\frac{d}{dt}\theta_2(t)\right)^2}{4} \\
&+ \frac{l_2^2 m_2 \sin^2(\beta) \cos(\beta) \frac{d^2}{dt^2}\theta_1(t)}{4} - \frac{l_2^2 m_2 \sin^2(\beta) |\cos(\beta)| \frac{d^2}{dt^2}\theta_1(t)}{4} \\
&- \frac{l_2^2 m_2 \sin^2(\beta) \frac{d^2}{dt^2}\theta_2(t)}{3} + \frac{l_2^2 m_2 \cos(\beta) \frac{d^2}{dt^2}\theta_1(t)}{12} \\
&+ \frac{l_2^2 m_2 |\cos(\beta)| \frac{d^2}{dt^2}\theta_1(t)}{4} + \frac{l_2^2 m_2 \frac{d^2}{dt^2}\theta_2(t)}{3} + \frac{m_2 w_2^2 \sin^2(\beta) \frac{d^2}{dt^2}\theta_2(t)}{12} \\
&+ \frac{m_2 w_2^2 \cos(\beta) \frac{d^2}{dt^2}\theta_1(t)}{12} + \frac{m_2 w_2^2 \frac{d^2}{dt^2}\theta_2(t)}{12} = 0,
\end{aligned}
\tag{A.2}
$$

which if we take $\beta = 0$ so the system collapses to a planar double pendulum, becomes

$$
\begin{aligned}
&-\frac{g l_1 m_1 \cos(\theta_1(t))}{2} - g l_1 m_2 \cos(\theta_1(t)) + \frac{g l_2 m_2 \sin(\theta_1(t)) \sin(\theta_2(t))}{2} \\
&- \frac{g l_2 m_2 \cos(\theta_1(t)) \cos(\theta_2(t))}{2} + \frac{l_1^2 m_1 \frac{d^2}{dt^2}\theta_1(t)}{3} + l_1^2 m_2 \frac{d^2}{dt^2}\theta_1(t) \\
&- l_1 l_2 m_2 \sin(\theta_2(t)) \frac{d}{dt}\theta_1(t) \frac{d}{dt}\theta_2(t) - \frac{l_1 l_2 m_2 \sin(\theta_2(t)) \left(\frac{d}{dt}\theta_2(t)\right)^2}{2} \\
&+ l_1 l_2 m_2 \cos(\theta_2(t)) \frac{d^2}{dt^2}\theta_1(t) + \frac{l_1 l_2 m_2 \cos(\theta_2(t)) \frac{d^2}{dt^2}\theta_2(t)}{2} + \frac{l_2^2 m_2 \frac{d^2}{dt^2}\theta_1(t)}{3} \\
&+ \frac{l_2^2 m_2 \frac{d^2}{dt^2}\theta_2(t)}{3} + \frac{m_1 w_1^2 \frac{d^2}{dt^2}\theta_1(t)}{12} + \frac{m_2 w_2^2 \frac{d^2}{dt^2}\theta_1(t)}{12} + \frac{m_2 w_2^2 \frac{d^2}{dt^2}\theta_2(t)}{12} = 0,
\end{aligned}
\tag{A.3}
$$

$$\begin{aligned}&\frac{g l_2 m_2 \sin\left(\theta_1(t)\right) \sin\left(\theta_2(t)\right)}{2} - \frac{g l_2 m_2 \cos\left(\theta_1(t)\right) \cos\left(\theta_2(t)\right)}{2} \\ &+ \frac{l_1 l_2 m_2 \sin\left(\theta_2(t)\right) \left(\frac{d}{dt}\theta_1(t)\right)^2}{2} + \frac{l_1 l_2 m_2 \cos\left(\theta_2(t)\right) \frac{d^2}{dt^2}\theta_1(t)}{2} \\ &+ \frac{l_2^2 m_2 \frac{d^2}{dt^2}\theta_1(t)}{3} + \frac{l_2^2 m_2 \frac{d^2}{dt^2}\theta_2(t)}{3} + \frac{m_2 w_2^2 \frac{d^2}{dt^2}\theta_1(t)}{12} + \frac{m_2 w_2^2 \frac{d^2}{dt^2}\theta_2(t)}{12} = 0.\end{aligned} \tag{A.4}$$